Experimental Measurements of Strains and Blast Waves Resulting From Detonations in Tubes

J. E. Shepherd, J. Karnesky, F. Pintgen, and J.C. Krok
Graduate Aeronautical Laboratories
California Institute of Technology
Pasadena, CA 91125

Explosion Dynamics Laboratory Report FM2006.010

July 3, 2008

Sponsored by the US DOE, NNSA through the Caltech ASC Alliance Program, Center for Simulation of Dynamic Response of Materials.

Abstract

We report the results of three sets of experiments on detonation-driven fracture that were performed in 2005. The aim of the experiments was to isolate and simplify the phenomena involved in detonation-driven fracture that had been observed in previous work. In each of the experiments, a detonation was propagated from an initiator into a test specimen consisting of a thin-wall aluminum tube held rigidly at each end. The goal of the first set of experiments was to obtain high-quality data that could be used for validation of a finite-element shell model. These tubes were instrumented with strain gages and an optical vibrometer was used to make displacement measurements close to the stain gage locations. The goal of the second set of experiments was to obtain data useful for validating fluid-dynamics simulations with the ASC Virtual Test Facility (VTF) to simulate three-dimensional compressible flow coupled to the large-scale deformation of shell structures. In the second series of experiments, a rigid machined slot was added in the middle of the tube in order to obtain blast waves that were independent of material deformation. The blast waves were recorded with blast gages and high-speed schlieren photography. In the third series of experiments, a simplified type of fluid-solid coupling involving plastic deformation was investigated by cutting pre-defined flaps into the tube. The pressure behind the detonation front opens the flaps in a much more defined manner than crack propagation so it is much more suitable for validating the VTF software.

Contents

List of Figures

List of Tables

1 Introduction

The Center for the Simulation of the Dynamic Response of Materials at Caltech has developed a software framework for simulating the coupled mechanics of solids and fluids under conditions of detonation loading and large deformation. The Explosion Dynamics Laboratory (EDL) has participated in the Center to develop experimental methods and provide high quality data that can be used for validating simulations. Our contributions build on our previous experimental studies of fluid-solid coupling that include shock-wave Beltman et al. (1999) and detonation wave (Beltman and Shepherd, 2002, 1998, Chao and Shepherd, 2005a) excitation of elastic vibrations in tubes. For the CSDRM program, we carried out a series of studies (Chao, 2004, Chao and Shepherd, 2005b, 2004) specifically designed to look at a more challenging regime in which the solid and fluid mechanics were strongly coupled. This program examined "detonation-driven fracture" using detonation waves inside a thin-wall tube to create propagating cracks originating from a deliberate flaw. The effects of flaw depth, flaw length, pre-stress (including torsion), and detonation parameters were examined in a series of carefully designed tests. These experiments proved difficult to use as validation tests since the crack propagation process was not sufficiently repeatable except at short times with substantial torsion on the tubes.

In order to isolate and simplify the phenomena involved in detonation-driven fracture that had been observed in previous work, a series of new experiments were performed in 2005. In each of the experiments, a detonation was propagated from an initiator into a test specimen consisting of a thin-wall aluminum tube held rigidly at each end. The goal of the first set of experiments was to obtain high-quality strain-time data that could be used for validation of a finite-element shell model developed by Cirak et al. (2000), Cirak and Ortiz (2001). These tubes were instrumented with strain gages and a vibrometer was used to make displacement measurements close to the stain gage locations. The goal of the second set of experiments was to obtain data useful for validating fluid-dynamics simulations with the ASC Virtual Test Facility (VTF) (Deiterding et al., 2006) using AMROC software to simulate three-dimensional compressible flow coupled to the large-scale deformation of shell structures (Cirak et al., 2006, Deiterding et al., 2007). In these tests, a rigid machined slot was added in the middle of the tube in order to obtain blast waves that were independent of material deformation. The blast waves were recorded with blast gages and high-speed schlieren photography. In the third series of experiments, a simplified type of fluid-solid coupling involving plastic deformation was investigated by cutting pre-defined flaps into the tube. The pressure behind the detonation front opens the flaps in a much more defined manner than crack propagation so it is much more suitable for validating the VTF software.

The blast pressures were recorded, and flap motion and blast waves were visualized with a schlieren system.

This report describes the test fixtures, experimental conditions, and test results. A companion report (Liang et al., 2008) describes some additional measurements that were carried out in order to quantify the repeatability of pressure and strain data in closed tubes.

2 Test Fixture

The test fixture is described in detail in Chao (Chap. 6 and App. B of 2004). The basic layout and dimensions are shown in Fig. 1, note that the details of the specimen tubing mounting and dimensions of the specimen tubes differ from what is shown and this figure only indicates the general layout. The fixture consists of a thick-wall detonation initiation tube coupled to the test specimen. The initiation tube is 1.53 m long with a 38 mm internal diameter and an outer diameter of 50.8 mm. All experiments used stoichiometric ethylene-oxygen mixtures ($C_2H_4 + 3O_2$), at initial pressures of 40, 50, and 100 kPa and room temperature 22-15°C. The method of partial pressures was used to fix the composition. The tube was evacuated to a pressure less than 20 Pa before adding the gases separately and mixing with a circulation pump.

Combustion was initiated with a capacitor discharge unit (0.4 J stored energy) and a modified aviation spark plug. Transition from deflagration to detonation was promoted by using a 300-mm long Schelkin spiral in the initiator portion of the tube. The initiator portion, as well as the reflecting end piece, were the same for all tests. These portions were instrumented with PCB piezoelectric pressure transducers, from which detonation pressure and velocity were obtained. The detonation velocity was usually within 1% of the computed (Reynolds, 1986a) Chapman-Jouguet value of 2375.6 m/s. Repeated tests carried out to examine the pressure histories showed (Liang et al., 2008) that these were highly reproducible.

The test specimen is a thin-wall cylindrical tube that is held by collets to the I-beam and mates to the detonation tube with slip-on fittings so it can be changed between tests. The standard specimen was the same as that used by Chao (2004) and was a section of extruded (seamless) 6061-T6 aluminum tube (Table 1) with an outer diameter of 41 mm and a nominal[1] wall thickness of 0.9 mm. The test specimen and detonation tube were fastened to an I-beam support structure described by Chao (2004, Chap. 6 and App. B)

[1] A systematic variation in wall thickness existed in these tubes. The precise measurement and inclusion of this effect in simulations is discussed in detail in this report.

Table 1: Test Specimen Properties, 6061-T6 Aluminum.

Thermal expansion coefficient	24.3	μm/m°C
Thermal Conductivity	155.8	W/m°C
Mass density	2780	kg/m^3
Young's modulus	69	GPa
Specific heat capacity	963	J/kg°C
Poisson's ratio	0.33	
Average (between inner and outer) radius	22.275	mm
Average wall thickness	0.87	mm

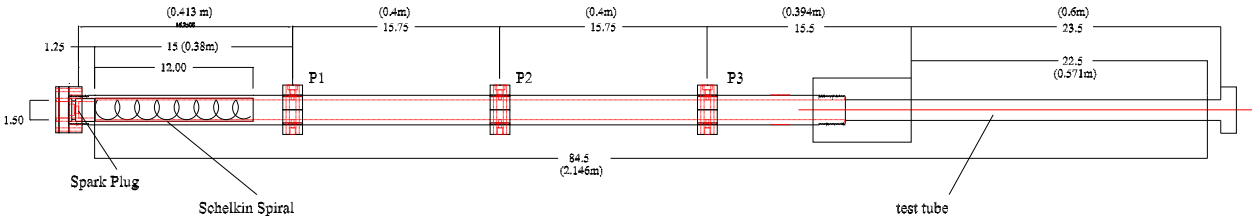

Figure 1: Basic layout and key dimensions of the experimental fixture.

2.1 Test Conditions

Three series of experiments were conducted.

The first series (shots 1-29) was aimed at investigating the elastic stress waves in the tube. Hoop strains were measured with both bonded strain gages and an optical displacement instrument. Related experiments (shots 30-34, and some tests in 2006) together with comparison of the computed and measured pressures are described in detail in the companion report Liang et al. (2008)

The second series (shots 35-53) dealt with the fluid mechanics of the blast wave expanding from a slit opening in the tube. The goal was to examine a situation that was simpler than dynamic fracture but still had some of the elements of the fluid dynamics connected with the flow through a crack. In order to do this, we used a fixed slot that was reinforced so the tube did not fracture. Two PCB pencil gages were used to measure the blast overpressure at various distances and angles to the slot. In addition, a Schlieren system was used with a high speed camera to obtain a sequence of images of the shock and reaction front which expand from the slot.

The third series (shots 54-58) studied a simplified case of fluid-solid coupling with the detonation opening pre-cut flaps in the tube. The pressure from the detonation caused the flaps to plastically deform, and the high speed camera was used to measure the rate at which they opened.

3 Closed tube tests

These tests were conducted to examine the issues of repeatability and accuracy in measurements of strain. The goal was to eliminate systematic sources of measurement error and quantify uncertainty in order to make the measurements as useful as possible for validating numerical simulations of the structural dynamics. Following a series of tests in 2004 and comparisons with numerical simulations by F. Cirak, systematic discrepancies were noted and some issues in the experimental data were identified. We sought to answer the following questions: What are the sources of scatter in the experimental data? How significant is the disagreement between experimental data and simulation? How repeatable is the detonation loading? Are bonded strain gage measurements reliable in this situation?

Our approach to answering these questions was to carry out repeated tests with careful control of experimental conditions. New instrumentation, a vibrometer, was used to measure radial displacement and compute hoop strain. The vibrometer is based on optical interferometry and being a noncontact instrument, eliminates the main drawbacks associated with bonded strain gages. In addition to these experiments, comparisons were made with new simulations that model the experiments more faithfully.

Figure 2 contains a schematic of the experimental setup for the elastic wave experiments. The two collets are 420mm apart, and are tightened so as to provide a good approximation of a built-in boundary condition. Photographs of the tube configuration and collets are shown in Fig. 3.

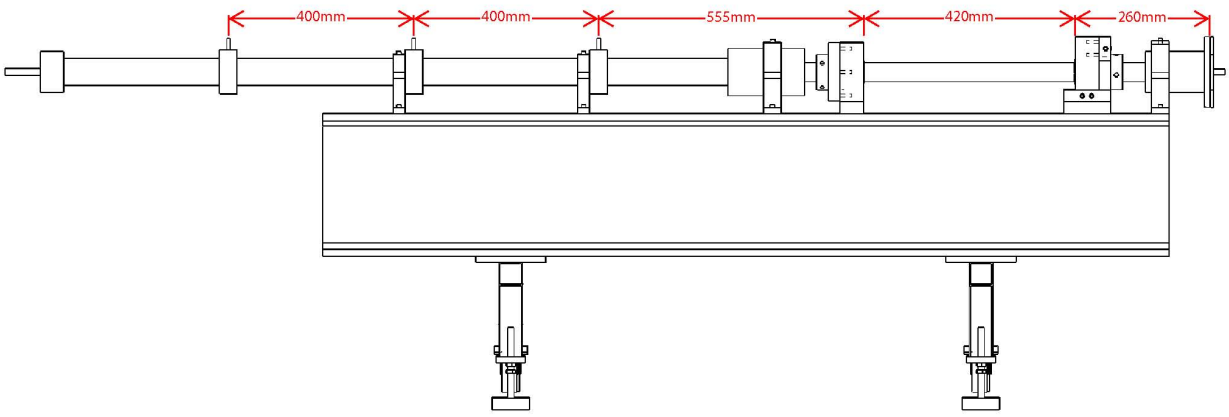

Figure 2: Tube setup for closed tube shots.

Halfway between the collets is the central strain measurement location on the test specimen. For most tests (except those noted in Table 3), the tube was instrumented with strain gages as in Fig. 4.

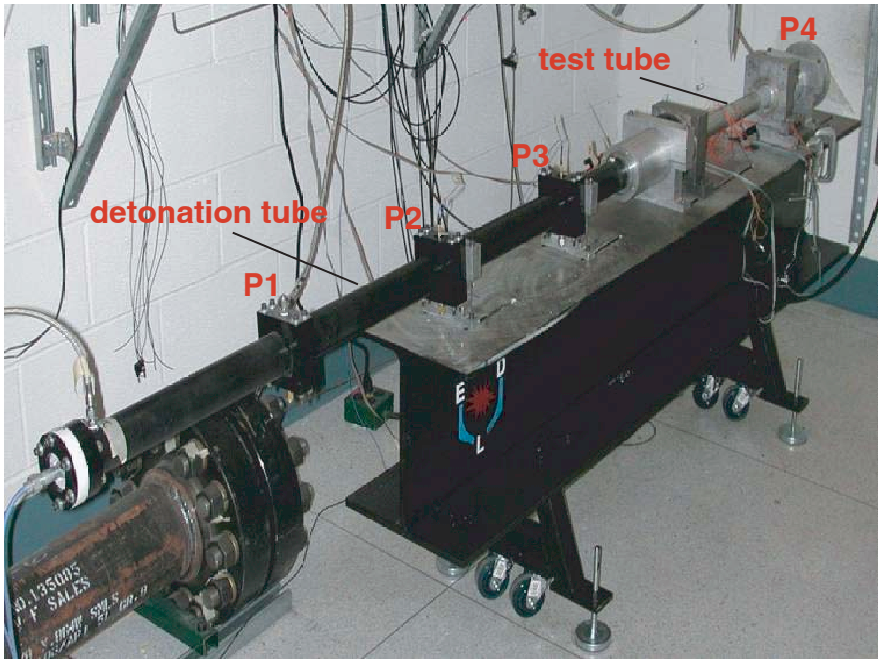

(a)

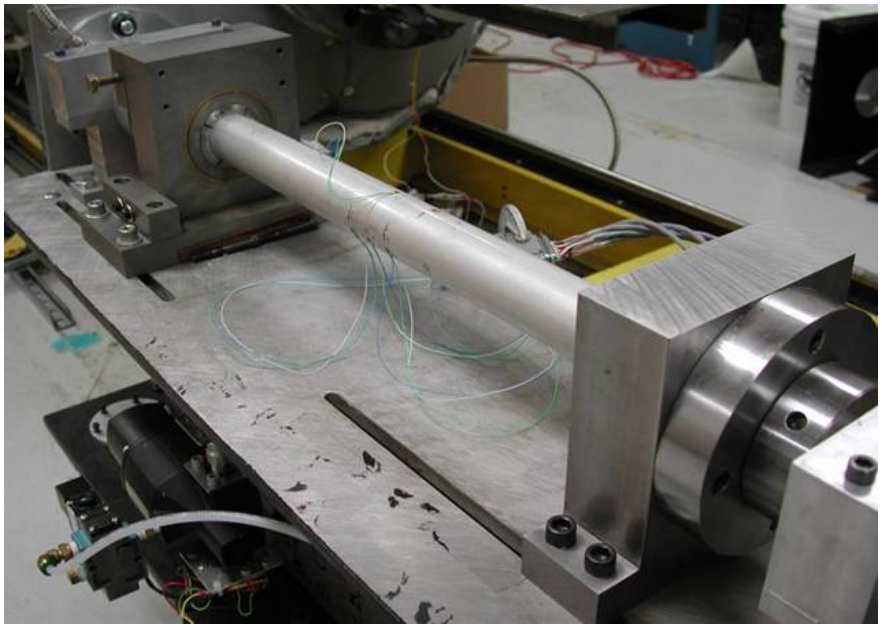

(b)

Figure 3: Test fixture photographs showing a) Detonation and specimen tubes and b) Close-up of collets and strain gages on specimen

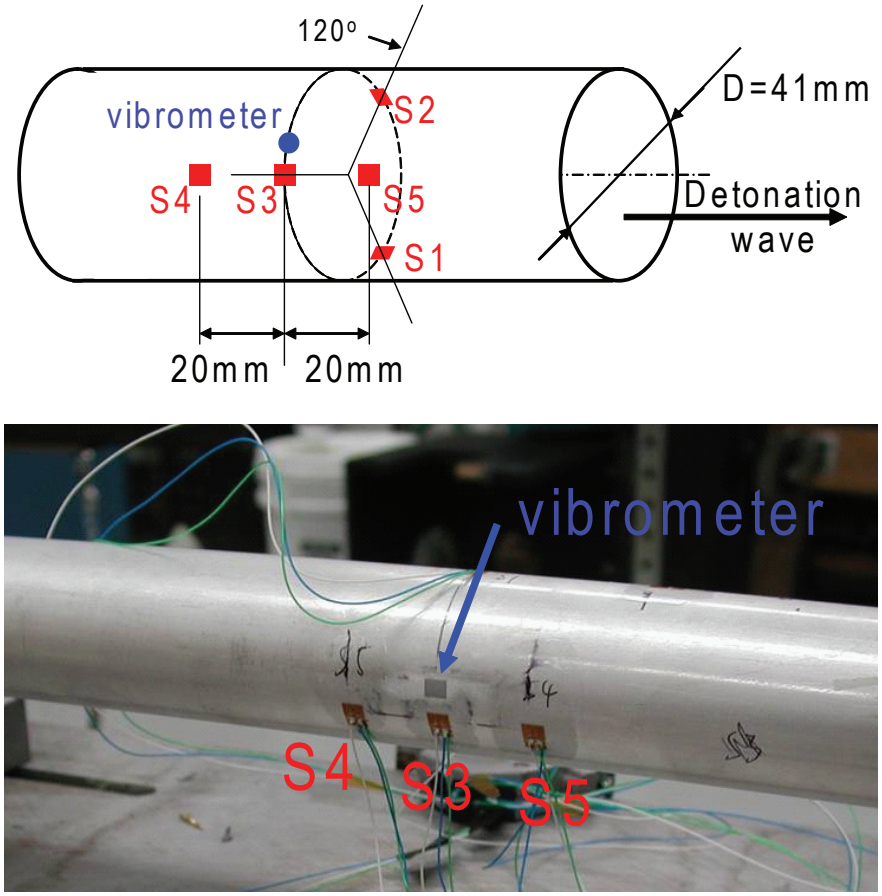

Figure 4: Measurement locations for closed tube tests

The first series of tests examined a number of issues associated with using bonded strain gages. Strain gages are well-studied and are known (see Chap. 2 of Kobayashi, 1993) to be subject to a number of effects that need to be considered in making high precision measurements. These include:

1. Bonding of gages
2. Fatigue of gages
3. Creep of gages
4. Bending of tube due to preloading
5. Temperature compensation of gages
6. Temperature control of tube
7. Differential thermal expansion of gage and substrate

8. Thermal stress induced by temperature gradient between inner and outer tube surfaces

In order to examine these issues, we carried out multiple (28) tests with the same sample using several levels of initial pressure, 40, 50 and 100 kPa. The conditions for all tests are given in Appendix A, Table 3. Plots of the stain and pressure signals for tests 10–29 area also given in Appendix A. The data for tests 30–34 are discussed in the companion report by Liang et al. (2008). We measured strain at five locations (Fig. 4) with bonded strain gages (Vishay Micromeasurements CEA-06-125UN-350 or CEA-06-125UN-120) using precision bridges and instrumentation amplifiers (Vishay 2310 Signal Conditioning Amplifier).

3.1 Baseline Tests With Strain Gages

These tests used only strain gages and examined the repeatability of the signals for replica tests at the same detonation conditions. Data from the strain gages in these tests is compared along the axial direction in Fig. 5 and along the azimuthal direction in Fig. 6 for shots 2–5.

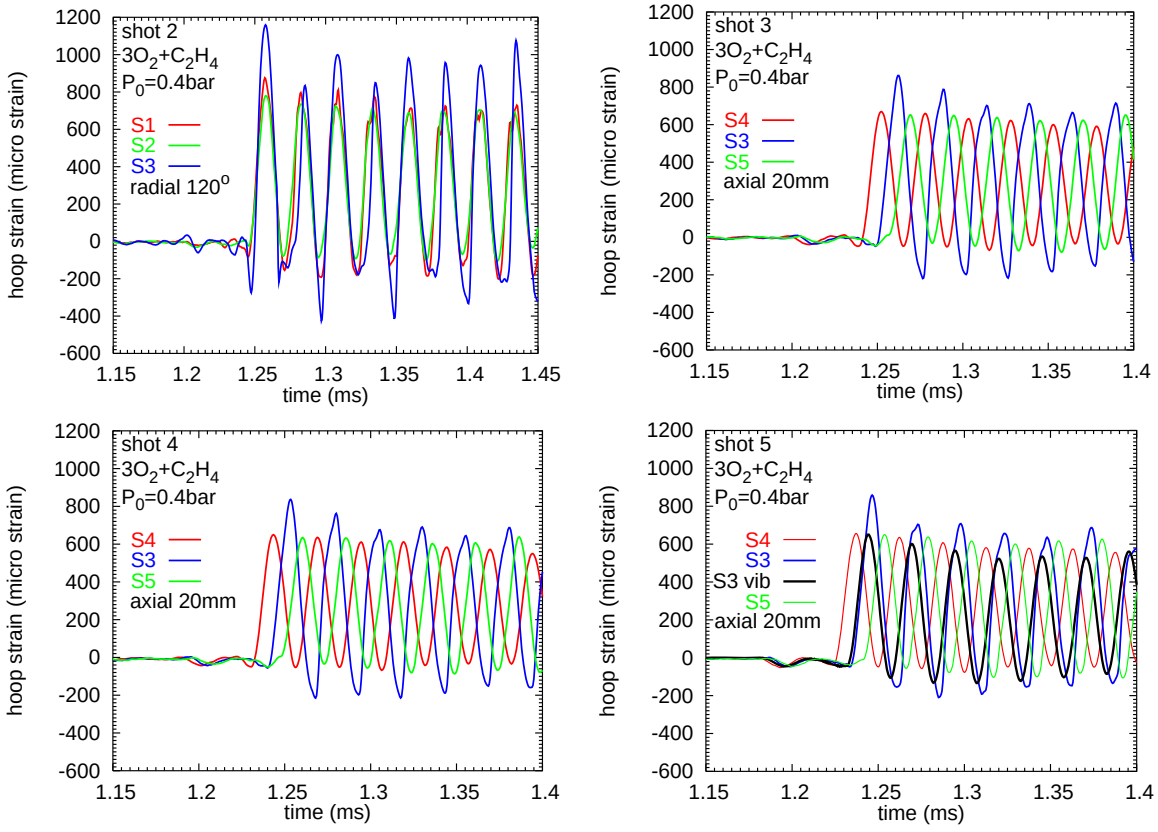

Figure 5: Hoop strains for the axial gage locations in tests 2–5. Initial pressure of 40 kPa.

The repeatability of the detonation was previously established in the tests reported in Liang et al. (2008). Velocity measurements in the first 20 tests are shown in Fig. 7. With the

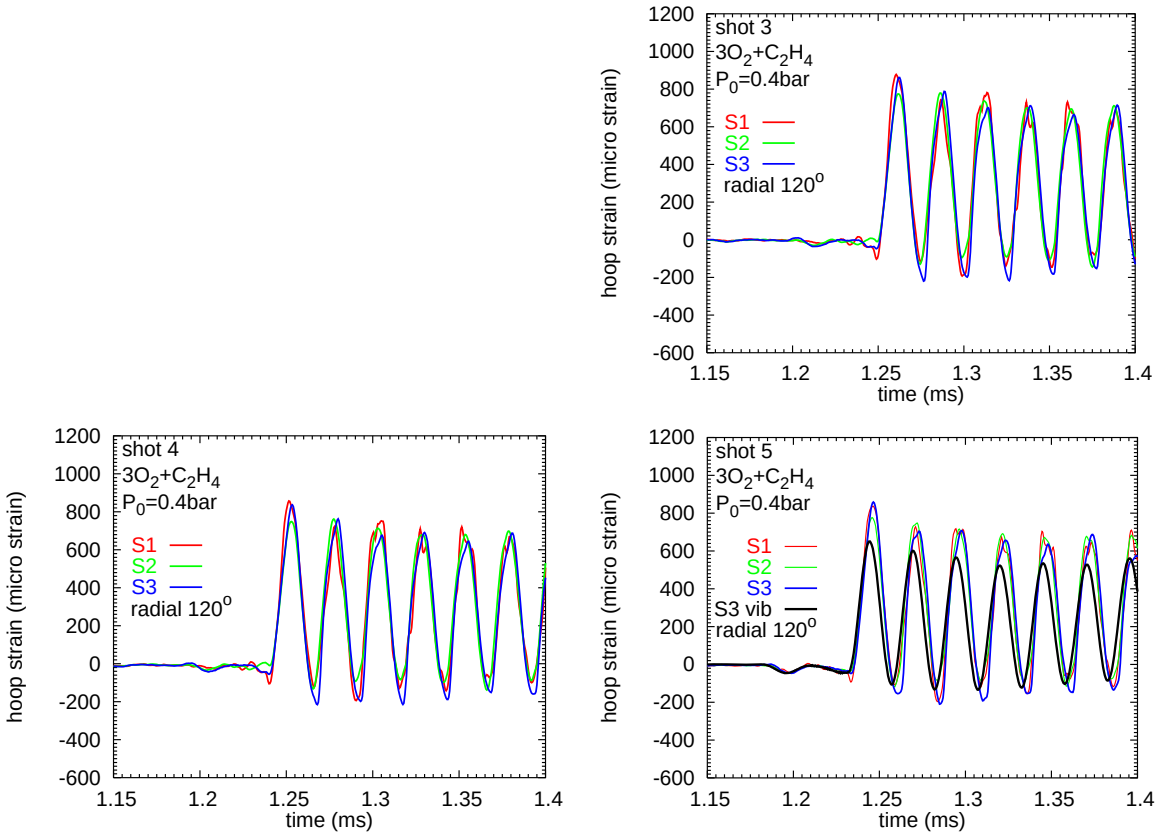

Figure 6: Hoop strains for the azimuthal gage locations in tests 2–5. Initial pressure of 40 kPa.

exception of tests 7-13, in which the gases were not properly mixed, the average detonation velocity is within 1% of the computed CJ value. Figure 10 shows the strain signals observed in shot 5. These data are representative of the results obtained in all of these tests. The signals show the characteristics observed in previous testing with detonation as documented in Beltman and Shepherd (2002). There is a small precursor prior to the arrival of the detonation wave and the main signal is an almost sinusoidal oscillation with a frequency of approximately 38 kHz. This is close to the hoop frequency of 41 kHz for a infinite cylindrical shell (Chap. 12 Blevins, 1979)

$$f = \frac{1}{2\pi R}\sqrt{\frac{E}{\rho(1-\nu^2)}}\,. \tag{1}$$

A more exact computation of the frequency requires solution of the dispersion relation as discussed by Beltman and Shepherd (2002).

It is apparent from the results shown in Figs. 5 and 6, that there are significant differences

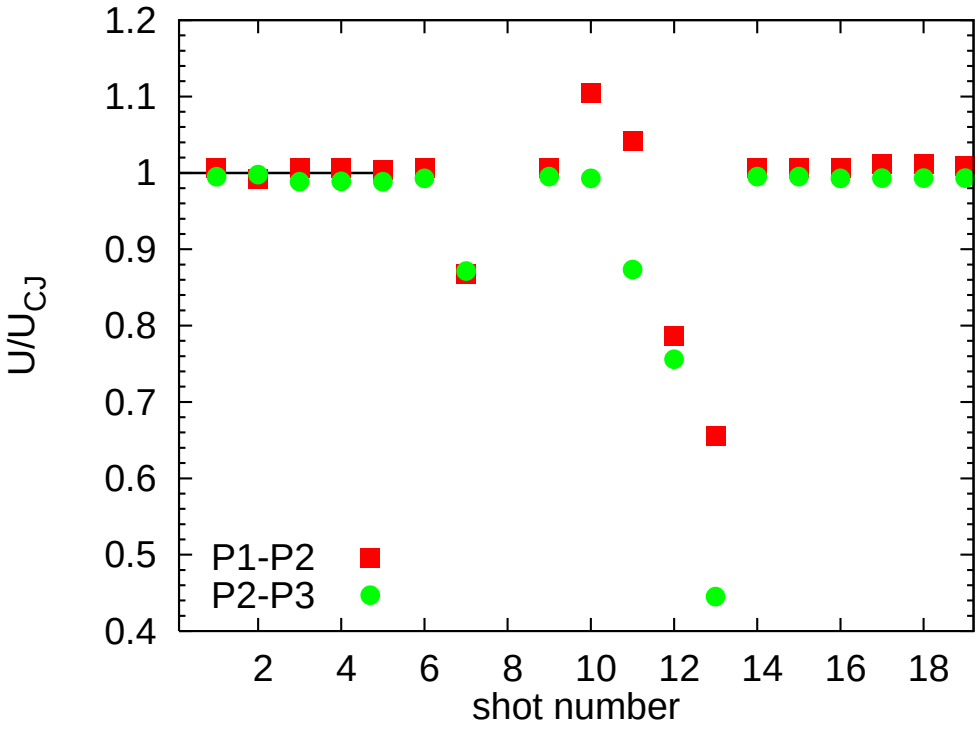

Figure 7: Detonation velocities for closed tube tests 1-20. Various initial pressures - see Table 3 for details.

in amplitude between strain gages that we would expect to have very similar signals. A shot to shot comparison of peak strains and oscillation period is shown in Fig. 8. There is a 20% variance in the amplitude and a 4% variance in the period of the strain signals. These variations are substantially larger than we expected given the repeatability of the detonation itself. There appear to be systematic differences in the stain gage amplitudes which indicate issues with particular gages or gage locations. In addition, the signals show peculiar jumps and depart from the smooth oscillatory behavior that we would expect for an elastic oscillation without wave interaction effects.

3.2 Vibrometer Measurements

In order to investigate the source of variability and tests for artifacts in the signals, we carried out a number of studies on individual effects. One of the main tools we used was an independent measurement of strain with a laser vibrometer (Polytec OFV-551 Fiber-Optic Interferometer and OFV-5000 controller) at one location on the tube. The laser vibrometer measures the Doppler shift of a laser reflected off of the tube surface to give a very accurate

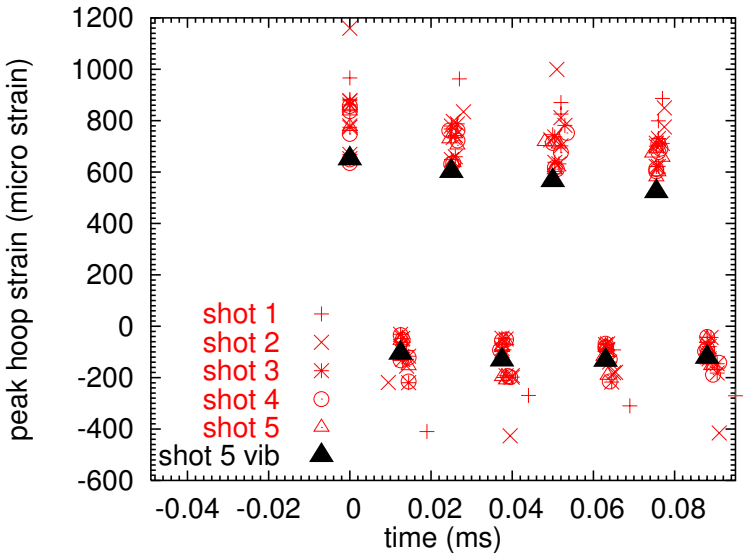

a)

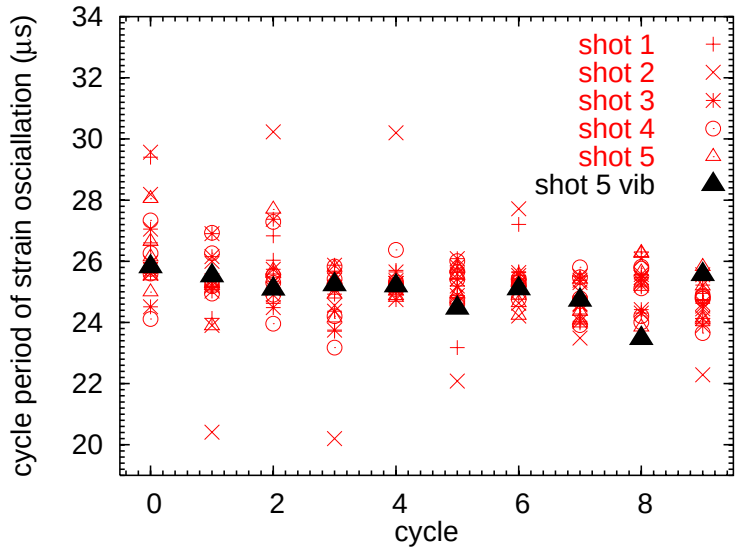

b)

Figure 8: Comparison of shots 1–5 results for a) peak hoop strain amplitudes and b) frequencies. Initial pressure of 40 kPa.

reading of the surface radial velocity v_r which can be integrated to obtain the deflection

$$\delta_r(t) = \int_0^t v_r(t')\, dt' \ . \tag{2}$$

The hoop strain ϵ_{hoop} for a thin-wall tube is computed from the displacement

$$\epsilon_{hoop} = \frac{\delta_r}{R} \tag{3}$$

and in this section we present the vibrometer data in terms of the computed hoop strain so that we can compare directly with the strain gage measurements. The raw and processed vibrometer data and the signal from the adjacent strain gage S3 are presented in Fig. 9 A

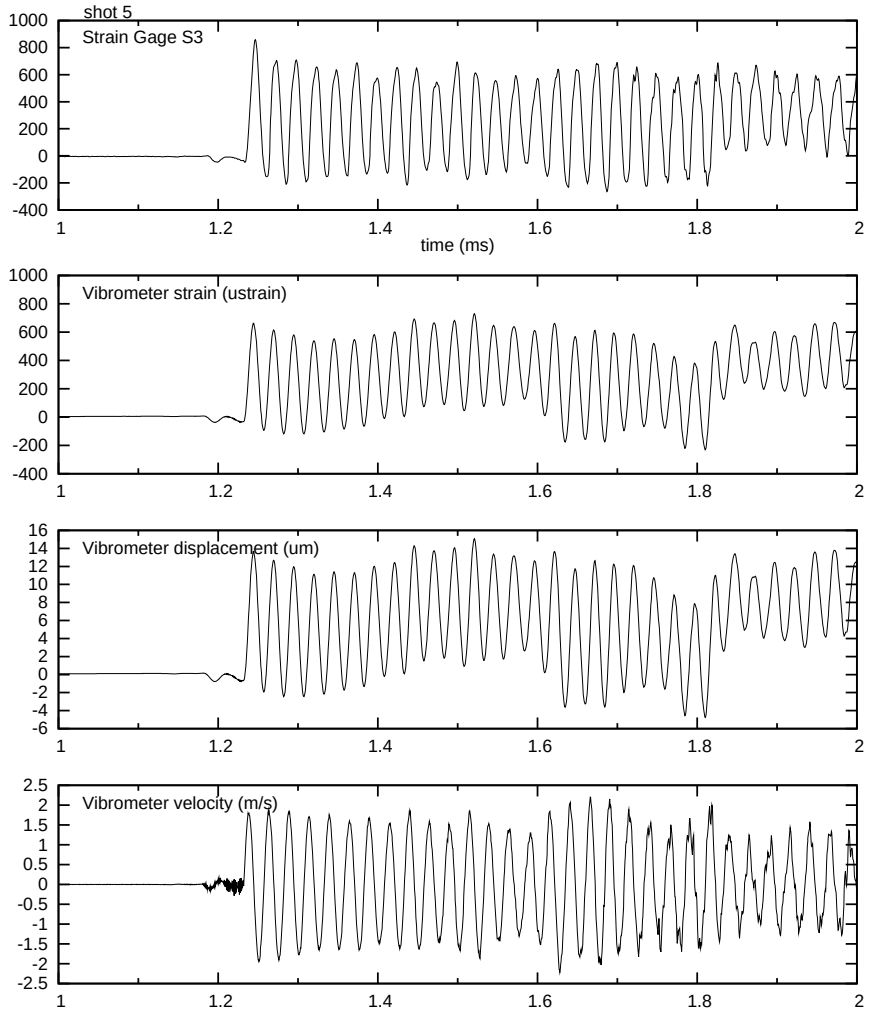

Figure 9: Raw and processed vibrometer data and comparison with strain gage S3 adjacent to the vibrometer measurement location.

comparison between the vibrometer and all strain gages for shot 5 is given in Fig. 10. Note the absence of jumps and the smooth appearance of the vibrometer data in comparison to the strain gages.

A number of tests were carried out with the vibrometer. For example, the shot-to-shot variation for tests 1–5 in the peak amplitudes is shown in Fig. 8. Note the smaller variance in the peak values measured with the vibrometer as compared to the strain gages. Additional data from simultaneous measurements with the vibrometer and strain gages are given in Appendix A. Comparisons of peak strains from three replica shots at 100 kPa are given in

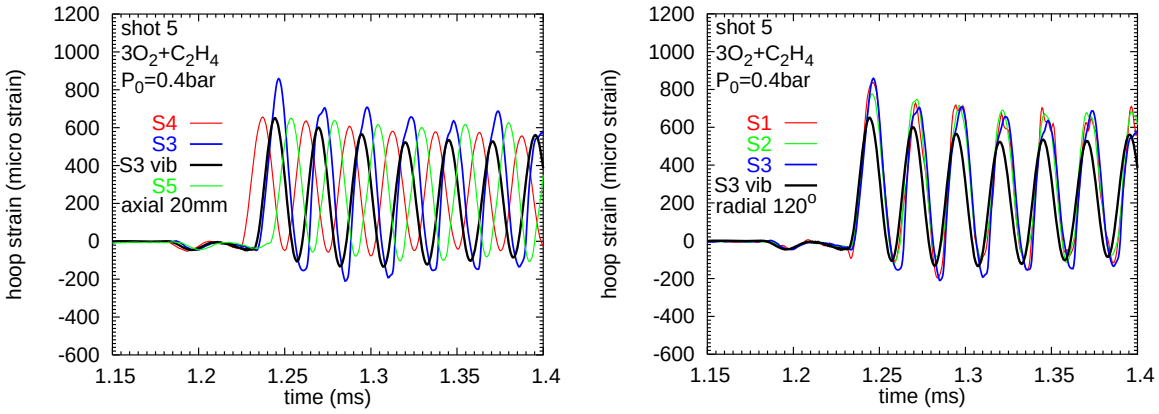

Figure 10: Hoop strain data from gages and vibrometer for a) gages distributed along the tube axis and b) gages distributed in azimuth at the central axial location. Shot 5 at 40 kPa initial pressure.

Fig. 11a and at 50 kPa in Fig. 11b. Note that the peak amplitudes are highly repeatable for both sets of tests with the variation less than 2%, consistent with the repeatability of the detonation itself.

The corresponding comparison for strain gage S3 is shown in Fig. 12. Note that the scatter is larger than in the vibrometer data, the maximum differences in the peak amplitude are up to 7% with the strain gage measurement. The damping rate (decrease in peak stain amplitude with successive cycles) appears to be higher for the strain gage than for the vibrometer data.

We concluded from these comparisons that the strain gages were introducing artifacts into the signals. These can be clearly observed in Fig. 9 in the strain signal between 1.7 and 2.0 ms. Near the peak values of strain there are jumps in the strain signal that do not appear in the vibrometer signal at the corresponding time. Examination of the raw vibrometer signal (bottom trace on Fig. 9) reveals that at these times there is a rapid variation in the velocity with a much higher frequency content (>100 kHz) than the main hoop oscillation. This high-frequency vibration appears to be causing the artifacts in the strain signal. The most likely explanation is that the high-frequency vibration results in low-cycle fatigue causing micro-cracking of the gage elements as described by Vishay TN508 (2007). This is known to introduce jump-like signal features due to sudden resistance changes as the cracks open and close. We are using these gages at the limit of the maximum allowed strain range and the application of repeated high-frequency oscillatory signals may contribute to premature degradation of the gages.

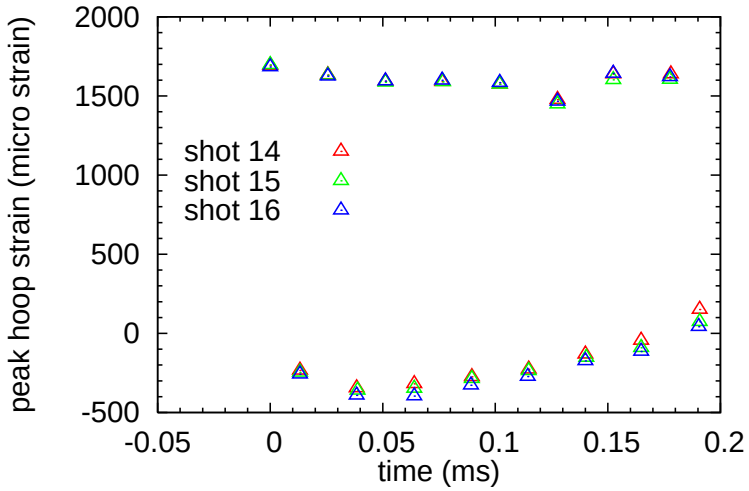

a)

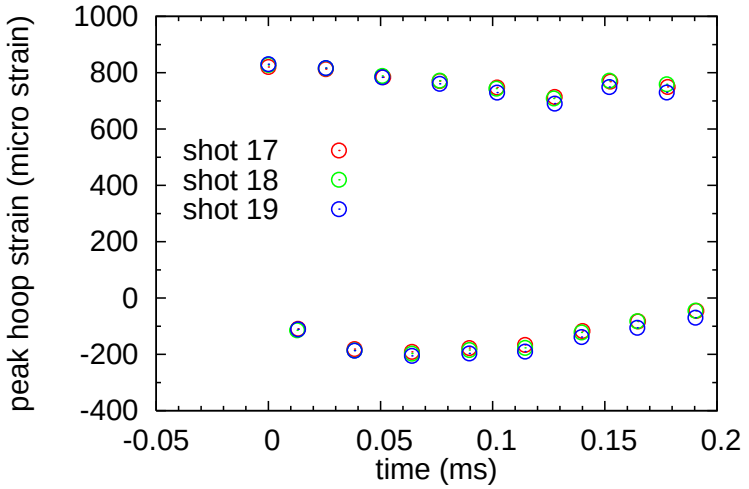

b)

Figure 11: Shot to shot comparison of peak hoop strains measured with the vibrometer at a) 100 kPa and b) 50 kPa.

3.3 Nonideal Effects on Strain Measurements

We have considered a number of issues that may contribute to errors or uncertainty in the experiment and measurement technique. The tube wall thickness uniformity was checked by using a vibrometer at two locations to compare with the strain gage results. In order to examine the role of prestress, we rotated specimen within fixture. The operation of strain gages was considered at length, using the substantial literature (Kobayashi, 1993) that is available on that subject. The gage operation was checked in separate effects experiments. Gage bonding and creep were studied by carrying out cyclic static loading and unloading. The possibility of nonlinear (plastic deformation) material response was investigated by

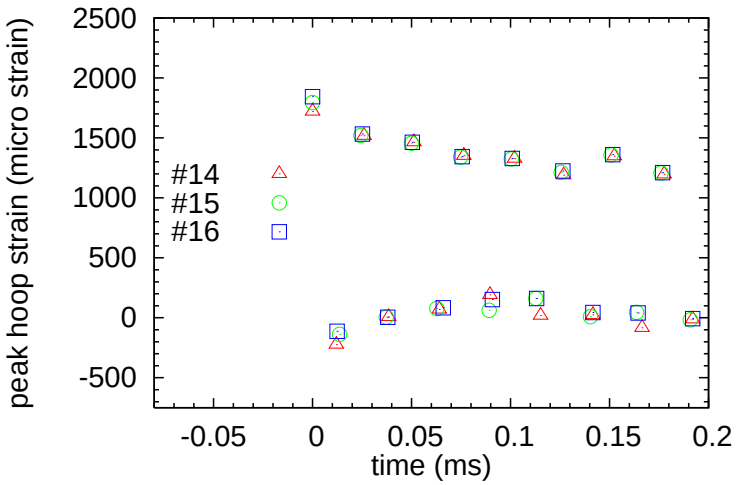

a)

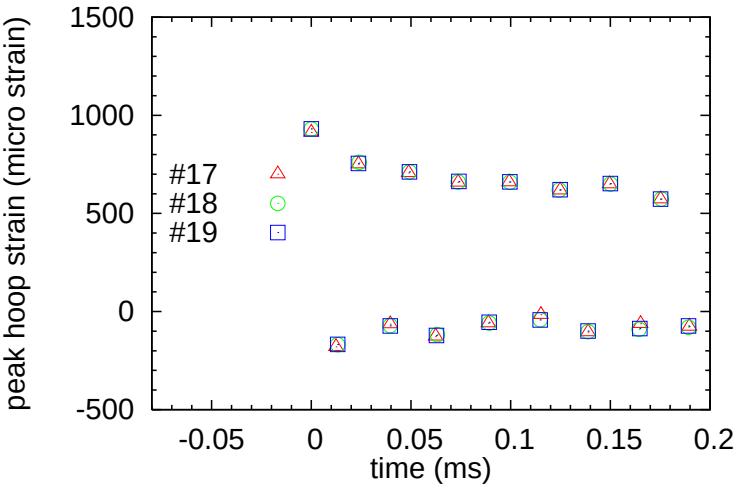

b)

Figure 12: Shot to shot comparison of peak hoop strains measured with strain gage S3 at a) 100 kPa and b) 50 kPa.

varying the initial pressure of the gas inside the tube. The variability in the detonation process itself was considered by Liang et al. (2008) and found to small compared to the observed scatter in the strain gage results.

3.3.1 Wall thickness variation

The systematic difference in peak strain between strain gage locations and tests using the vibrometer at different circumferential locations (Shots 20,21, 25–29) lead us to conclude that the tube wall had a nonuniform thickness. Sectioning the tube and measuring the thickness with a micrometer confirmed this. The nonuniform cross section is most likely due to a

slight eccentricity in the mandrel that is used in the extrusion process which is necessary to manufacture seamless tubes. This nonuniformity was found to result in a greater amount of variation between the strain gages at different azimuthal locations. The measured thickness variation is shown in Fig. 13. Two of the gage locations, numbers one and three, were (except where noted in Table 3) located at 0° and 240° respectively, which are close to the extrema of thickness. The relationship between thickness and hoop strain for thin-wall cylindrical tube of uniform wall thickness h is

$$\epsilon_{hoop} = \Phi \frac{R}{h} \frac{\Delta P}{E} \ . \tag{4}$$

where Φ is the dynamic load factor and ΔP is characteristic pressure difference between the inside and outside of the tube. For a static load, $\Phi = 1$ and the ΔP is just the applied internal pressure. For a detonation ΔP is a reference value characterizing the peak pressure in the detonation wave. The dynamic load factor Φ depends on the wave speed, construction and size of the tube, see the discussion in Beltman and Shepherd (2002). For the present case, if we use the CJ pressure as the reference pressure, see (App. D Liang et al., 2008), $\Delta P = 3.261$ MPa and for the nominal tube dimensions, we compute that

$$\frac{R}{h} \frac{\Delta P}{E} = 1210 \quad \mu\text{strain} \ . \tag{5}$$

However, if we use the local tube thick at the location of gage S3 or V3, then the computed reference strain (5) will be lower, 1136 μstrain, since the tube is thicker at this location. Using the actual thickness, we find that $\Phi \approx 1.5$ for the first peak in hoop strain of 1700 μstrain. This is consistent with the values and analysis discussed in Beltman and Shepherd (2002).

Treating the tube as a cylindrical shell (see Chap 13 Ugural and Fenster, 1987), (4) will also apply locally to a shell of nonuniform thickness so that for a constant applied pressure difference ΔP and dynamic load factor Φ, the local hoop strains are inversely related to the local shell thickness.

$$\frac{\epsilon_2}{\epsilon_1} = \frac{h_1}{h_2} \ . \tag{6}$$

Using the results of the vibrometer measurements at two locations V1 (at 15°) and V3 (at 225°), we have tested the relationship between thickness and peak strain, given in Table 2. The ratio of thicknesses $h_1/h_3 = 0.87$, and the inverse ratio of strains $\epsilon_3/\epsilon_1 = 0.83$ as measured by the vibrometer. From these results, we conclude that the wall thickness variation appears to be the most significant factor in systematic differences in peak strain amplitudes between measurement locations. In order to make quantitative comparisons and validation of the

Table 2: Thickness and peak hoop strain variation with azimuthal location.

Location	h (mm)	ϵ_{max} μstrain
V1	0.815	2050
V3	0.926	1695

numerical simulations of the elastic wave propagation, this thickness variation has to be modeled. The effect appears to primarily azimuthal in orientation and the wall thickness is measured to be almost constant in the axial direction.

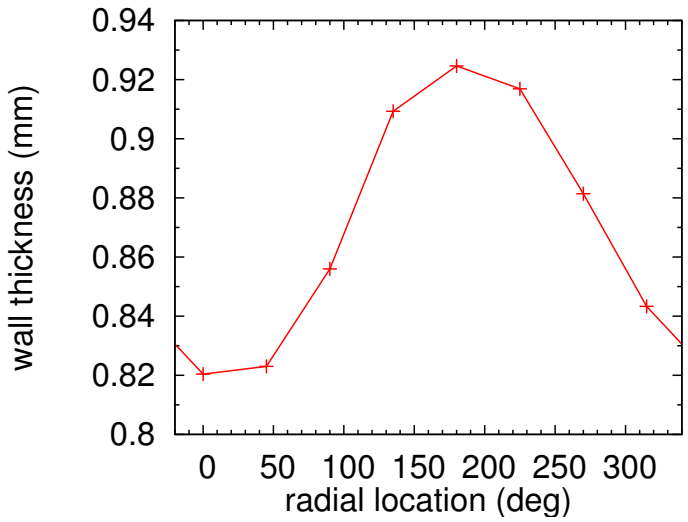

Figure 13: Wall thickness variation at the measurement location as a function of azimuthal coordinate.

3.3.2 Prestress

The tubing is clamped into collets that are held by rigid blocks that are fastened to the I-beam that supports the detonation and specimen tubes. The collet blocks (shown in Fig. 3) can be adjusted to approximately align the specimen tube with the detonation tube and minimize any prestress in the specimen. However, it is difficult to complete eliminate prestress. The most common type of prestress will be a bending moment applied to the tube due to the misalignment of the collet blocks at each end of the specimen. A bending moment will create differences in the response at different azimuthal locations and may contribute to the differences in strain gage response that we observe in our tests. We carried out shot 22 with deliberate and substantial misalignment of the collet blocks to test the sensitivity of

the measured strains to the prestress. Vibrometer measurements were made at location S1 in tests 20, 21, 22, 23, 24 and at location S3 in tests 13, 14, 15, 16, 25, 29. All of these tests were done at 100 kPa initial pressure and the peak strain amplitudes for the first 6 cycles of oscillation are shown in Fig. 14. Prestress was not deliberately introduced in the other tests but no special efforts were made to minimize it either. There is no distinct effect of prestress observable in these results.

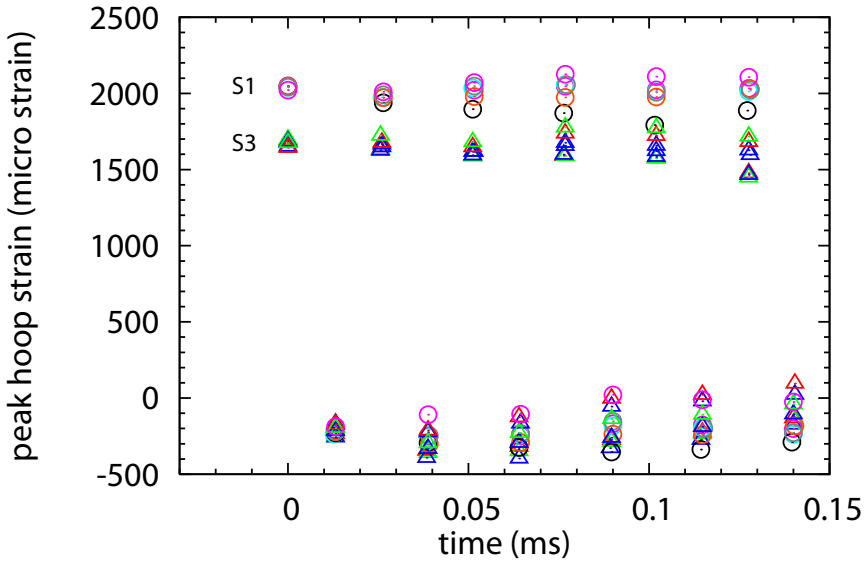

Figure 14: Test of prestress effect. The open black circle is data from test 22 with prestress.

3.3.3 Gage bonding and creep

If the gages are not properly bonded or the bond has a creep response, this can be determined by carrying out static testing and determining if there is hysteresis. This is done by recording data while applying stepwise increasing and decreasing pressure. This can also be used as static calibration on the strain measurement, comparing the measured strains with the values computed using elasticity theory. Our testing was done with nitrogen and a room temperature of 21°C. The strain gage signals were measured for measured for a static pressure load at pressure differences of 0,20,40,60,...,140 psi. The tube was clamped by collets mounted solidly to the beam on both sides during this test so that the section with the strain gauges was not able to expand in the axial direction. The tube "caps" with the O-rings were solidly mounted to the I-beam, so that no force (neither hoop nor longitudinal) could be exerted onto the tube from the caps. The strain gage excitation voltage was 10 V, the signal conditioner gain was 1000, the gage factor was 2.09, and 120 Ohm gages were used.

The bridges were initially zeroed (balanced) at atmospheric pressure and no load applied for one hour before the test. The total loading duration was 12 minutes (2 minutes per step of 20 psi). The tube was held at 140 psi for 5 minutes before starting the unloading process. The duration for unloading was also 12 minutes (2 minutes per step of 20 psi). The results are shown in Fig. 15, which indicate a modest (12 μstrain) level of hysteresis that can be neglected compared to the peak strains measured in the present tests.

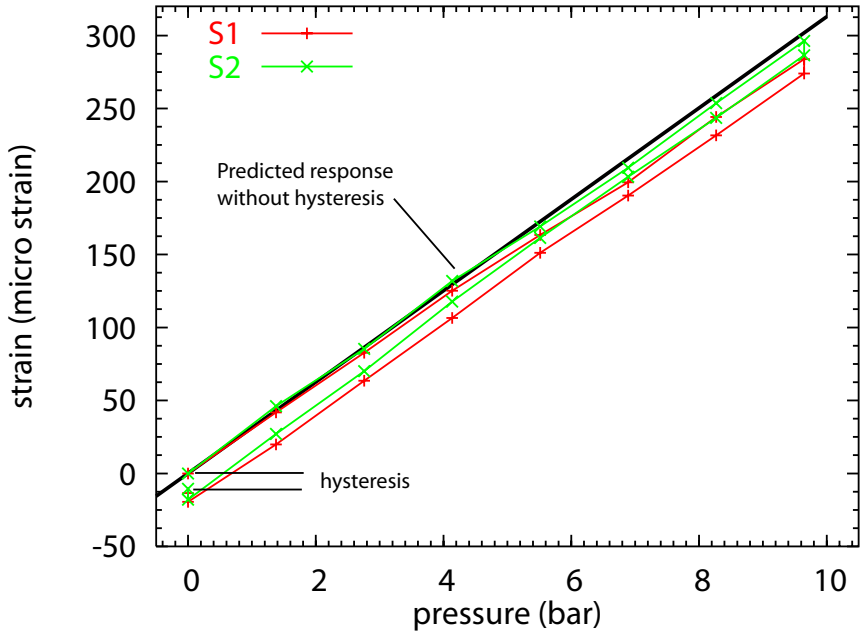

Figure 15: Test of gage bonding and calibration using static loading and unloading.

3.3.4 Initial pressure variation

To check the linearity of the tube response at initial pressures up to 100 kPa, we have compared the results of tests at 50 and 100 kPa in Fig. 16. The 50 kPa tests have been scaled by a factor of the ratio of the computed CJ pressures for the two cases, the scaling factor is 33.4/16.2 = 2.06. The coincidence of the scaled data with the 100 kPa data indicate that response is clearly in the linear regime. The magnitude of the peak strain is less than 1700 μstrain. Strains less than 2000 μstrain are conventionally associated with linear response.

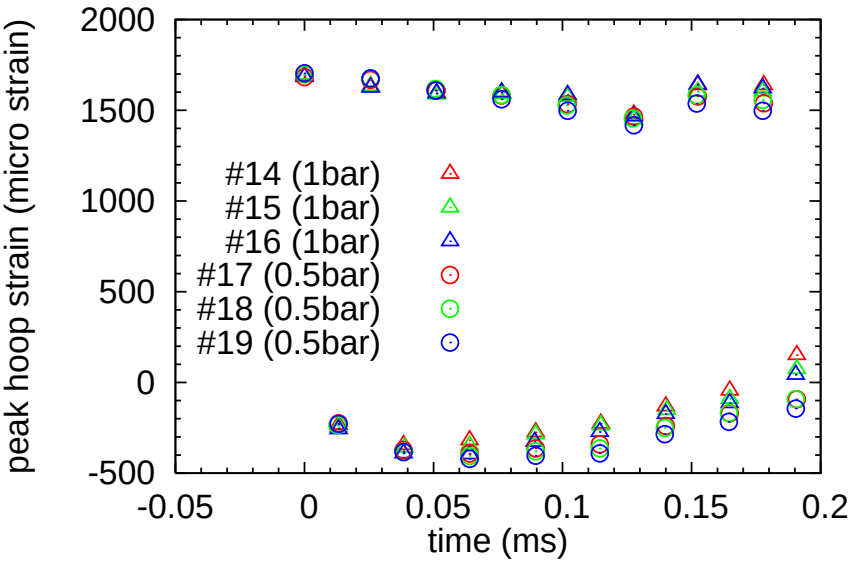

Figure 16: Comparison of peak hoop strain amplitudes for two initial pressure levels. The results for the 50 kPa initial pressure tests have been scaled by a factor of two to test the linearity of the tube response.

3.3.5 Thermal Effects

There are two types of thermal effects. 1) bulk temperature rise of the tube and gage. 2) thermal stress created by temperature difference between inside and outside of test specimen. The maximum bulk temperature rise can estimated by assuming that all of the thermal energy in the combustion products is absorbed into the tube. A thermal energy balance assuming there are no other losses yields a temperature rise of

$$\Delta T = \frac{\Delta e_{gas} \rho_{gas}}{\rho_s C_{p,s}} \frac{R}{2h} \,, \tag{7}$$

where $\Delta e_{gas} = 10.67$ MJ/kg is the energy change of the products in cooling from the constant volume combustion conditions to room temperature, $\rho_{gas} = 1.26$ kg/m^3 is the gas density, $\rho_s = 2780$ kg/m^3 is the specimen metal density, and $C_{p,s} = 963$ J/k kg is the specific heat capacity of the specimen metal. For an initial pressure of 100 kPa, the bulk temperature rise is predicted to be 63°C. The characteristic time over which this temperature rise occurs is on the order of the thermal diffusion time of h^2/κ, where $\kappa = k/\rho C_p = 5.82\times10^{-5}$ m^2/s is the thermal diffusivity of the specimen metal. The thermal diffusion time is 14 ms for the present experiment, about 500 times longer than the period of hoop oscillation. We conclude that on the time scale of the measurements, 0.2-0.5 ms, the strain gage temperature and substrate temperatures are essentially unchanged. However, there will be a substantial temperature gradient between the inside and outside of the tube and this has to be considered.

Bulk Temperature Effects The gages used in the present study are made for "self compensation" with a substrate that has a thermal expansion coefficient of 6 ppm/°F (1.32×10^{-5} K^{-1}). This value is matched to the thermal expansion of steel but aluminum alloys have a higher value, closer to 11–13 ppm/°F (2.43×10^{-5} K^{-1} for 6061T6). This mismatch in the gage self-temperature coefficient (STC) with the substrate coefficient of thermal expansion will result in a thermal artifact in the gage output if there are significant thermal changes during the measurement period (Vishay TN504, 2007). The resistance change due to thermal response for very small temperature changes is

$$\frac{\Delta R}{R_o} = \left[\beta_G + S_g \left(\frac{1+K_t}{1-\nu_o K_t}\right)(\alpha_s - \alpha_g)\right] \Delta T \,, \tag{8}$$

where K_t is the gage transverse sensitivity coefficient Vishay TN509 (2007), β_g is the resistance coefficient of temperature of the gage, α_s - α_g is the difference between the substrate and gage coefficient of thermal expansion. For A-alloy gages, the factor involving transverse sensitivity is close to unity and resistance coefficient of temperature is actually extremely

small over the range of interest in the present experiment. The last term $2(\alpha_s - \alpha_g)\Delta T$ represents the effect of differential thermal expansion and amounts to 22 μstrain K^{-1}. For temperature changes of a few Kelvin during the measurement period, this is negligible compared to the peak strains of 2000 μstrain.

An additional effect is that the gage constant S_g is a function of temperature and for large temperature variations, this must be accounted for in analyzing the data. For a strain gage in a quarter-bridge configuration that is used in the present experiments, the conversion of the strain ϵ to voltage output E of the signal conditioner is (Kobayashi, 1993) given by

$$E = \frac{1}{4} E_i G S_g \epsilon \ , \tag{9}$$

where S_g is the gage factor (approximately 2 for the gages used in the present study), G is the amplifier gain (typically 100 for peak strains of 2×10^{-3}), and E_i is the excitation voltage (10 V in the present study). Variations in the gage factor will therefore directly translate to variations in the output voltage of the signal conditioner. For the CEA type gages, the gage metal is constantan (A-alloy) and the variation of gage factor with temperature is 1.1% per 100°C or 1.1 $\times 10^{-4}$ K^{-1}. Over the range of interest in the present experiment, the effect of temperature on the gage constant can be neglected.

Thermal Stress The strain induced by thermal stress associated with the temperature gradient through the tube wall thickness is discussed in Appendix D. The theory of elasticity can be used to show that contribution to the hoop stress at the outer wall due an energy deposition Q' per unit length of the tube, is

$$\sigma_{\theta\theta} = \frac{\alpha E}{2\pi \rho_s C_{p,s}} \frac{2}{r_o^2 - r_i^2} Q' \ . \tag{10}$$

This expression is valid for the case of no axial force, i.e., no restraint in the axial direction. We can evaluate the energy input per unit length by carrying out an energy balance and expressing this in terms of Δe, the energy per unit mass of combustion products that is transferred to the wall. Using the stress-strain relationship for plane stress (p. 442 Timoshenko and Goodier, 1970), the hoop strain increment due to the thermal effects for a thin-wall tube is approximately

$$\epsilon_{\theta\theta} = \alpha \frac{\rho_g}{\rho_s} \frac{\Delta e}{C_{p,s}} \frac{R}{2h} \ . \tag{11}$$

This is valid for both uniform and nonuniform heating. In the case of uniform heating (constant temperature), there will be thermal expansion but no thermal stress. For the present situation, we can evaluate the constants in (11) to obtain $\epsilon_{\theta\theta} = 145$ μstrain per

MJ/kg of energy. If all the energy from the gas is absorbed into the tube wall, this results in 1547 μstrain. The fraction of this that is absorbed during the measurement period can estimated using the results of Radulescu and Hanson (2005), who showed that the heat transfer occurs primarily during the time when the gas is moving inside the tube. Using an estimated peak heat flux of 30 MW/m^2 and a Taylor wave duration of 0.3 ms, the thermal energy per unit length transferred into the tube wall is 1130 J/m. According to (10), this will result in 82 μstrain or about 4% of the peak value of 2000 μstrain. We infer from (11) that only about 5% of the thermal energy is lost from the gas in this time period, which is consistent with the very slight droop observed in the pressures measured in shots 30-34 by the first transducer inside the detonation tube. The effect on the first few cycles of the strain signal will be negligible since each cycle only takes 26 ms, during which we would expect a maximum thermally-induced strain of 7 μstrain per cycle.

3.3.6 Transient Response

Strain gages are typically calibrated for static (or low speed, i.e., quasi-static) measurements of strain but in the present experiments are being used to measure dynamic strain. Capturing and interpreting dynamic strain signals with fidelity requires considering a number of factors. First, the instrumentation must have the proper bandwidth so that the high frequency signals are not attenuated and aliasing is avoided during the recording process. The typical hoop frequency is about 38 kHz and the bandwidth of the signal conditioners used in the present experiments is nominally 100 kHz on the "wideband" setting. The actual bandwidth of the amplifiers depend on the gain setting. For the present experiments, a nominal gain of 100 was used to record strain signals with a maximum of 2000 μstrain. For this gain value, the -0.5 dB point for the amplifier is 80 kHz (Vishay 11255, 2006). The signals were digitized with a sampling rate of at least 1 MHz and in some cases, we used 2 MHz to check some of the artifacts that were observed in the signals. The digitizers have a nominal resolution of

We estimate that the maximum error introduced by the frequency response and digitizing error of the measuring system is on the order of 0.5%.

The gage element area is approximately 2.5 $\times$ 3.0 mm. For gages of this size, Ueda and Umeda (1998) showed that with the appropriate signal conditioning equipment, these gages could be used with frequency content up to 300 kHz and strain rates up to 750 S^{-1} with less than 5% attenuation when measuring longitudinal pulses in Hopkinson bars. In the present case, the primary frequency of the signals is 38 kHz so that for peak strains of 2000 μstrain, the strain rate will be about 600 s^{-1} and the conditions of Ueda and Umeda's experiments are satisfied by the present tests.

There is a slight averaging effect due to the propagating wave nature of the disturbance.

The hoop oscillations have a period of 26 μs and propagate with the wave front which is moving at the detonation velocity, about 2300 m/s. This means that the wavelength is 60 mm, about 20 times larger than the gage element width. This means that a small amount of averaging will occur due to the strain variation across the gage. The magnitude of the averaging will depend on the phase of the wave, with the greatest effect occurring at the maxima and minima of the signals. For the peak of a sinusoidal waveform with wavelength λ centered on a gage with width w, the strain averaged over the width will be

$$\epsilon = \epsilon_m \left[1 - \frac{(2\pi)^2}{24} \left(\frac{w}{\lambda} \right)^2 + O\left(\frac{w}{\lambda} \right)^4 \right] . \tag{12}$$

Using the values appropriate for the present tests, the measured peak strain will be at most reduced by 0.4% from the actual peak value.

3.3.7 Gage location and angular misalignment

The gages were intended to measure strain in the hoop direction only but due to slight errors in aligning the gage during the gluing operation the gage output may be slightly in error, see Fig. 17. The axial location error can be eliminated by careful measurement of the

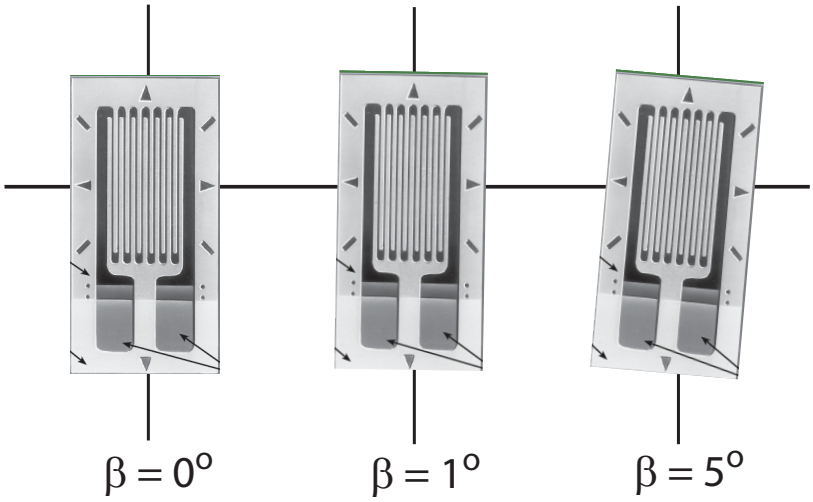

Figure 17: Appearance of gages with perfect, 1°, and 5° angular misalignment showing that detection of of misalignment is possible to do visually at these levels.

final position but the direction that the gage is pointing (angular alignment) is harder to control or measure. The error due to angular misalignment depends on the strain field and the orientation of the gage relative to the principal axes of the strain, see the discussion in Vishay TN511 (2007). For a single gage that is misaligned by an angle $\pm\beta$ relative to the

intended angle ϕ relative to the major strain axis, the gage indication will be in error by

$$\frac{\epsilon_p - \epsilon_q}{2} \left[\cos 2(\phi \pm \beta) - \cos 2\phi\right] \ , \tag{13}$$

where ϵ_p is the maximum value of the principal strain and ϵ_p is the minimum value of the principal strain. For the present situation, the hoop strain is the maximum principal strain for gages aligned with the hoop direction, and the error is

$$\frac{\epsilon_p - \epsilon_q}{2} \left[\cos 2\beta - 1\right] \ . \tag{14}$$

Consider measurements of hoop strain. The hoop direction is the direction of maximum principal strain for axially-symmetric loading on a tube so that $\epsilon_p = \epsilon_{hoop}$. For a thin tube with zero axial prestress (see Appendix B, part I Beltman and Shepherd, 1998), the relationship between the hoop and axial strain is ϵ_{axial} = - $\nu\epsilon_{hoop}$. The relative error in hoop strain for gage that is intended to be aligned with the hoop direction ($\phi = 0$) but is misaligned by an angle β is

$$\text{Error} = \frac{(1+\nu)}{2} \left[\cos 2\beta - 1\right] \ . \tag{15}$$

For a gage that is intended to measure axial strain, the relative errors are a factor of $1/\nu$ higher. A plot of relative error (in terms of percentages) is given in Fig. 18 for the hoop strain case. Based on these considerations and our visual estimations of alignment error, we expect that the strain gage output may systematically be in error by as much as 3%. Note that the effect of the misalignment is to systematically reduce the measured strain relative to the actual value.

3.4 Comparison with simulations

The response of a thin-wall shell was simulated by F. Cirak using the methods described in Cirak et al. (2006) and Deiterding et al. (2007). In doing the simulations, it was necessary to take careful account of the azimuthal variation of tube wall properties and calibration of the detonation model to the data as discussed in Liang et al. (2008). Instead of actually computing the hydrodynamics of unsteady detonation, the detonation was treated as a traveling internal pressure load. The wave speed was given by the ideal detonation (CJ) model and the spatial distribution of pressure behind the front was computing using an approximation to the analytical solution to the perfect gas Taylor-Zeldovich expansion wave. The approximate model of a traveling pressure load is described in the Appendix to Beltman

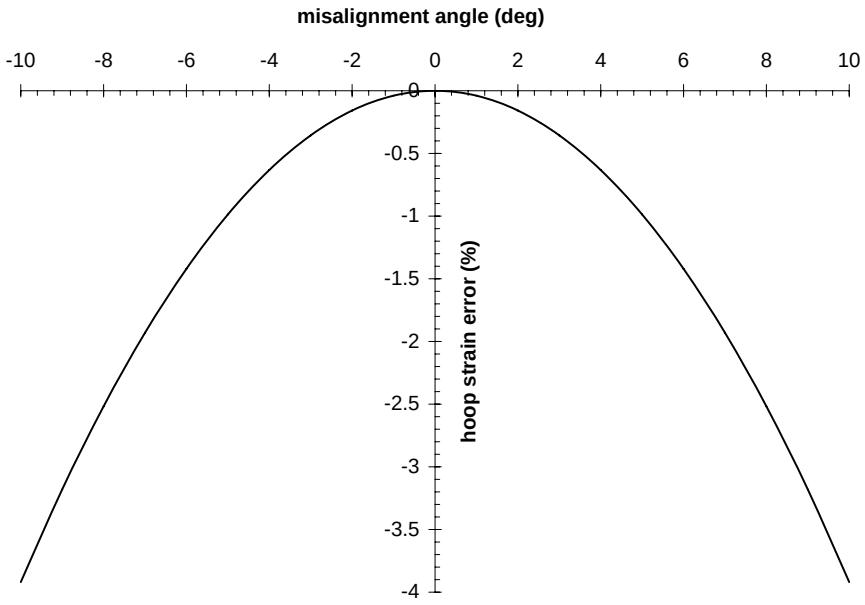

Figure 18: Percentage error is hoop strain as a result of angular misalignment, computed with (15).

and Shepherd (2002). The calibration of the decay time used the pressure transducer data from tests 30-34 at the location corresponding to the axial measurement station (see Section 8 Liang et al., 2008).

The effect of using a nonuniform wall thickness is shown in the results of Fig. 19 in which the strain history is given corresponding to locations S1, S2 and S3 in our experiments. The simulated radial displacements are compared with vibrometer measurements for two locations (V1 and V3) in Figs. 20 and 21 using the same detonation case.

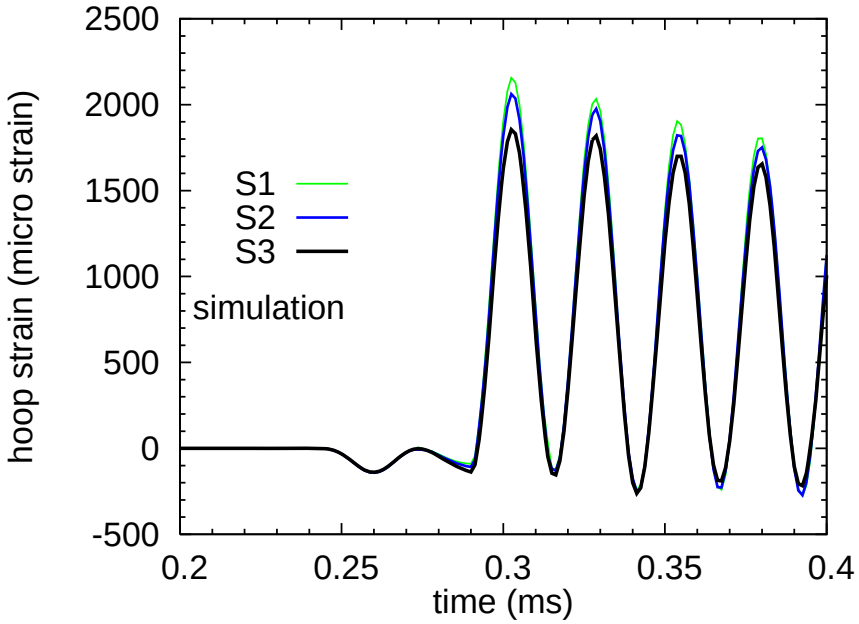

Figure 19: Computed strain response to stoichiometric ethylene-oxygen detonation (100 kPa initial pressure) in an aluminum tube with wall thickness variation shown in Fig. 13.

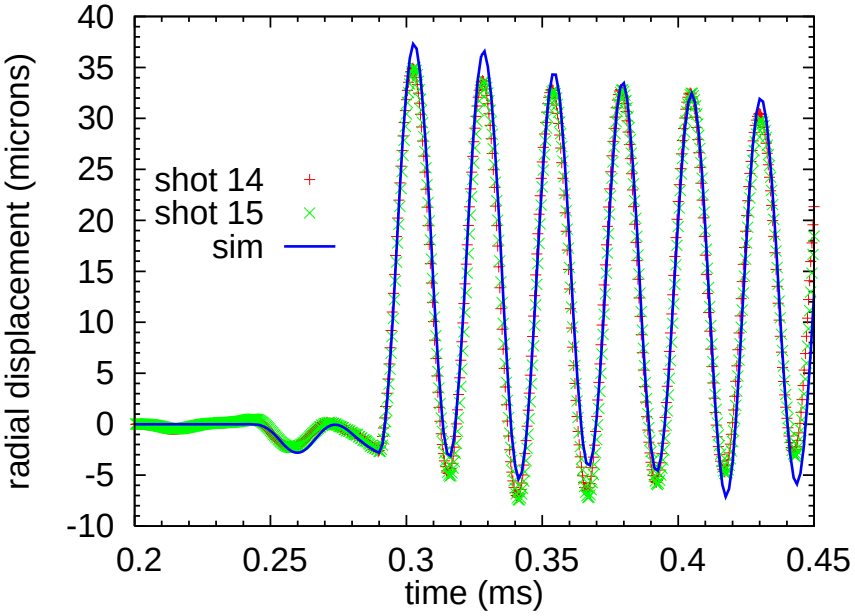

Figure 20: Comparison of measured and simulated displacement response at location V3 (225°). Stoichiometric ethylene-oxygen detonation (100 kPa initial pressure) in an aluminum tube with wall thickness variation shown in Fig. 13.

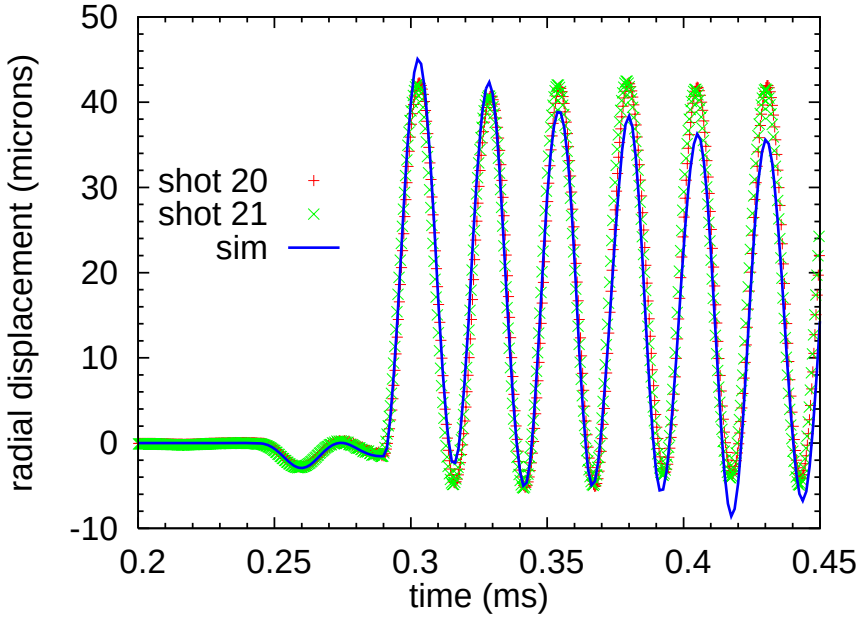

Figure 21: Comparison of measured and simulated displacement response at location V1 (15°). Stoichiometric ethylene-oxygen detonation (100 kPa initial pressure) in an aluminum tube with wall thickness variation shown in Fig. 13.

4 Tests in Tubes With Slots and Flaps

The blast waves were imaged using a Cordin 220C 8-frame CCD camera operating through a continuous-light schlieren system with a 100 mm diameter field of view. A PCB gage was installed in the tube opposite the center of the slot or the flaps, and the signal from this transducer was used to trigger the camera. It is important to note that the camera frames are referenced to this signal, rather than the ignition time. By default in the camera software, the first frame is exposed 1-μs after the trigger signal. Gain settings were adjusted for each CCD to give as consistent an image as possible across an image run, although they were typically set near 180 for 8-frame runs, and 150 for 4-frame runs.

Figure 22: Blast gage installation.

To measure the blast wave pressures, PCB model 137A23 pencil-type blast gages were installed as shown in Fig. 22. The gages were mounted in different combinations of 0, 45 and 90 degree angles, at 250, 500 and 750 mm from the tube. Only two gages could be recorded at one time, so some tests were repeated to complete the data package. The measurement surfaces of the blast gages were aligned with the center of the slot/flap cuts. The gage bases were bolted to Unistrut rails for ease of position changes. There is some concern over the influence of reflected and refracted waves from the end of the rails on the blast pressure signals; however, the cross-sectional area of the rails is limited, and the initial blast wave should arrive at the gage sensors before any secondary waves, preserving the peak blast pressure.

4.1 Slot Tests

The slotted tube was formed by joining two half-length tubes in a 51 mm long by 57 mm diameter aluminum collar. The tubes were bonded into the collar using Loctite 410 toughened anaerobic adhesive. The tube junction was not centered in the collar, but was approximately 15 mm from the upstream end. The tube halves were aligned using a machining fixture, although the fixture did not provide fully co-axial alignment. When the tubes were later taken apart and reassembled, they were clamped in the detonation tube collets for alignment.

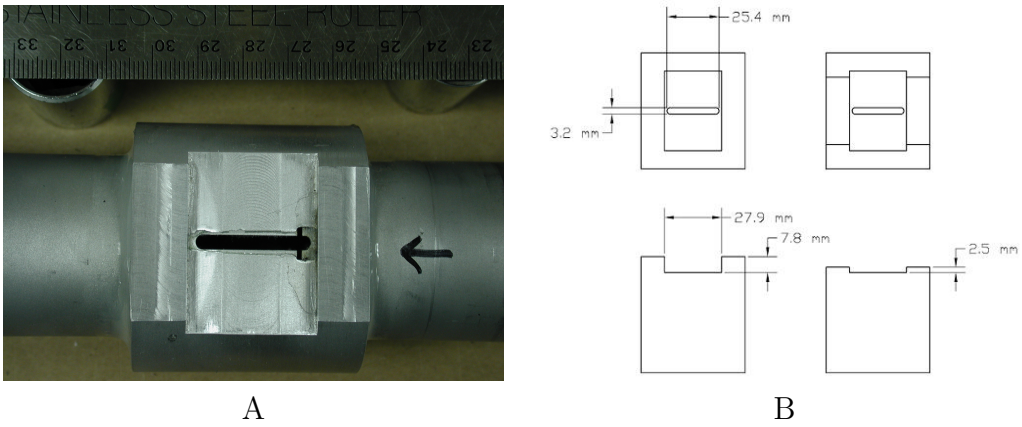

Figure 23: A. Photograph of slotted tube and reinforcing collar. Arrow indicates direction of detonation propagation. Note gap on right caused by tube end cut. B. Slot dimensions.

The underside of the collar was drilled, tapped and spotfaced to accept a threaded PCB gage mount. The slot was cut in the top of the collar, opposite the PCB mount. First, a 28 mm wide flat was machined across the collar, down to the outer tube wall. This allowed the slot to match the thickness of the tube wall, and provided an unobstructed path for imaging. "Ears" were left on either end of the flat to reinforce the tubes and prevent them from failing at the slot. These ears were left at full height (7.6 mm) for tests 39 and 40, but were then milled down to 2.3 mm to minimize interference with the exiting blast wave.

The slot was 3 mm wide and 25 mm long overall. However, the slot had an irregular shape due to the tube junction. The tube ends had not been squared in the lathe prior to assembly, and they did not meet evenly all of the way around. The result was a small "cross-slot" at the upstream end of the slot. The proximity of this gap to the end of the slot created sealing problems in some of the tests. Initially, the slot was sealed with packing tape, which was forced down into the corners at the base of the ears, and burnished onto the surface of the collar to promote sealing. The tape was later replaced with a strip of 1.5 mm thick rubber, cut to match the width of the flat. The rubber was coated with silicone vacuum grease and pressed against the flat surface of the collar. The axial center of the slot

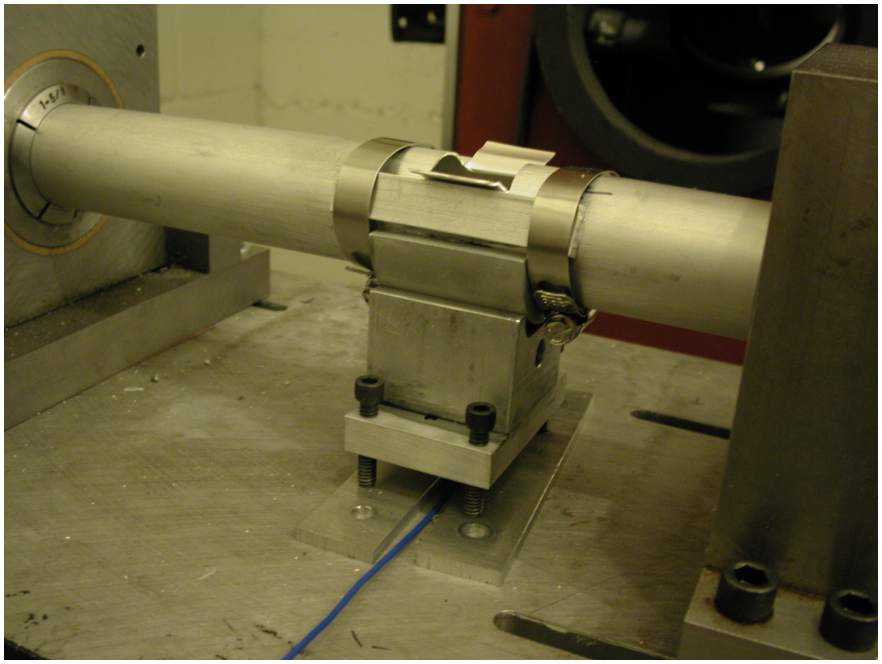

Figure 24: Support Saddle for tube collars. Shown installed under a flap tube, but the support was also used with slotted tubes

(and the slot pressure transducer) was located approximately 2.03 m from the ignition point.

In practice, the atmospheric pressure was often slightly lower than the specified mixture starting pressure, and some venting/equalization would occur during the final moments of filling or mixing. While the amount of loss should not create any significant mixture errors, the problem was prevented in later shots by placing a steel weight on the rubber seal, creating enough force to prevent leakage. Immediately before each shot, the tape or rubber seal was removed and the slot exposed to the atmosphere.

After the first few shots, the collar assembly began to leak near the upstream end, where there is only a short length of tube inserted in the collar. The leakage occurred due to lateral force on the joint created by the blast wave and venting gasses. The collar was taken apart, cleaned and reassembled (this time with Loctite 680, which has a longer working time), and a support saddle was built and installed under the collar to minimize stress on the bonded joints.

4.2 Tubes with opening flaps

Five tubes were prepared with a pre-cut pattern of slots that would cause them to rupture in a very well-defined fashion, rather than with random, jagged tears in the tube wall. Slots were cut with a hand-held rotary tool, and were slightly irregular. The main (lengthwise)

slot was 25 mm long, as in the previous tests, and circumferential slots were cut on either end that extended over of the tube circumference. A hole was drilled in the tube opposite the slot for pressure gage mounting. A half-collar with a threaded and spot-faced hole was bonded to the underside of the tube with Loctite 410 adhesive for pressure gage mounting and tube reinforcement. For tube evacuation and filling, the cut pattern was sealed with aluminum adhesive tape. The axial center of the flap system (and the associated pressure transducer) was located approximately 2.03 m from the ignition point.

Initially, we had expected that the uncut edge of the flaps would simply bend like a hinge, and that no additional cracks would form at the base of the cuts. However, the flaps folded back and continued to tear at the hinge line, creating radiused corners at the base of the flaps.

After tubes 1 and 2 were tested, additional aluminum reinforcing bars were epoxied and clamped to the tube, with their upper edges close to the hinge line (proximity to the hinge line was limited by the need to seal the cuts with aluminum tape). A sharp awl was used to score the hinge line in a further effort to control the opening of the flaps and limit tearing of the tube wall. The tube wall still tore at the hinge line, but the extent of the tears was limited by the reinforcing bars. The flaps opened with such force that they bent over the corners of the reinforcing bars before springing back. The epoxy holding the reinforcing bars on was often broken after the test, but the hose clamps kept the bars in position.

Schlieren images from one test (shot 56) are shown in Fig. 30 and the associated blast pressures are shown in Fig. 31. Note that the larger opening above the slot gage results in a much faster reduction in the pressure at this location than in shot 42 and other tests with the fixed slot. The blast pressures are much larger in amplitude for opening flaps than the fixed slot. This is a simple consequence of the much greater flow area in the flap case once the flaps are opened.

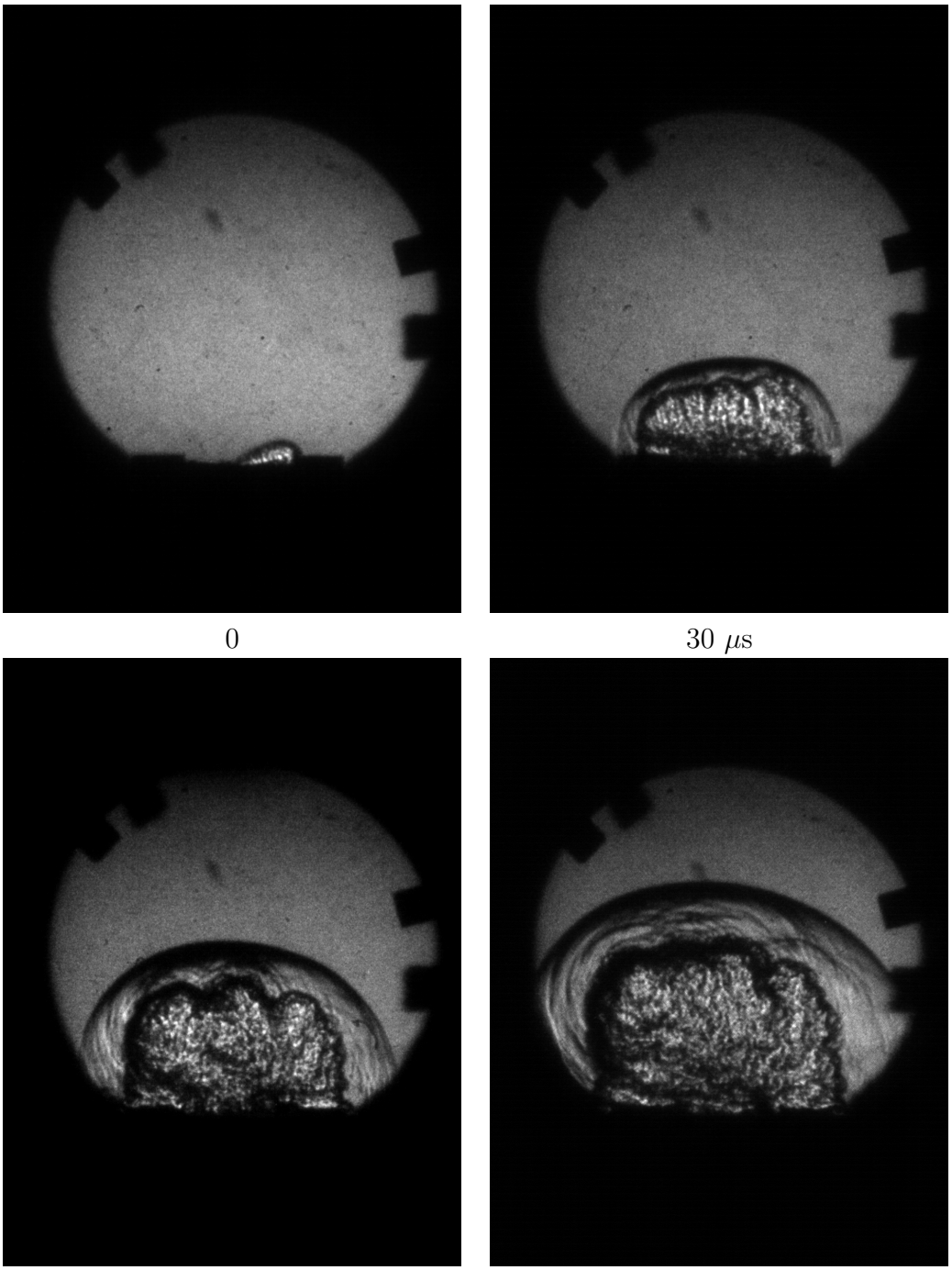

Figure 25: Representative images of blast wave venting through 3 mm slot, shot 42. Detonation wave is traveling from right to left. Note that camera is triggered by P4, the pressure transducer under the slot. Camera times are referenced to the arrival of the detonation at the middle of the slot.

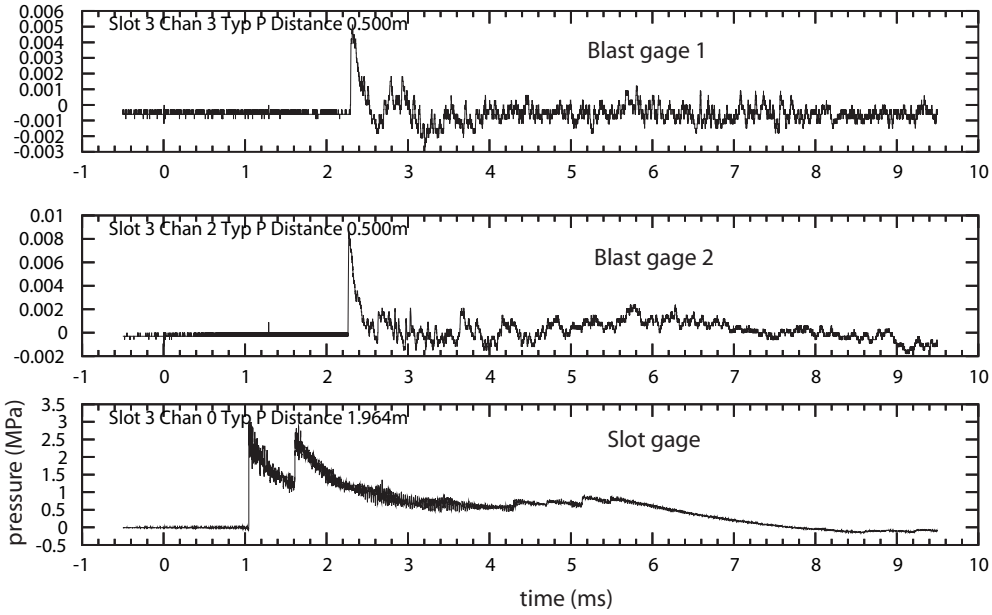

Figure 26: Blast gage and slot pressure transducer signals, shot 42.

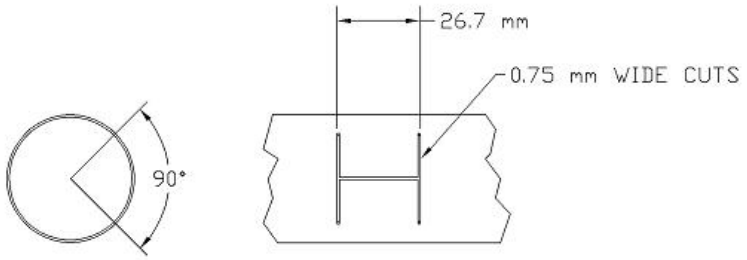

Figure 27: Tube flap dimensions.

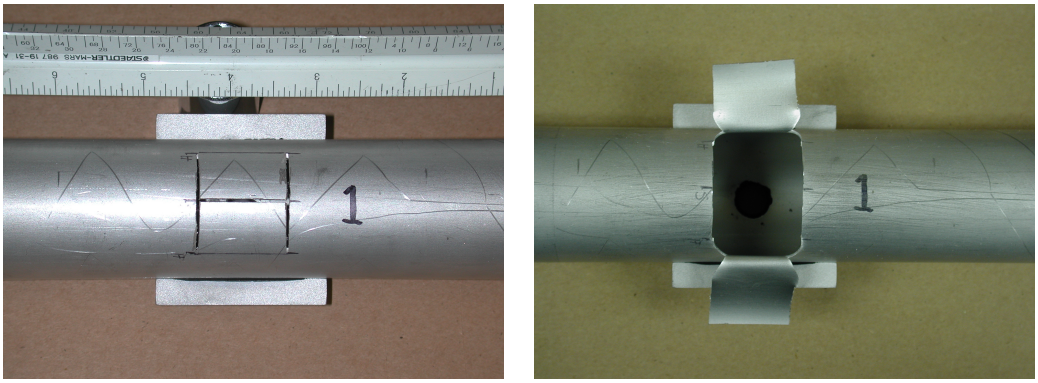

A B

Figure 28: Before and after photographs of flap tube 1. Note that the tube wall tore at the end of the cut, creating radiused corners extending to a new hinge line.

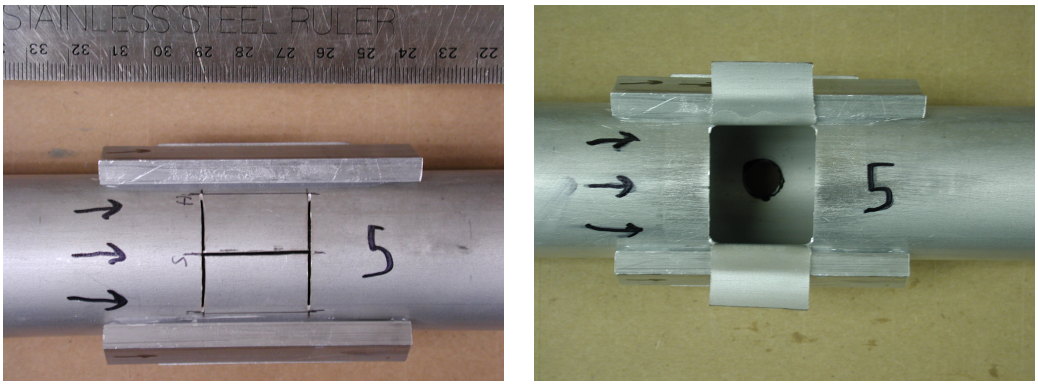

A B

Figure 29: Before and after photographs of flap tube 5. The added reinforcing bars limited the amount of tearing at the corners.

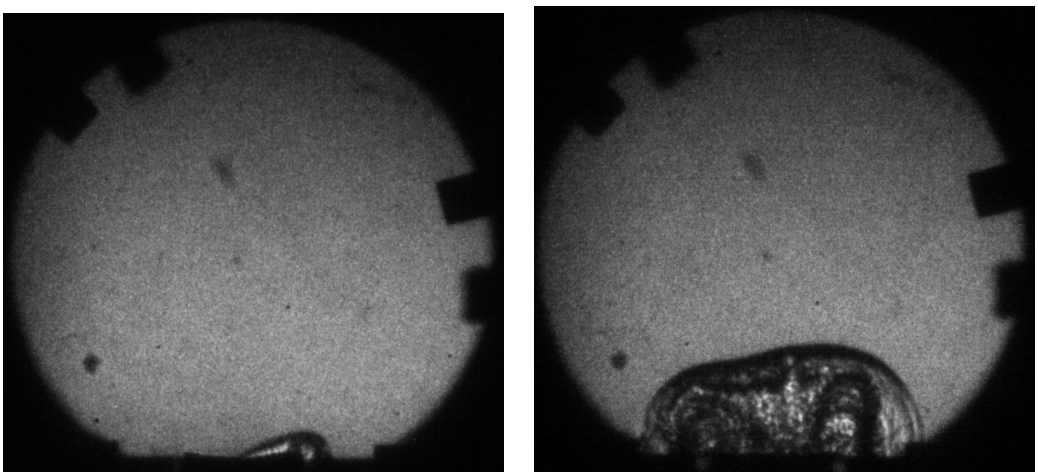

1 31 μs

61 μs 91 μs

Figure 30: Detonation wave rupturing pre-cut flaps in tube. Wave is traveling from right to left. Note the two "fingers" that appear to vent from the slot junctions. Flaps appear to be vertical at 211 s, and have reached (or passed) horizontal at 421 s. Images from tests 56 and 58. Note that camera is triggered by P4, pressure transducer under slot. Camera times are therefore referenced to the arrival of the detonation at the middle of the slot.

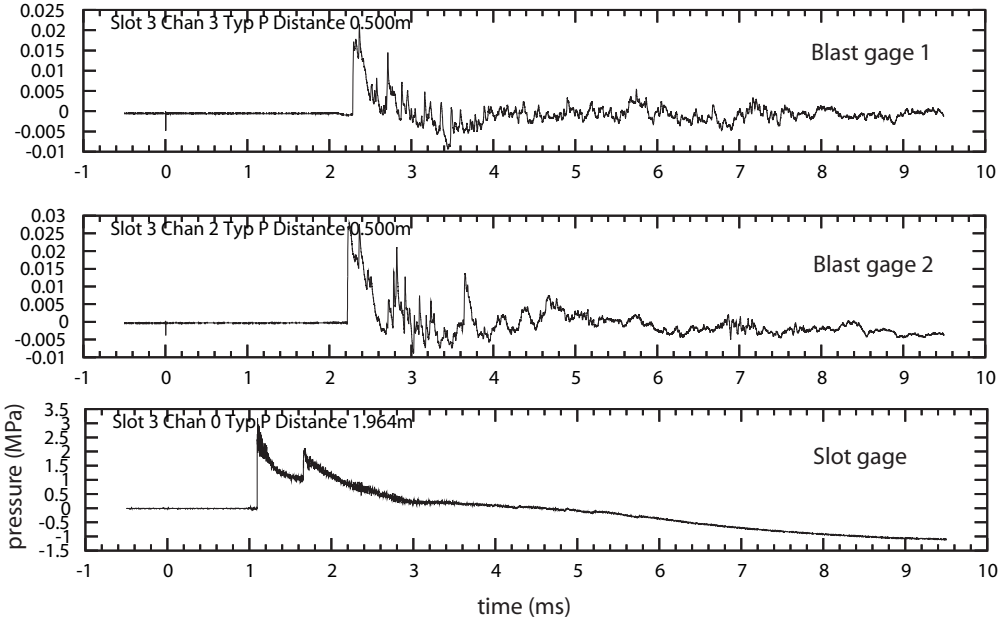

Figure 31: Blast gage and slot pressure transducer signals, shot 56.

5 Summary and Conclusions

Three series of tests were carried out to quantify uncertainties in the measurements of strain in closed tube and provide new data on blast waves and fluid-solid coupling in a simple geometry. Our main conclusions are:

Closed tube studies

The detonation loading process is repeatable. The vibrometer measurements of displacement were very repeatable and much more useful for validation than the strain gage signals. The vibrometer data had a $\pm$ 2% shot-to-shot variation in peak amplitude with systematic differences between gage locations and no noticeable effect of prestress. The strain gages had 7% shot-to-shot variation in peak amplitude and showed artifacts characteristic of micro-cracking in the gage element.

The companion study (Liang et al., 2008) showed that the detonation pressure and velocity were very ($< 0.5\%$ shot-to-shot variation) reproducible, and there was significant high frequency structure in the pressure signal. Tube wall thickness variation is significant for making accurate comparisons with simulations. These variations are apparently due to eccentric mandrel locations used in manufacturing. The wall thickness variations was measured by destructive testing and the circumferential variation was found to be much more significant than the longitudinal variation. Tests at two different initial pressures demonstrated linear scaling of the strains with the applied load and a static loading test demonstrated a small amount of hysteresis in the strain gage response.

Slots and Flaps

Two methods were developed to look at the coupling of fluid and structural mechanics as validation cases. Using a fixed slot in the tube effectively decouples the fluid and structural mechanics. This greatly simplifies the structural mechanics but the remaining fluid mechanics problem is challenging since the flow is three dimensional and validation against blast signatures requires computing the propagation of a blast wave at a large distance from the slot. Using a pre-cut flaps with reinforcement on the tube retains some of the coupling between structural and fluid mechanics. The situation is however much simpler than computing the detonation-driven fracture experiments of Chao (2004), see the efforts of Deiterding et al. (2007) in this direction.

6 Acknowledgement

The ASC Center for Simulation of Dynamic Response of Materials is based at the California Institute of Technology and operated under U. S. Department of Energy contract W-7405-ENG-48. We thank Dan Meiron for his support of the validation projects. Fehmi Cirak (currently at Cambridge University) and Ralf Deiterding (currently at Oak Ridge National Laboratory) carried out the companion validation simulations as part of the ASC center activities.

Bibliography

W. M. Beltman and J. E. Shepherd. Structural response of shells to detonation and shock loading. Technical report, Graduate Aeronautical Laboratories, California Insititute of Technology, 1998. 9, 32

W.M. Beltman, E.N. Burcsu, J.E. Shepherd, and L. Zuhal. The structural response of cylindrical shells to internal shock loading. *Journal of Pressure Vessel Technology*, 121: 315–322, 1999. 9

W.M. Beltman and J.E. Shepherd. Linear elastic response of tubes to internal detonation loading. *Journal of Sound and Vibration*, 252(4):617–655, 2002. 9, 16, 23, 32

R. D. Blevins. *Formulas for natural frequency and mode shape*. van Nostrand Reinhold Company, 1979. 16

T. W. Chao. *Gaseous detonation-driven fracture of tubes*. PhD thesis, California Institute of Technology, 2004. 9, 10, 45

T. W. Chao and J. E. Shepherd. Comparison of fracture response of preflawed tubes under internal static and detonation loading. *Journal of Pressure Vessel Technology*, 126(3): 345–353, 2004. 9

T. W. Chao and J. E. Shepherd. Detonation loading of tubes in the modified shear wave regime. In Z. Jiang, editor, *Proceedings of the 24th International Symposium on Shock Waves, volume 2*, pages 865–870. Springer, 2005a. 9

T. W. Chao and J. E. Shepherd. Fracture response of externally flawed aluminum cylindrical shells under internal gaseous detonation loading. *International Journal of Fracture*, 134 (1):59–90, 2005b. 9

F. Cirak, R. Deiterding, and S. P. Mauch. Large-scale fluid-structure interaction simulation of viscoplastic and fracturing thin shells subjected to shocks and detonations. *Computers & Structures*, 85((11-14)):1049–1065, 2006. 9, 32

F. Cirak and M. Ortiz. Fully c^1-conforming subdivision elements for finite deformation thin-shell analysis. *Internat. J. Numer. Methods Engrg.*, 51:813–833, 2001. 9

F. Cirak, M. Ortiz, and P. Schröder. Subdivision surfaces: A new paradigm for thin-shell finite-element analysis. *Internat. J. Numer. Methods Engrg.*, 47(12):2039–2072, 2000. 9

R. Deiterding, F. Cirak, S. Mauch, and D. Meiron. A virtual test facility for simulating detonation-induced fracture of thin flexible shells. *Int. J. Multiscale Computational Engineering*, 5(1):47–63, 2007. 9, 32, 45

R. Deiterding, R. Radovitzky, S.P. Mauch, L. Noels, J. C. Cummings, and D. I. Meiron. A virtual test facility for the efficient simulation of solid material response under strong shock and detonation wave loading. *Engineering with Computers*, 22((3-4)):325–347, 2006. 9

A. S. Kobayashi, editor. *Handbook on Experimental Mechanics*. Society of Experimental Mechanics, second revised edition, 1993. 14, 21, 29

Z. Liang, J. Karnesky, J.E. Shepherd, and R. Deiterding. Detonations in C_2H_4-O_2. experimental measurements and validation of numerical simulation for incident and reflected waves. Technical Report FM2006.009, Graduate Aeronautical Laboratories, California Insititute of Technology, June 2008. 10, 11, 15, 22, 23, 32, 33, 45

N. Noda, R.B. Hetnarski, and Y. Tanigawa. *Thermal Stresses*. Taylor and Francis, 2002. ISBN 1-56032-971-8. 158

F. Pintgen and J. E. Shepherd. Structural response to deflagration-to-detonation transition events in a tube. Technical Report FM2005.005, Graduate Aeronautical Laboratories, California Insititute of Technology, Pasadena, CA 91125, 2005. 153, 161

M. Radulescu and R. K. Hanson. Effect of heat loss on pulse detonation flow fields and performance. *Journal of Propulsion and Power*, 21(2):275–285, 2005. 30

W.C. Reynolds. The element potential method for chemical equilibrium analysis: implementation in the interactive program STANJAN. Technical report, Mechanical Engineering Department, Stanford University, 1986a. 10

W.C. Reynolds. The element potential method for chemical equilibrium analysis: implementation in the interactive program STANJAN. Technical report, Mechanical Engineering Department, Stanford University, 1986b. 159

S.P. Timoshenko and J. N. Goodier. *Theory of Elasticity*. McGraw-HIll Publishing Company, third edition, 1970. 29

K. Ueda and A. Umeda. Dynamic response of strain gages up to 300 mhz. *Experimental Mechanics*, 38(2):93–98, 1998. 30

A.C. Ugural and S.K. Fenster. *Advanced Strength and Applied Elasticity*. Elsevier, 2nd si edition, 1987. 23

Vishay 11255. 2300 system. Technical Report 11255, Vishay Micro-Measurements, October 2006. URL http://www.vishay.com/doc?11255. 30

Vishay TN504. Strain gage thermal output and gage factor variation with temperature. Technical Report TN-504-1, Vishay Micro-Measurements, August 2007. URL http://www.vishay.com/doc?11054. 28

Vishay TN508. Fatigue characteristics of micro-measurements strain gages. Technical Report TN-508-1, Vishay Micro-Measurements, August 2007. URL http://www.vishay.com/doc?11058. 20

Vishay TN509. Transverse sensitivity errors. Technical Report TN-509, Vishay Micro-Measurements, August 2007. URL http://www.vishay.com/doc?11059. 28

Vishay TN511. Strain gage misalignment errors. Technical Report TN-511, Vishay Micro-Measurements, August 2007. URL http://www.vishay.com/doc?11061. 31

A Closed Tube Data

Table 3: Closed Tube tests with stoichiometric ethylene-oxygen.

Shot	Average V_{det} (m/s)	P_O (kPa)	Notes
1		0.8	no vibrometer. no data
2	2318.9	40	no vibrometer 1.1kPa of air added to tube, this is to get pump going by bleeding up between isolation valves
3	2319.2	40	no vibrometer
4	2325.8	40	no vibrometer
5	2315.7	40	vibrometer in place
6	2375.4	100	Test shot. No pretrigger. Das triggered by falling edge from scope back panel output
7	2036.7	50	all good
8		100	no vibrometer. no data - wrong edge
9	2378.2	100	no vibrometer
10	2491.6	100	With vibrometer. prestress might introduce difference in strain
11	2275.0	100	with vibrometer
12	1832.2	100	with vibrometer
13	1307.4	100	with vibrometer
14	2378.2	100	with vibrometer
15	2378.2	100	with vibrometer
16	2375.4	100	with vibrometer
17	2347.6	50	with vibrometer
18	2347.6	50	with vibrometer
19	2344.8	50	with vibrometer
20	2378.2	100	tube turned by 120 deg compared to shot 19. Collets unaltered. Vibrometer measurement point is now also 120 degrees turned , so now close to S1.
21	2375.4	100	same conditions as shot 20
Continued on next page			

Table 3 – Continued from previous page

Shot	Average V_{det} (m/s)	P_0 (kPa)	Notes
22	2378.2	100	Measurement setup same as shot 21. Tube was prestressed by setting collet on end in a slight angle such that side with vibrometer measurement point is in compression
23	2375.4	100	measurement setup unchanged - no prestress.
24	2372.6	100	setup unchanged, just pressed on reflector to make sure its no attachment
25	2372.6	100	tube turned back into original position (shot 10-19). Vibrometer laser diaode position was not changed from shot 10 till shot 25 (this shot) (position in room)
26	2375.4	100	vibrometer moved to other side of tube. Tube turned such that measurement location on the tube surface is unchanged; the measurement location still S3.
27	2378.2	100	repeat of last shot, nothing altered
28	2372.6	100	measurement position unaltered, but (S4 (in axial directon of sparc plug) was removed. Tube polished aferwards - no epoxy rests
29	2375.4	100	tube turned back such that vibrometer points on S1. Vibrometer itself has not been moved
30	2379.0	100	no vibrometer, closed tube
31	2377.4	100	no vibrometer, closed tube
32	2376.5	100	no vibrometer, closed tube
33	2374.7	100	no vibrometer, closed tube
34	2373.8	100	no vibrometer, closed tube

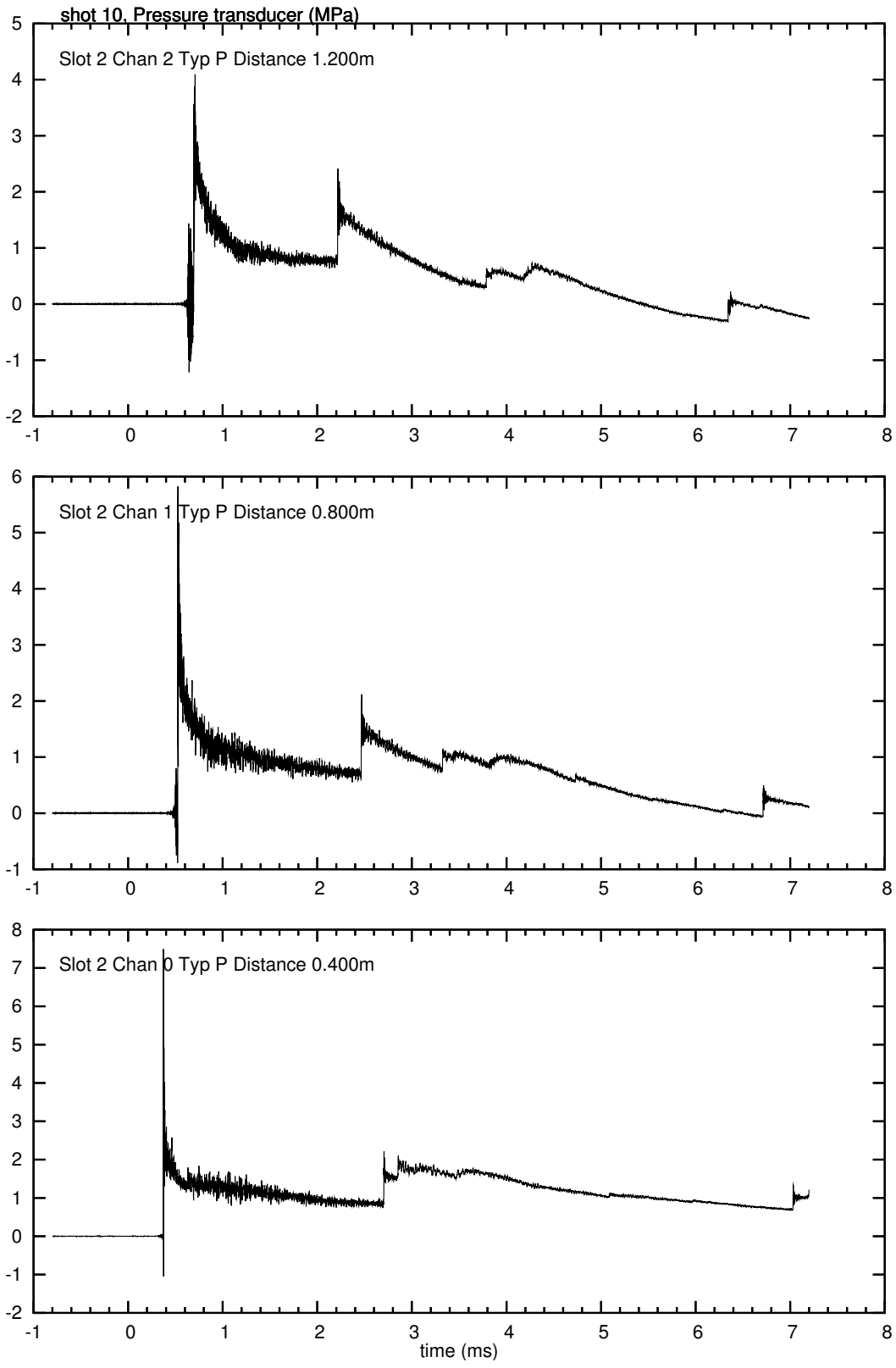

Figure 32: Pressure traces for shot 10

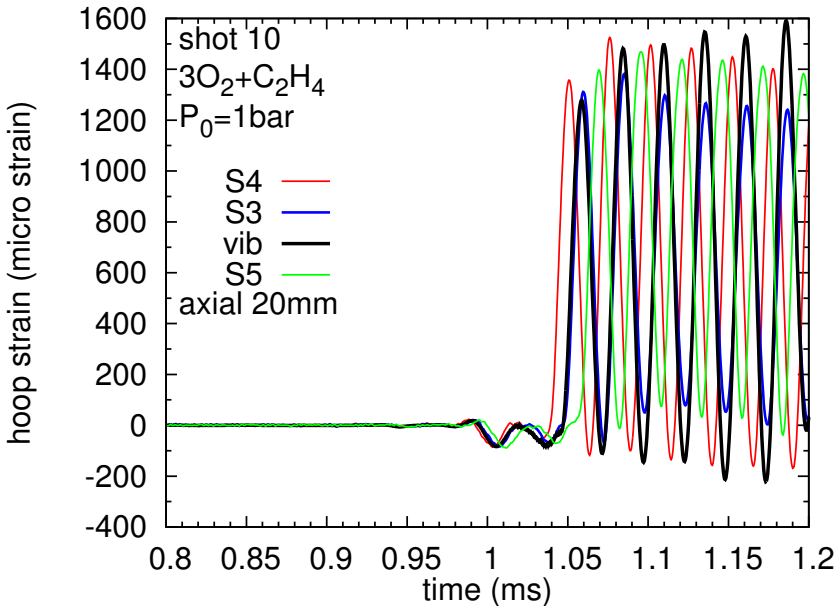

Figure 33: Axial location hoop strain comparisons for shot 10.

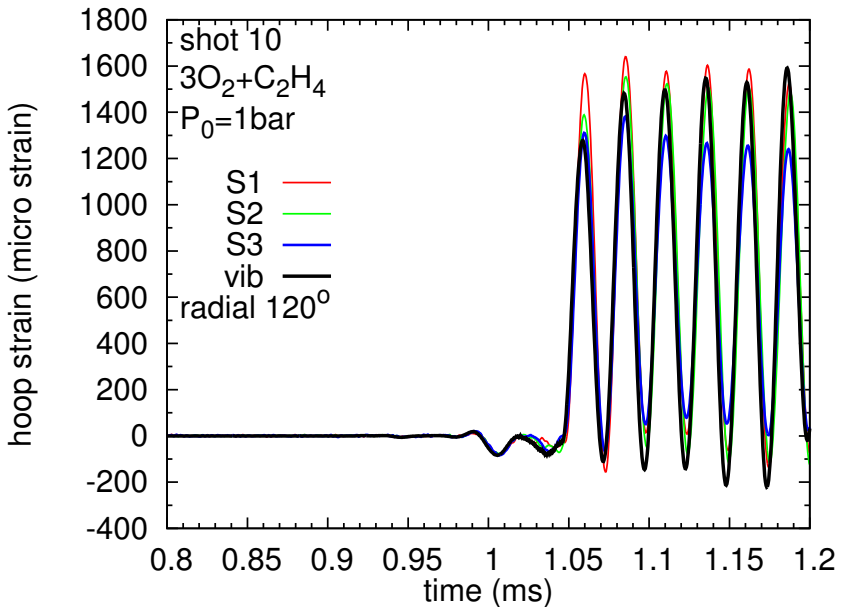

Figure 34: Radial strain comparisons for shot 10

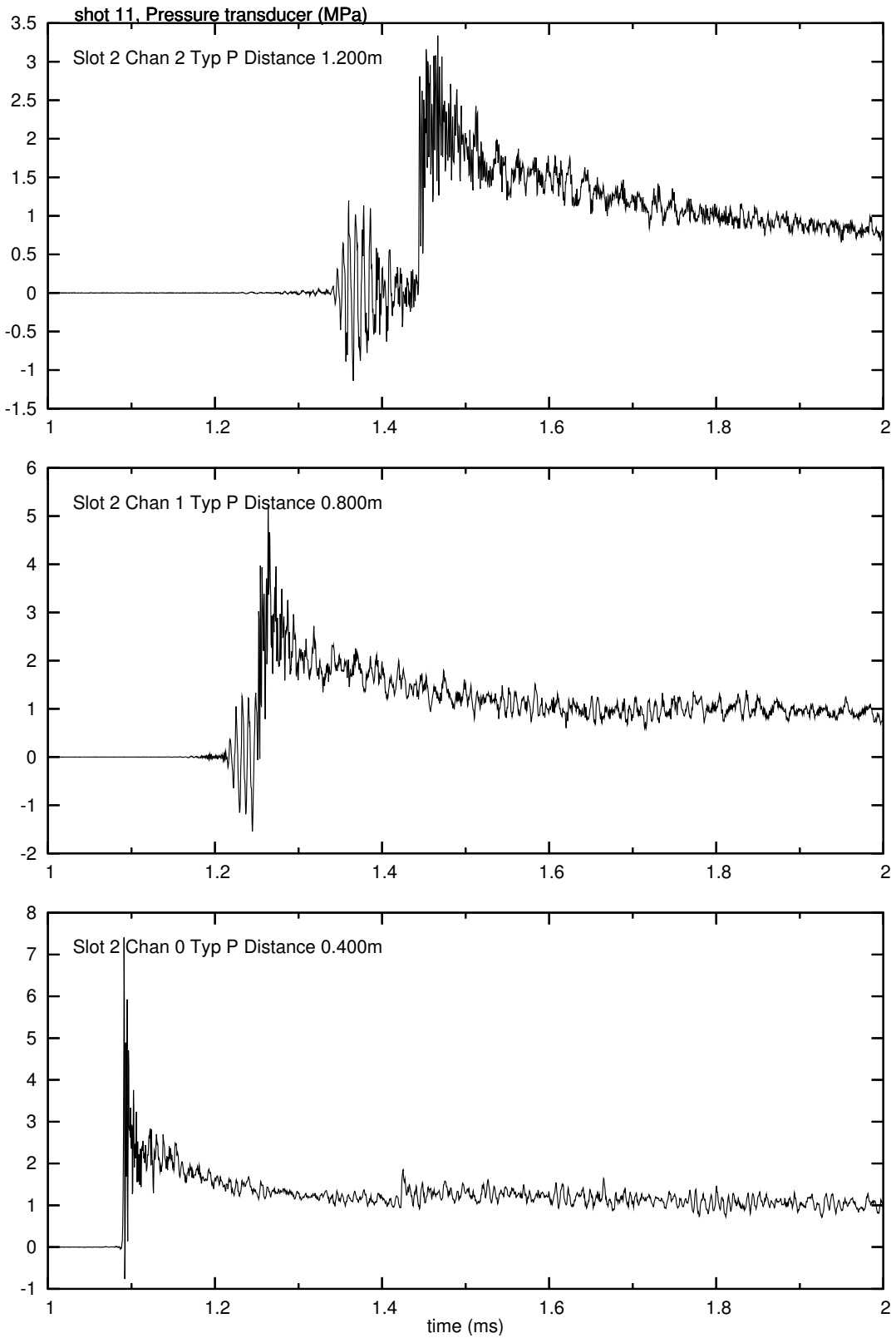

Figure 35: Pressure traces for shot 11

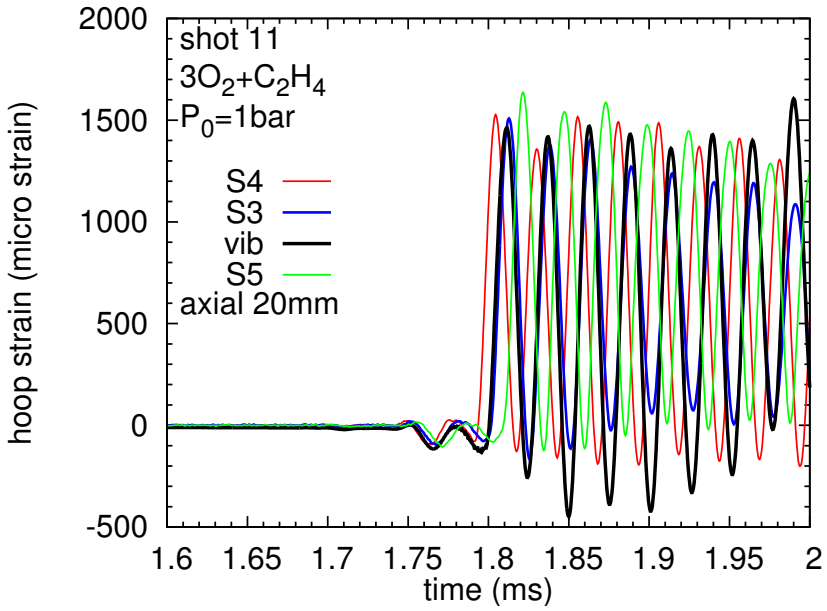

Figure 36: Axial location hoop strain comparisons for shot 11.

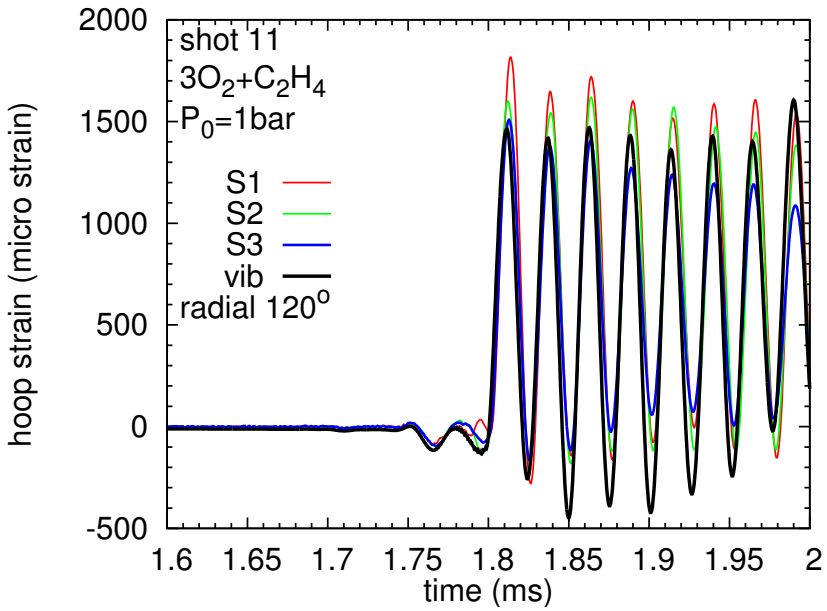

Figure 37: Azimuthal location hoop strain comparisons for shot 11

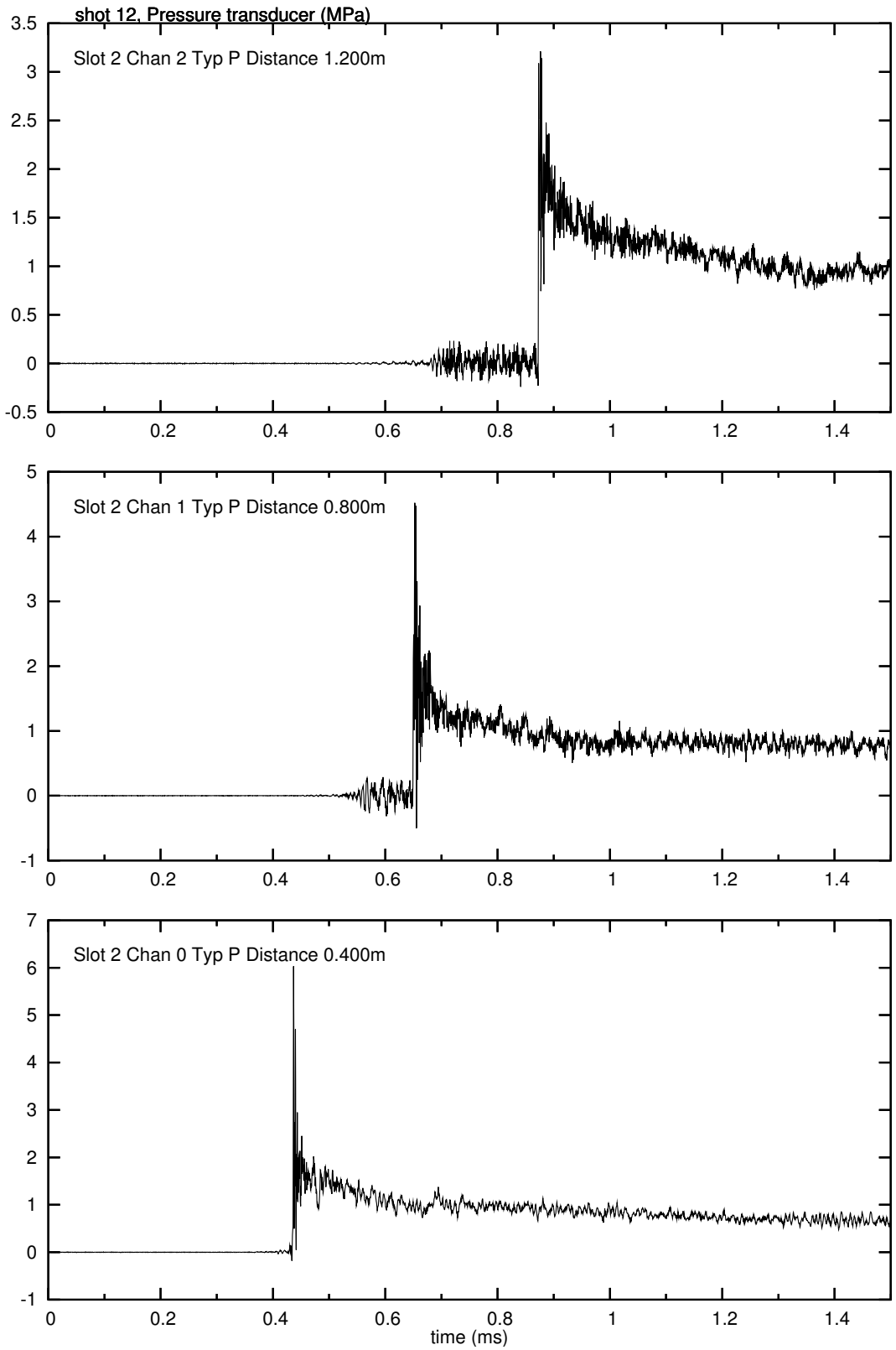

Figure 38: Pressure traces for shot 12

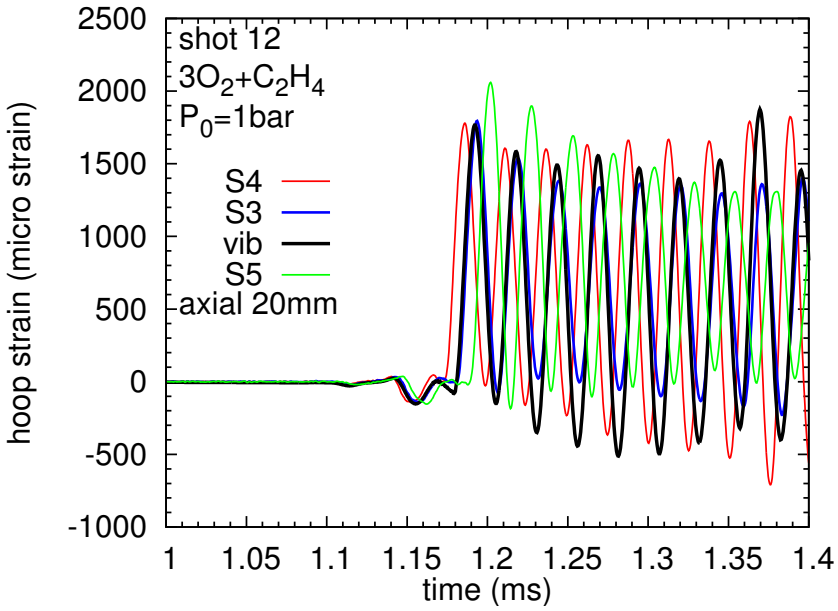

Figure 39: Axial location hoop strain comparisons for shot 12.

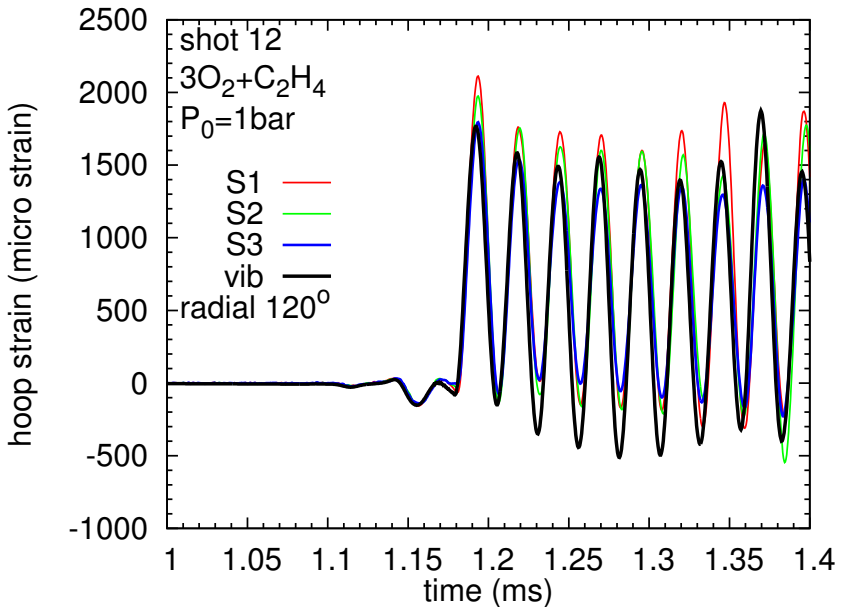

Figure 40: Azimuthal location hoop strain comparisons for shot 12

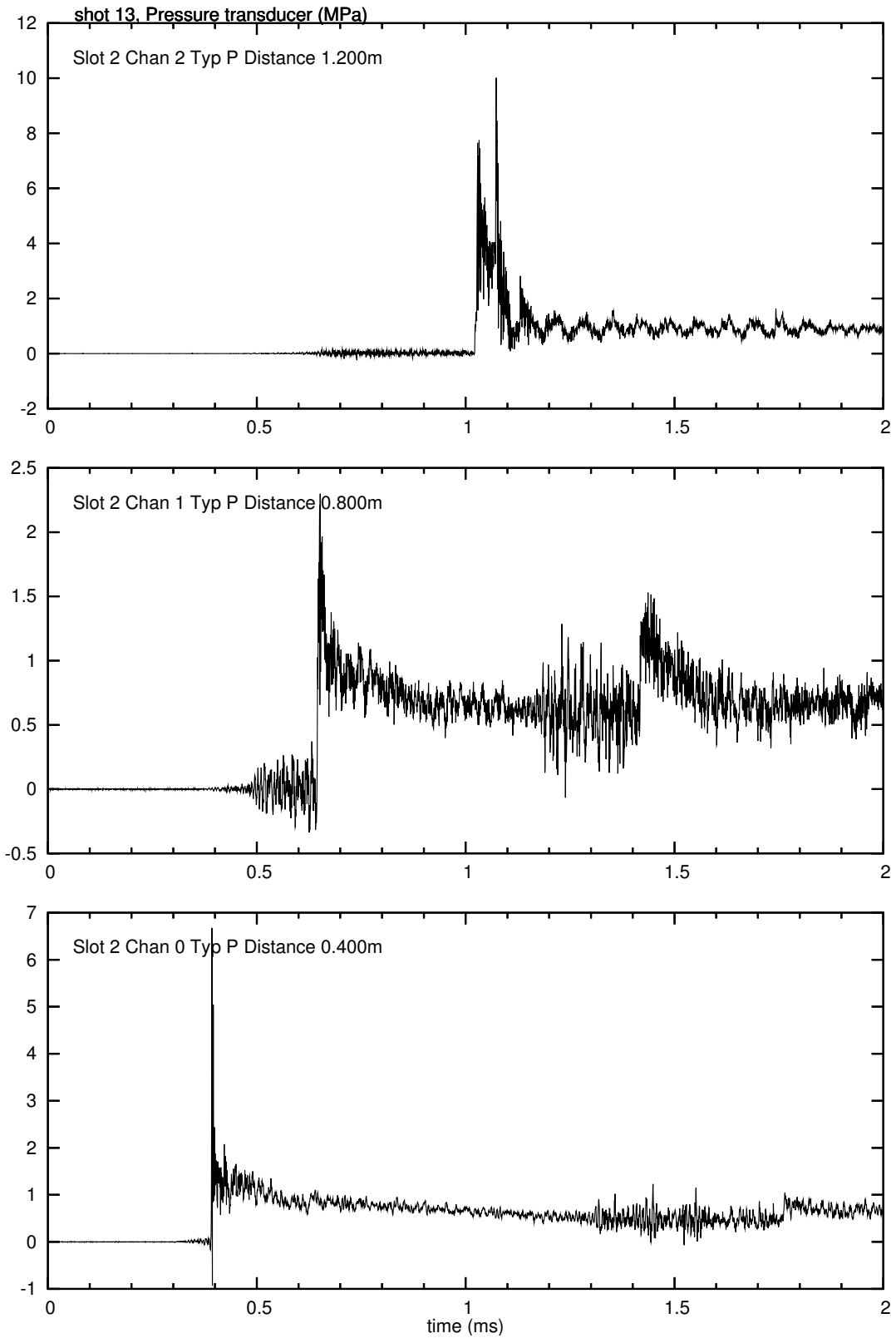

Figure 41: Pressure traces for shot 13

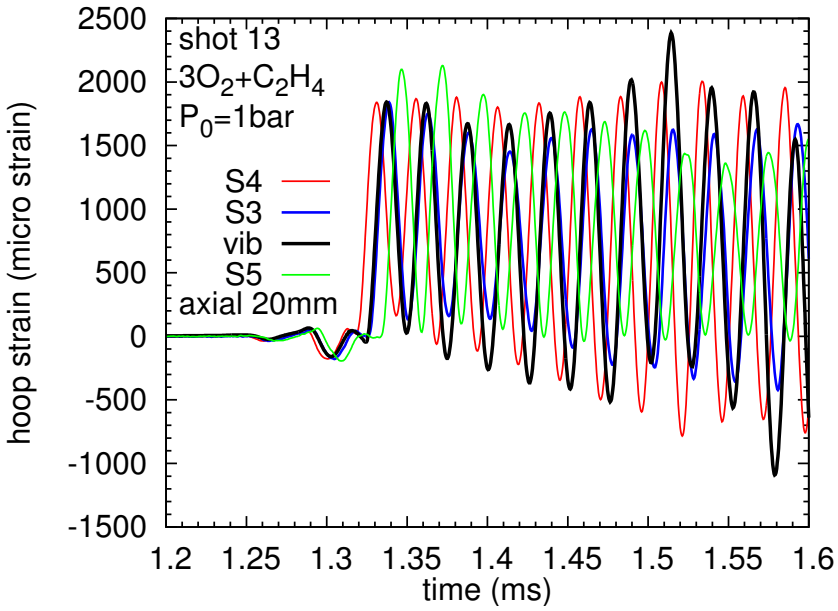

Figure 42: Axial location hoop strain comparisons for shot 13.

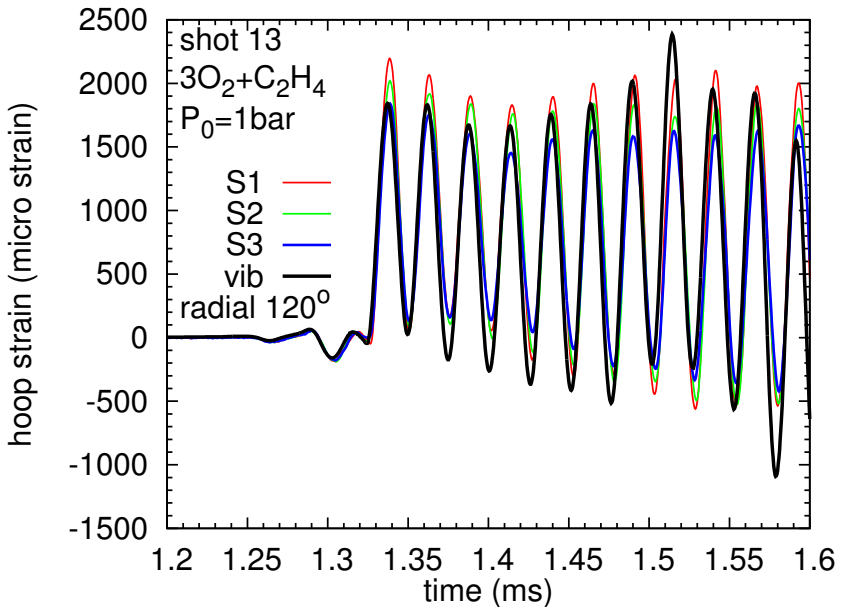

Figure 43: Azimuthal location hoop strain comparisons for shot 13

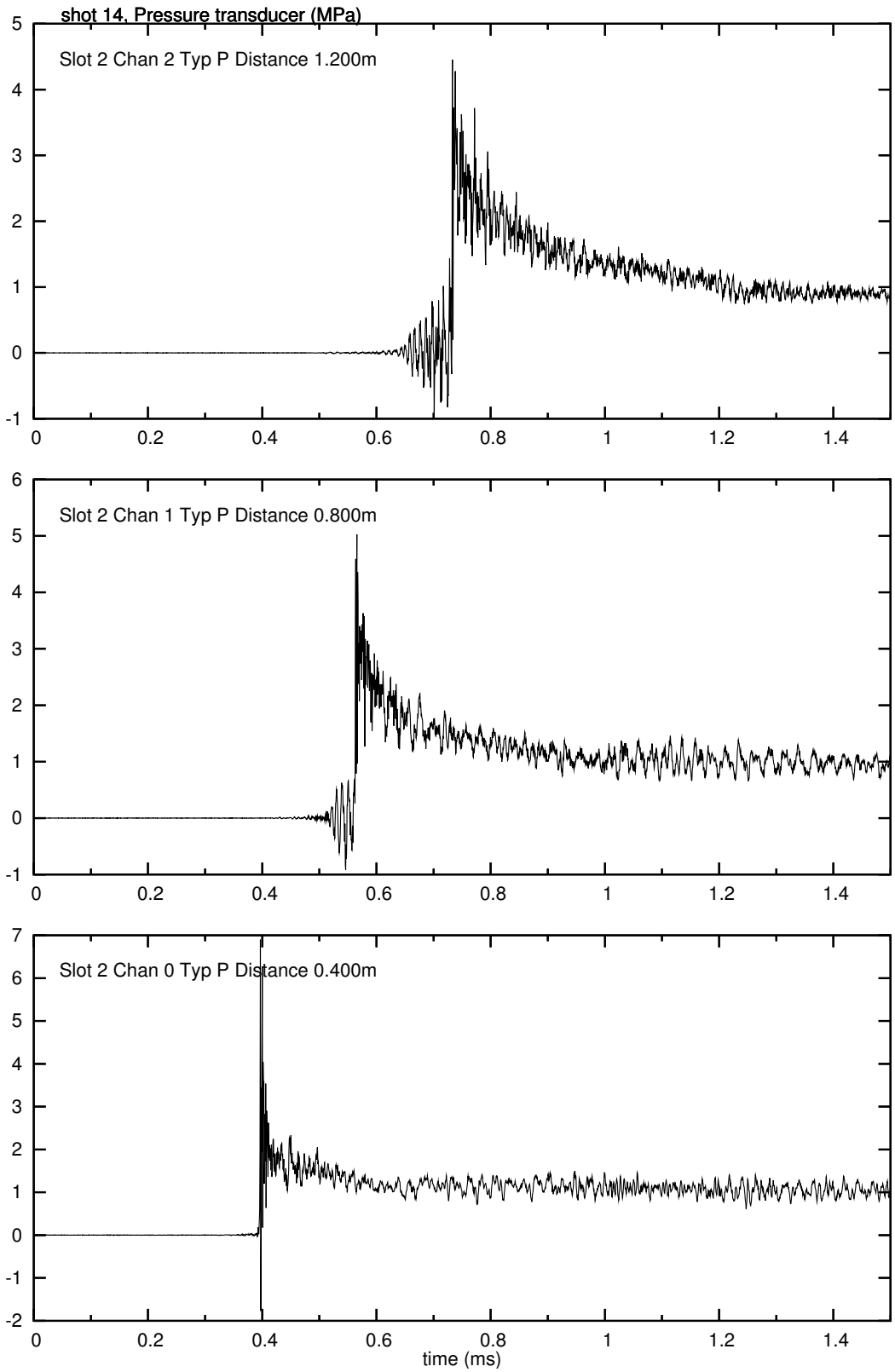

Figure 44: Pressure traces for shot 14

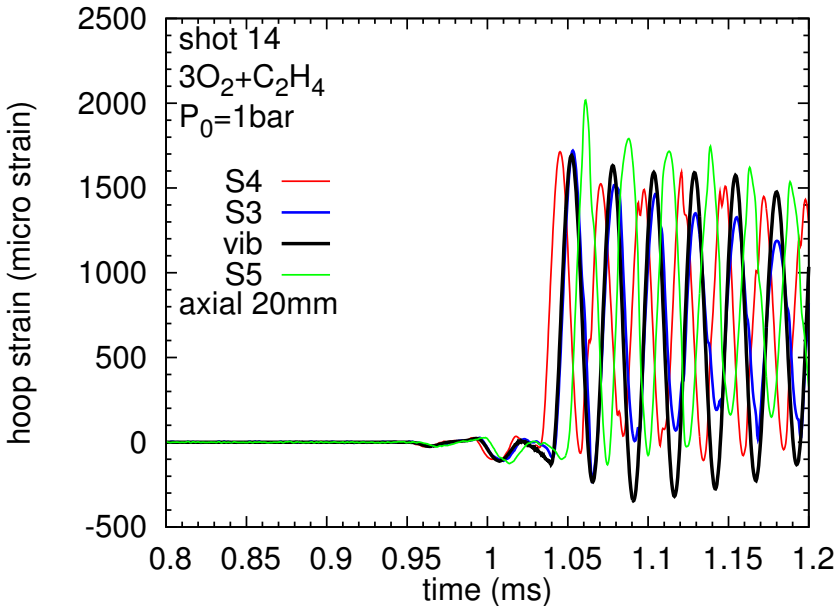

Figure 45: Axial location hoop strain comparisons for shot 14.

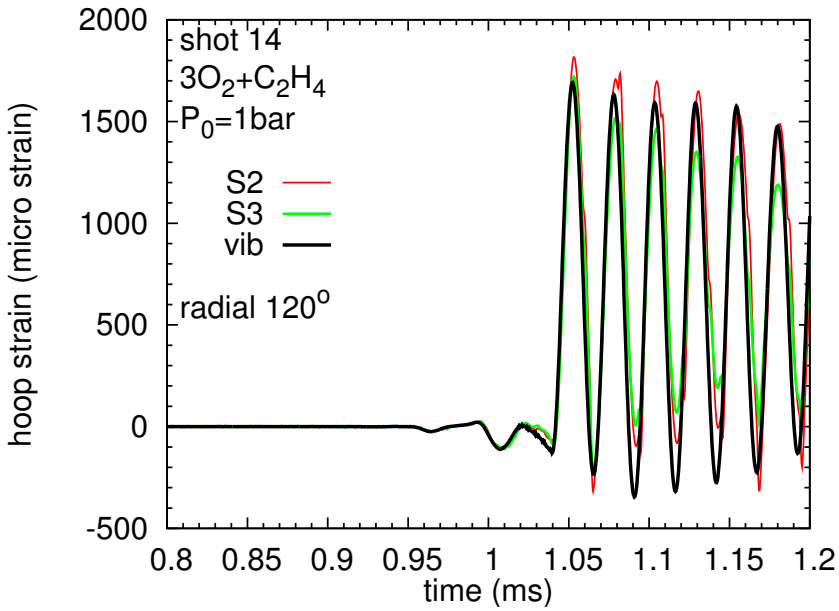

Figure 46: Azimuthal location hoop strain comparisons for shot 14

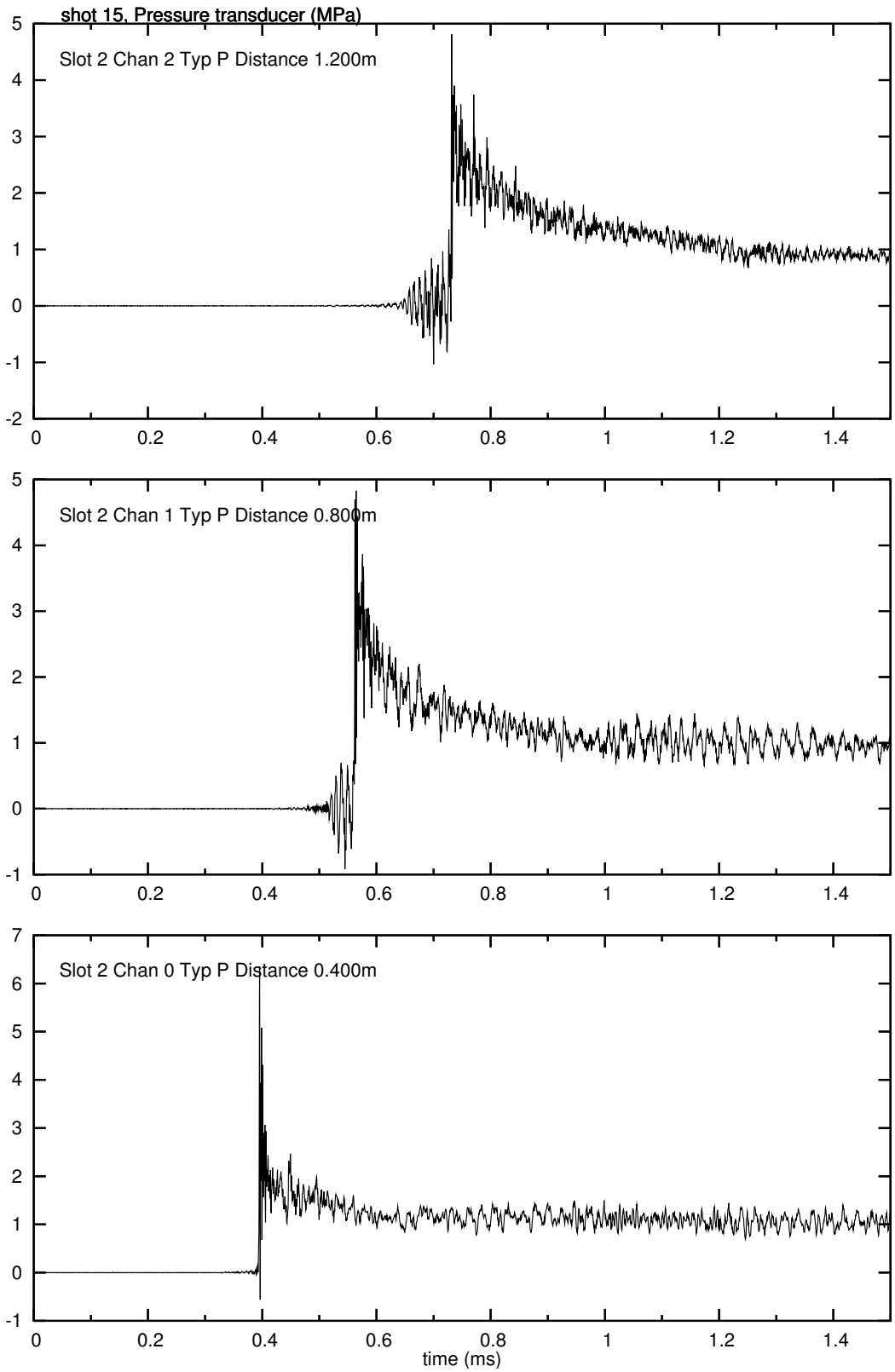

Figure 47: Pressure traces for shot 15

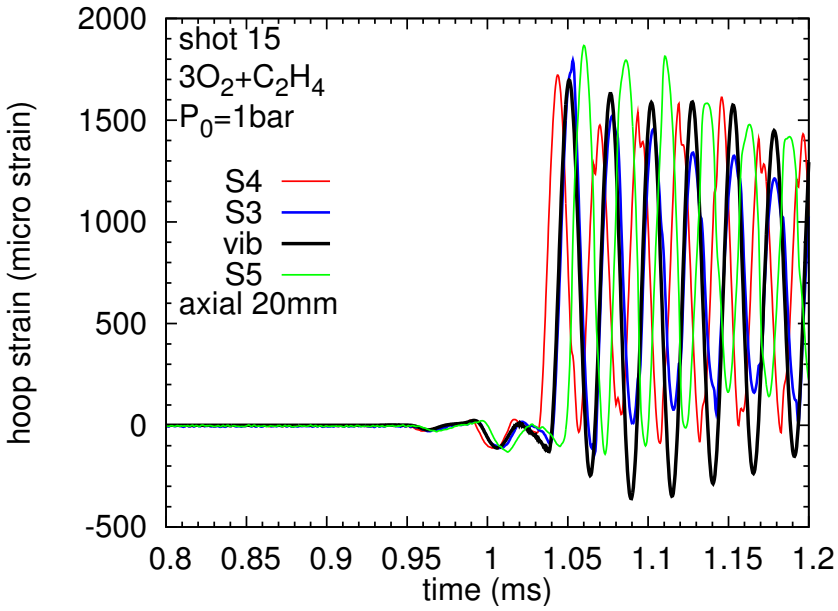

Figure 48: Axial location hoop strain comparisons for shot 15.

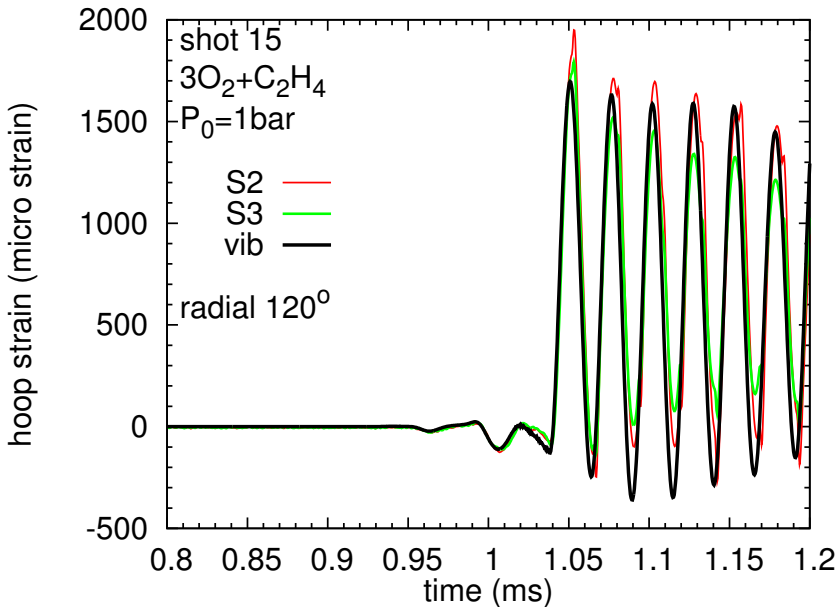

Figure 49: Azimuthal location hoop strain comparisons for shot 15

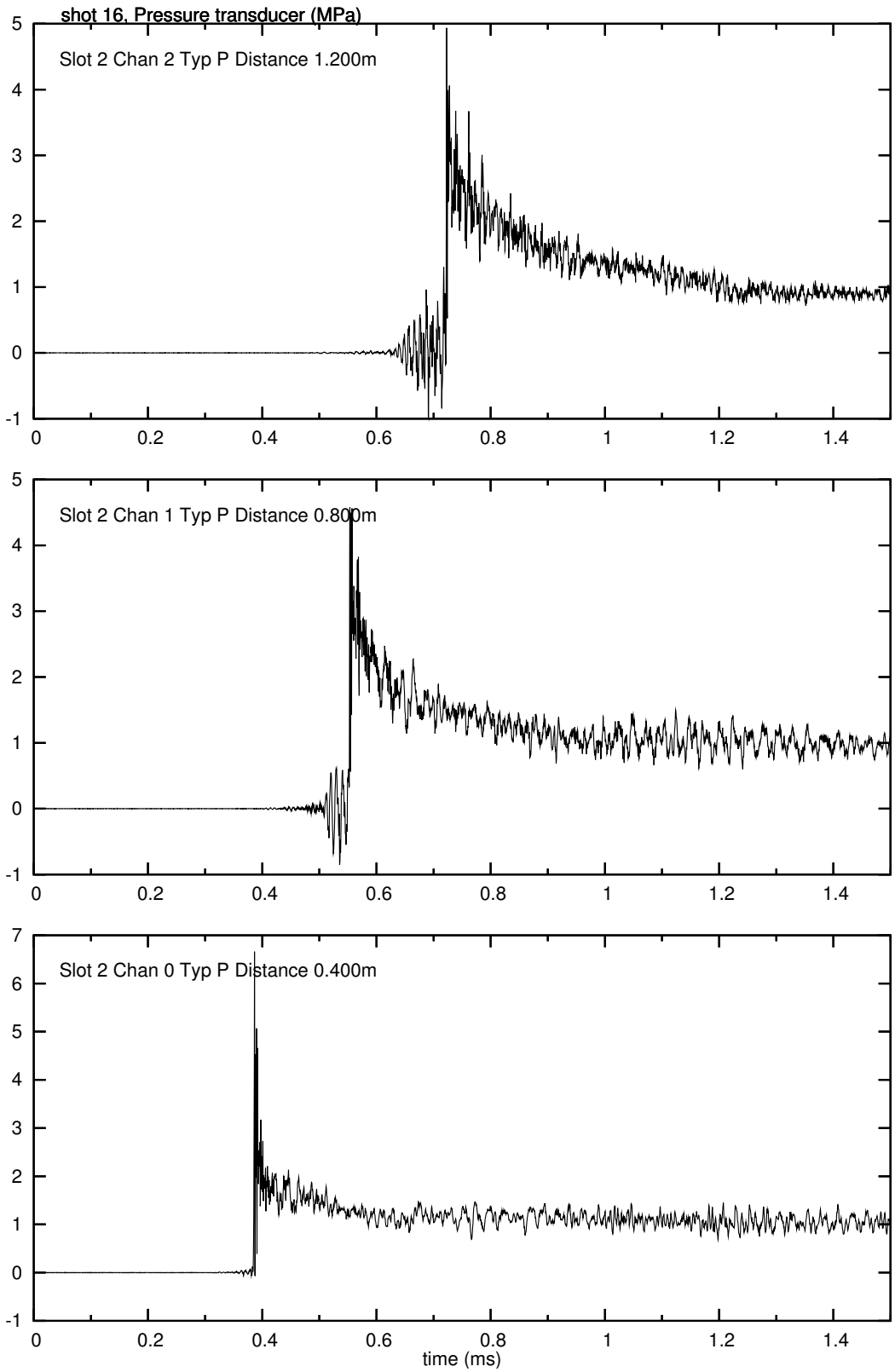

Figure 50: Pressure traces for shot 16

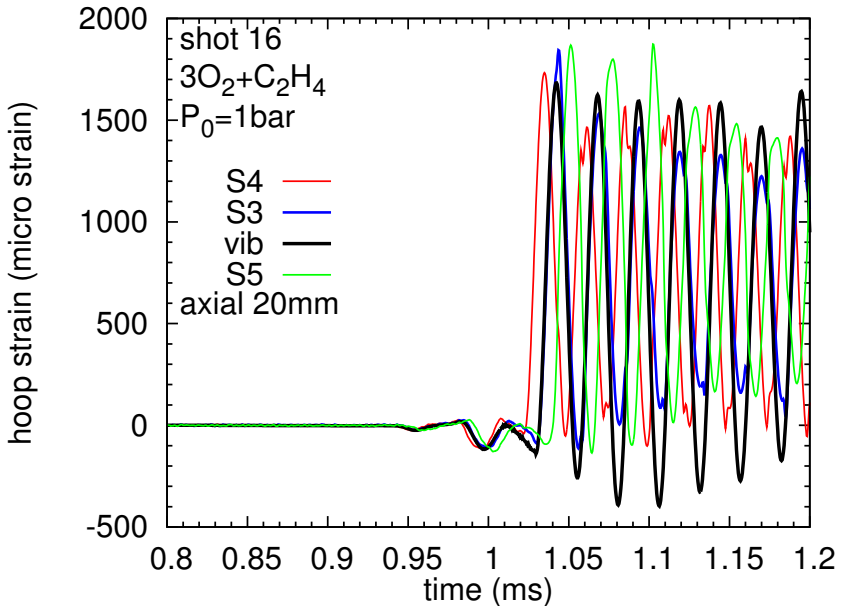

Figure 51: Axial location hoop strain comparisons for shot 16.

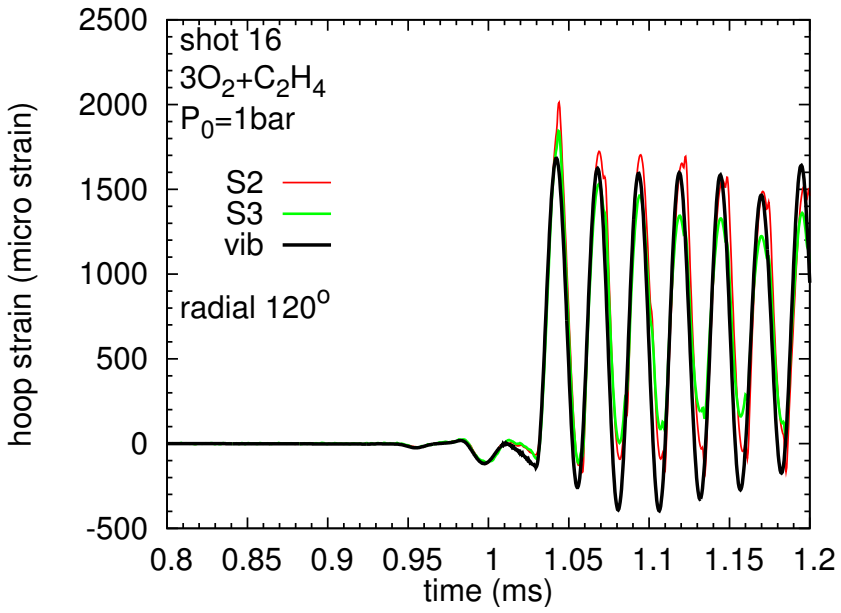

Figure 52: Azimuthal location hoop strain comparisons for shot 16

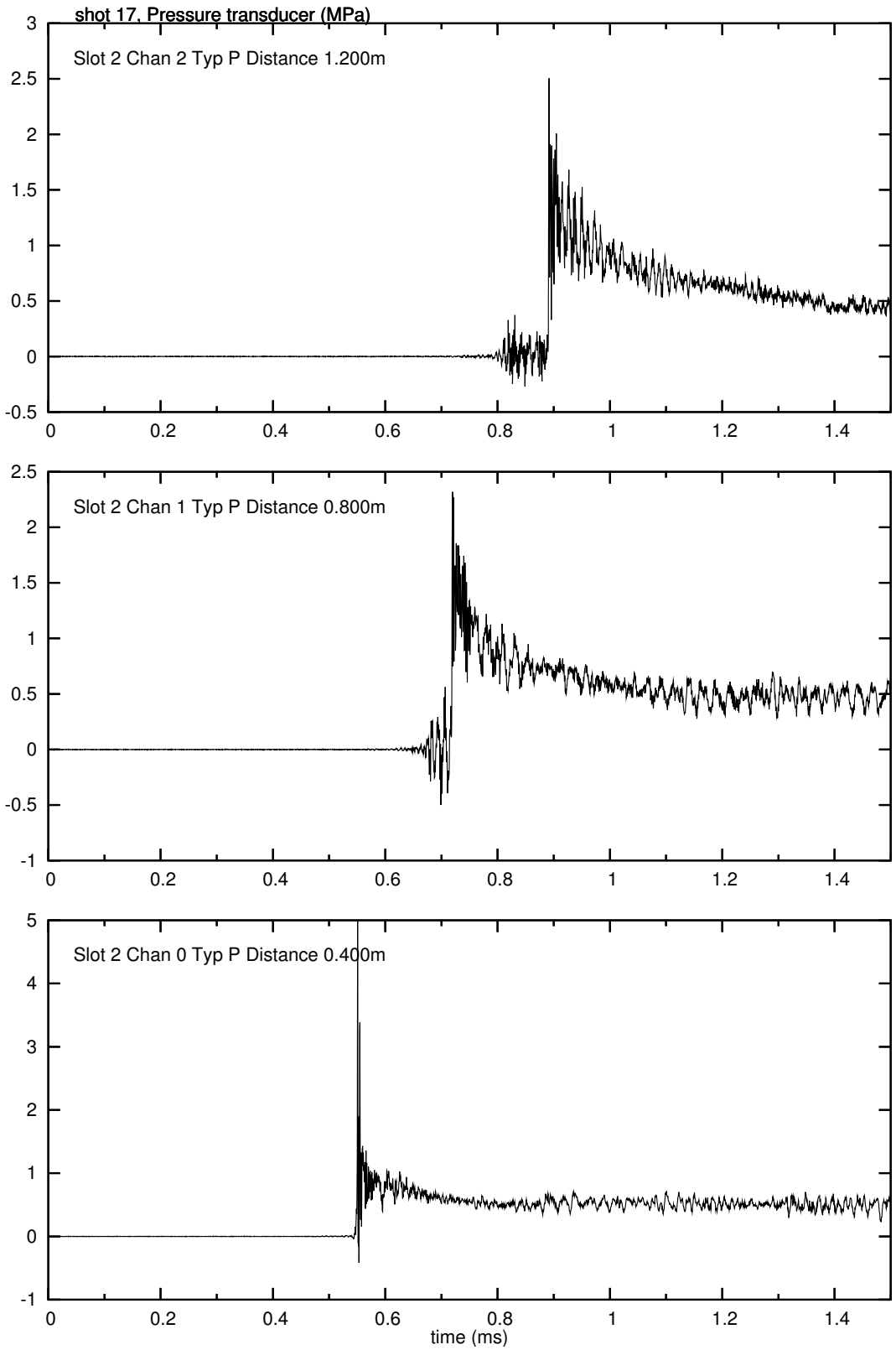

Figure 53: Pressure traces for shot 17

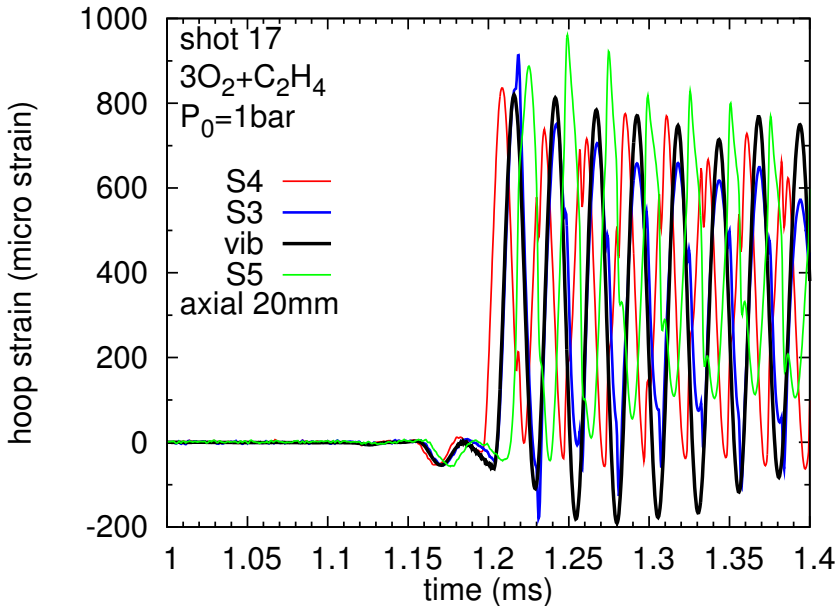

Figure 54: Axial location hoop strain comparisons for shot 17.

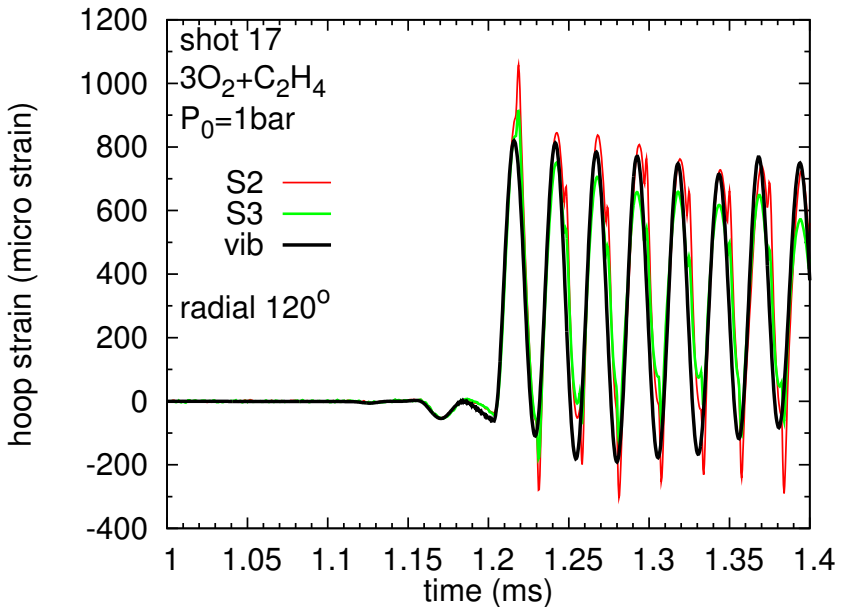

Figure 55: Azimuthal location hoop strain comparisons for shot 17

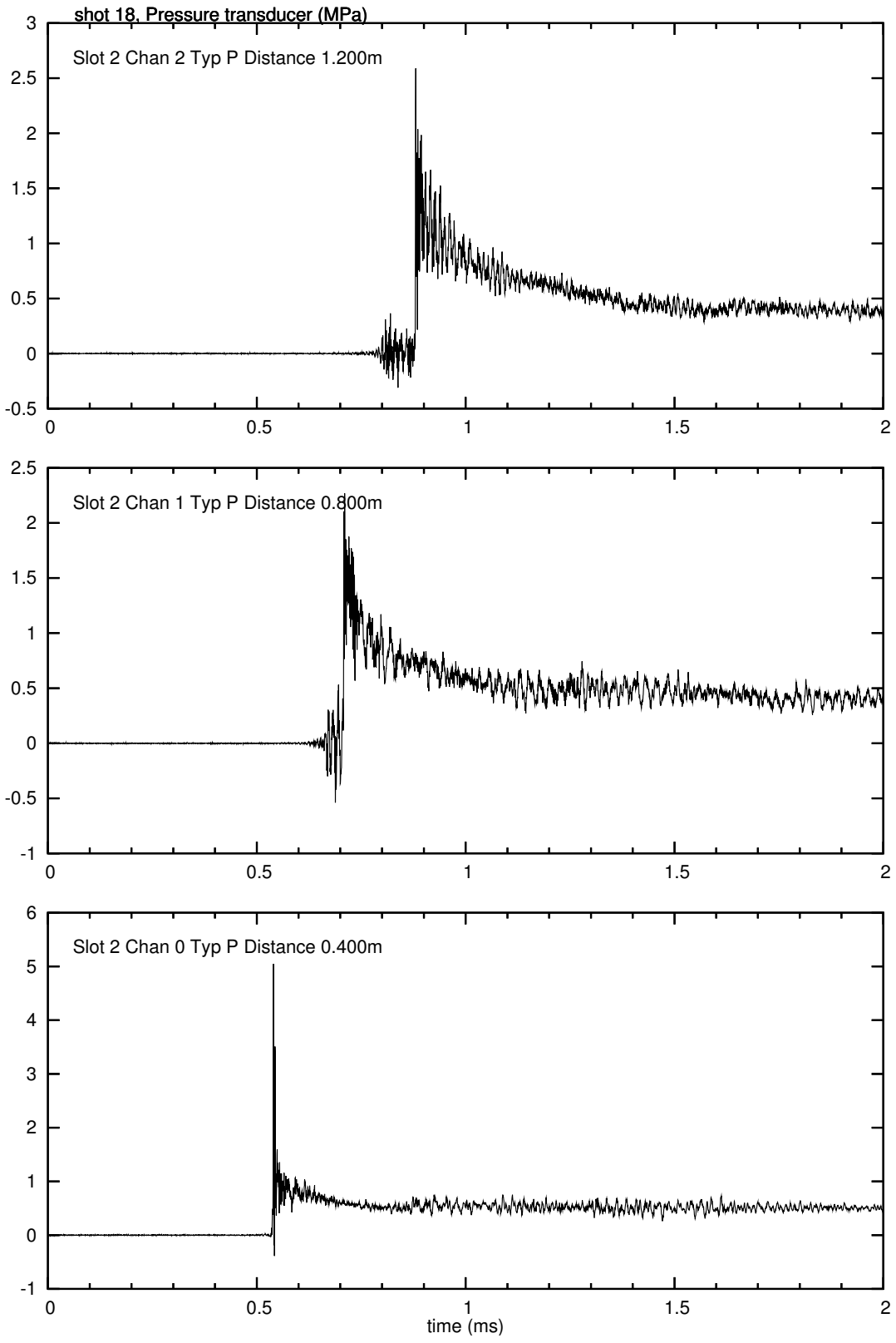

Figure 56: Pressure traces for shot 18

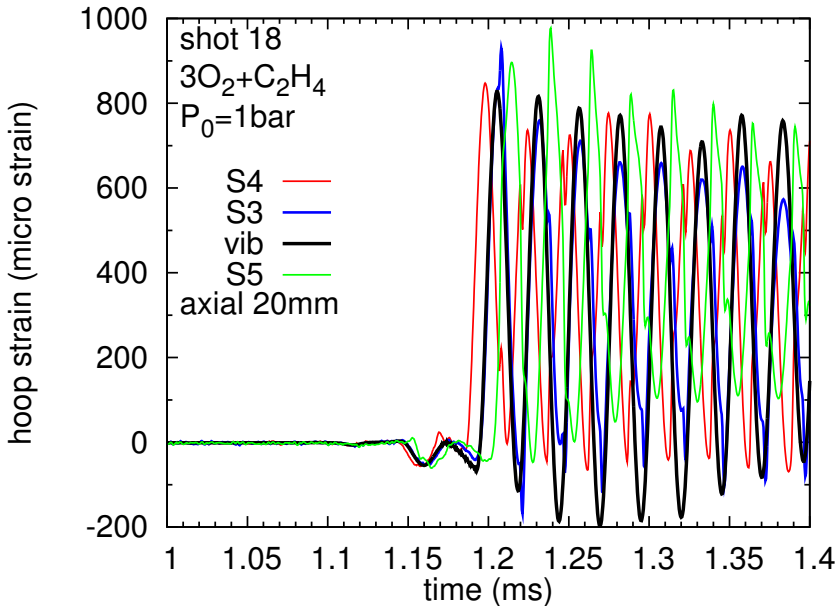

Figure 57: Axial location hoop strain comparisons for shot 18.

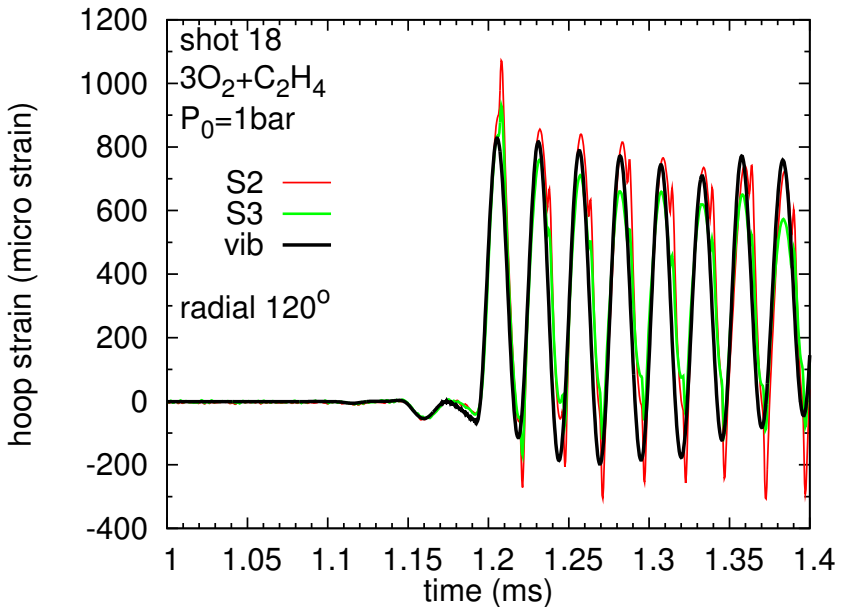

Figure 58: Azimuthal location hoop strain comparisons for shot 18

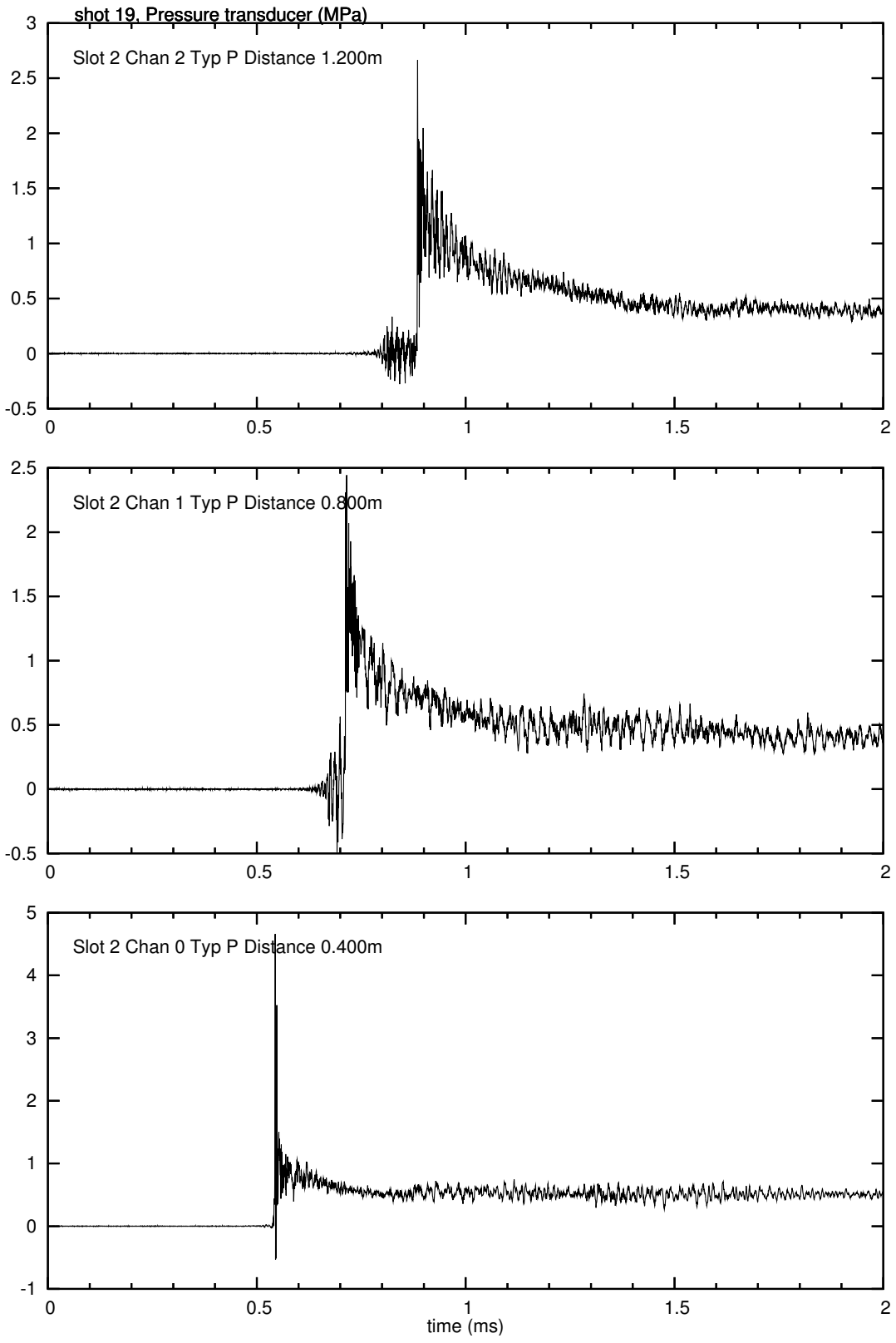

Figure 59: Pressure traces for shot 19

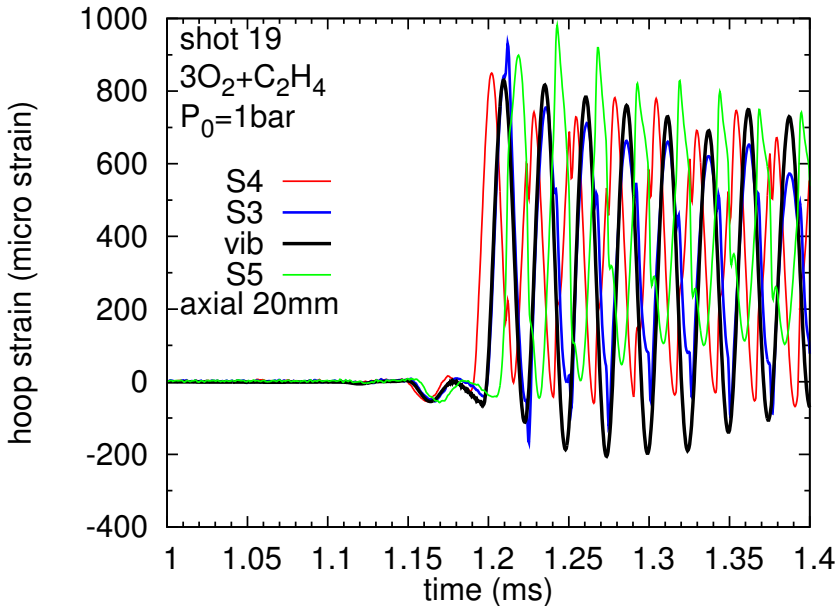

Figure 60: Axial location hoop strain comparisons for shot 19.

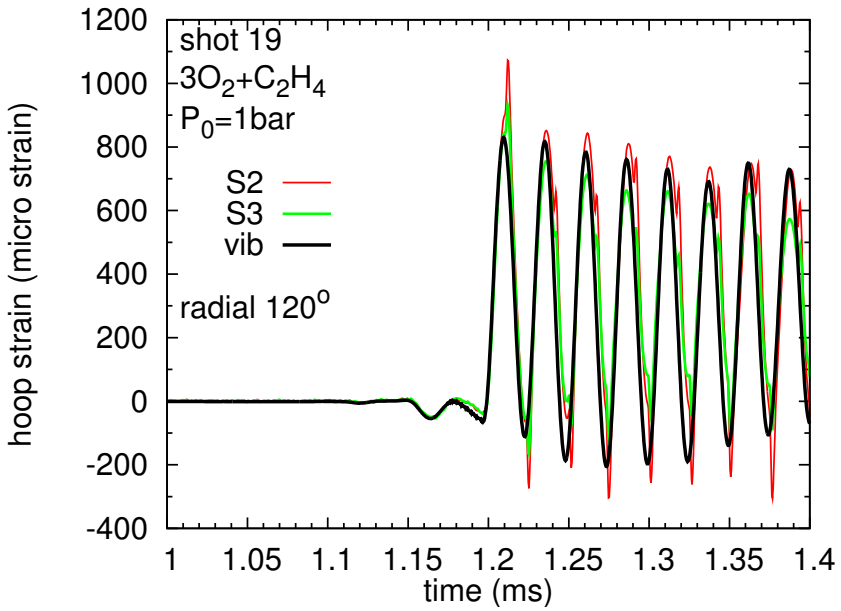

Figure 61: Azimuthal location hoop strain comparisons for shot 19

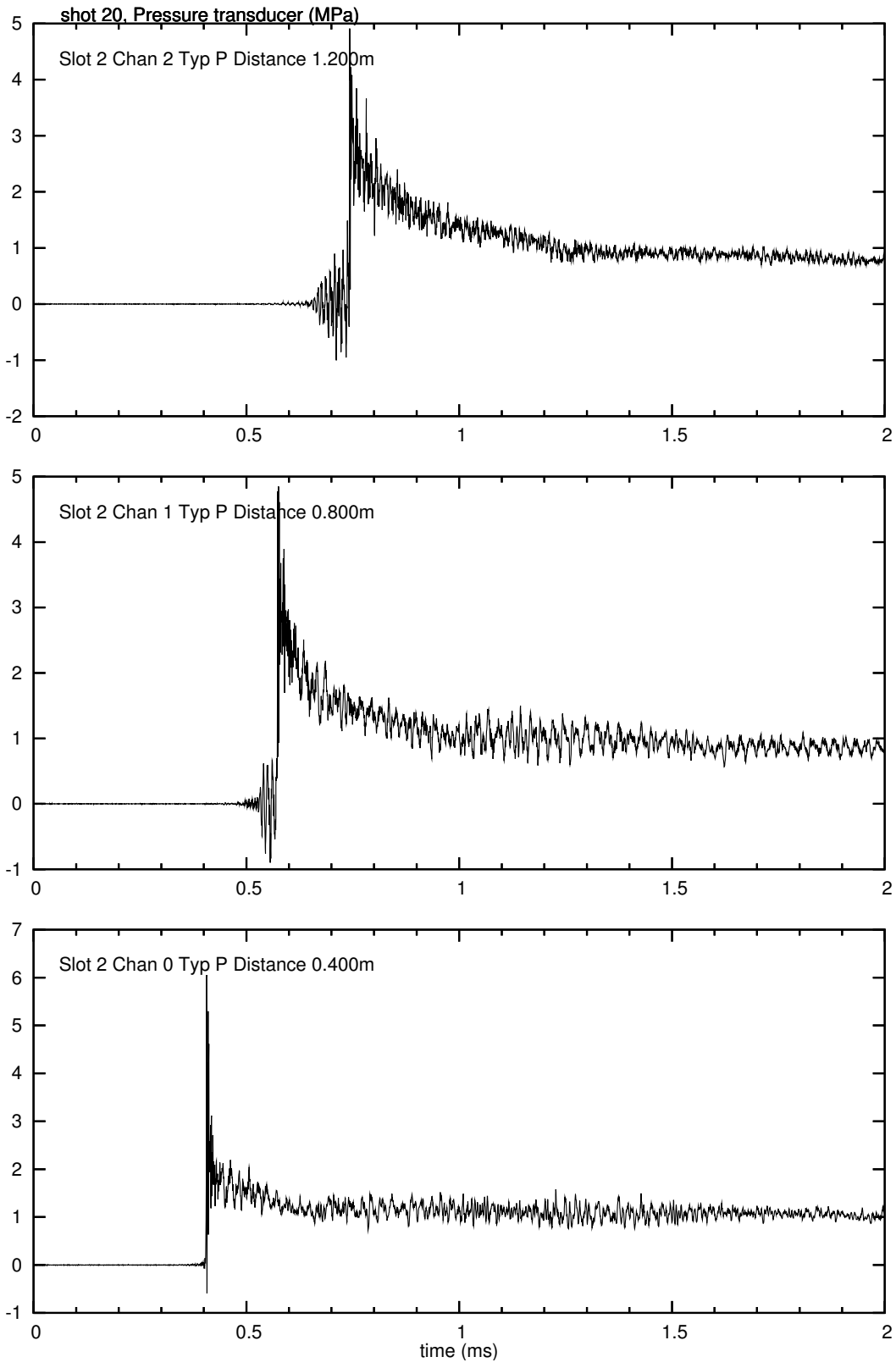

Figure 62: Pressure traces for shot 20

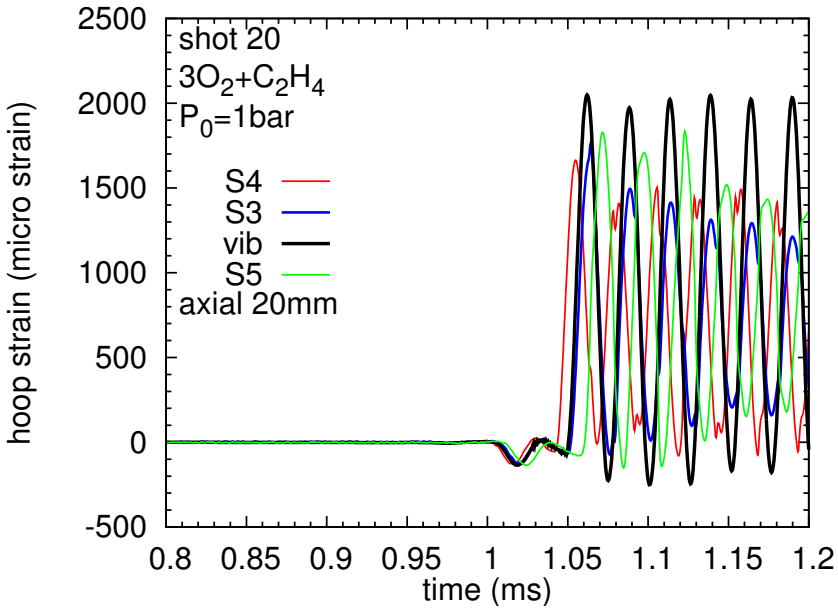

Figure 63: Axial location hoop strain comparisons for shot 20.

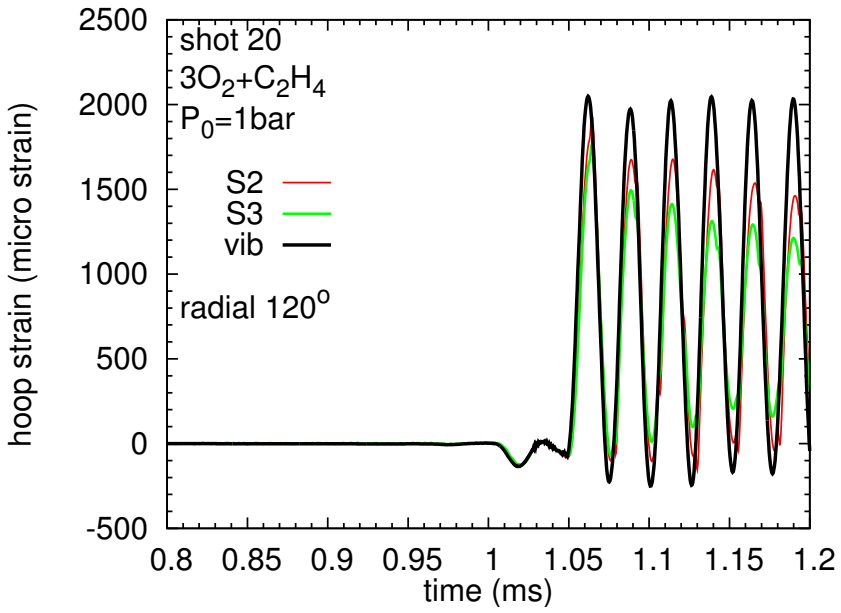

Figure 64: Azimuthal location hoop strain comparisons for shot 20

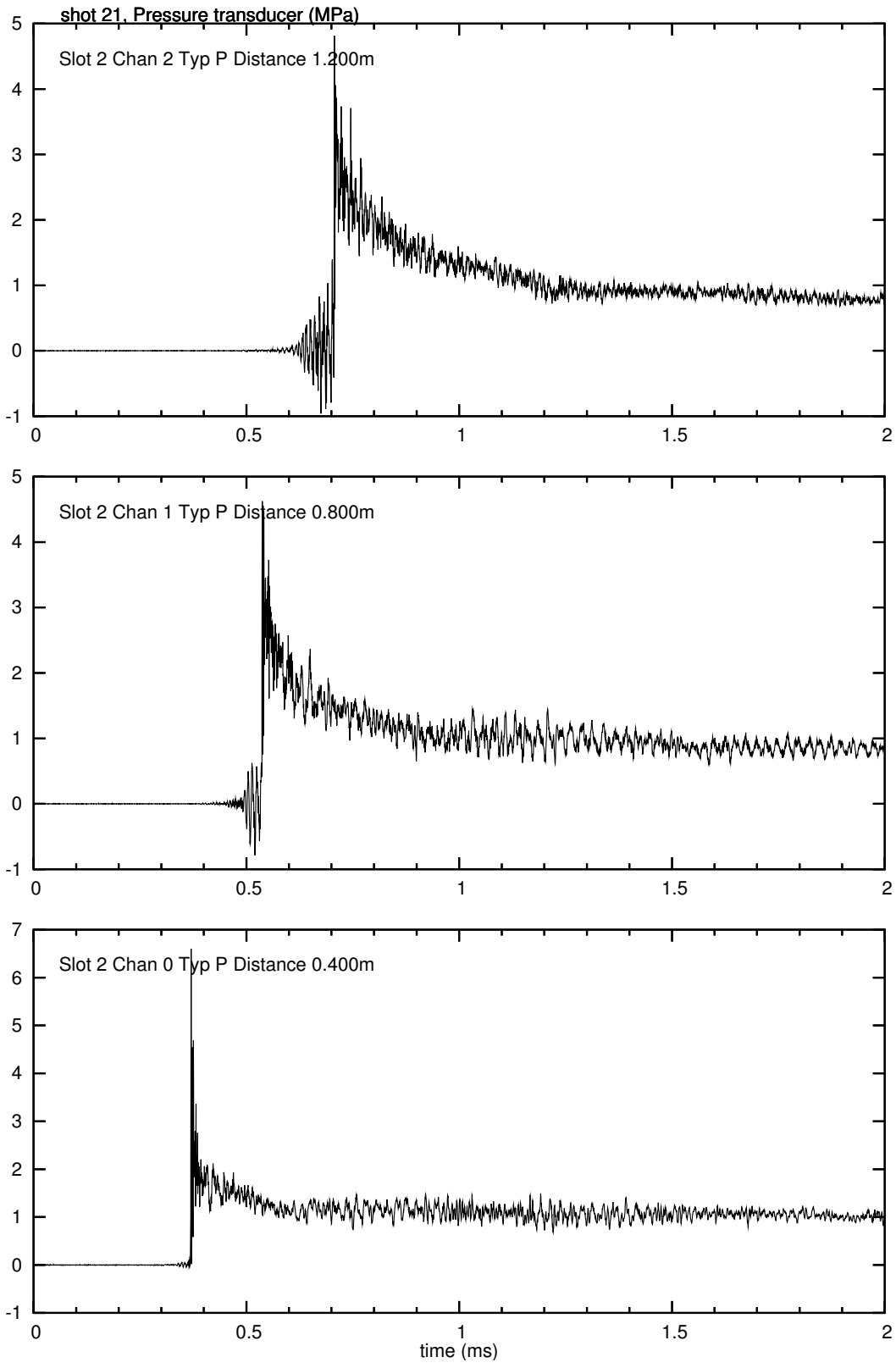

Figure 65: Pressure traces for shot 21

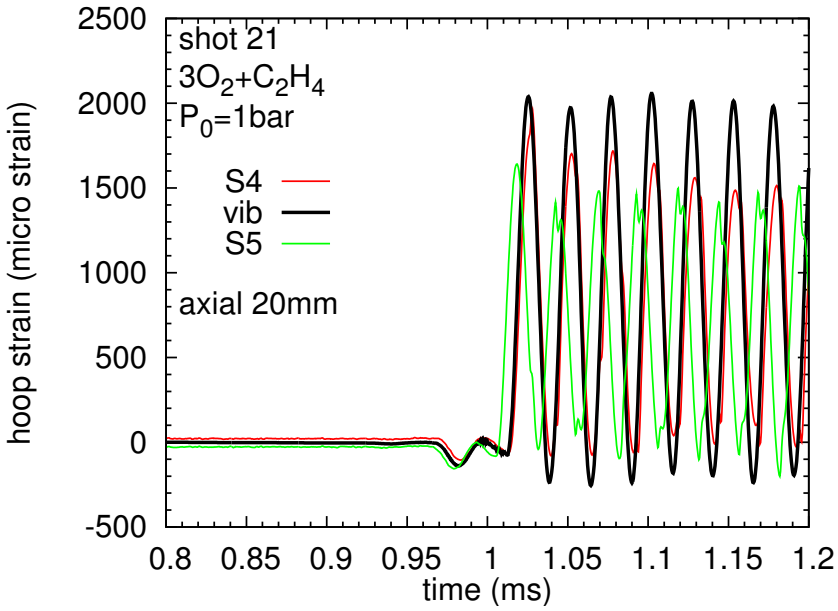

Figure 66: Axial location hoop strain comparisons for shot 21.

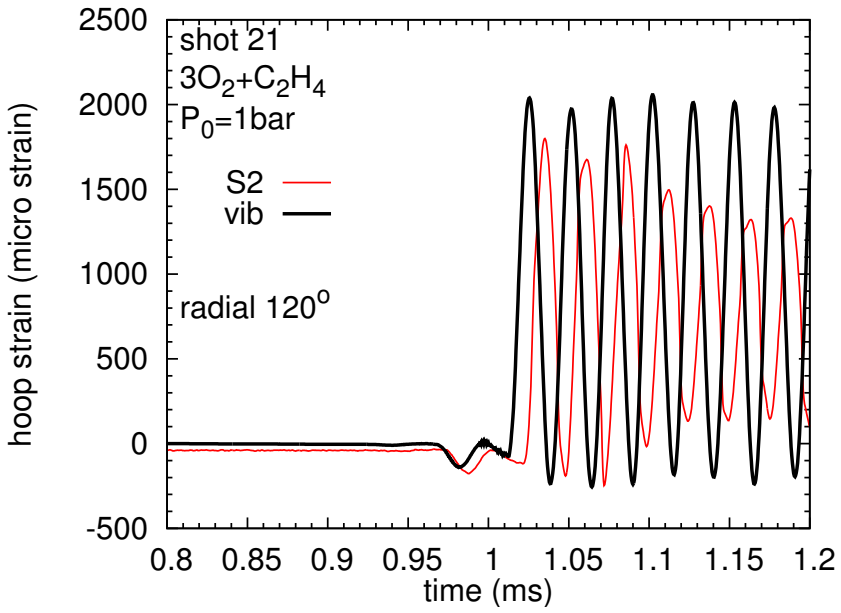

Figure 67: Azimuthal location hoop strain comparisons for shot 21

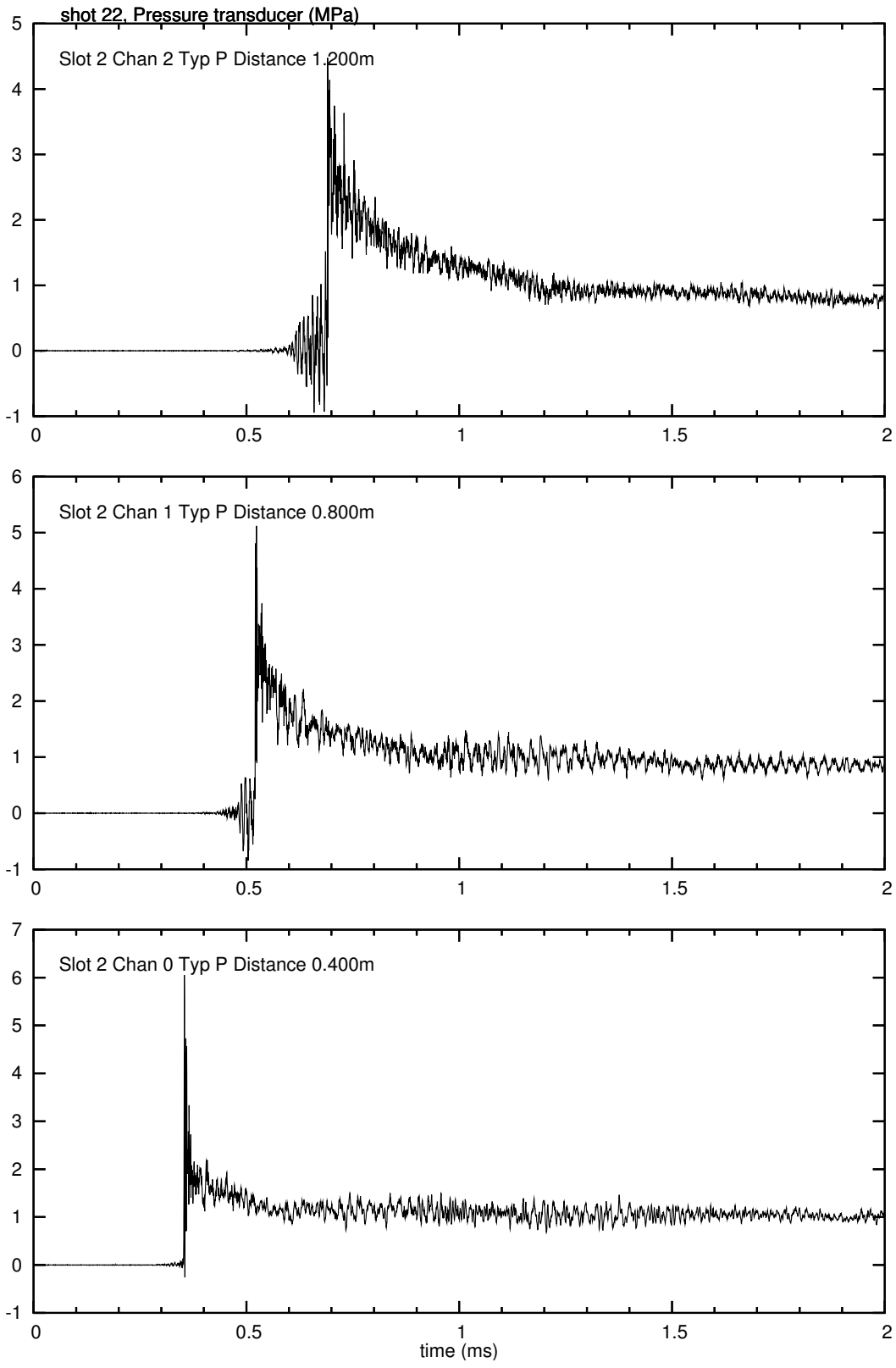

Figure 68: Pressure traces for shot 22

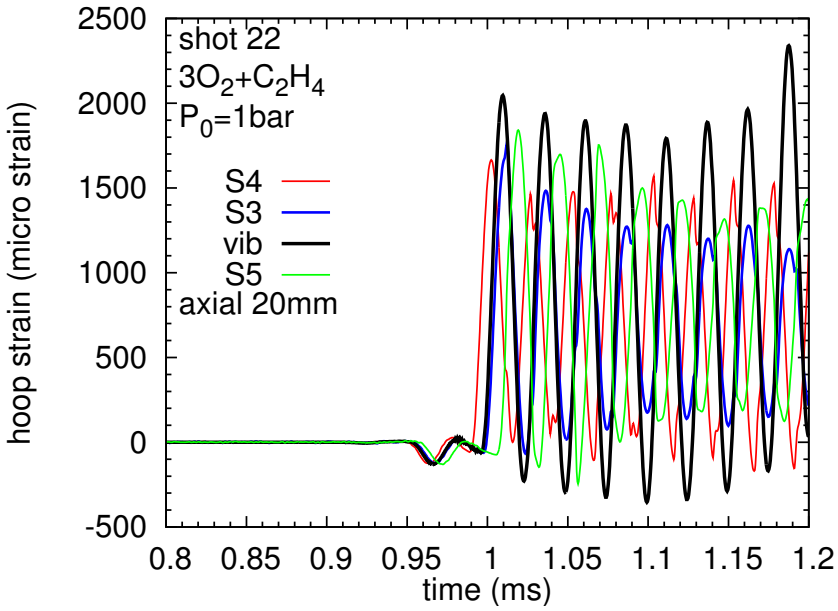

Figure 69: Axial location hoop strain comparisons for shot 22.

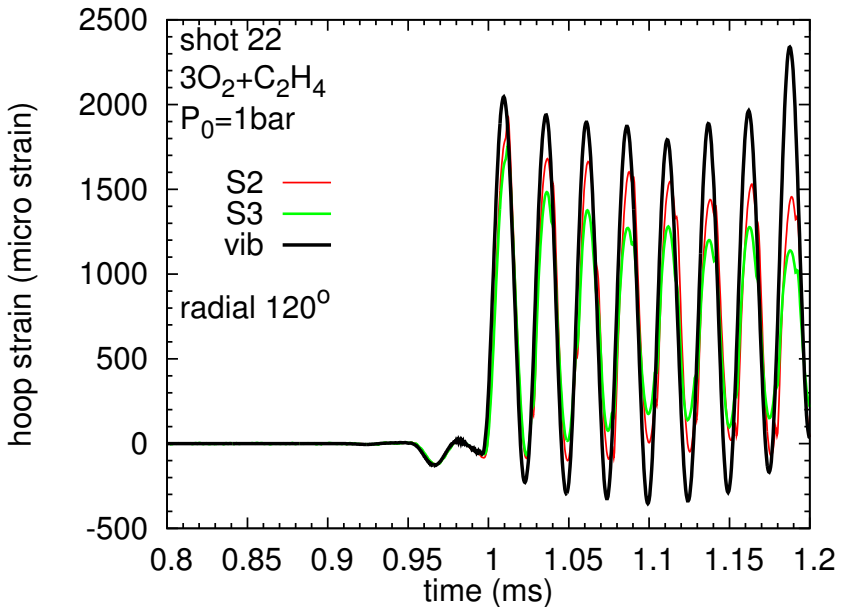

Figure 70: Azimuthal location hoop strain comparisons for shot 22

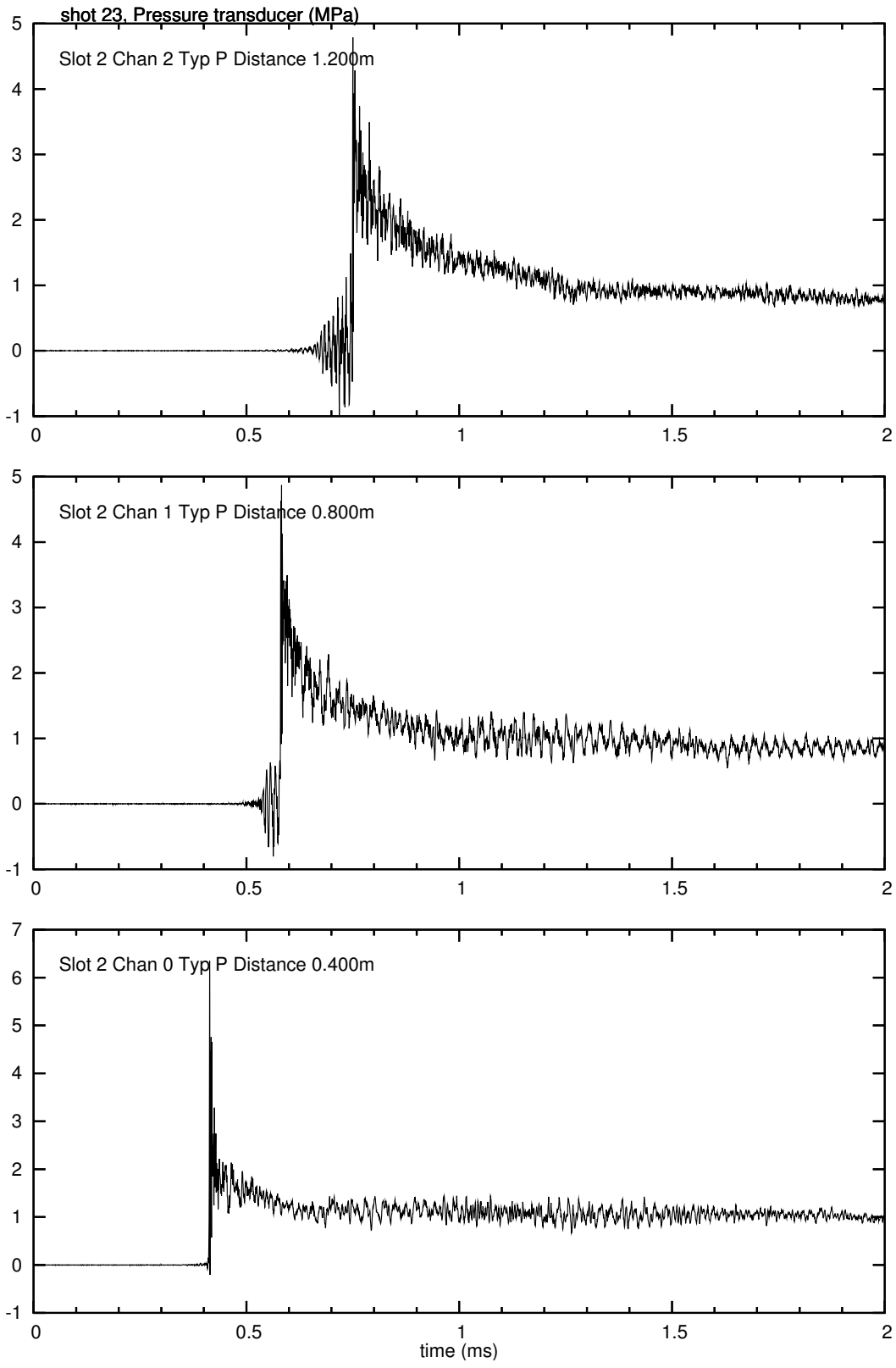

Figure 71: Pressure traces for shot 23

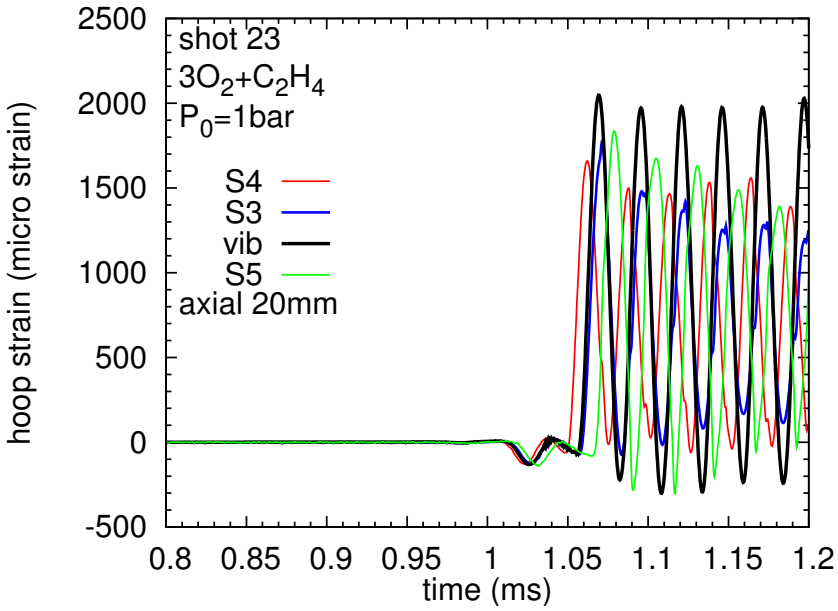

Figure 72: Axial location hoop strain comparisons for shot 23.

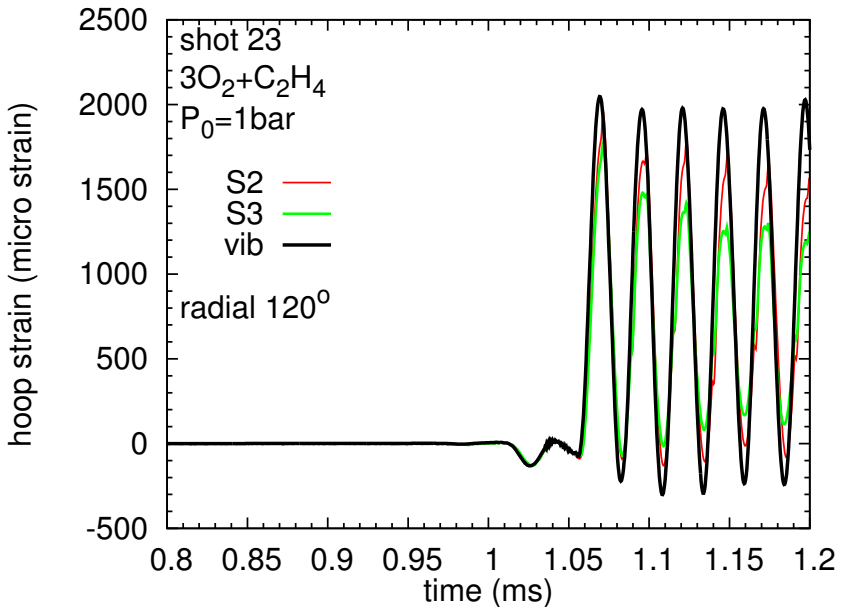

Figure 73: Azimuthal location hoop strain comparisons for shot 23

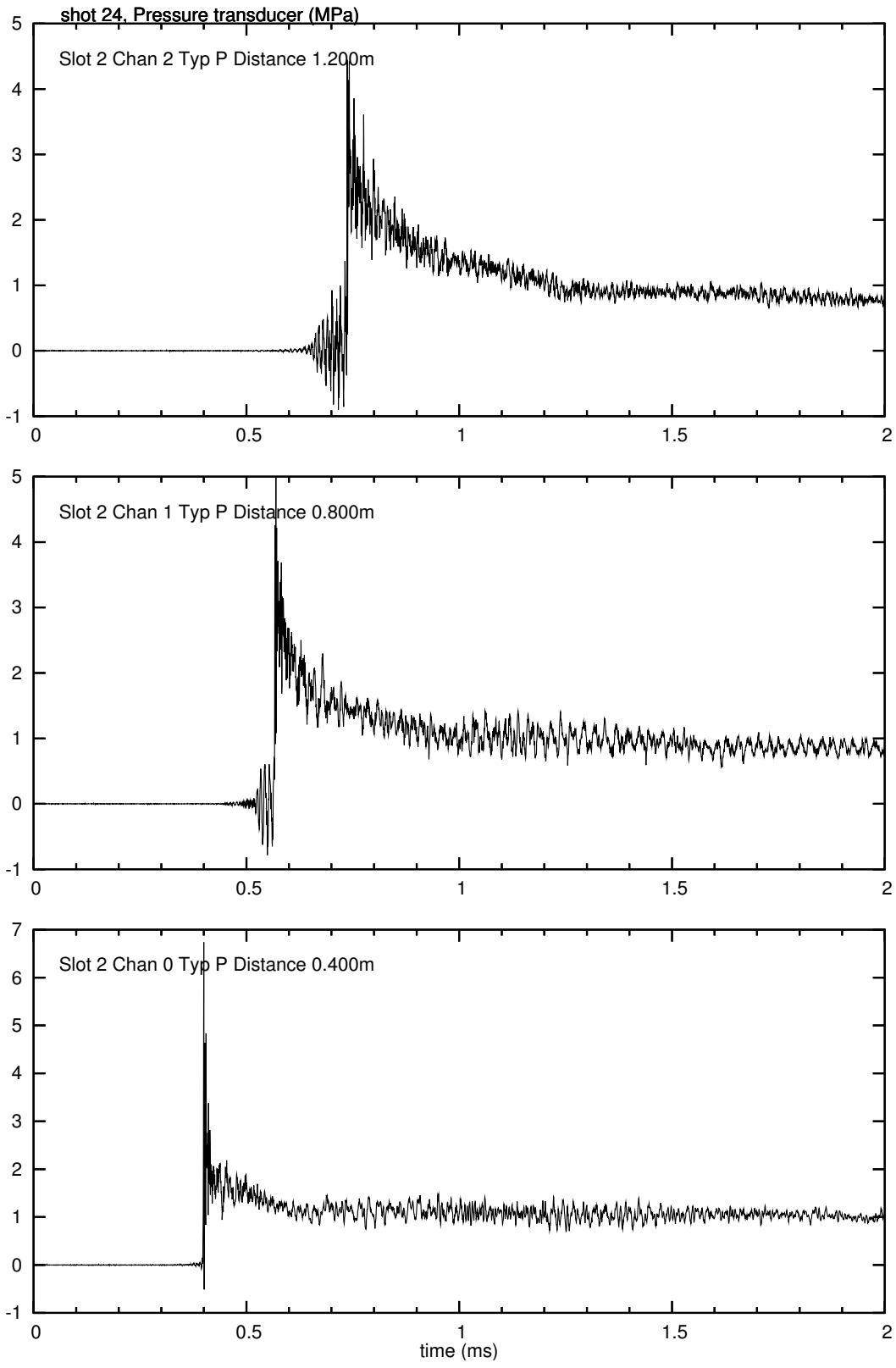

Figure 74: Pressure traces for shot 24

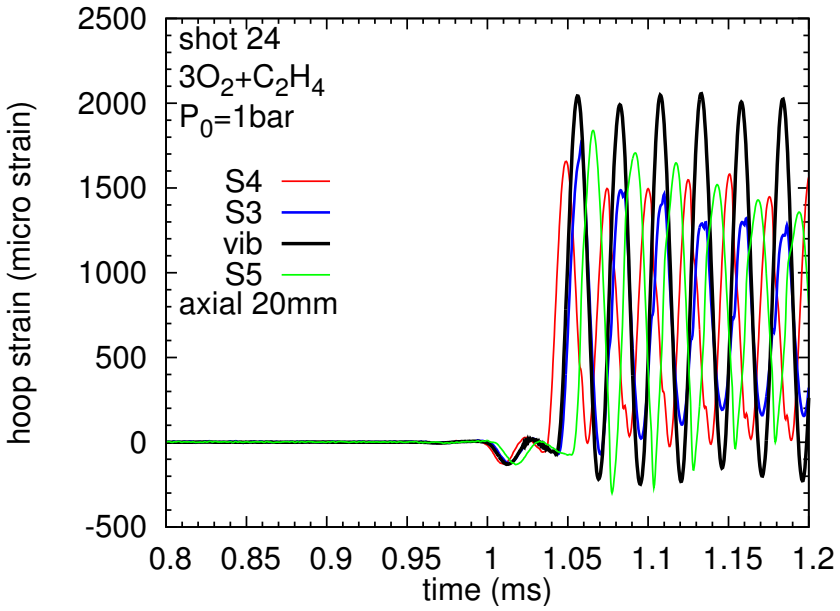

Figure 75: Axial location hoop strain comparisons for shot 24.

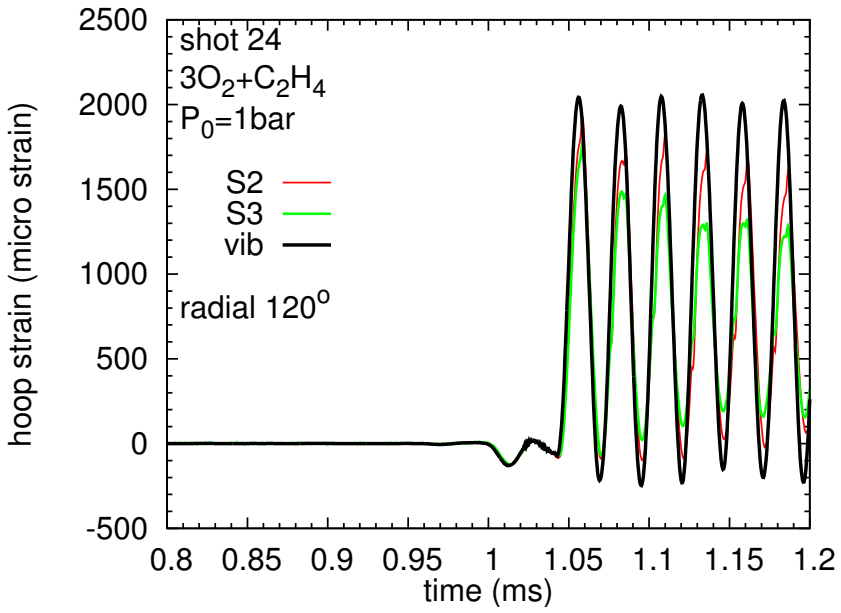

Figure 76: Azimuthal location hoop strain comparisons for shot 24

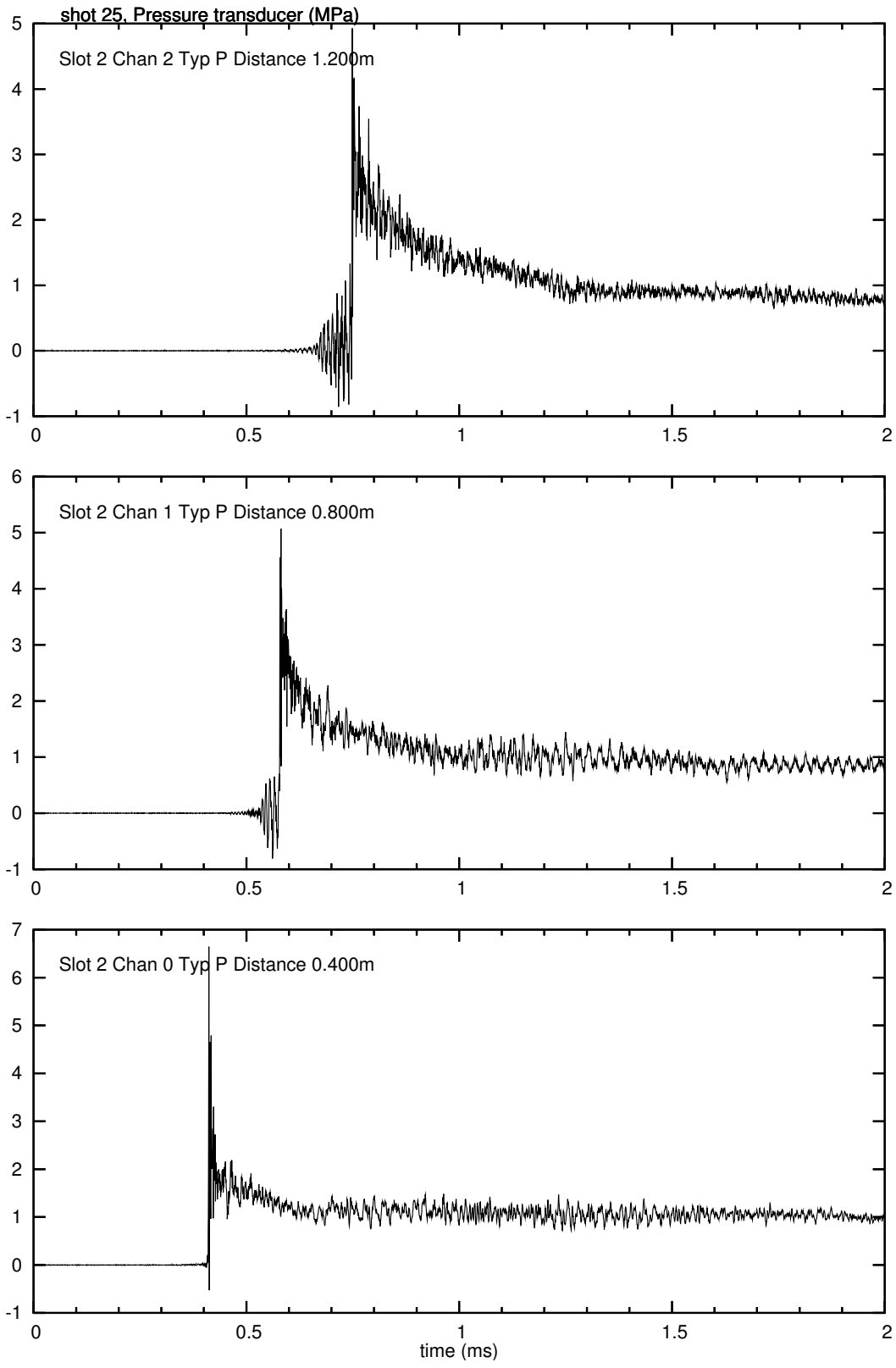

Figure 77: Pressure traces for shot 25

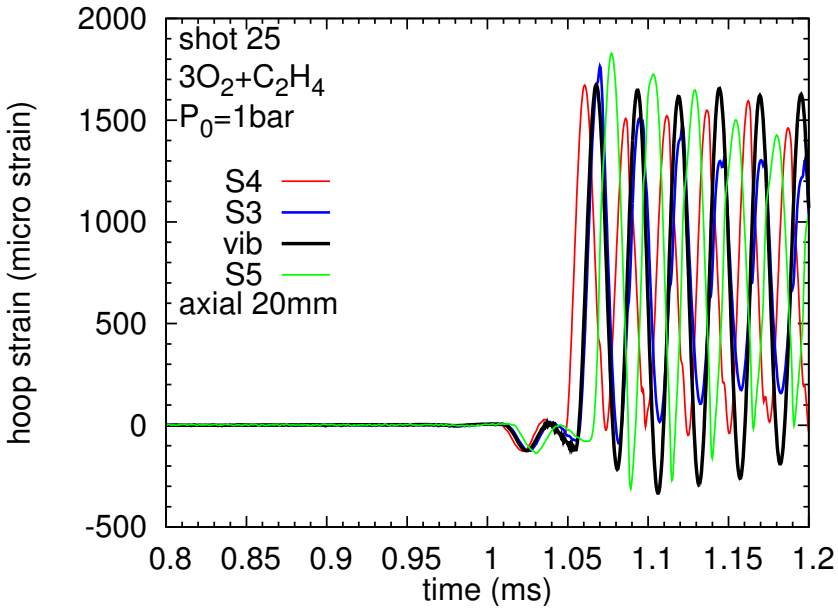

Figure 78: Axial location hoop strain comparisons for shot 25.

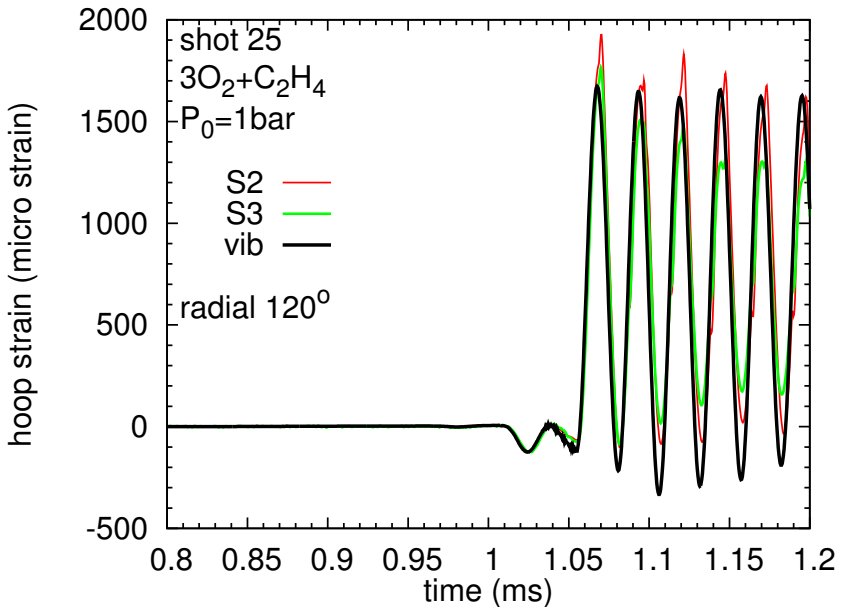

Figure 79: Azimuthal location hoop strain comparisons for shot 25

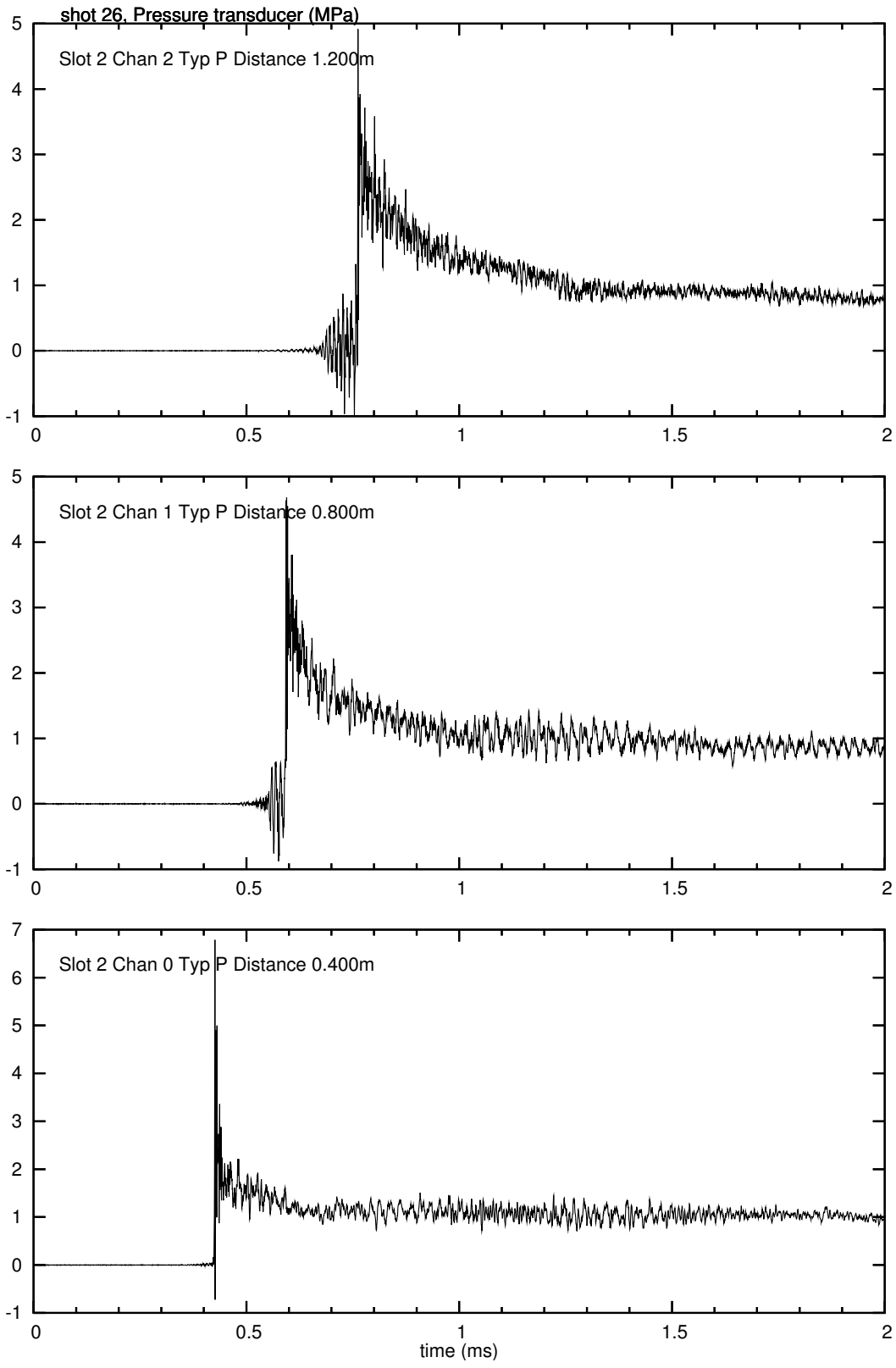

Figure 80: Pressure traces for shot 26

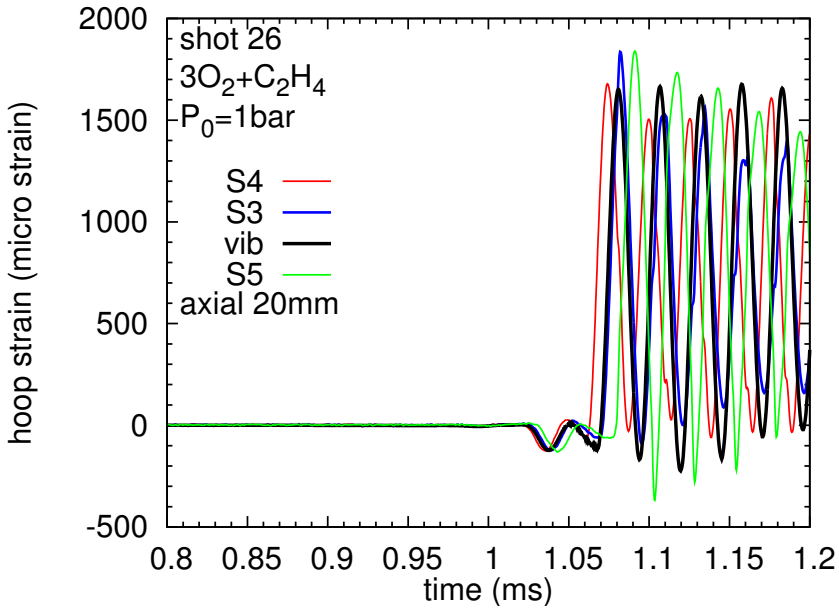

Figure 81: Axial location hoop strain comparisons for shot 26.

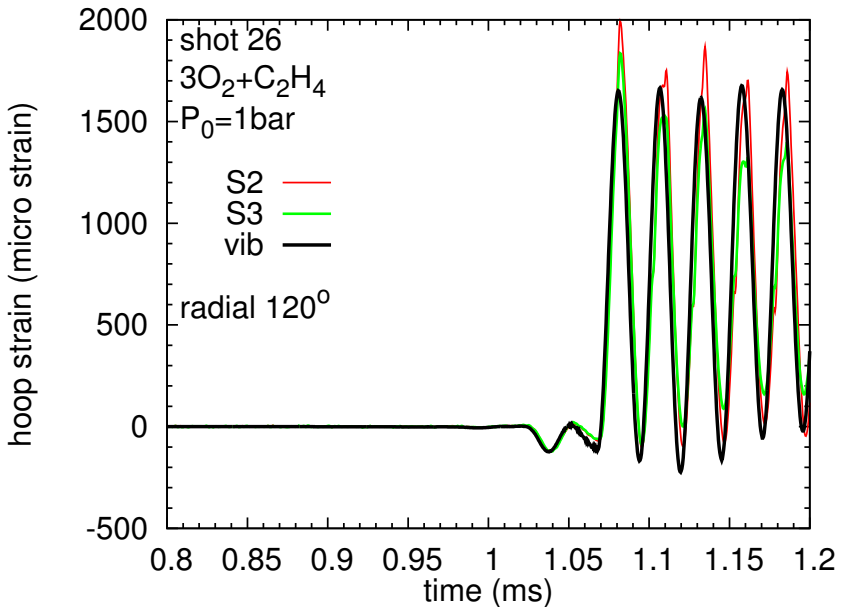

Figure 82: Azimuthal location hoop strain comparisons for shot 26

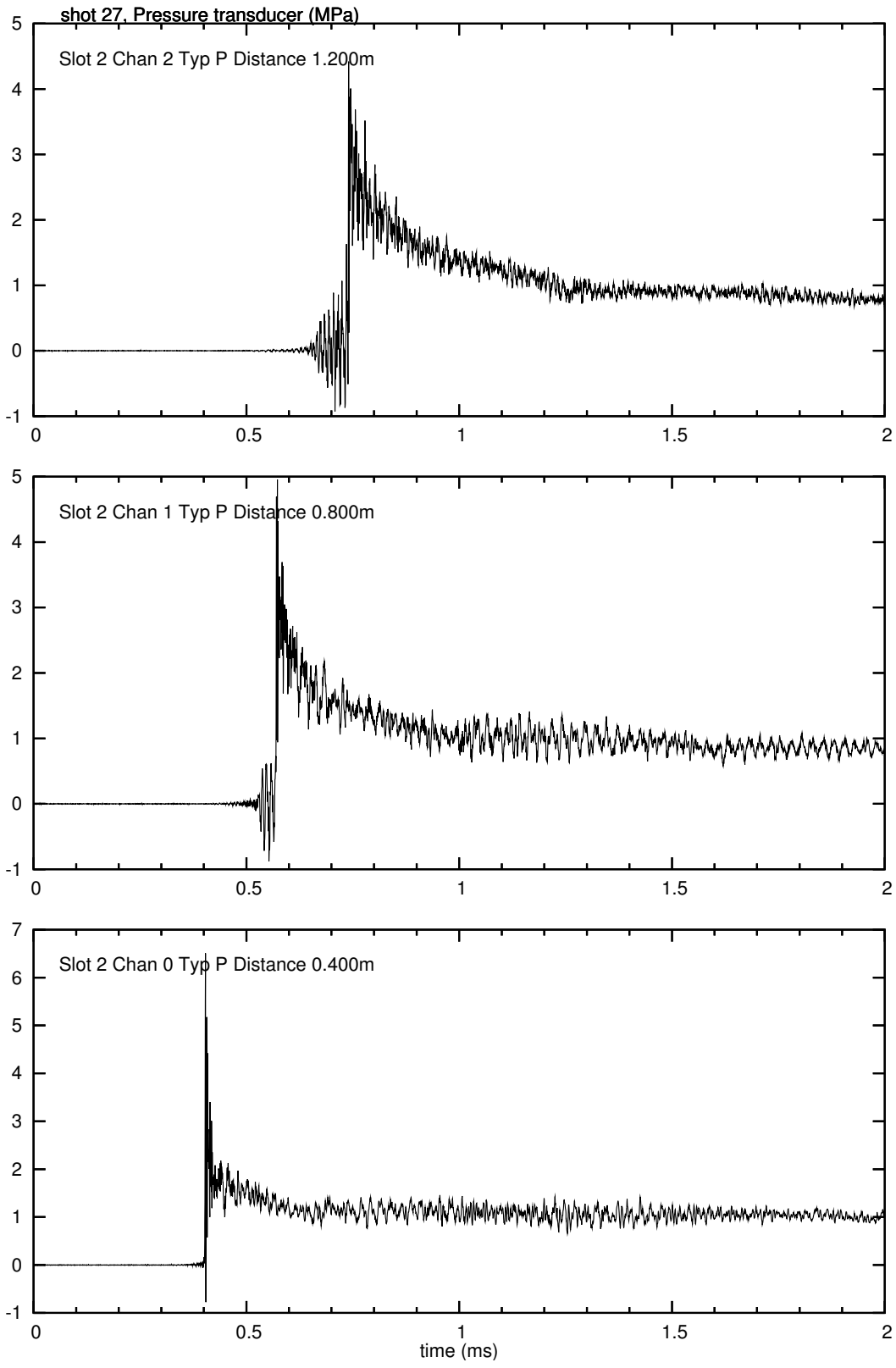

Figure 83: Pressure traces for shot 27

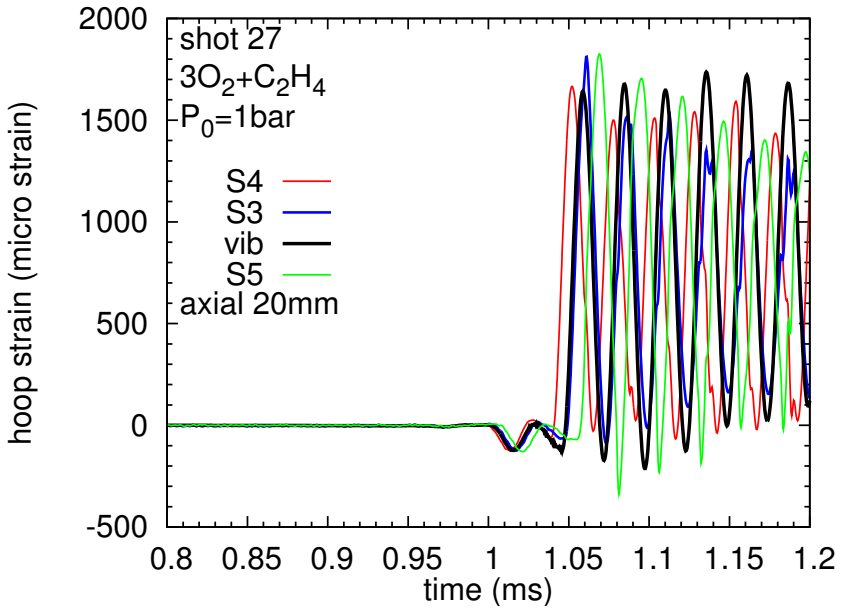

Figure 84: Axial location hoop strain comparisons for shot 27.

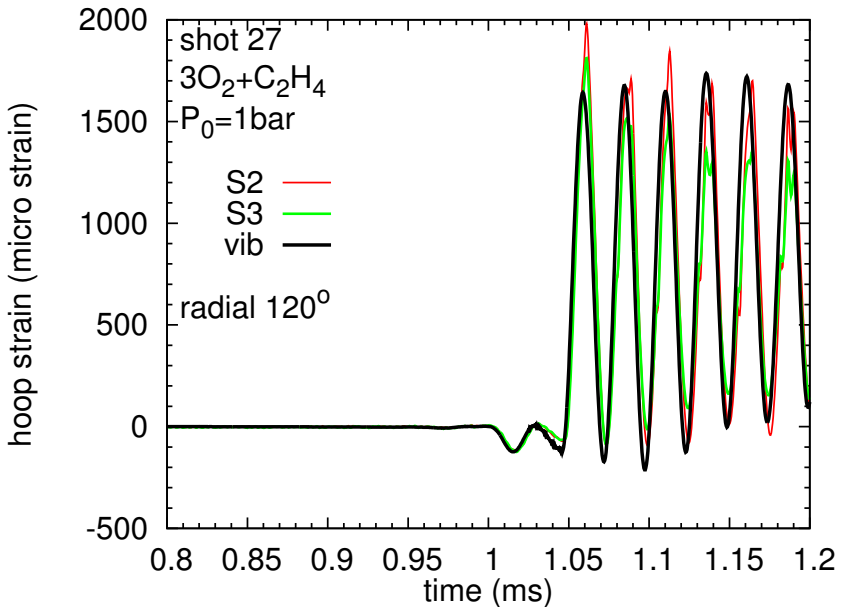

Figure 85: Azimuthal location hoop strain comparisons for shot 27

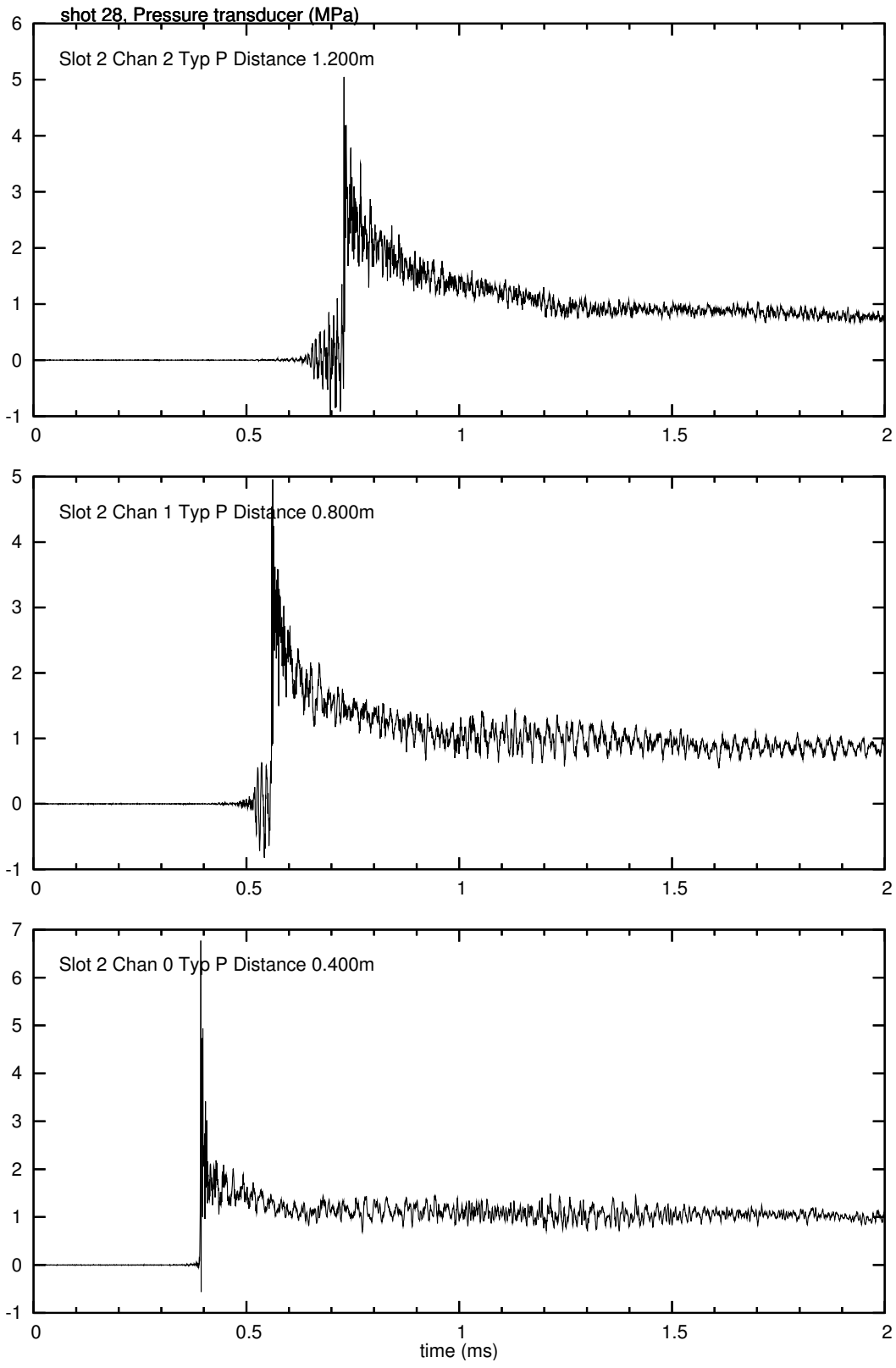

Figure 86: Pressure traces for shot 28

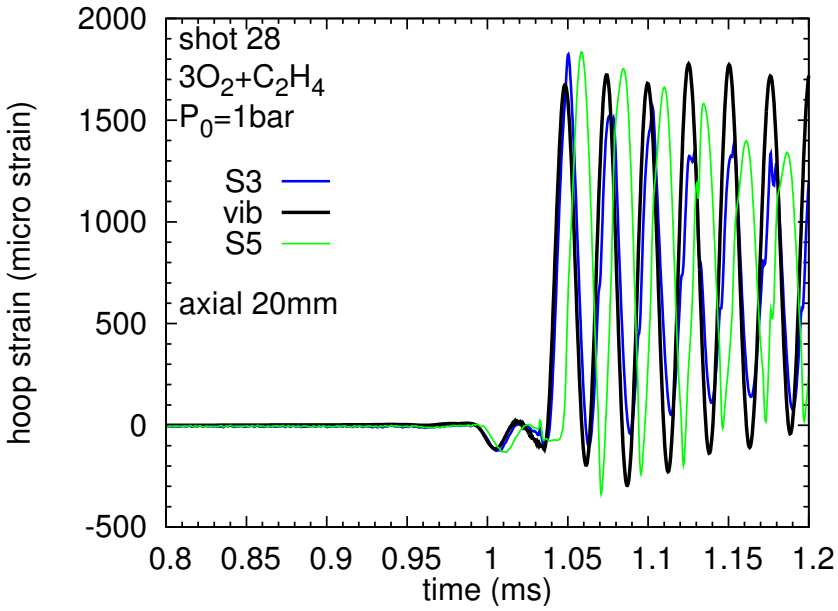

Figure 87: Axial location hoop strain comparisons for shot 28.

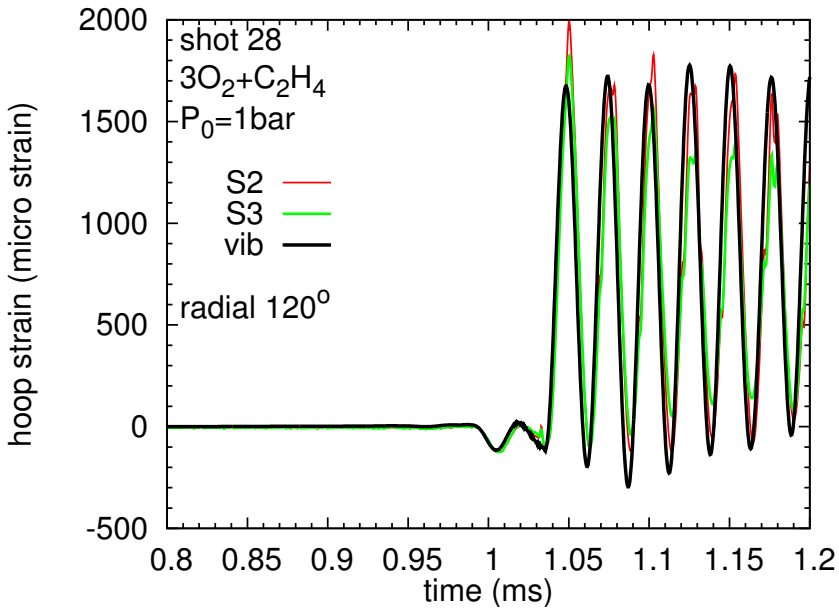

Figure 88: Azimuthal location hoop strain comparisons for shot 28

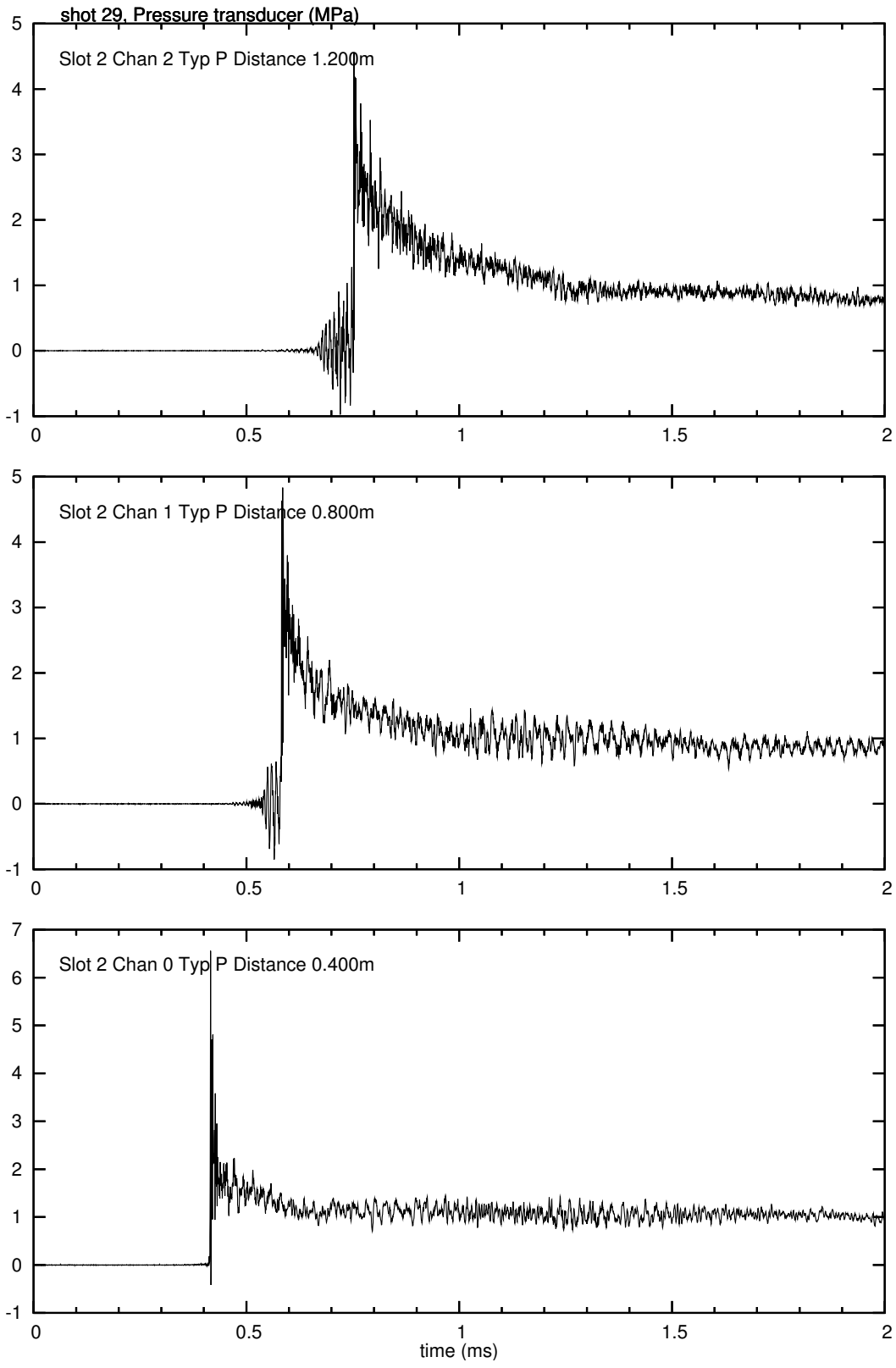

Figure 89: Pressure traces for shot 29

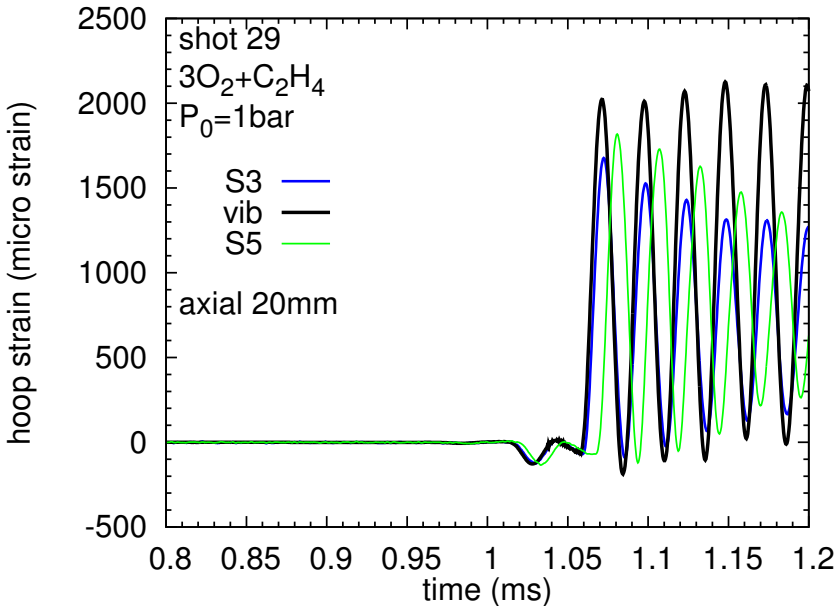

Figure 90: Axial location hoop strain comparisons for shot 29.

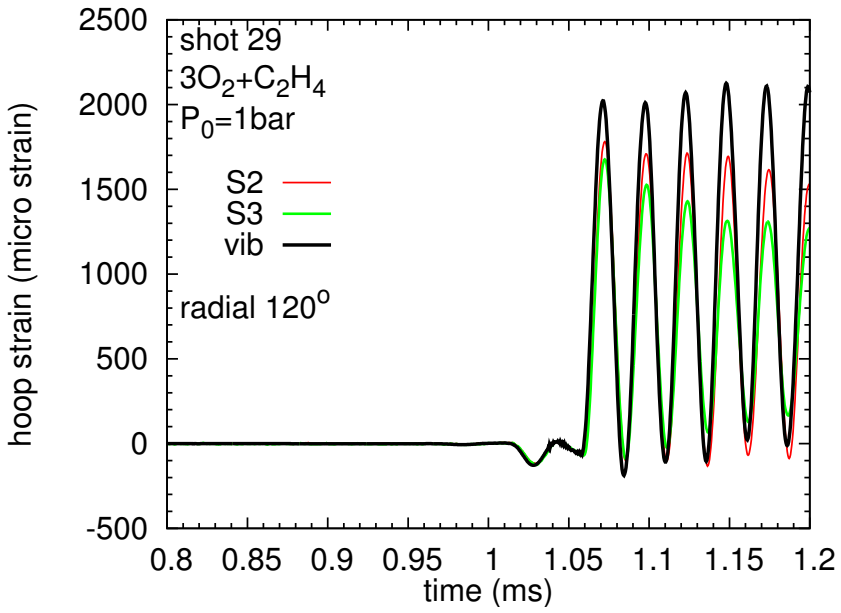

Figure 91: Azimuthal location hoop strain comparisons for shot 29

B Slot Data

Table 4: Slot tests. All shots used stoichiometric ethylene-oxygen at 100 kPa.

Shot	Vi_{det} avg (m/s)	Notes
35		Gate width: 500ns, MCP-voltage: 520V, Delay to To: 1.090ms, No data from PT as trigger channel set wrong
36		delay on PG200: 0.1ms; gate width 500ns; MCP 550V; trigger of P5 and scope back panel output (falling edge) directly into PG200. No Pressure data.
37	2374.9	delay on PG200 0.5ms; gate width 500ns; MCP 550V; trigger of P5 and scope back panel output (falling edge) directly into PG200
38	2374.1	No picture due to camera degredation.
39	2340.7	Cordin Camera 1us width, 10us delay increment, 180 gain on all ccds. Triggered off P4.
40	2375.7	Cordin Camera 15us delay, otherwise same settings as shot 39
41	2375.9	Blast transducers at 45, 90deg, and 500mm camera: 4 frames@30us 45deg probe not connected
42	2379.5	Same as 41 with 45deg probe connected
43	2380.2	Repeat of 42
44		Blast transducers at 250mm (45 and 90). No Pressure data.
45	2376.2	Repeat of 44. Got pressure traces this time.
46	2388.1	Found loose PCB on End Flange. No 45 degree data.
47	2384.0	
48	2380.4	Blast Gages at 45,90 degrees, 750mm
49	2376.0	Atmospheric pressure=747.0, may have leaked in 1Torr air during fill
50	2381.7	Blast Gages at 0,90 degrees, 250mm. Tightened End Flange xducer mount, fixed leak. Placed weight on gasket to seal during mix, re-read P after removing gasket =747.1
51	2381.5	Repeat of 50, frames at 61,91,121,151us
52	2378.6	Blast Gages at 0,90 degrees, 500mm.
53	2380.2	Repeat of 52

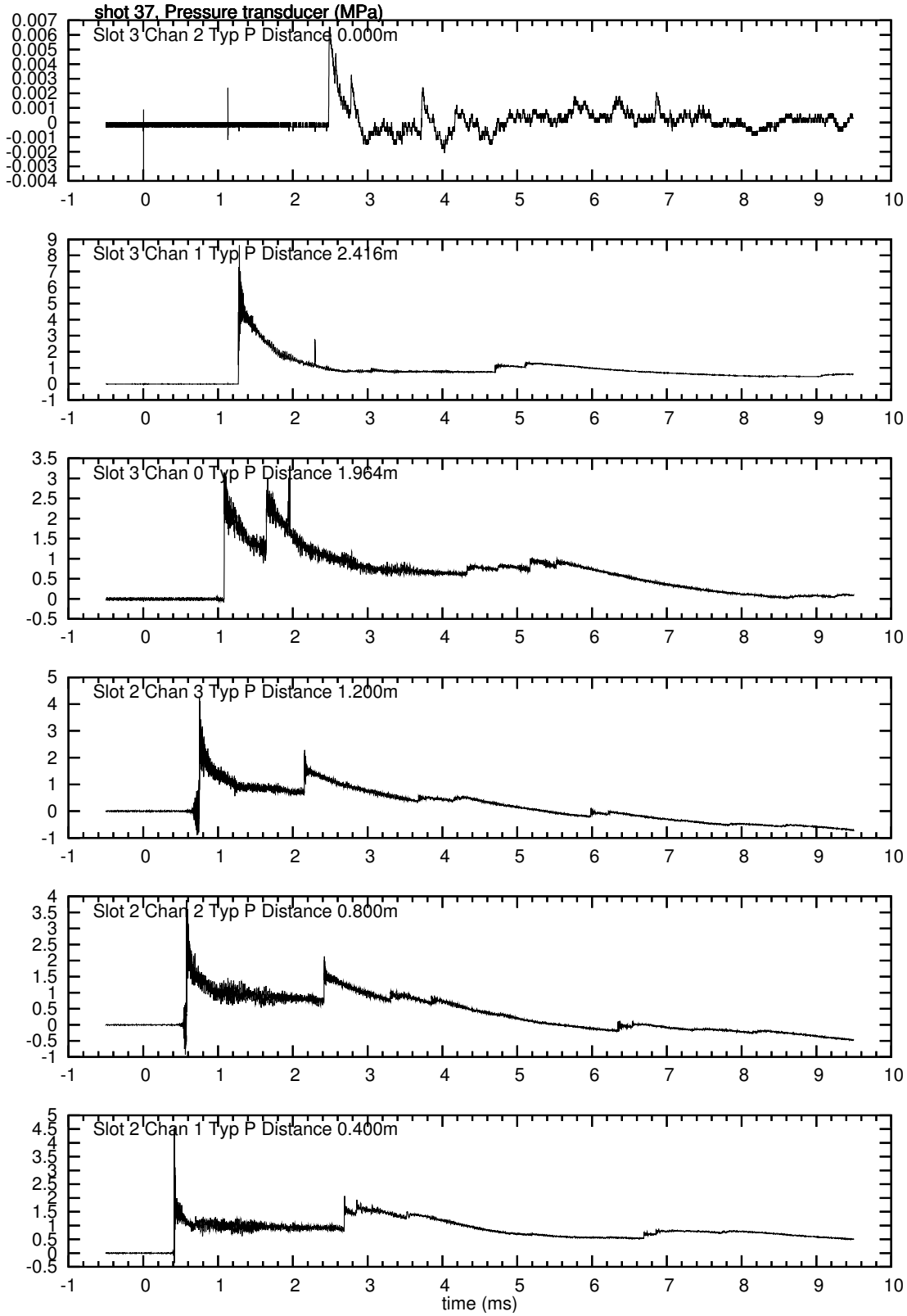

Figure 92: Pressure traces for shot 37

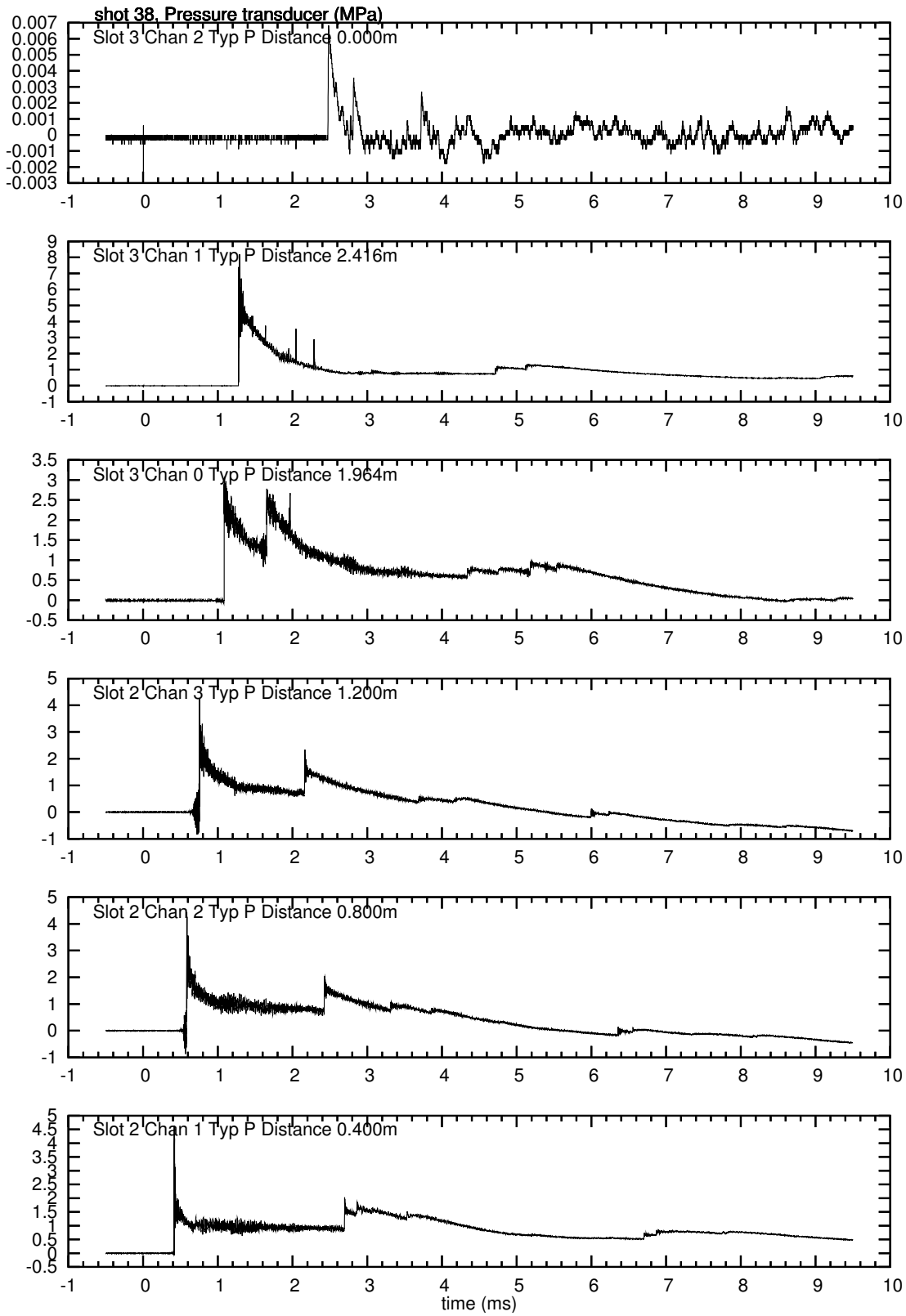

Figure 93: Pressure traces for shot 38

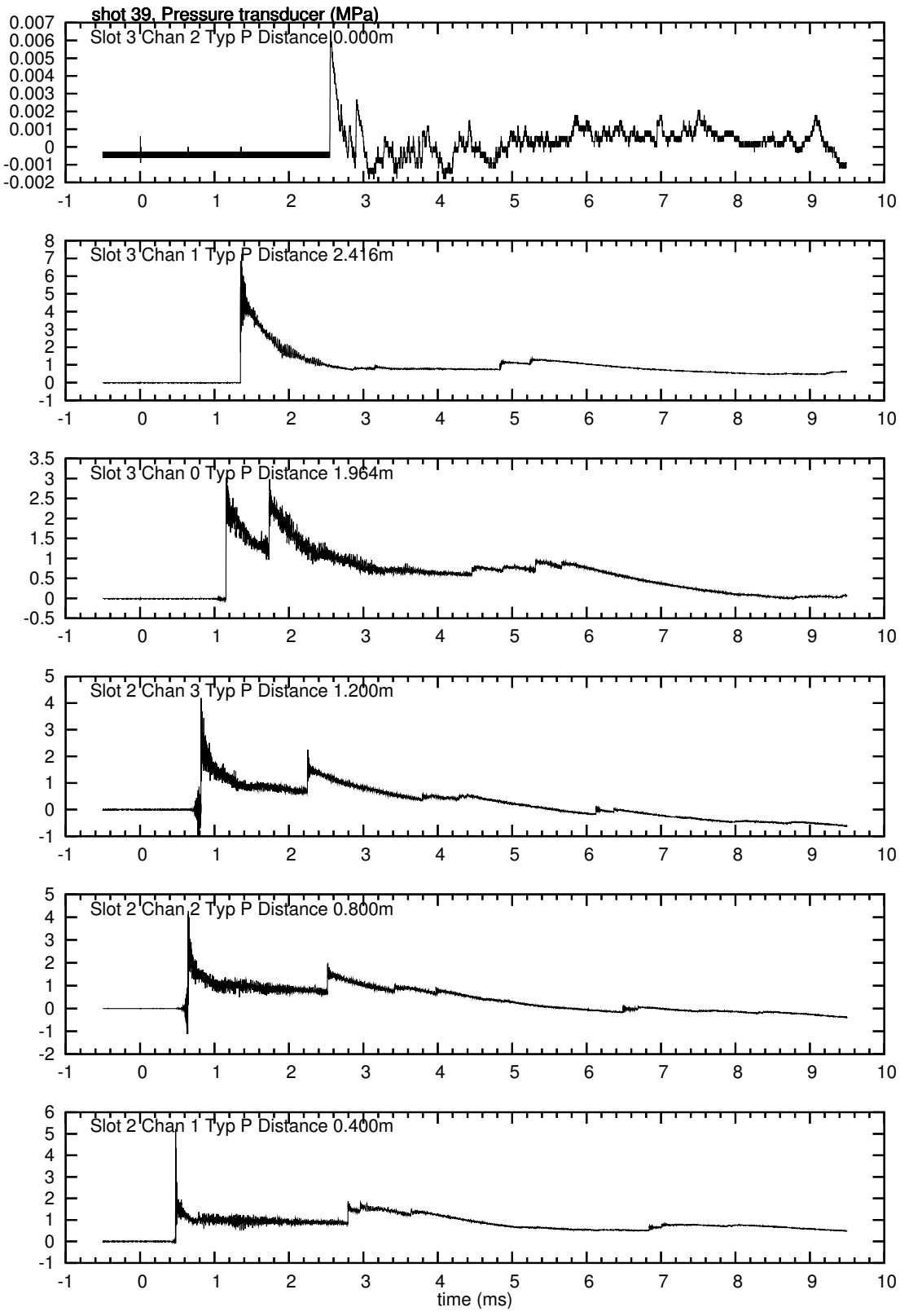

Figure 94: Pressure traces for shot 39

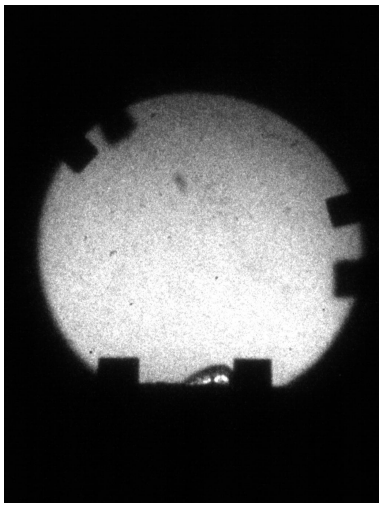

t=0μs

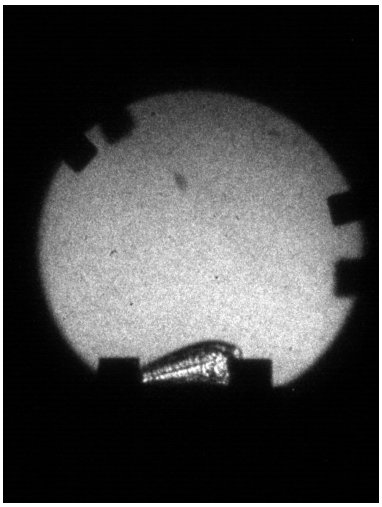

t=10μs

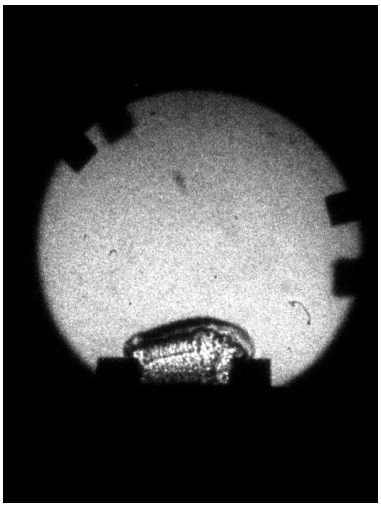

t=20μs

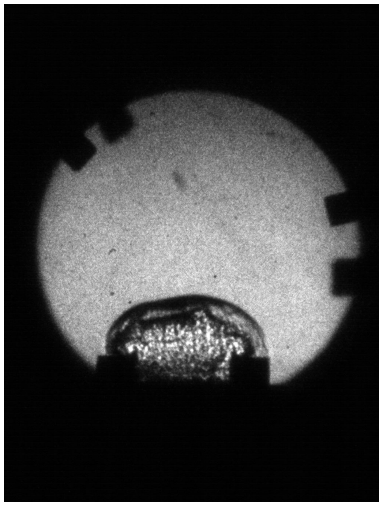

t=30μs

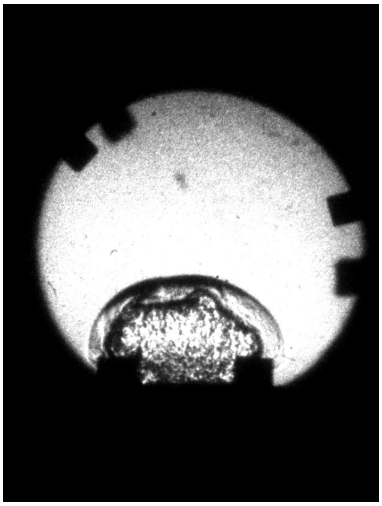

t=40μs

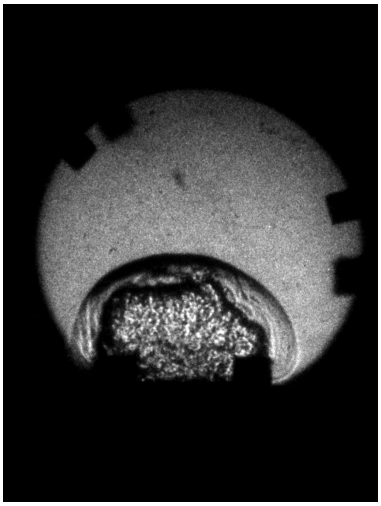

t=50μs

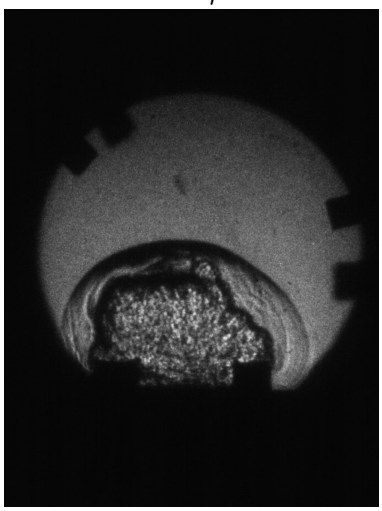

t=60μs

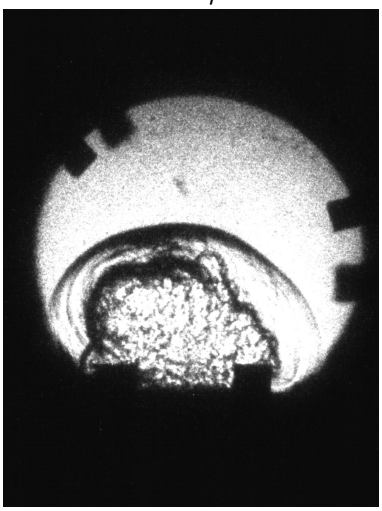

t=70μs

Figure 95: Blast wave images for shot 39.

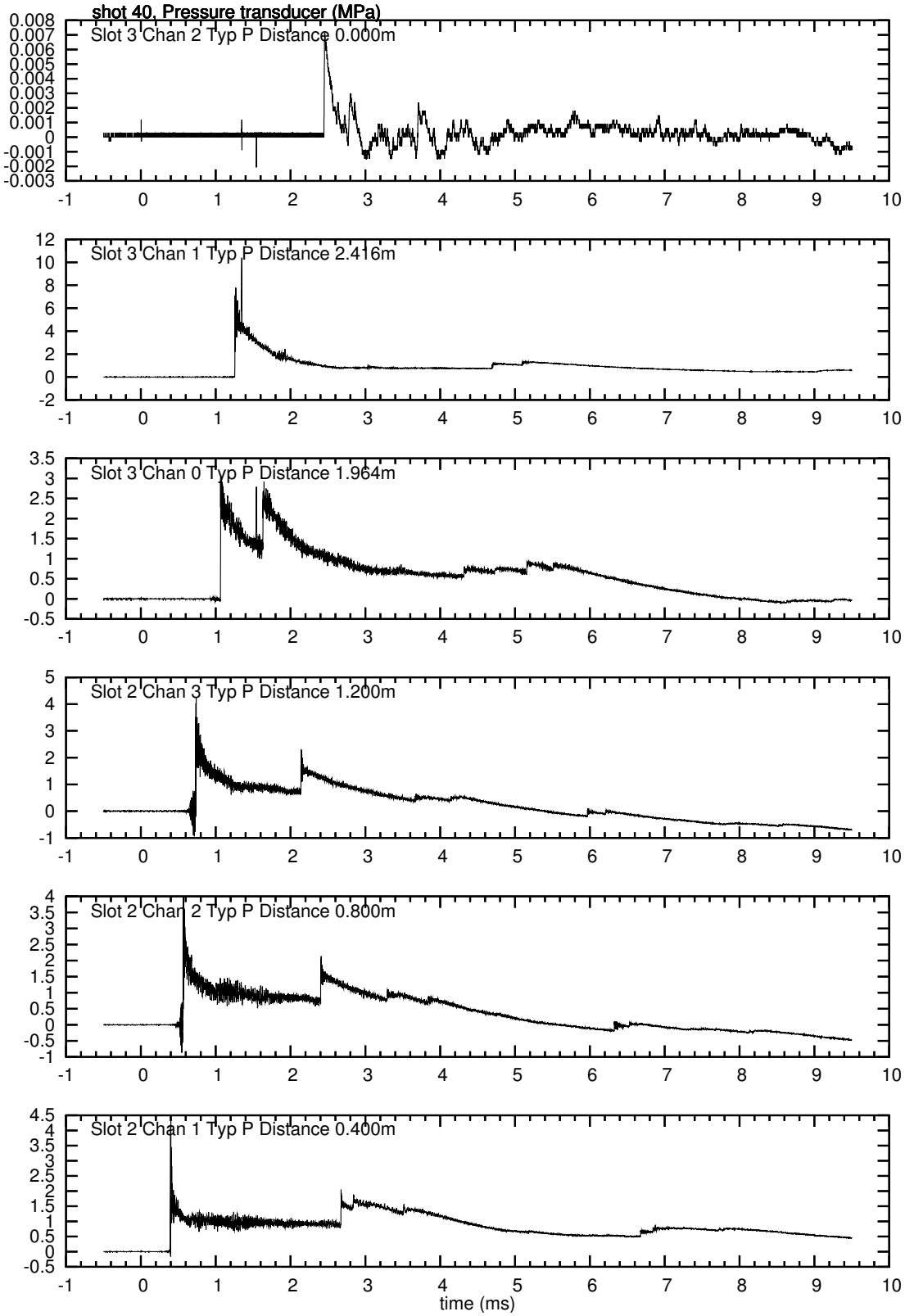

Figure 96: Pressure traces for shot 40

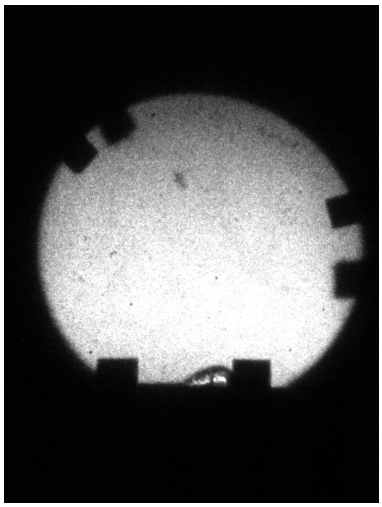

t=0μs

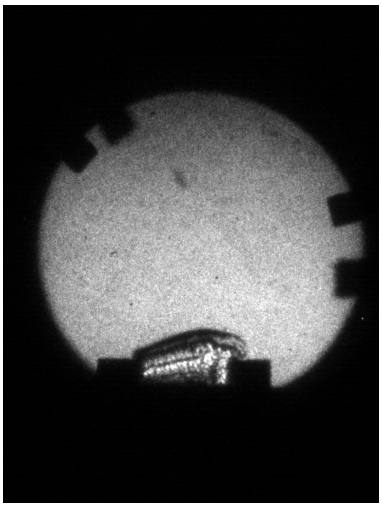

t=15μs

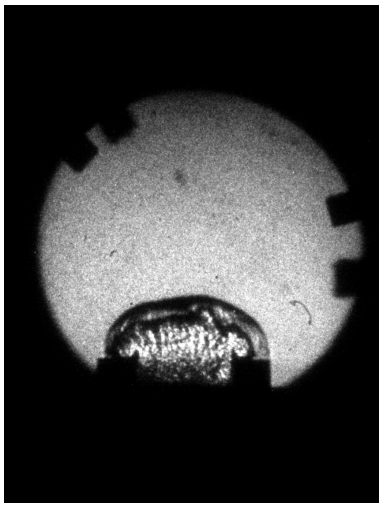

30μs

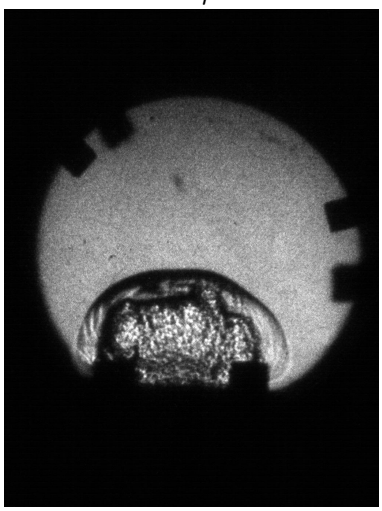

t=45μs

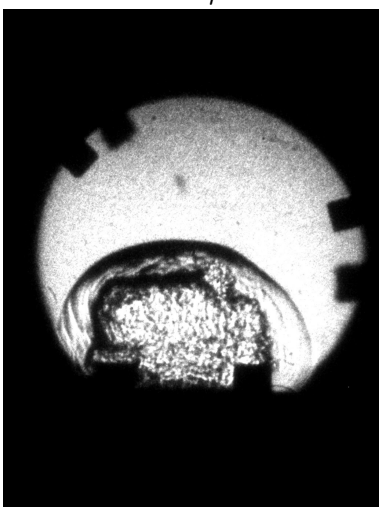

t=60μs

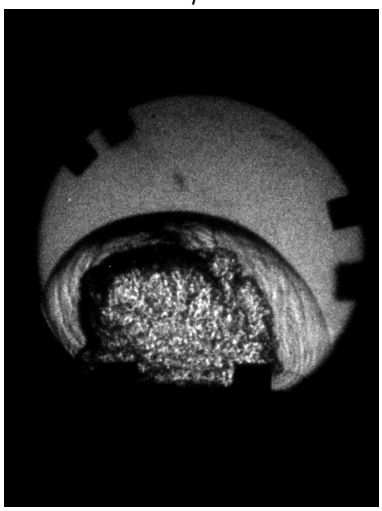

75μs

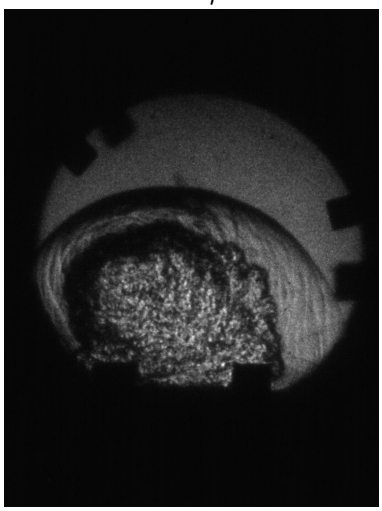

t=90μs

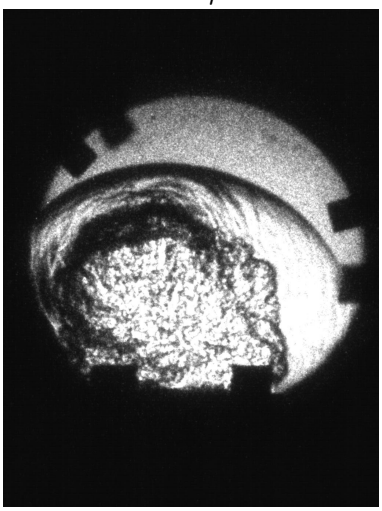

t=105μs

Figure 97: Blast wave images for shot 40.

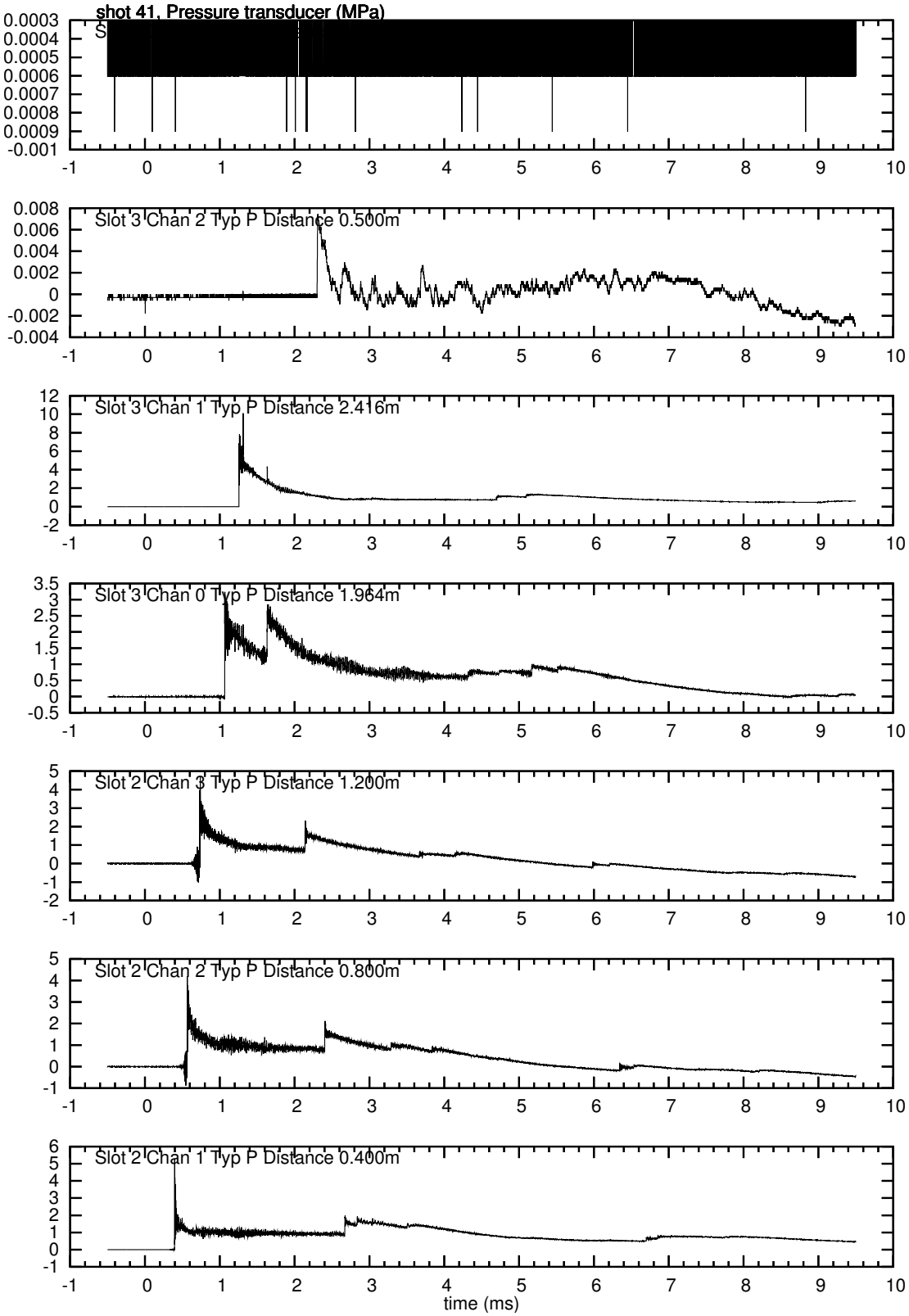

Figure 98: Pressure traces for shot 41

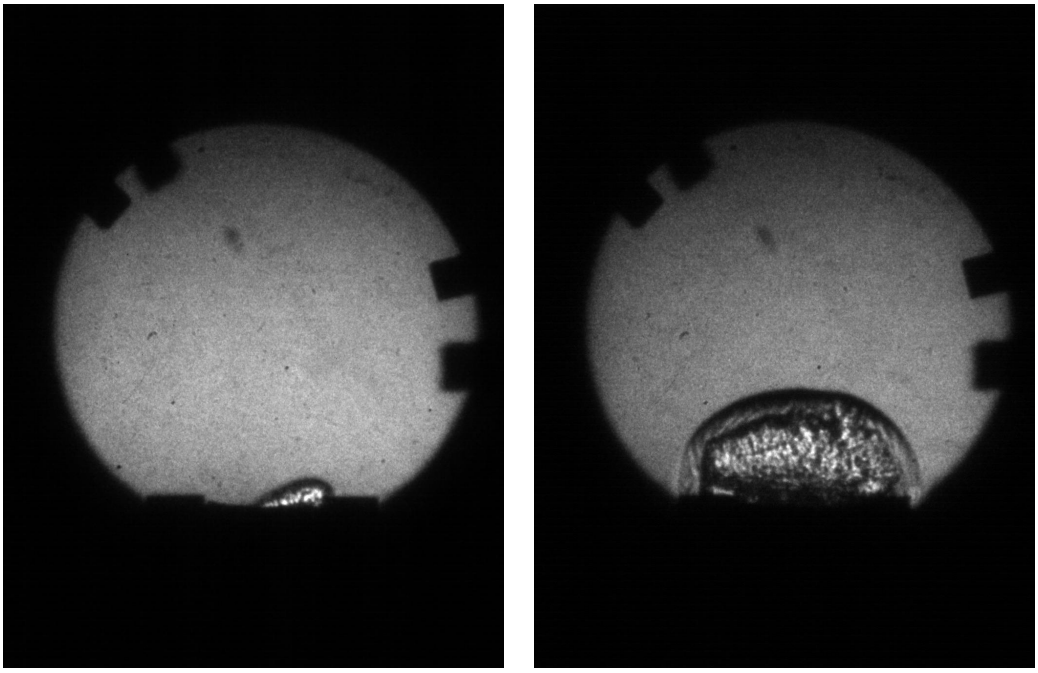

t=0μs t=30μs

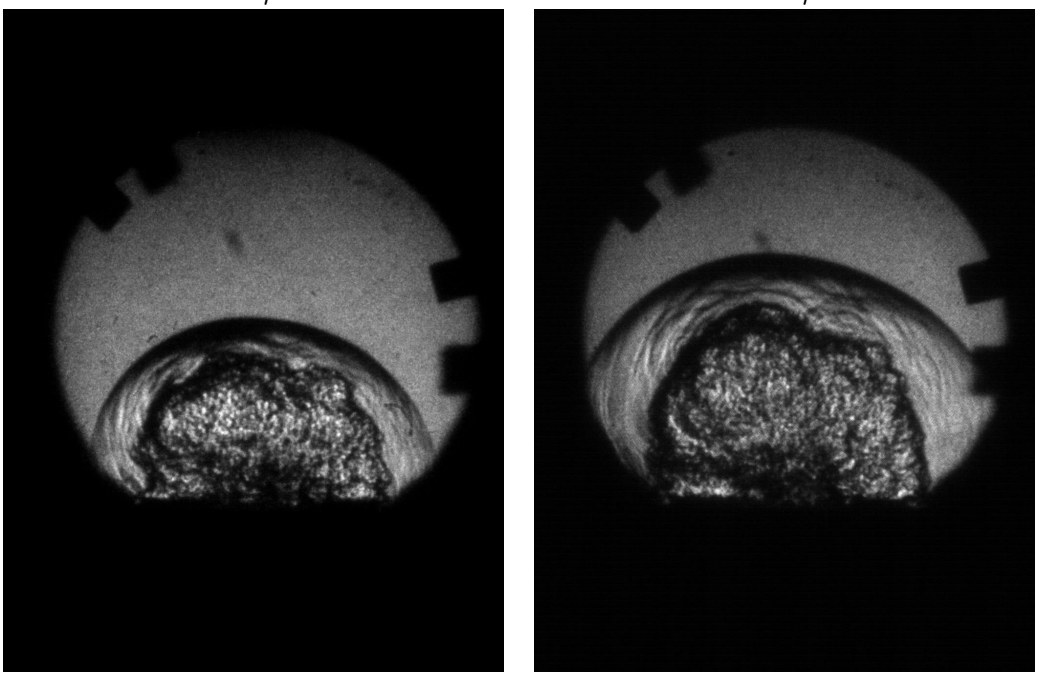

t=60μs t=90μs

Figure 99: Blast wave images for shot 41.

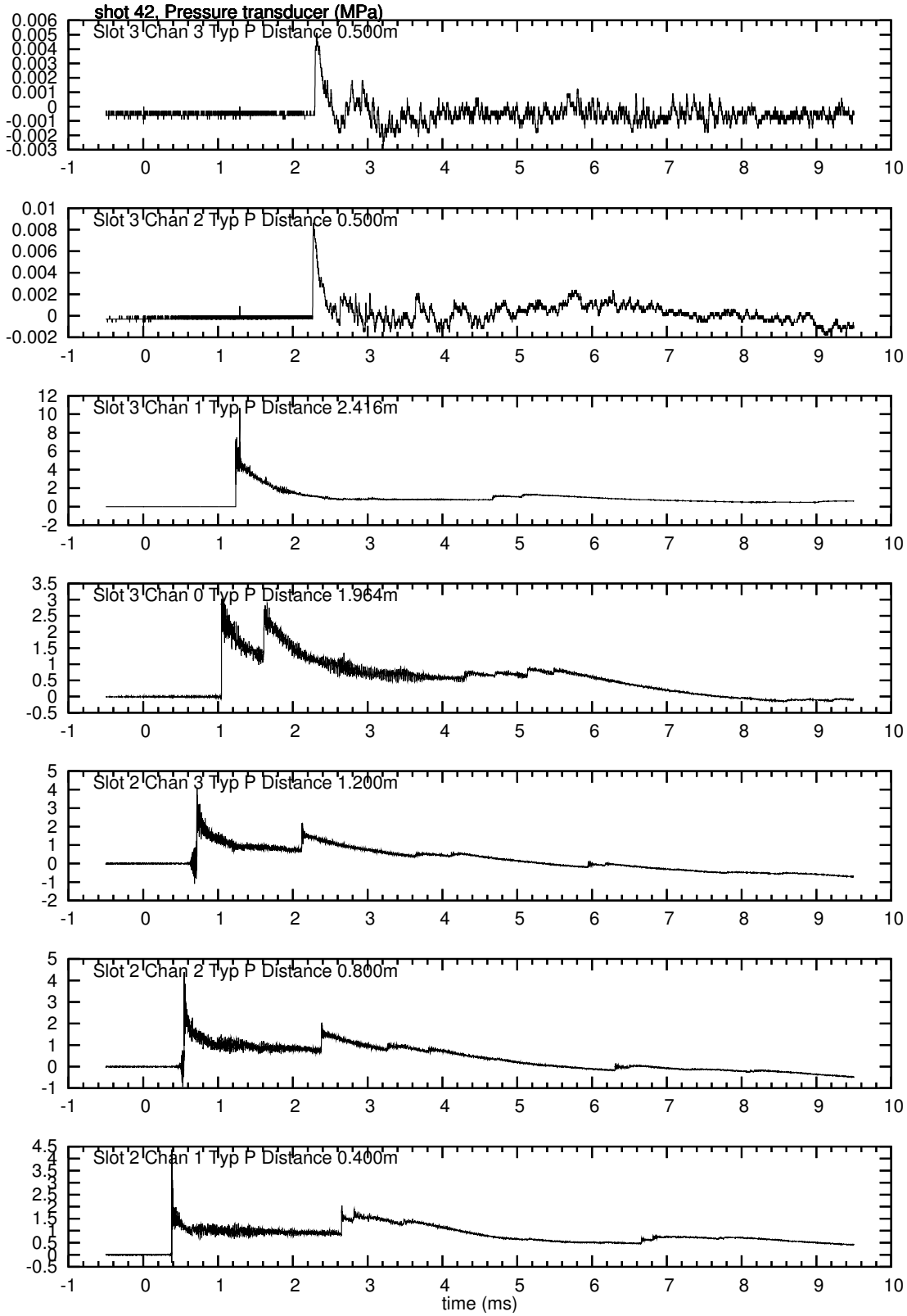

Figure 100: Pressure traces for shot 42

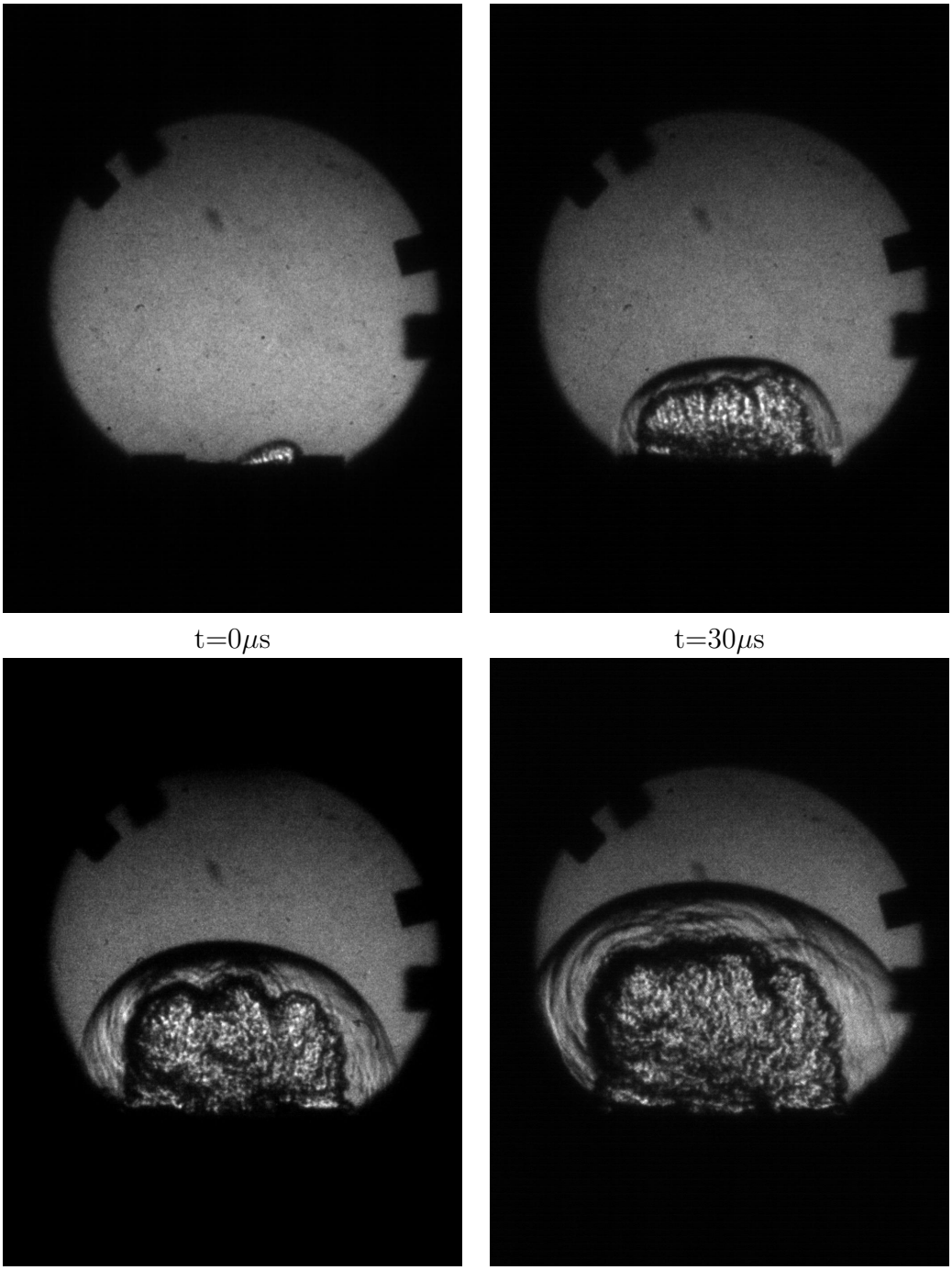

t=0μs t=30μs

t=60μs t=90μs

Figure 101: Blast wave images for shot 42.

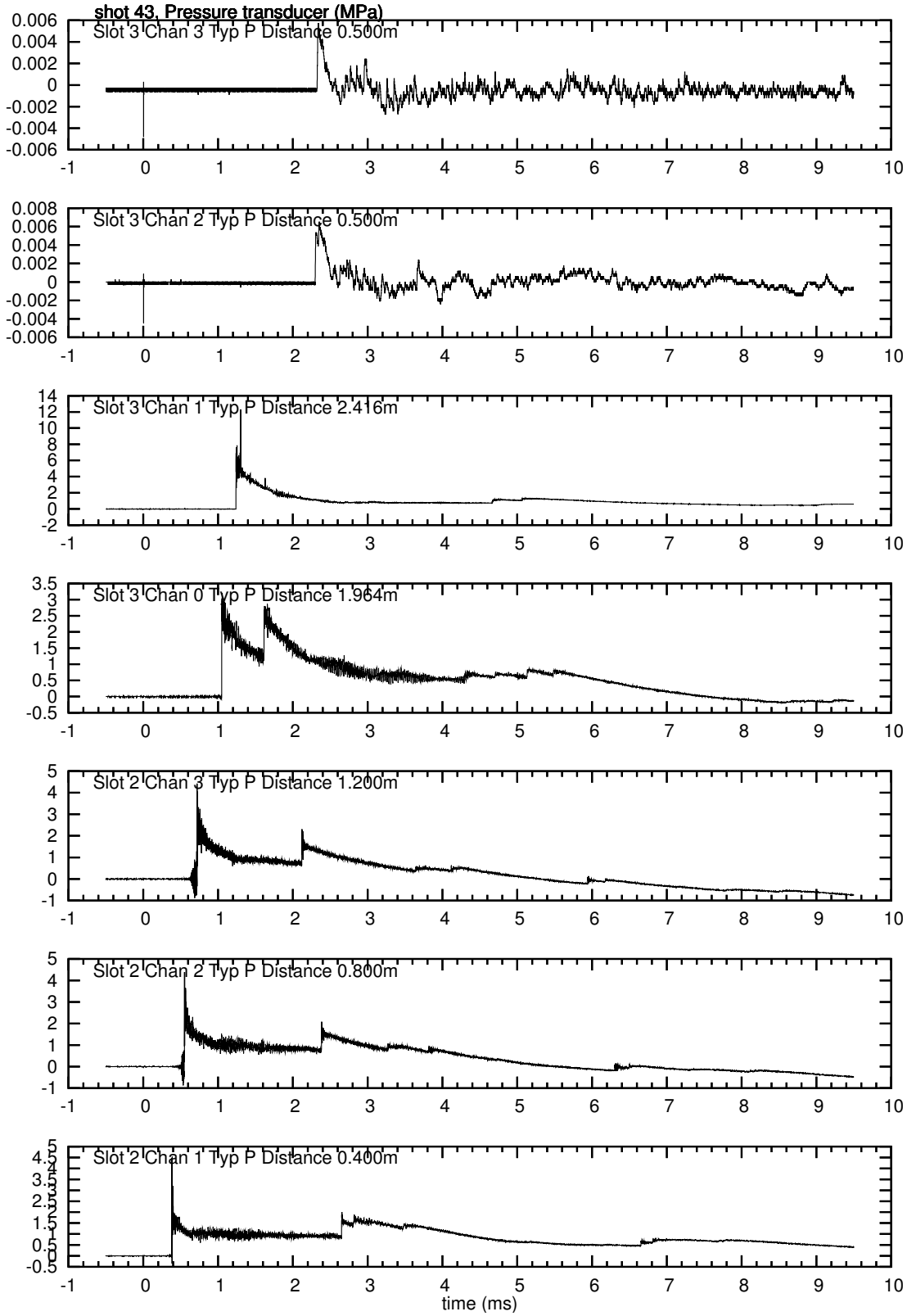

Figure 102: Pressure traces for shot 43

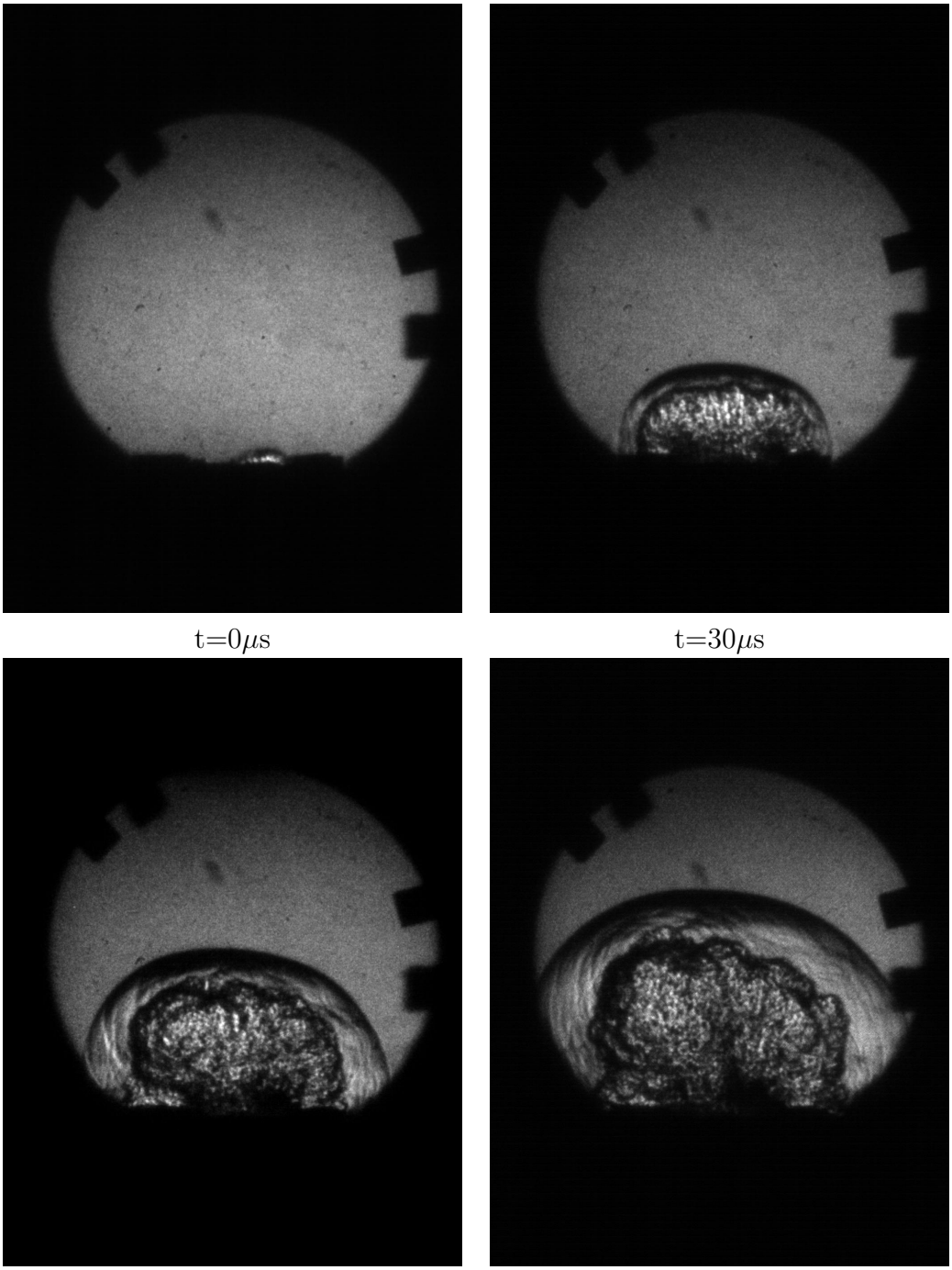

t=0μs t=30μs

t=60μs t=90μs

Figure 103: Blast wave images for shot 43.

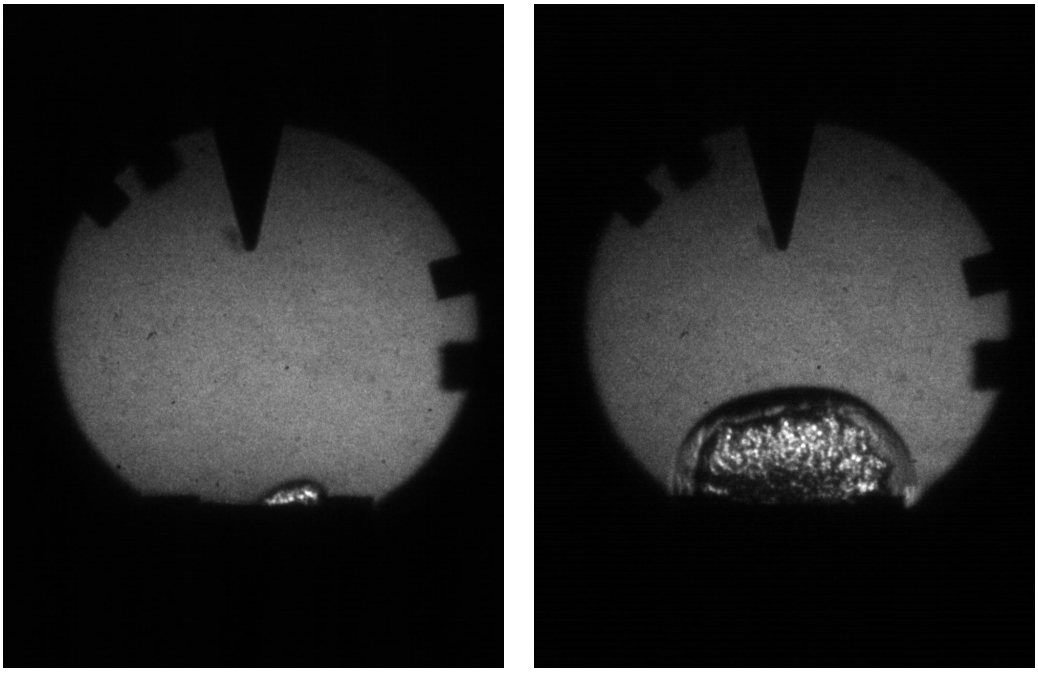

t=0μs t=30μs

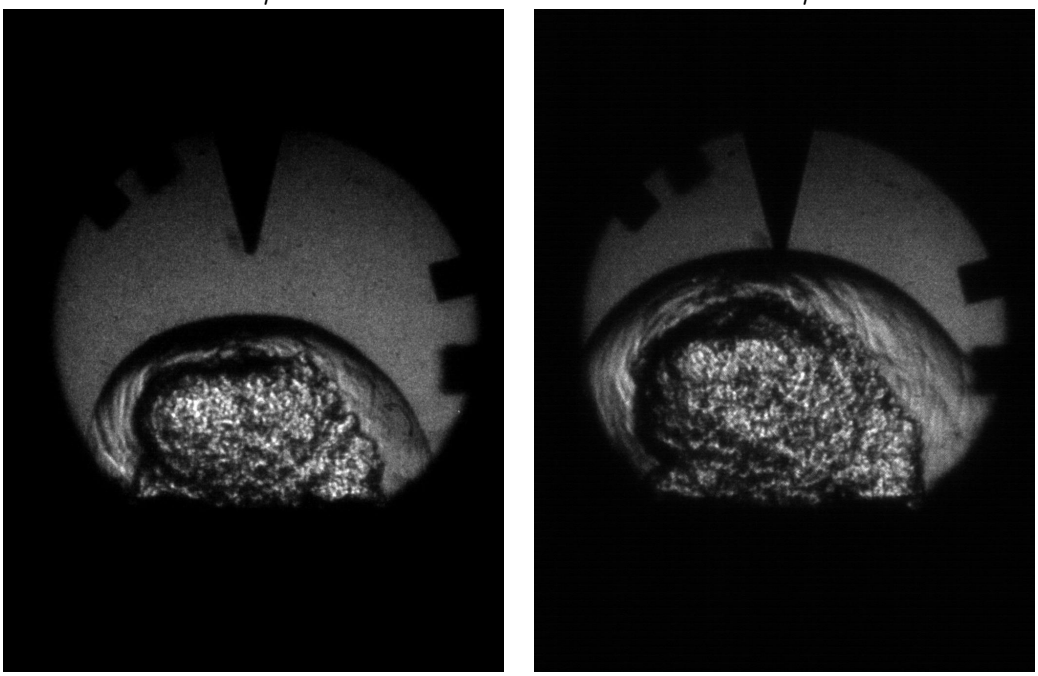

t=60μs t=90μs

Figure 104: Blast wave images for shot 44.

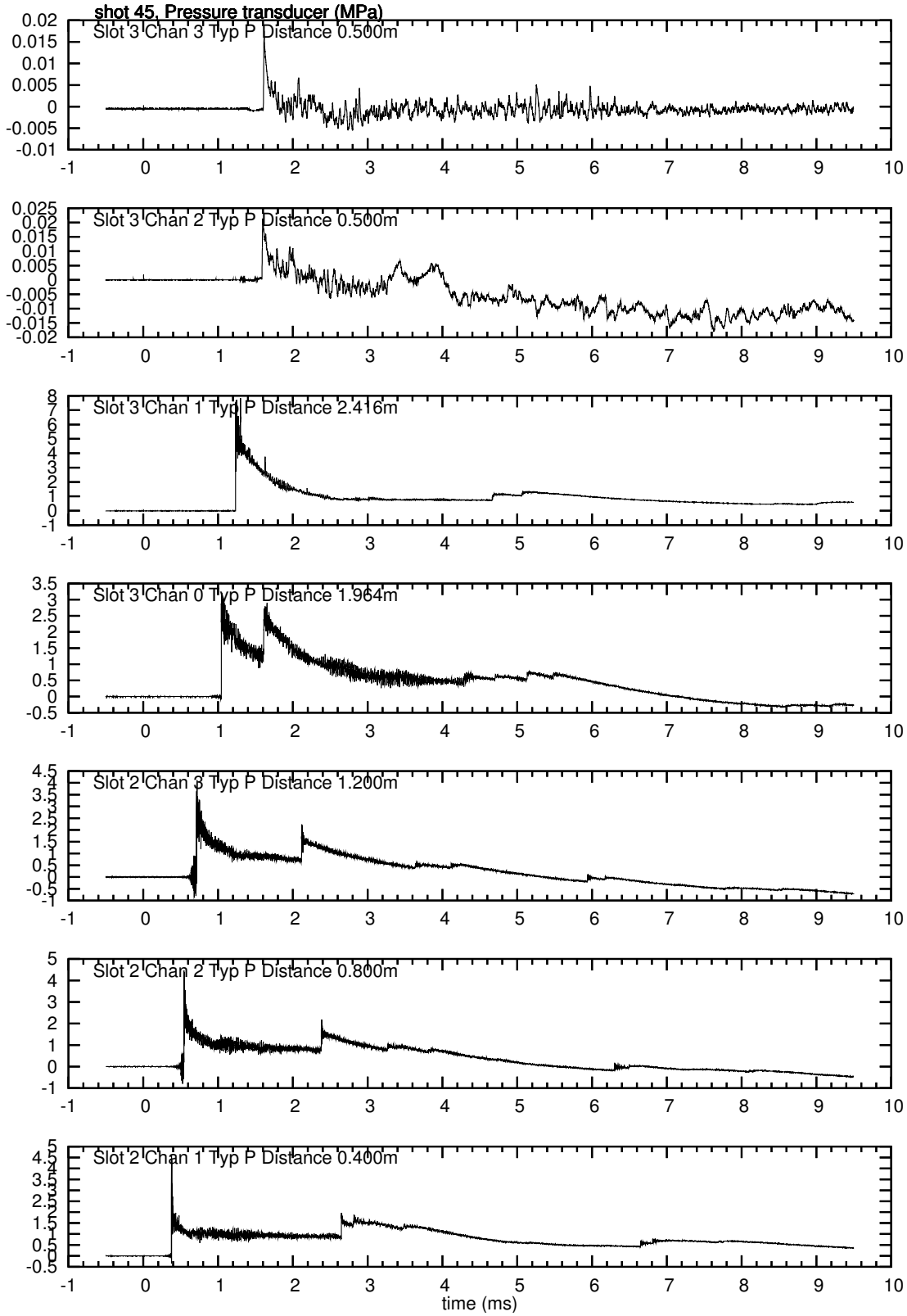

Figure 105: Pressure traces for shot 45

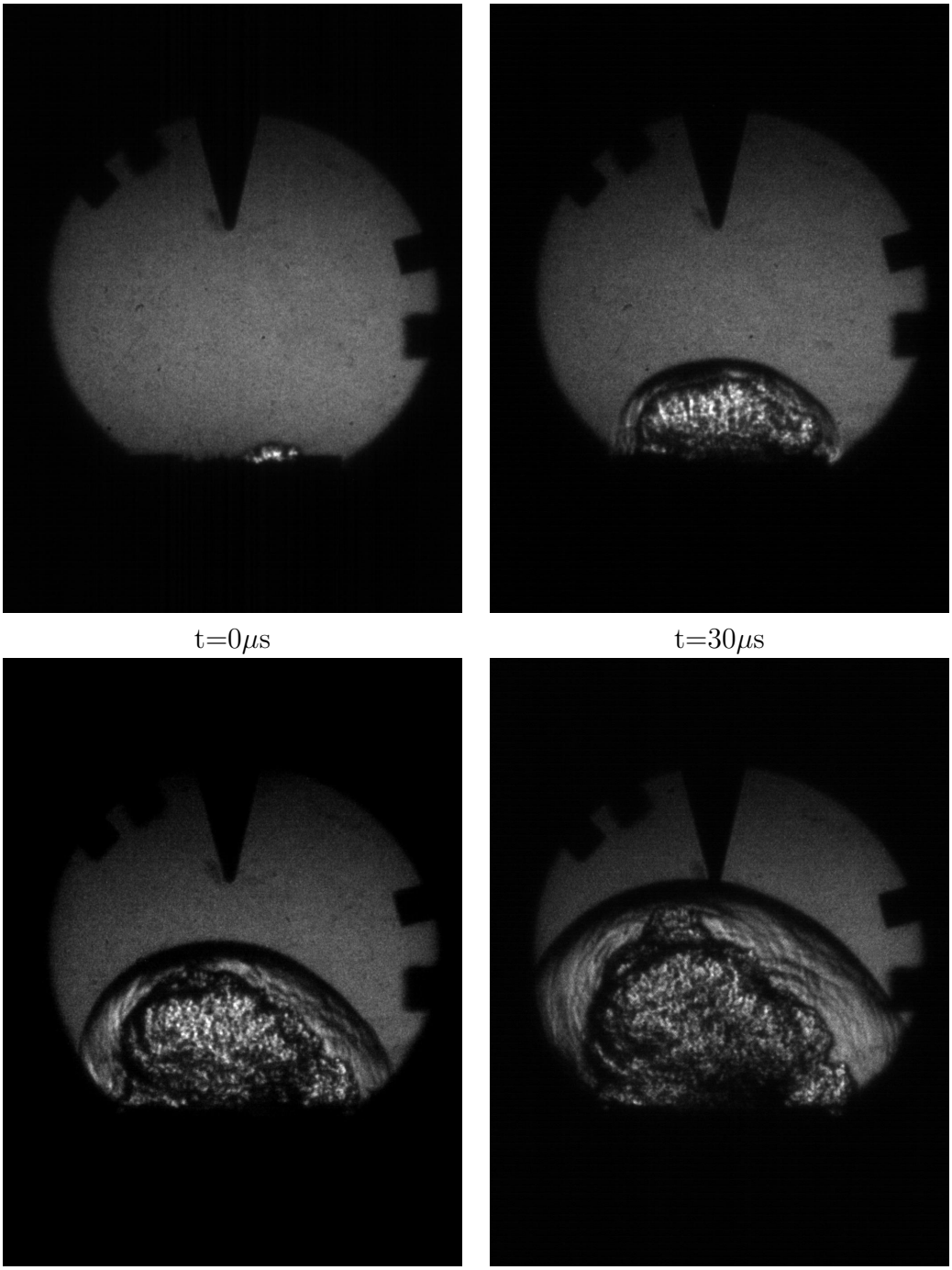

t=0μs t=30μs

t=60μs t=90μs

Figure 106: Blast wave images for shot 45.

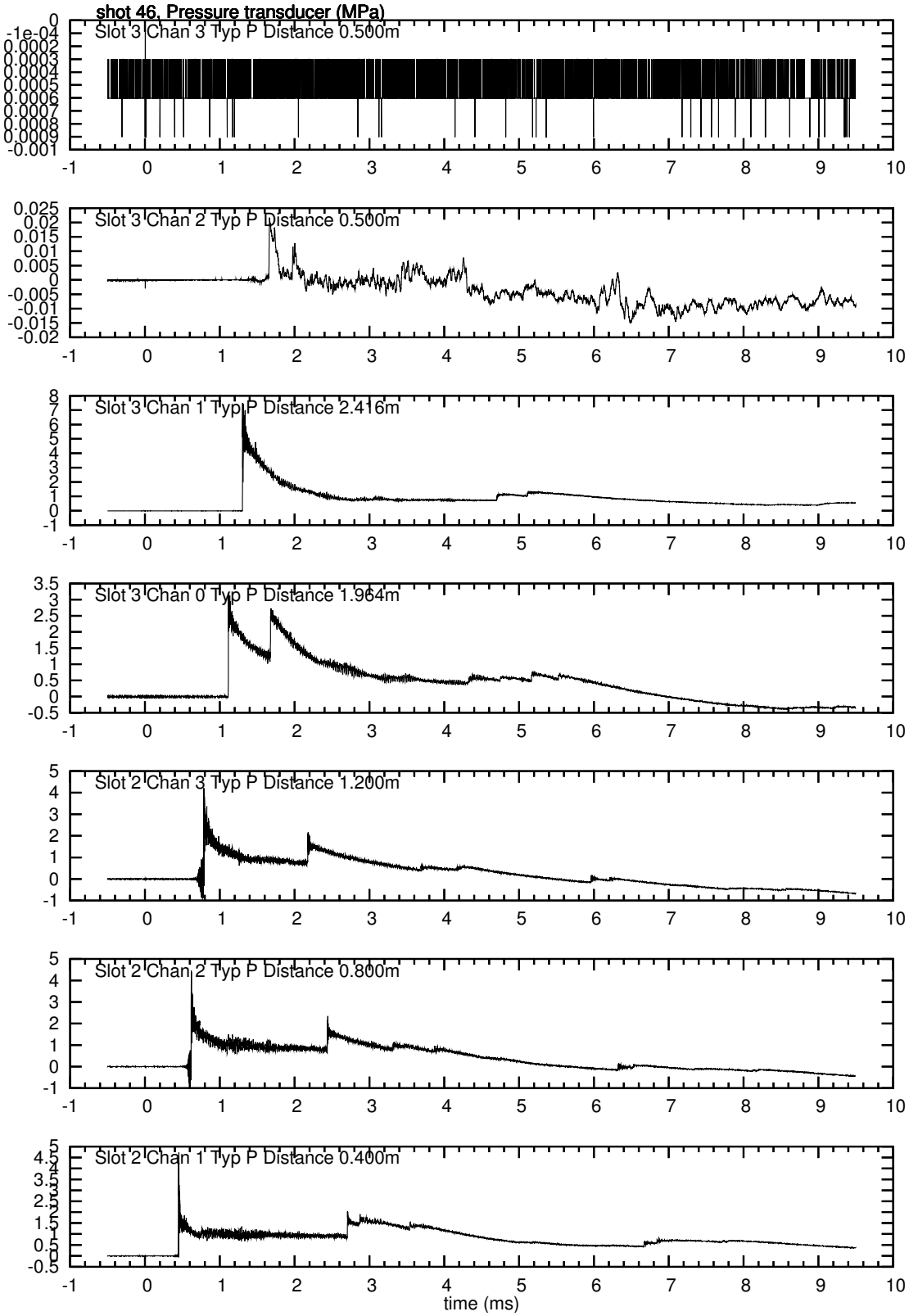

Figure 107: Pressure traces for shot 46

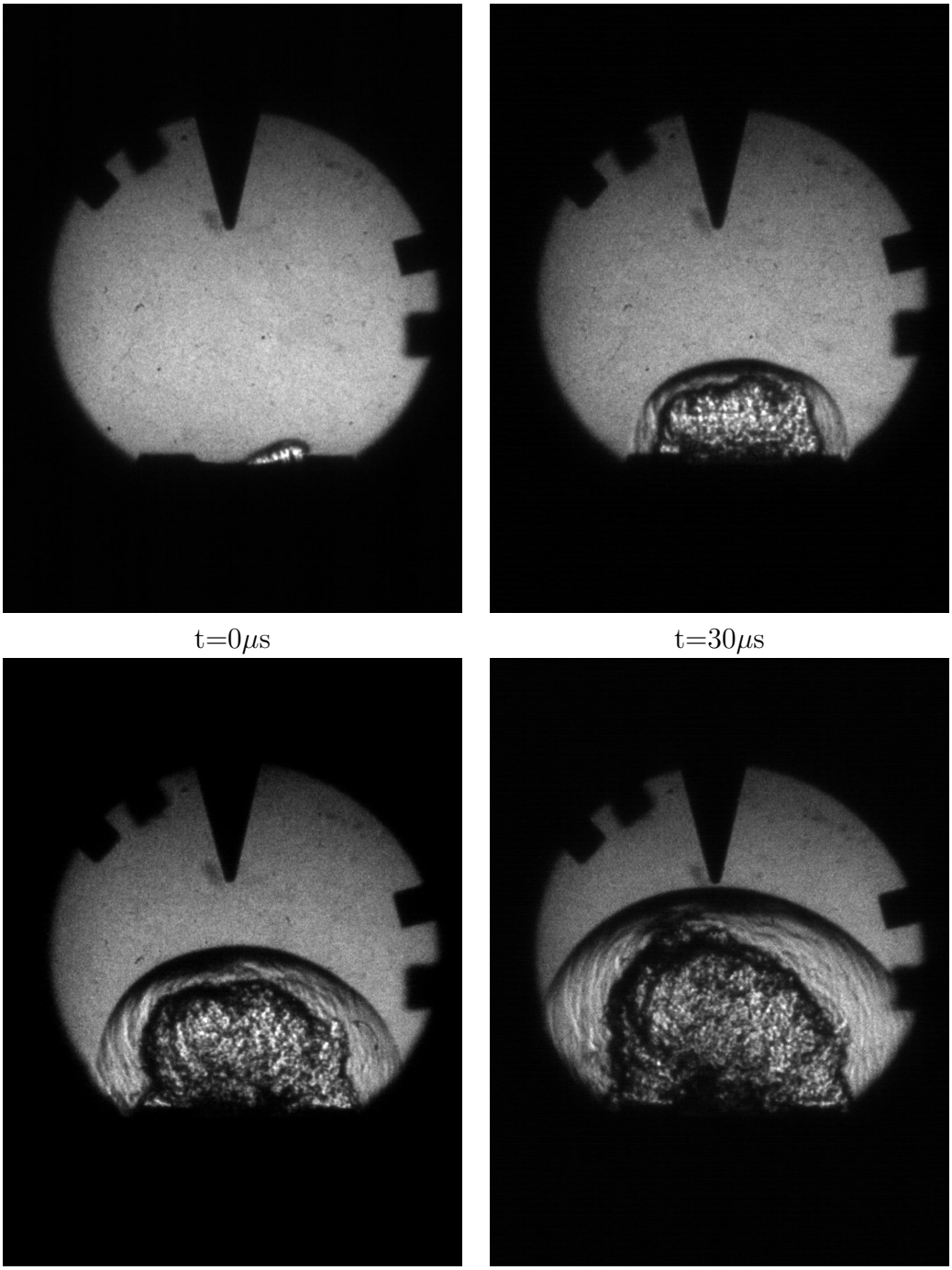

t=0μs t=30μs

t=60μs t=90μs

Figure 108: Blast wave images for shot 46.

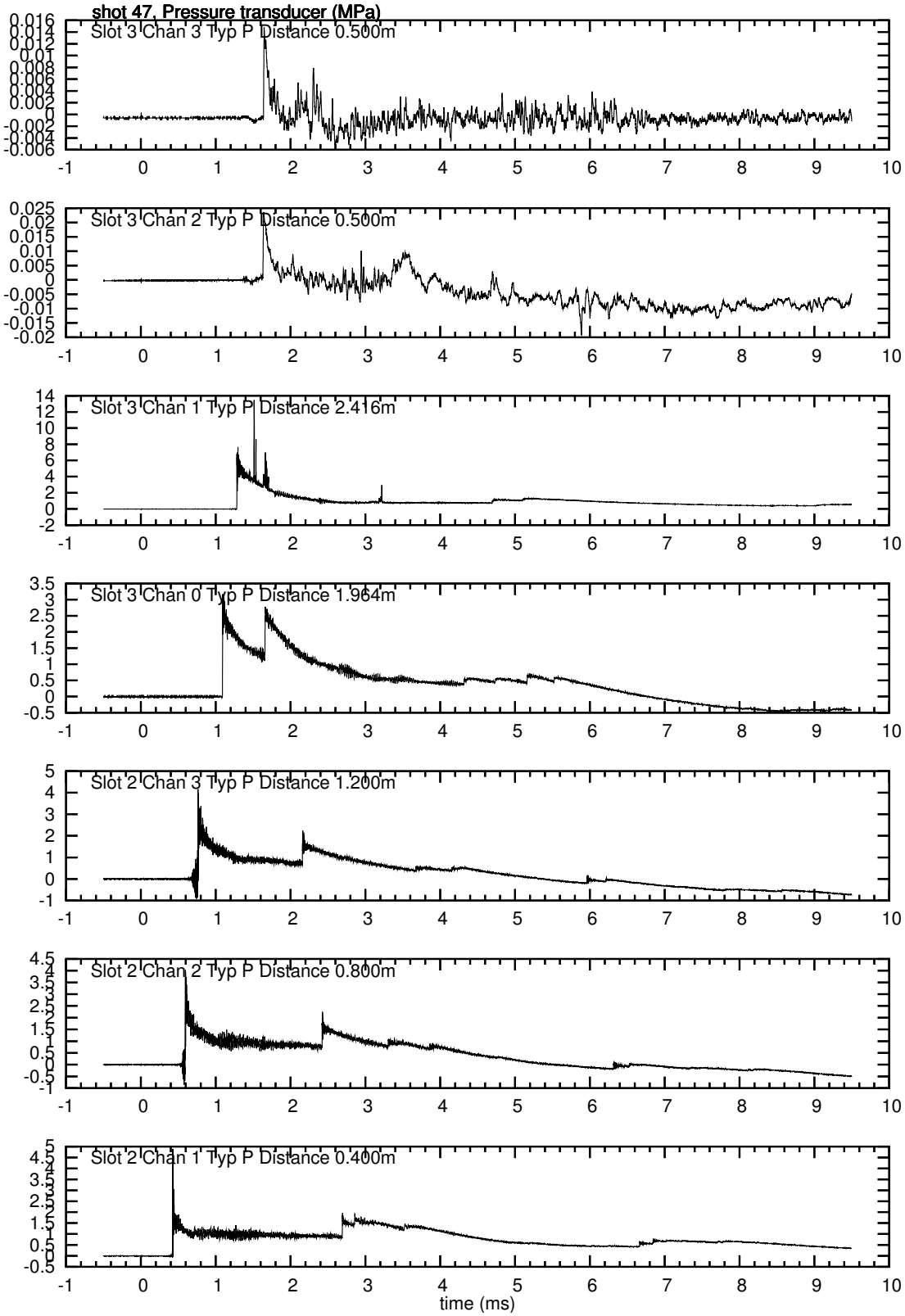

Figure 109: Pressure traces for shot 47

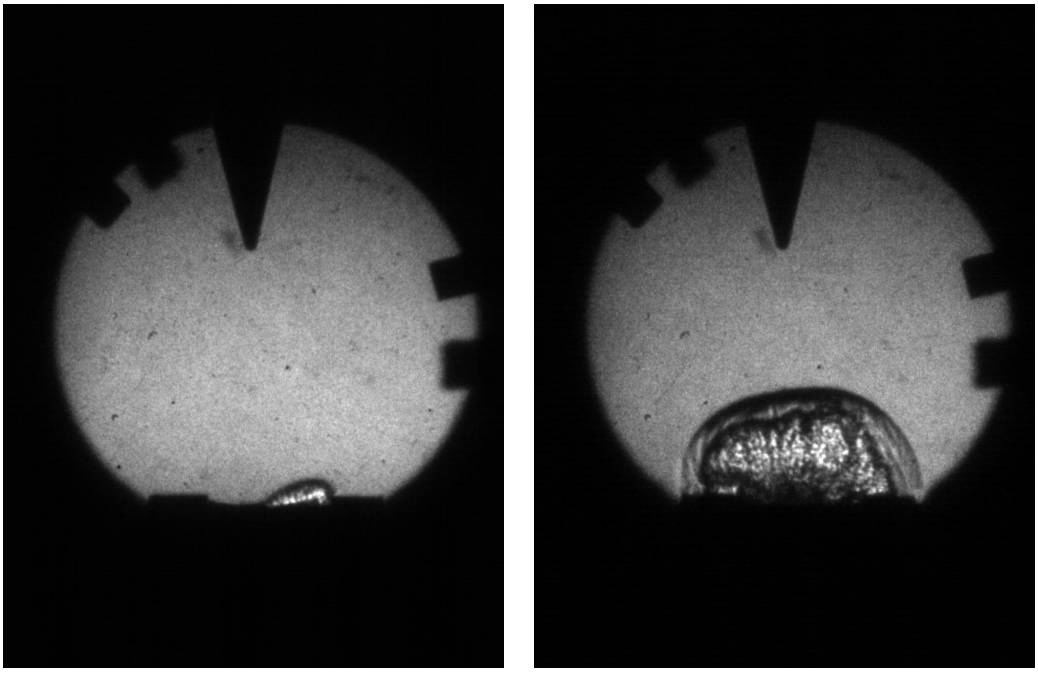

t=0μs t=30μs

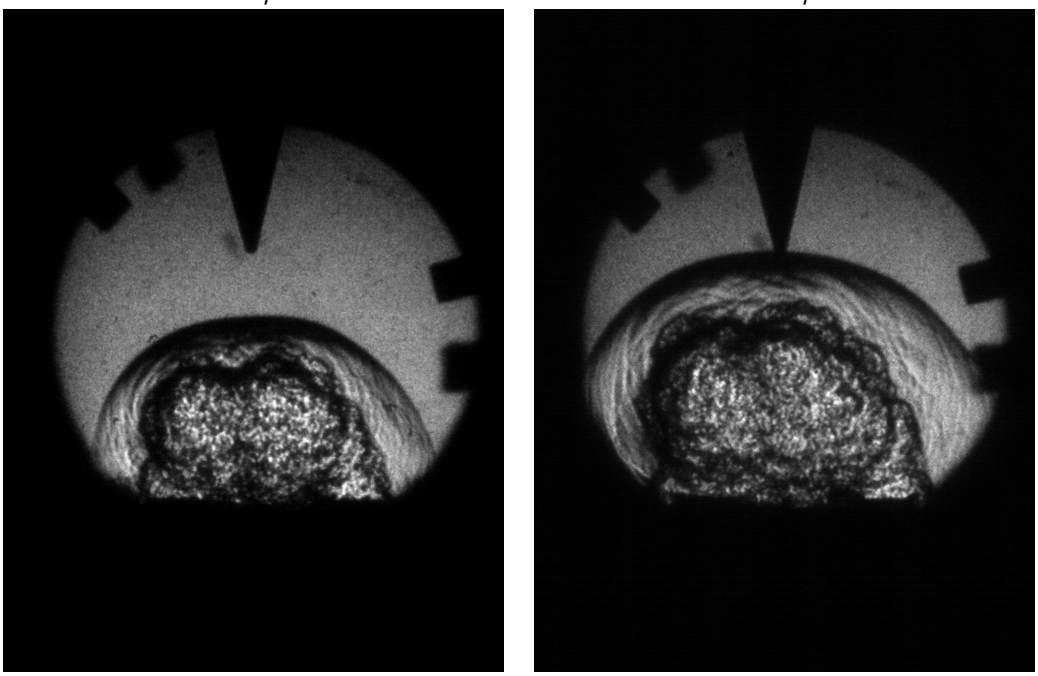

t=60μs t=90μs

Figure 110: Blast wave images for shot 47.

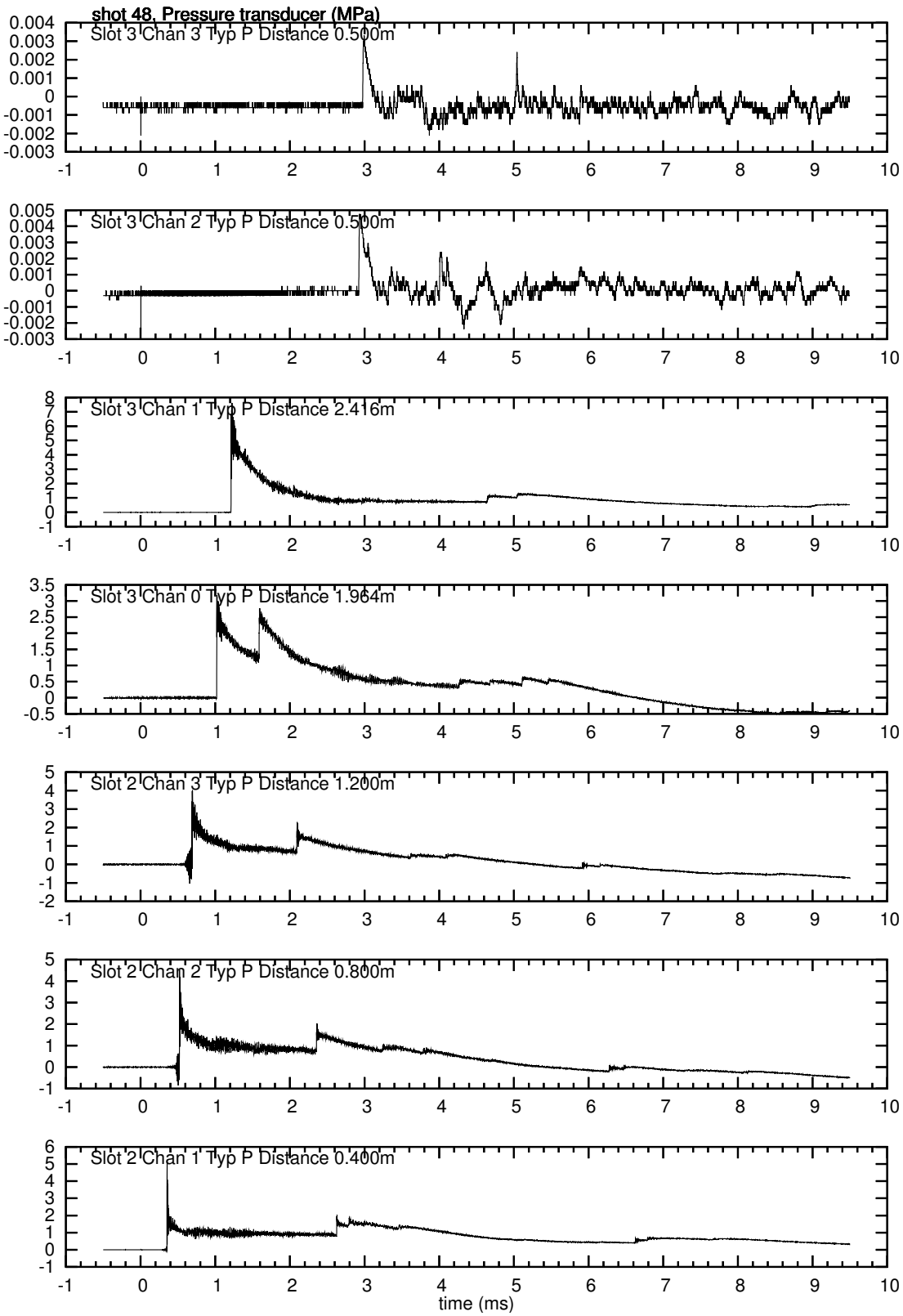

Figure 111: Pressure traces for shot 48

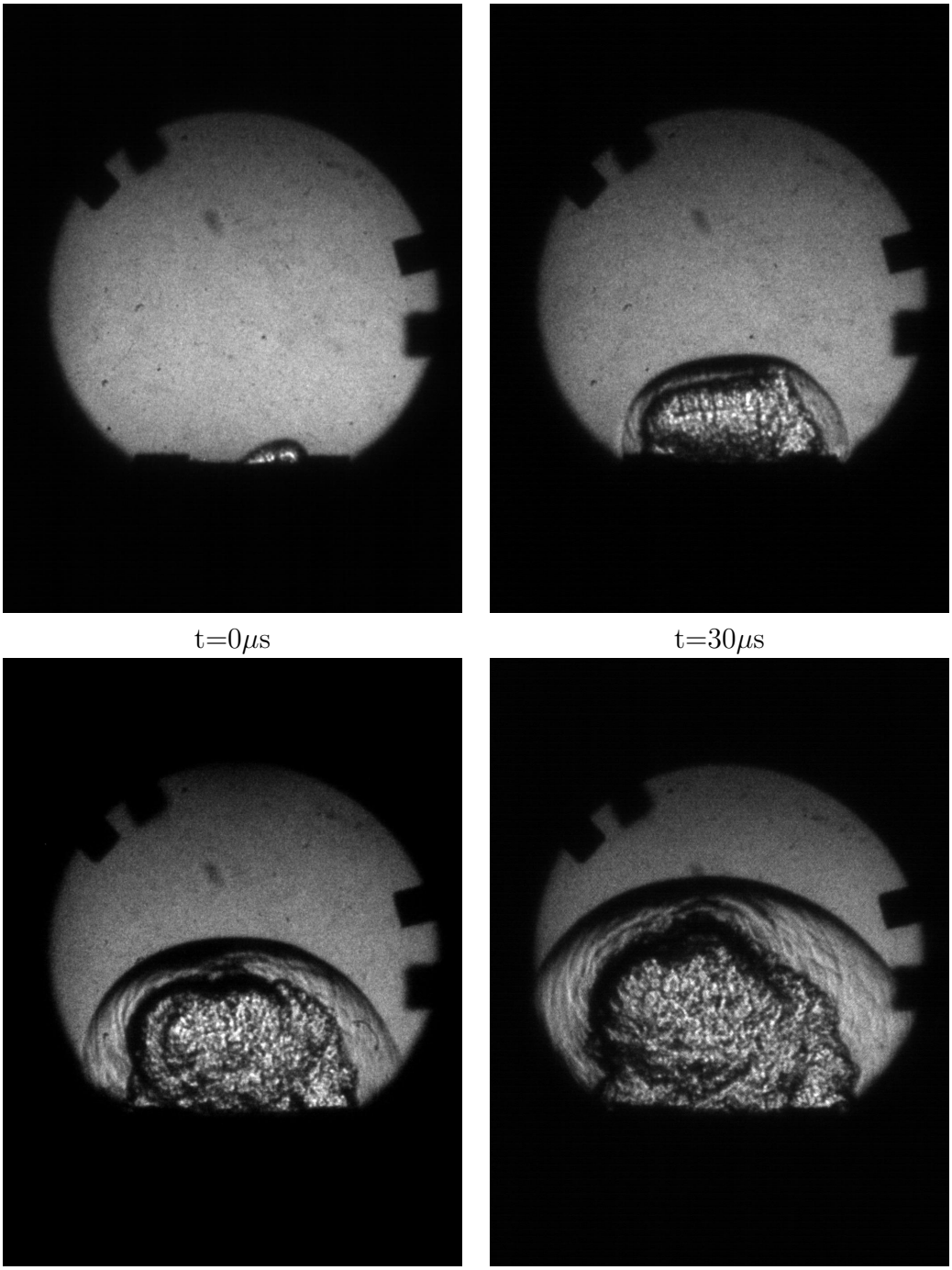

t=0μs t=30μs

t=60μs t=90μs

Figure 112: Blast wave images for shot 48.

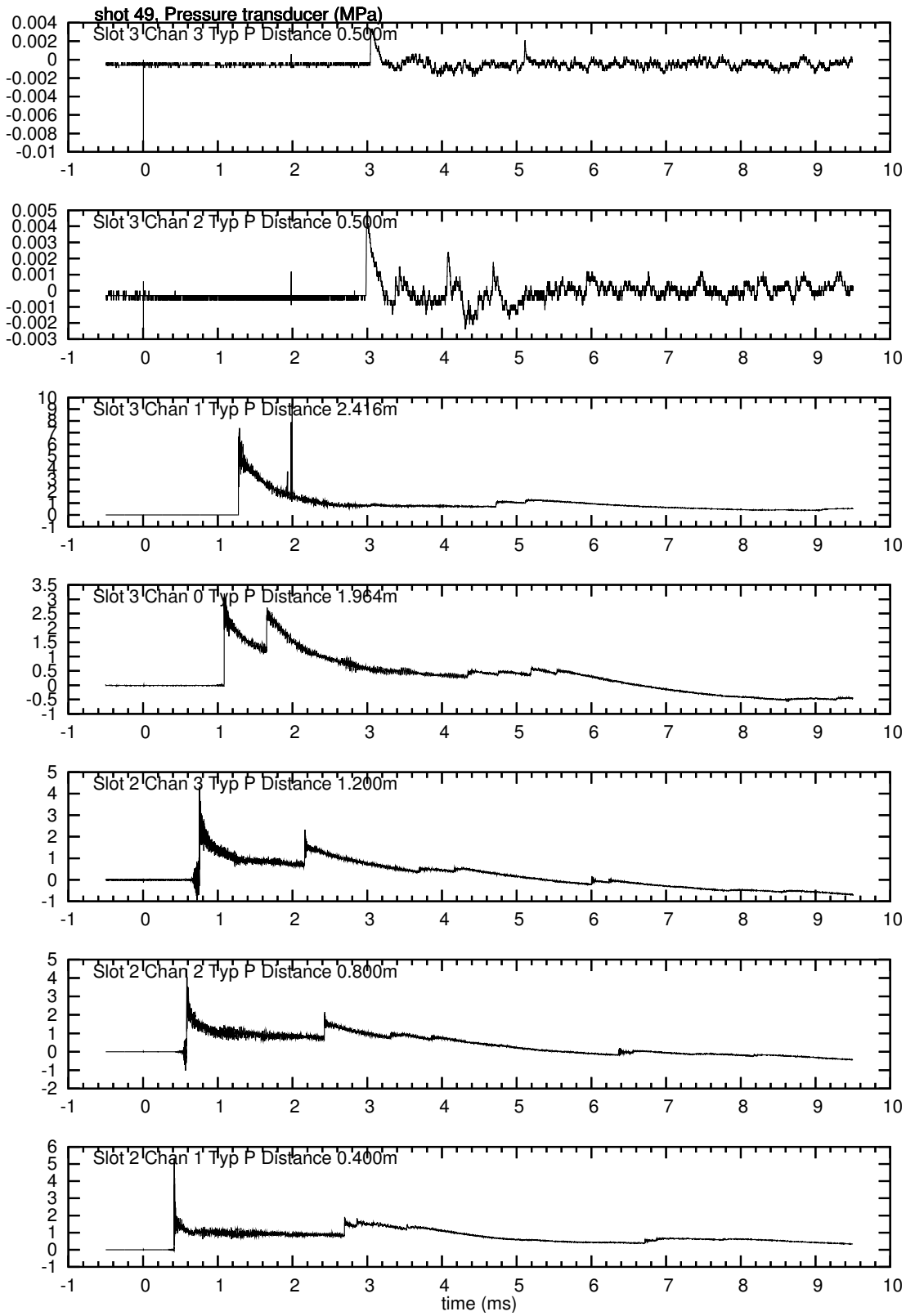

Figure 113: Pressure traces for shot 49

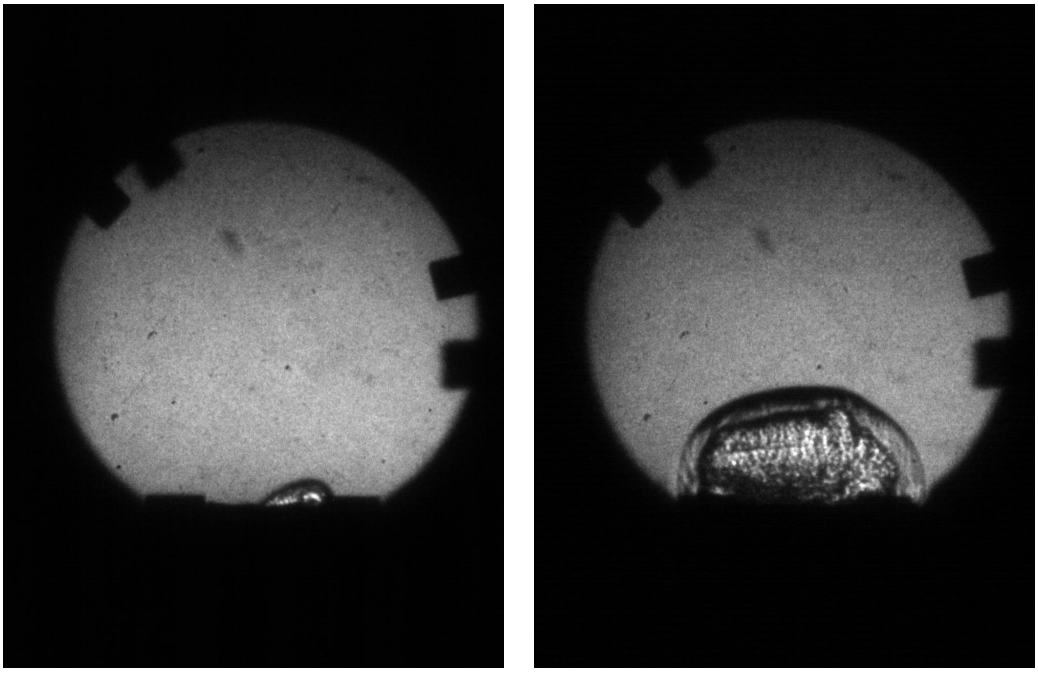

t=0μs t=30μs

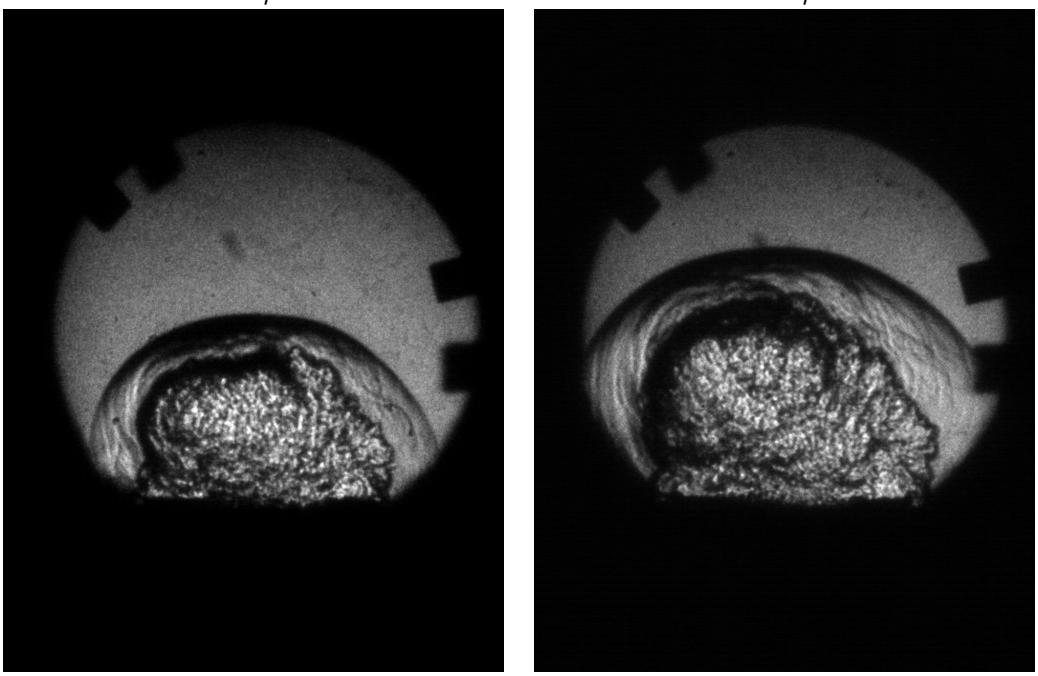

t=60μs t=90μs

Figure 114: Blast wave images for shot 49.

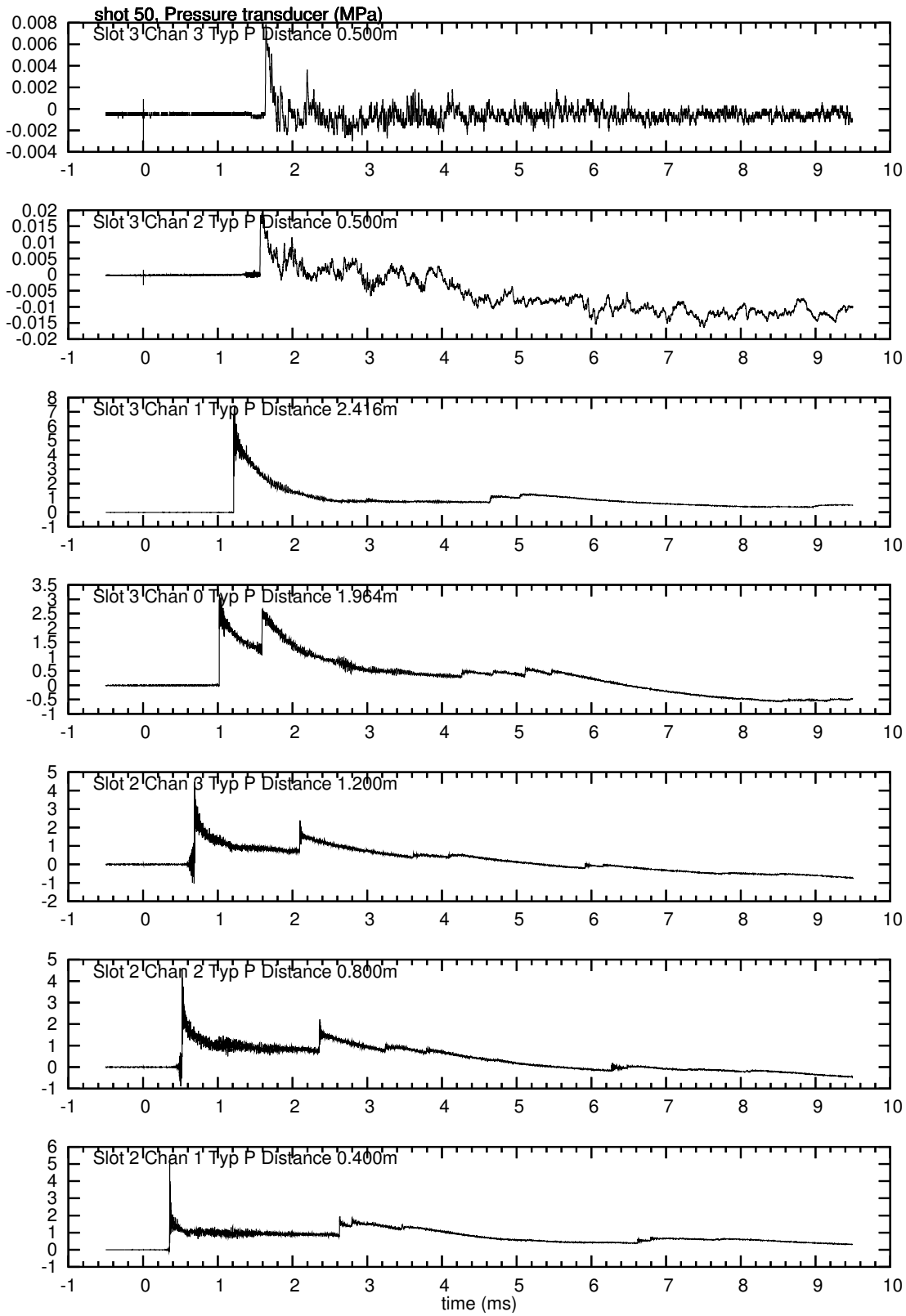

Figure 115: Pressure traces for shot 50

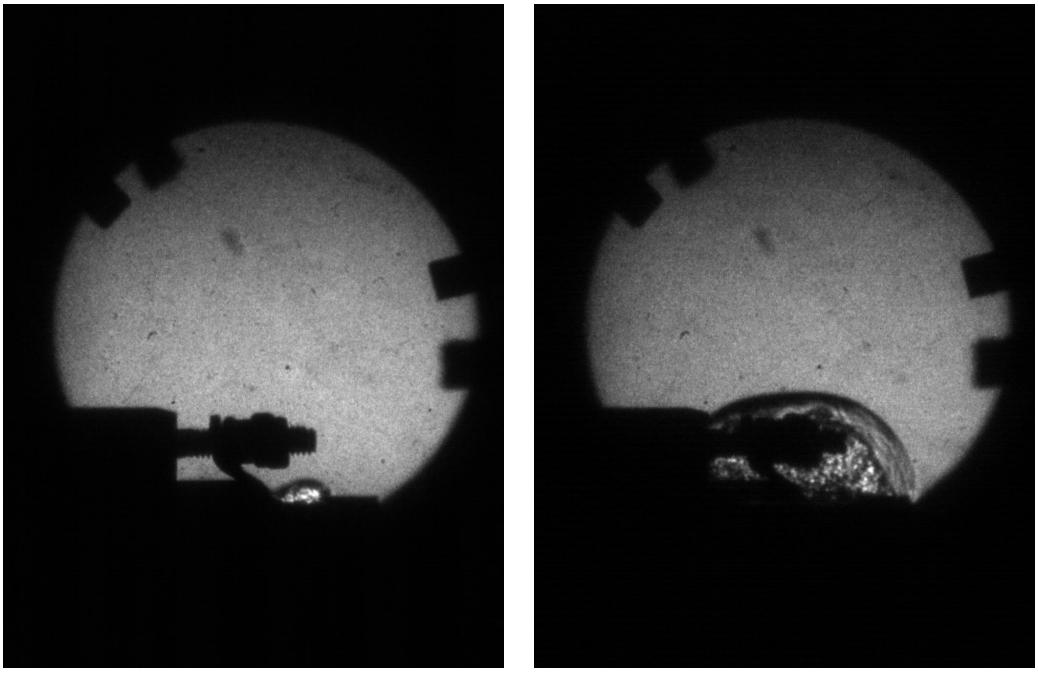

t=0μs t=30μs

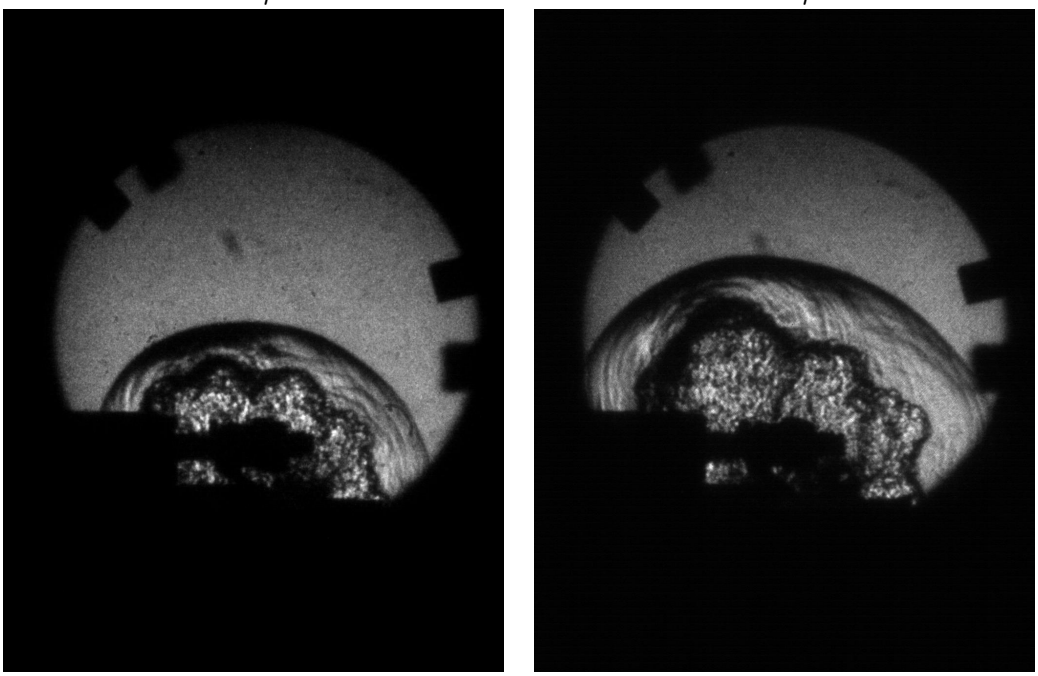

t=60μs t=90μs

Figure 116: Blast wave images for shot 50.

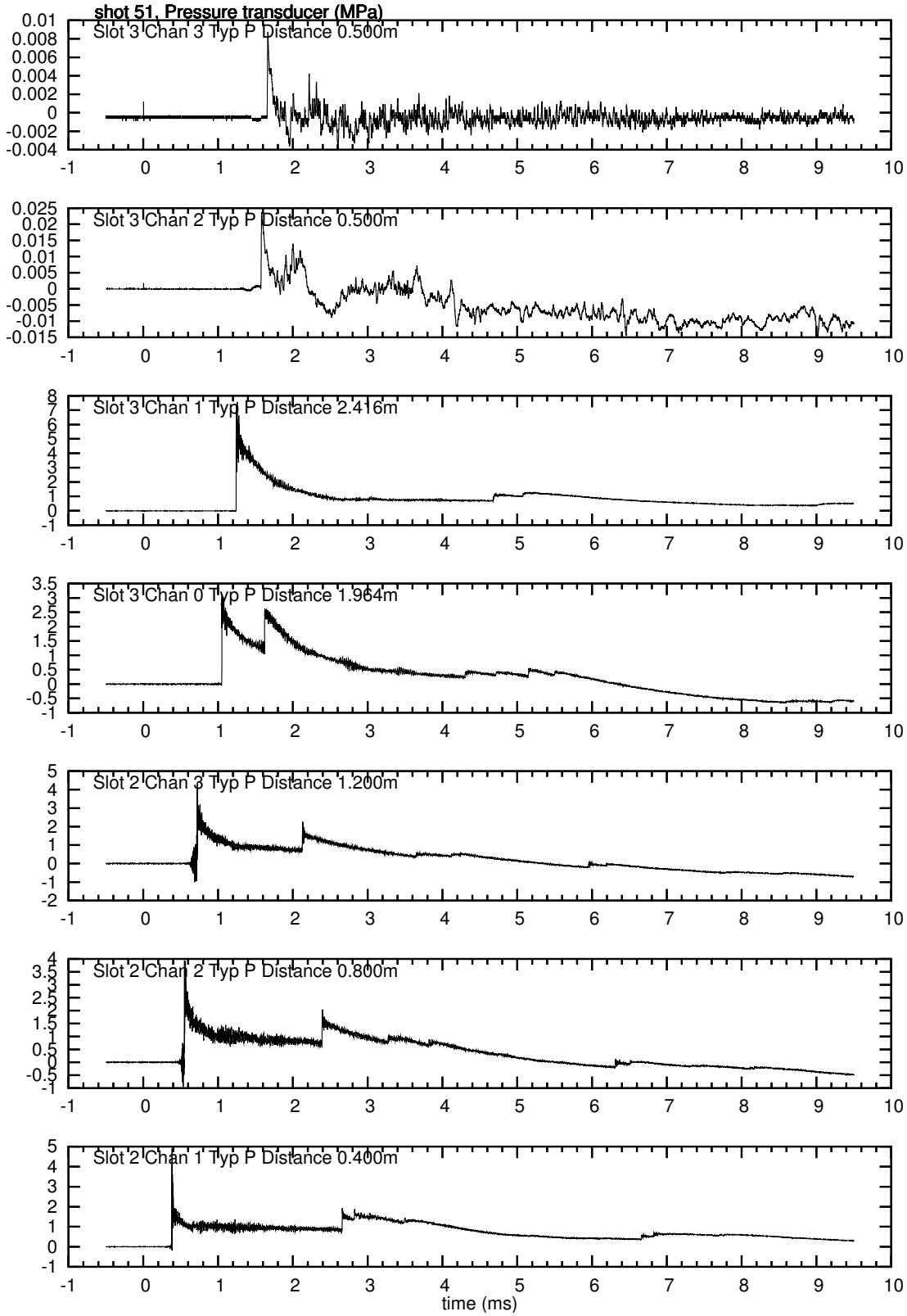

Figure 117: Pressure traces for shot 51

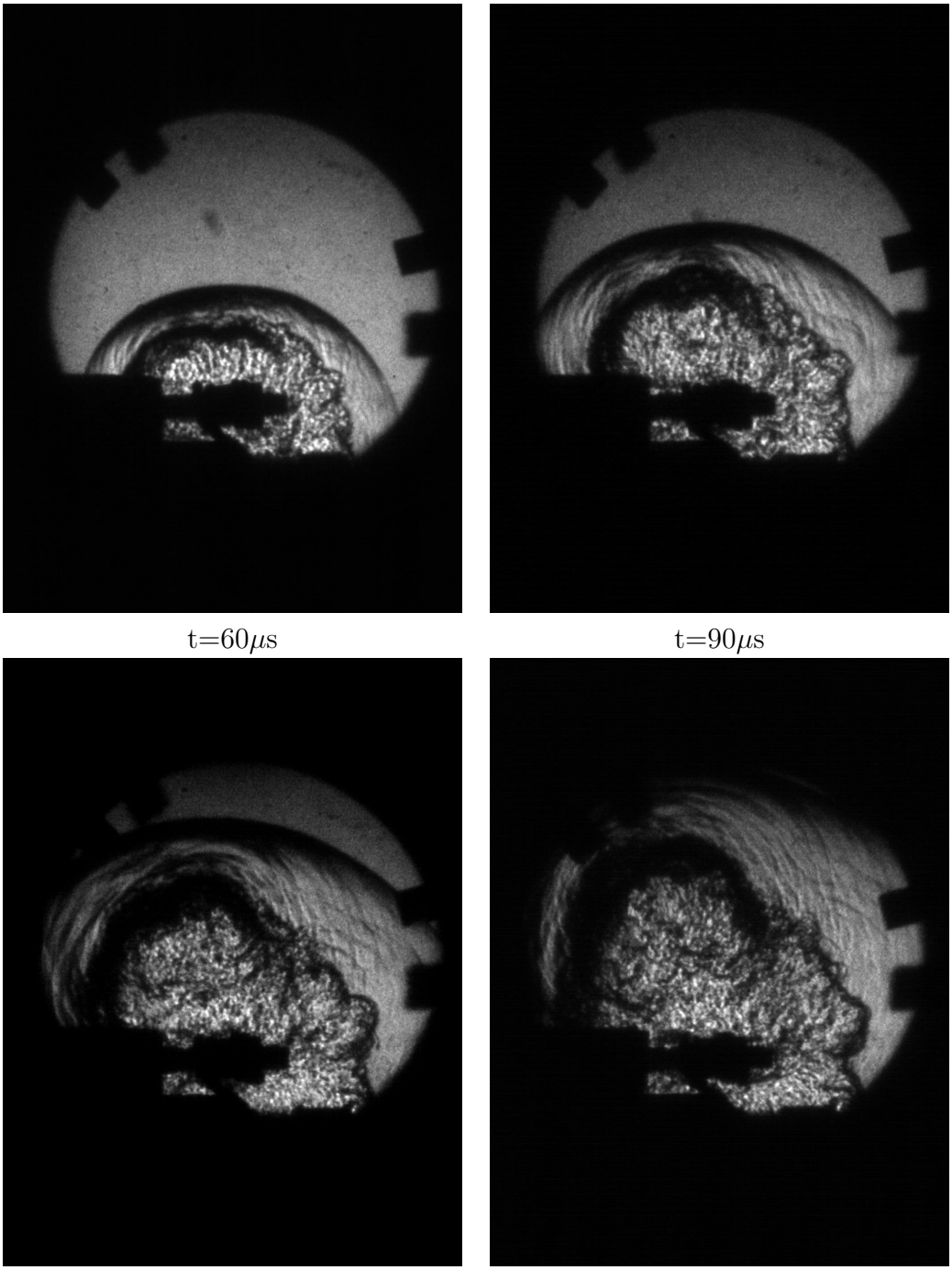

t=60μs t=90μs

t=120μs t=150μs

Figure 118: Blast wave images for shot 51.

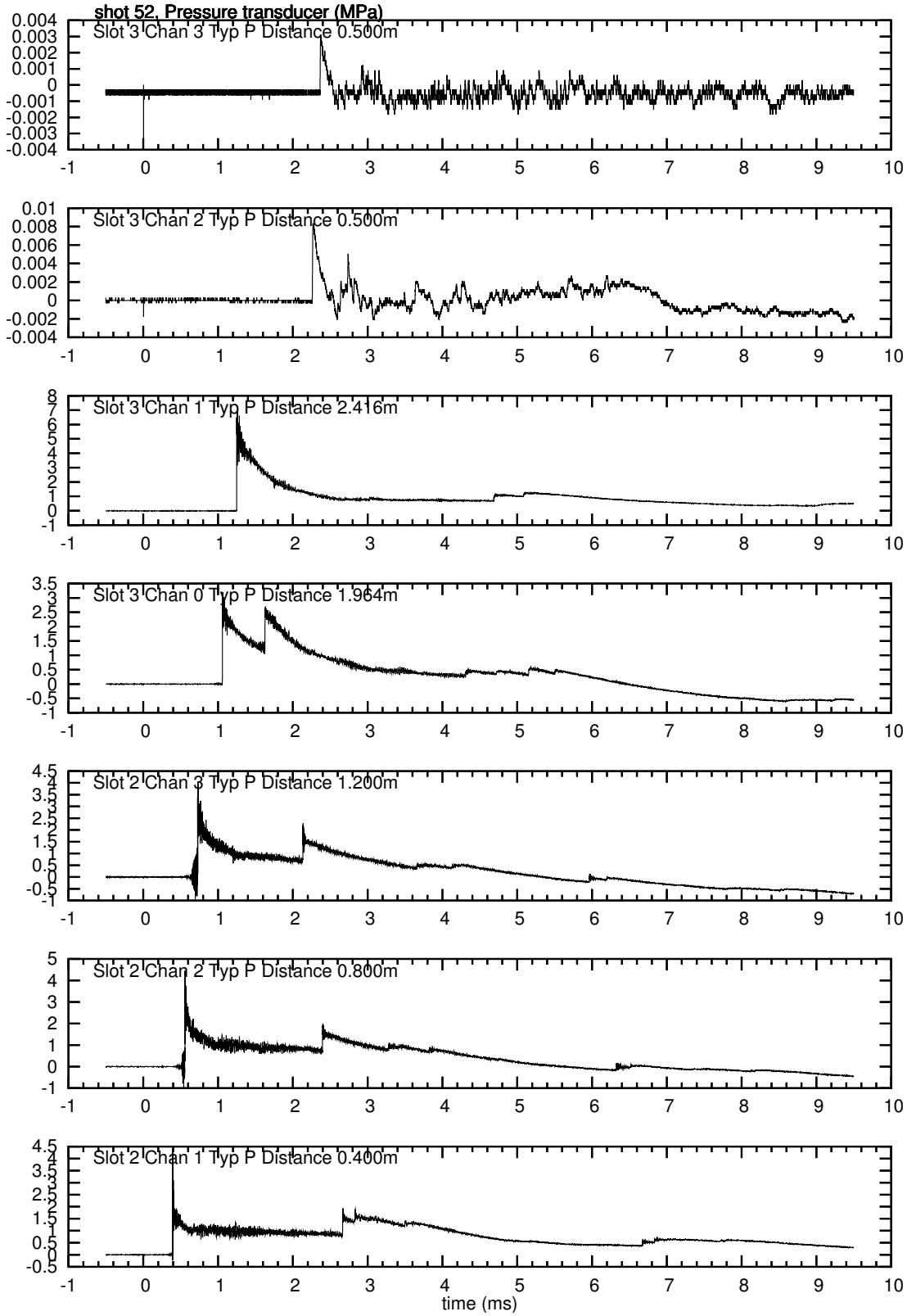

Figure 119: Pressure traces for shot 52

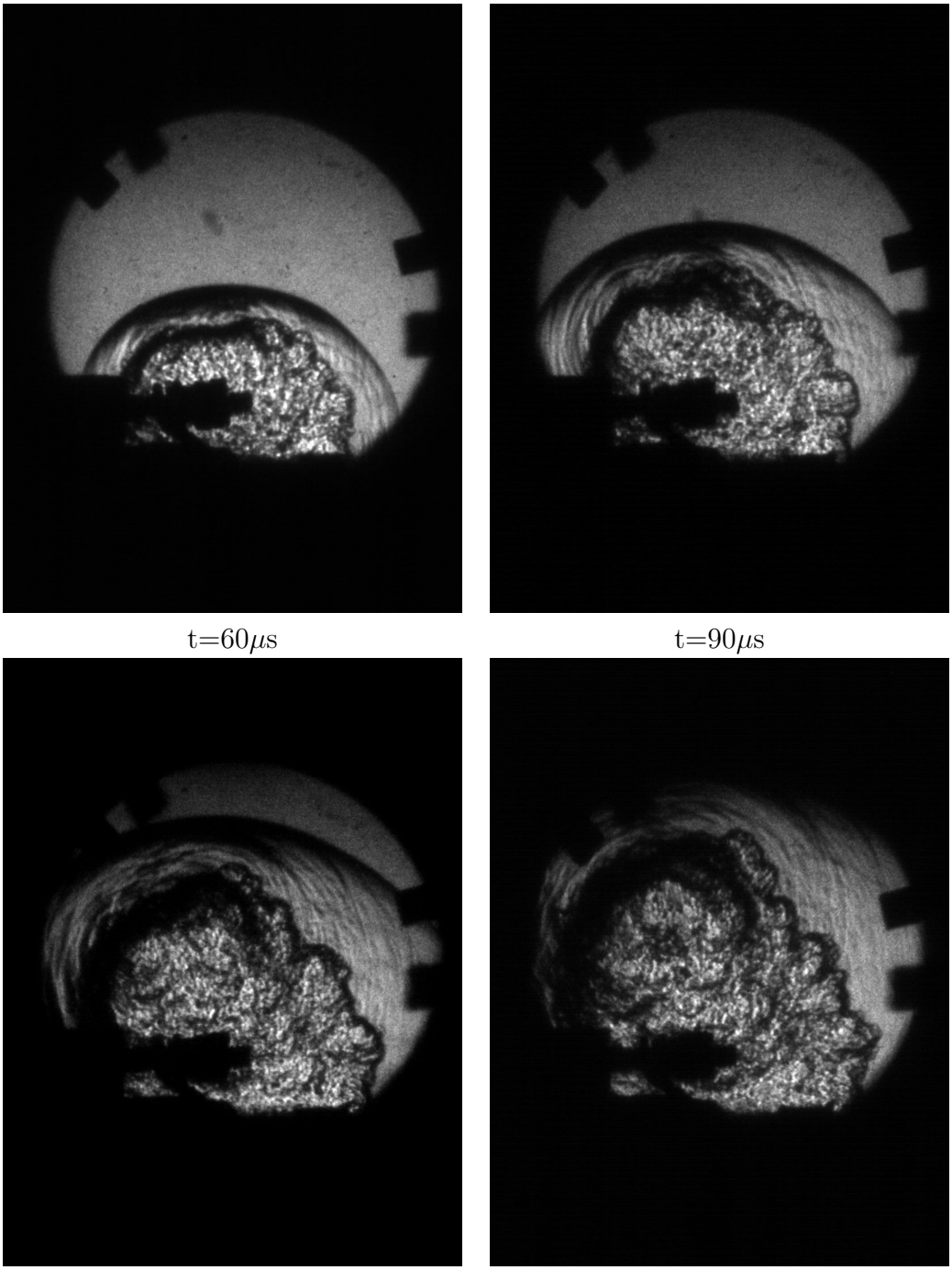

t=60μs t=90μs

t=120μs t=150μs

Figure 120: Blast wave images for shot 52.

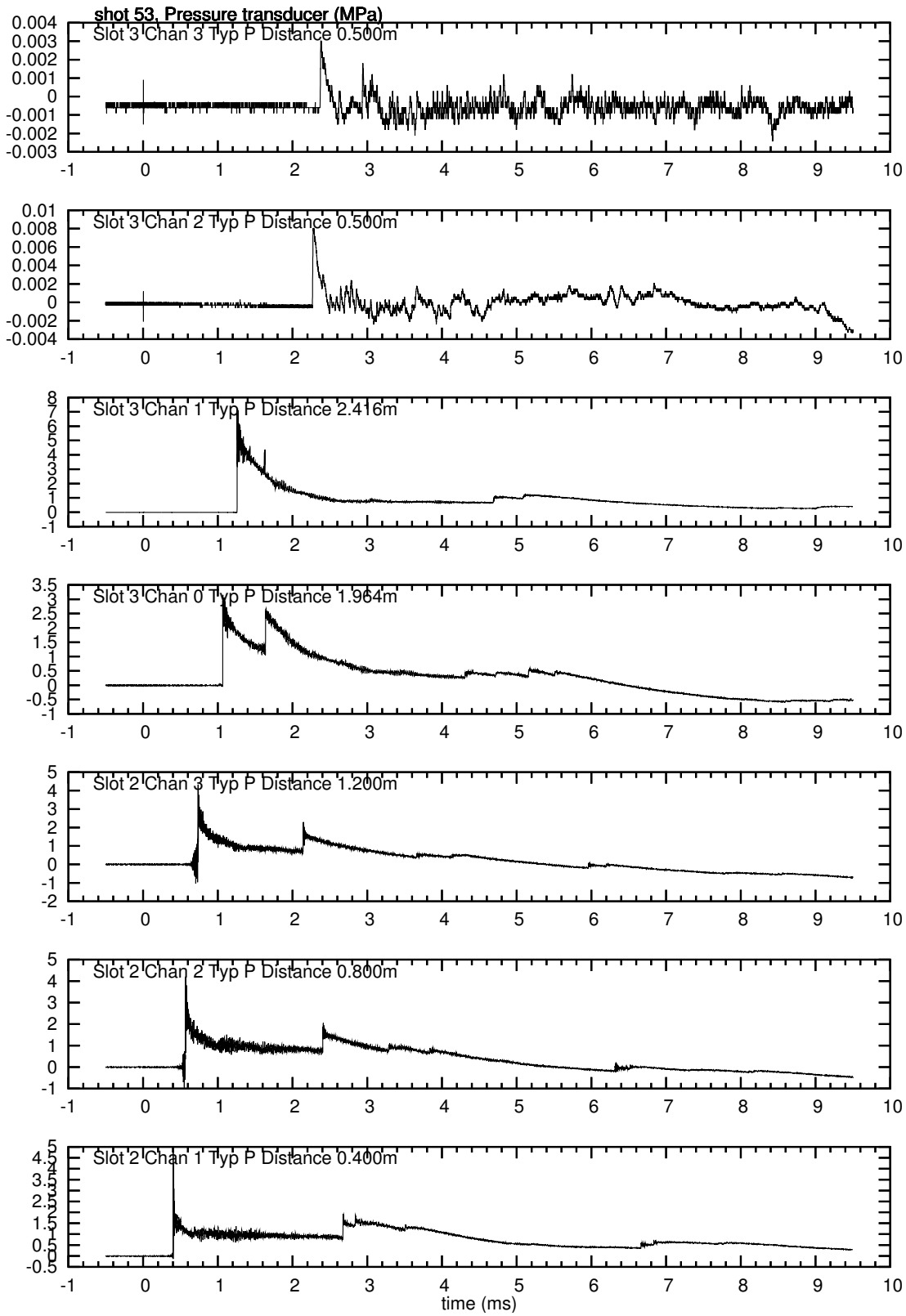

Figure 121: Pressure traces for shot 53

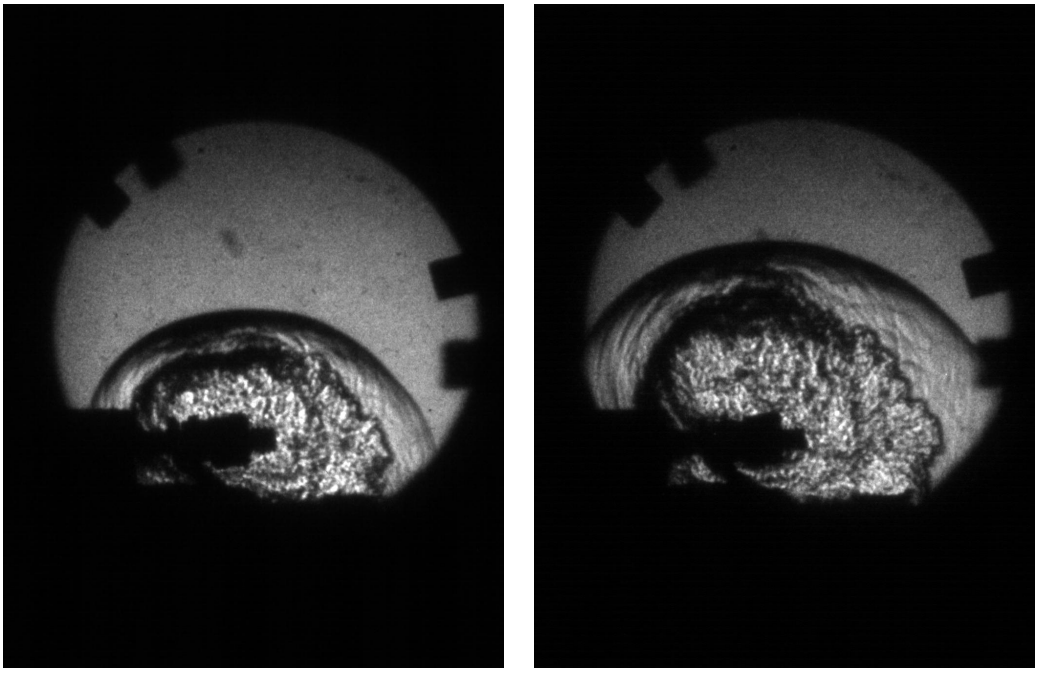

t=60μs t=90μs

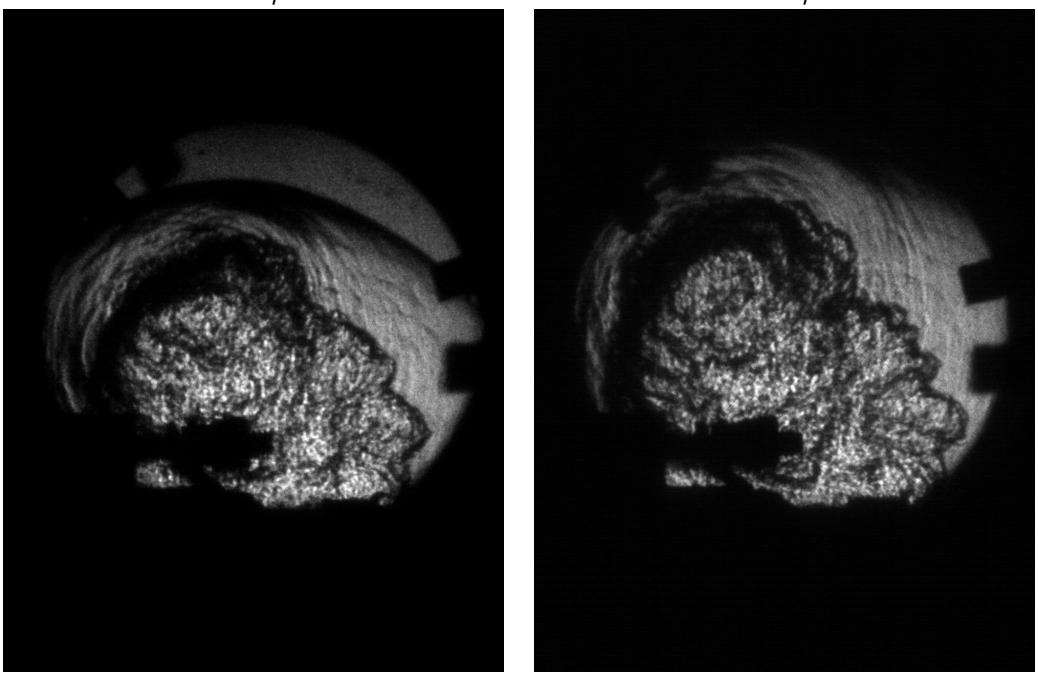

t=120μs t=150μs

Figure 122: Blast wave images for shot 53.

C Flap Data

Table 5: Flap tests. All shots used stoichiometric ethylene-oxygen at 100 kPa.

shot	V_{det} avg (m/s)	Notes
54	2358.9	Flap Tube #1. Flaps start at 18" rather than 19". Blast probes at 45, 90degrees, 500mm. Camera at 1,21,61,91us
55	2372.1	Flap Tube #2. Camera at 11,41,71,101. Blast Probes at 45, 90degrees, 500mm
56	2365.9	Flap Tube #3. Camera at 1,31,61,91,121,151,181,211. Blast probes at 45, 90degrees, 500mm. Flaps still pulled past line. Epoxy under hinge supports fractured and broke free. CCD 5 returned no image.
57	2367.5	Tube #4 increased score depth. Camera triggered early, so no pics. Blast Gages same.
58	2388.2	Tube #5. Repeat of 57. Camera at 211,241,271,301,331,361,391,421. Again #5 malfunctioned, but there are some specks of light this time. Worked fine after shot.

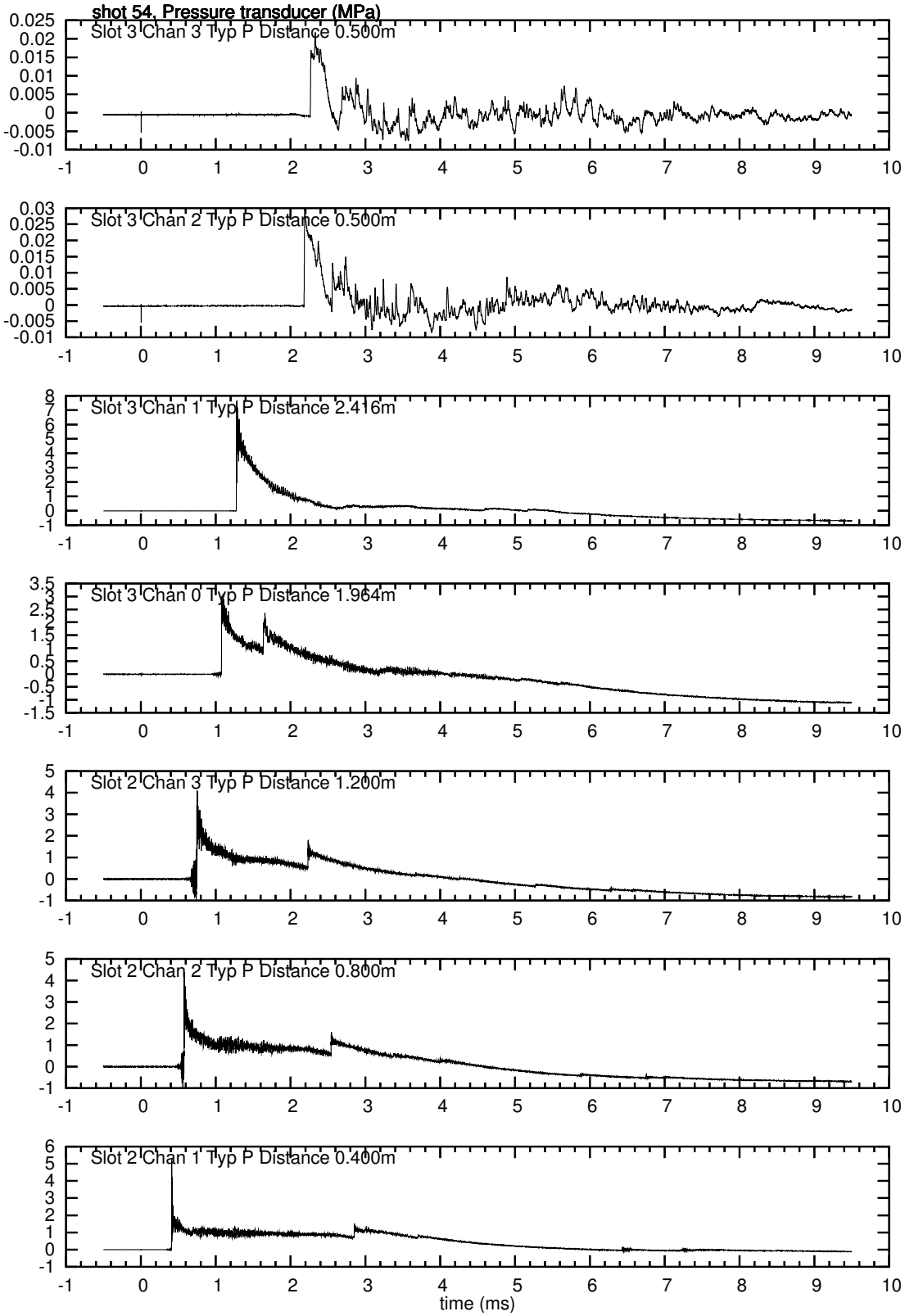

Figure 123: Pressure traces for shot 54

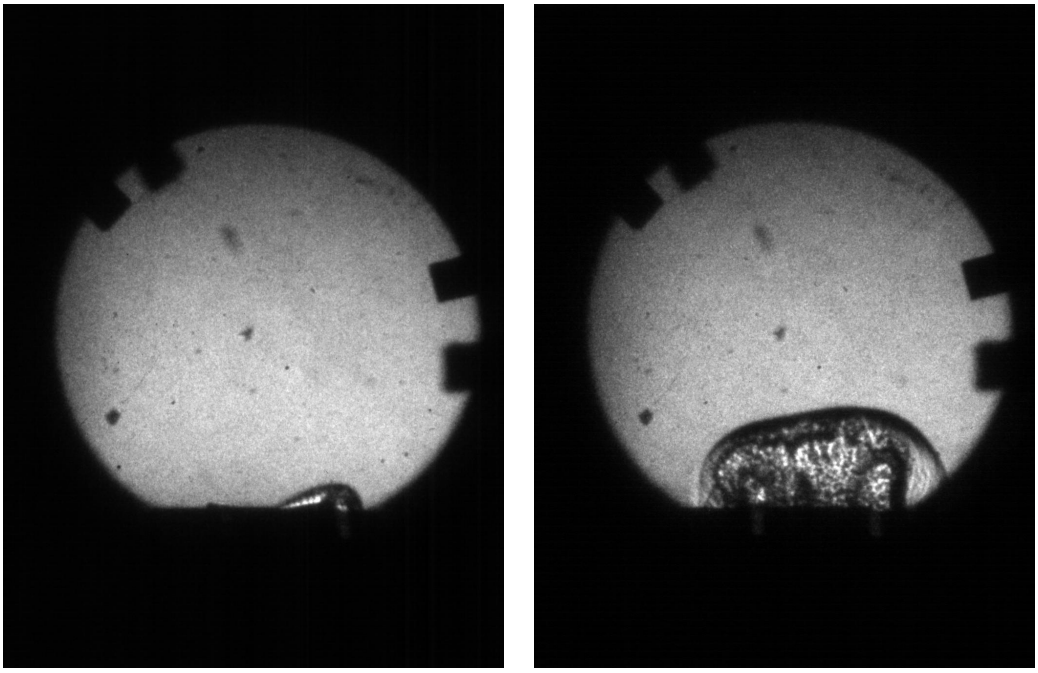

t=0μs t=20μs

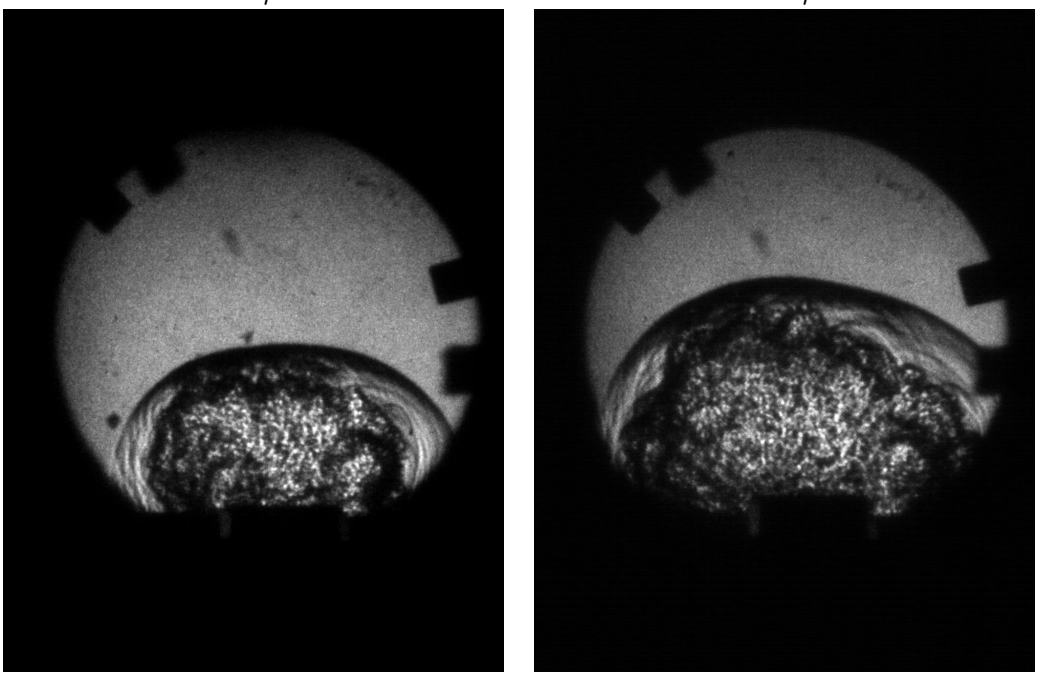

t=60μs t=90μs

Figure 124: Blast wave images for shot 54.

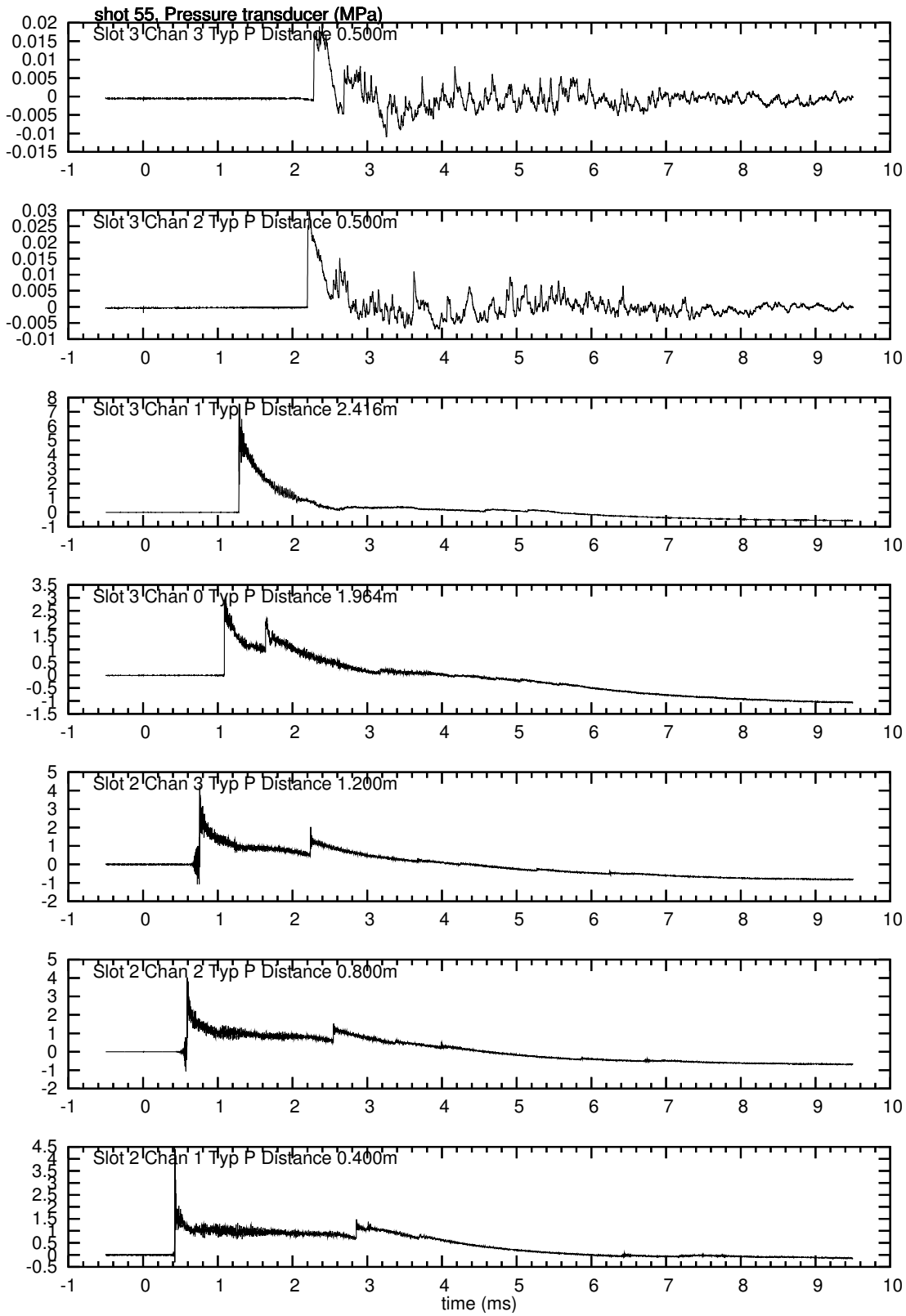

Figure 125: Pressure traces for shot 55

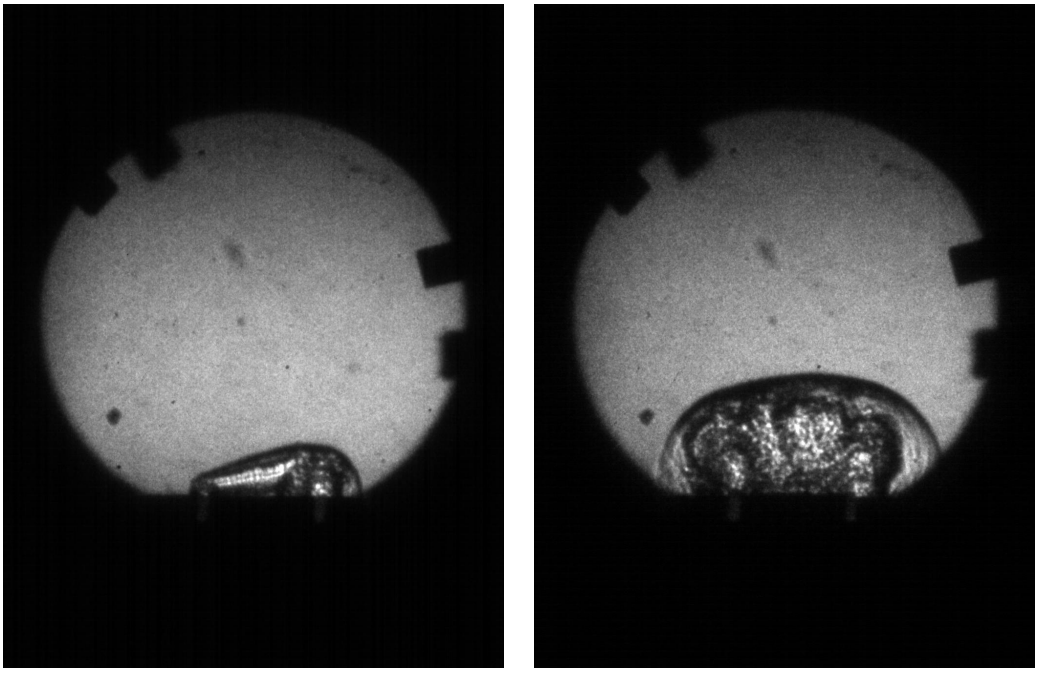

t=10μs t=40μs

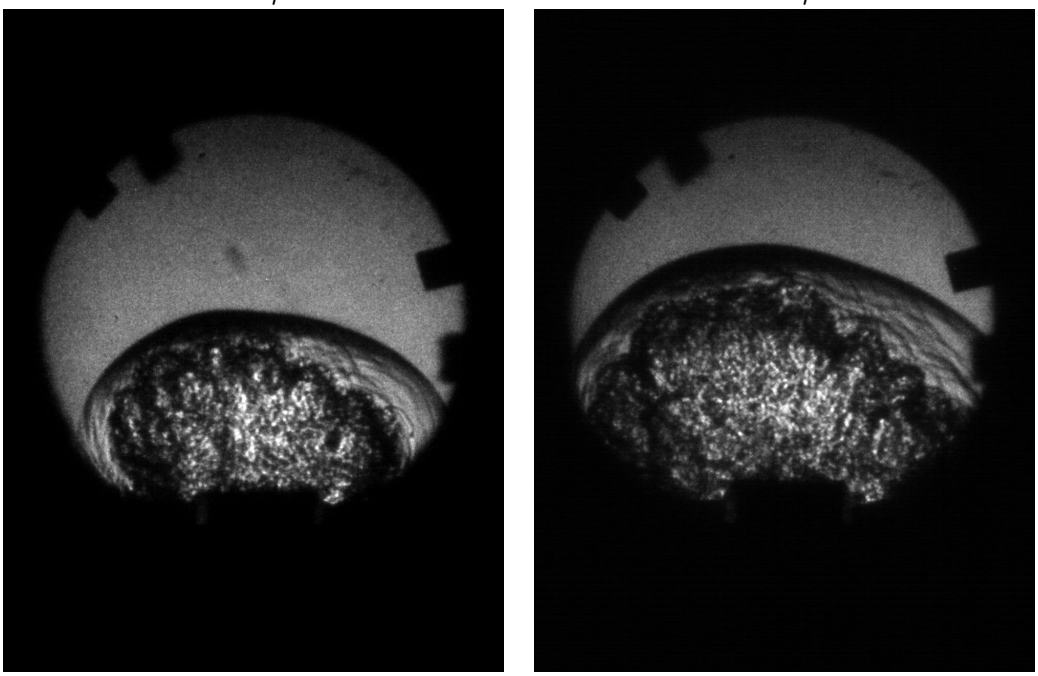

t=70μs t=100μs

Figure 126: Blast wave images for shot 55.

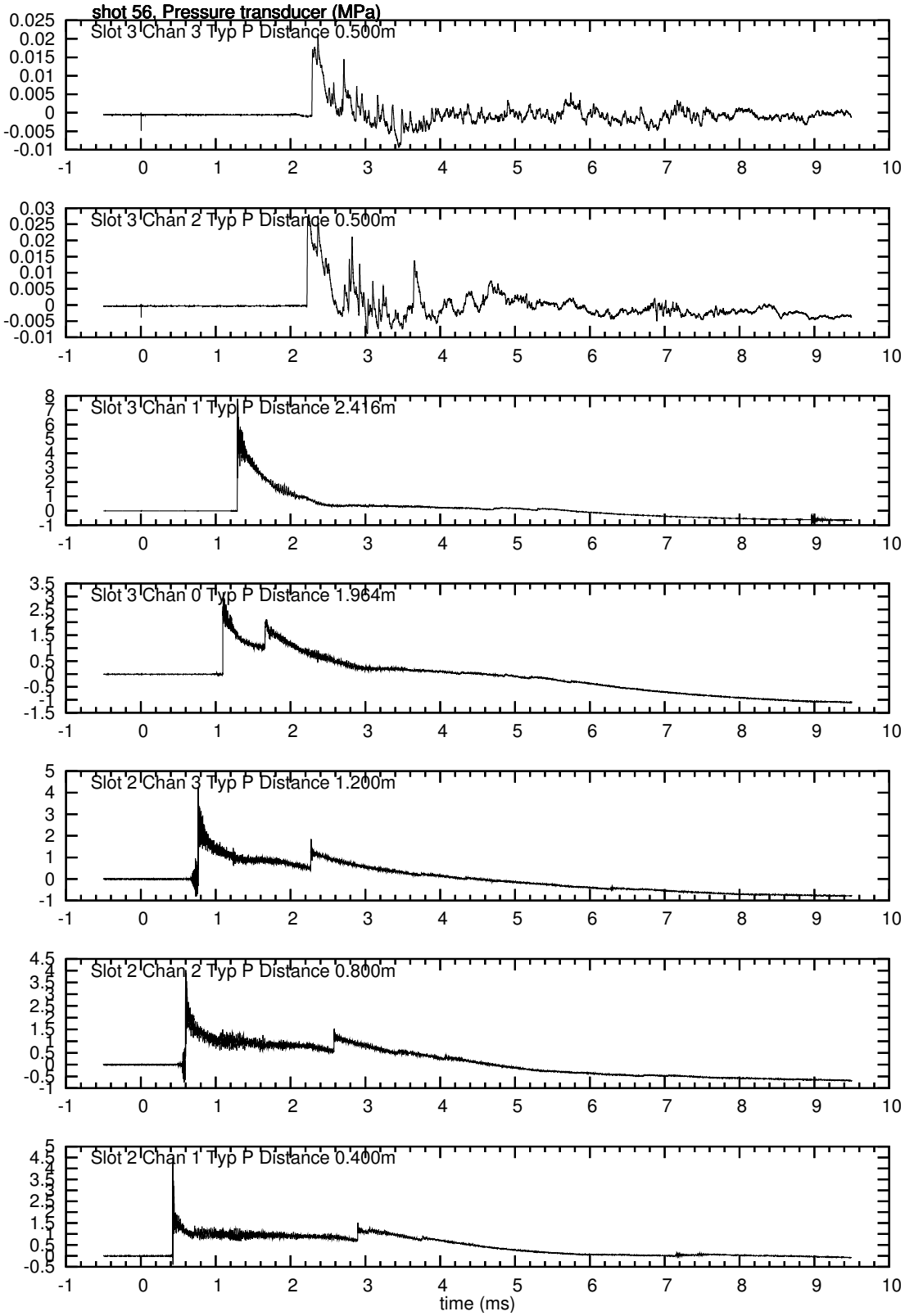

Figure 127: Pressure traces for shot 56

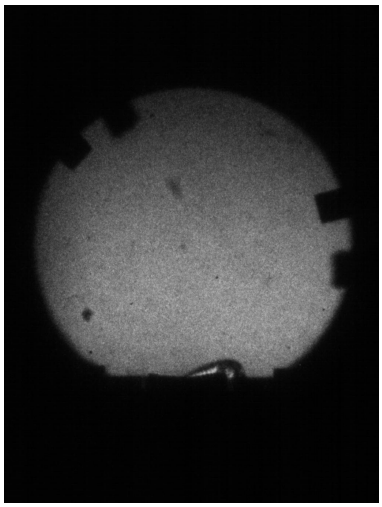

t=0μs

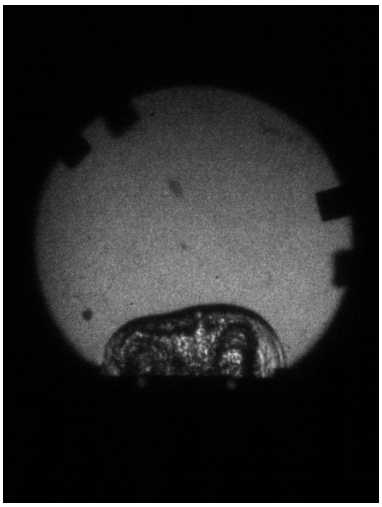

t=30μs

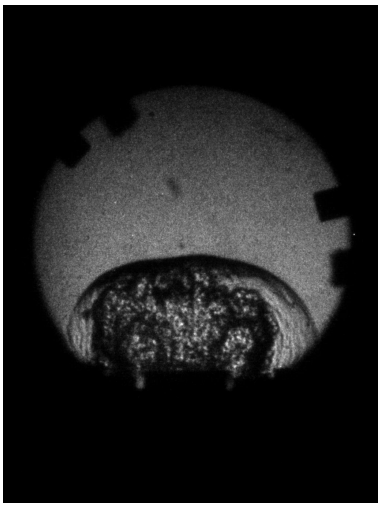

t=60μs

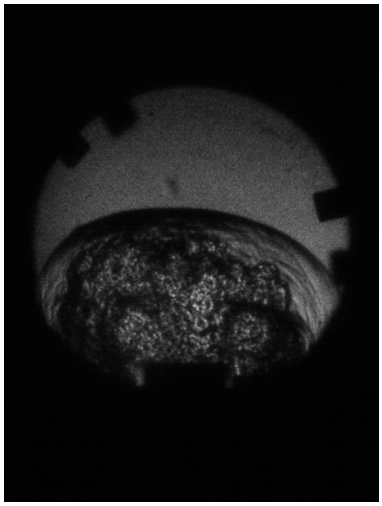

t=90μs

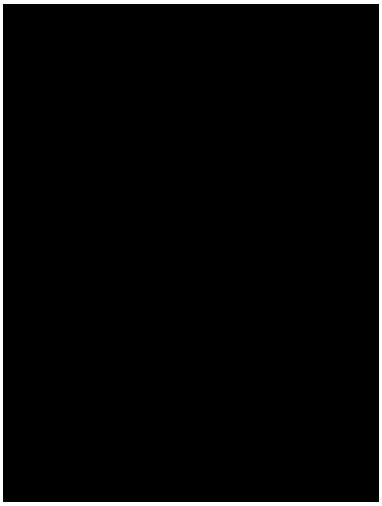

t=120μs

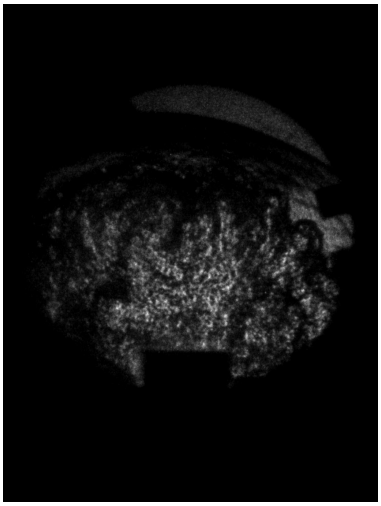

t=150μs

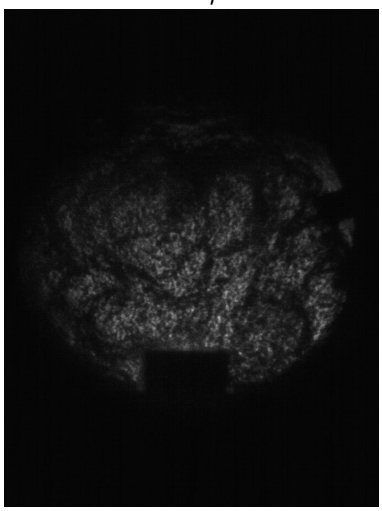

t=180μs

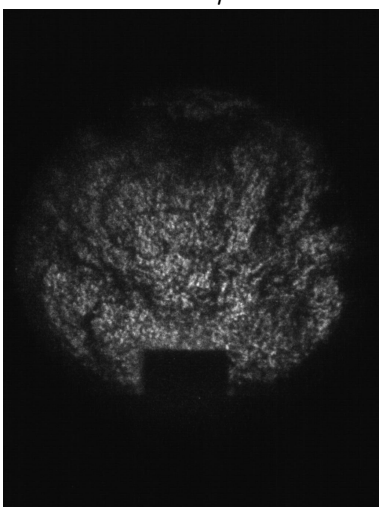

t=210μs

Figure 128: Blast wave images for shot 56.

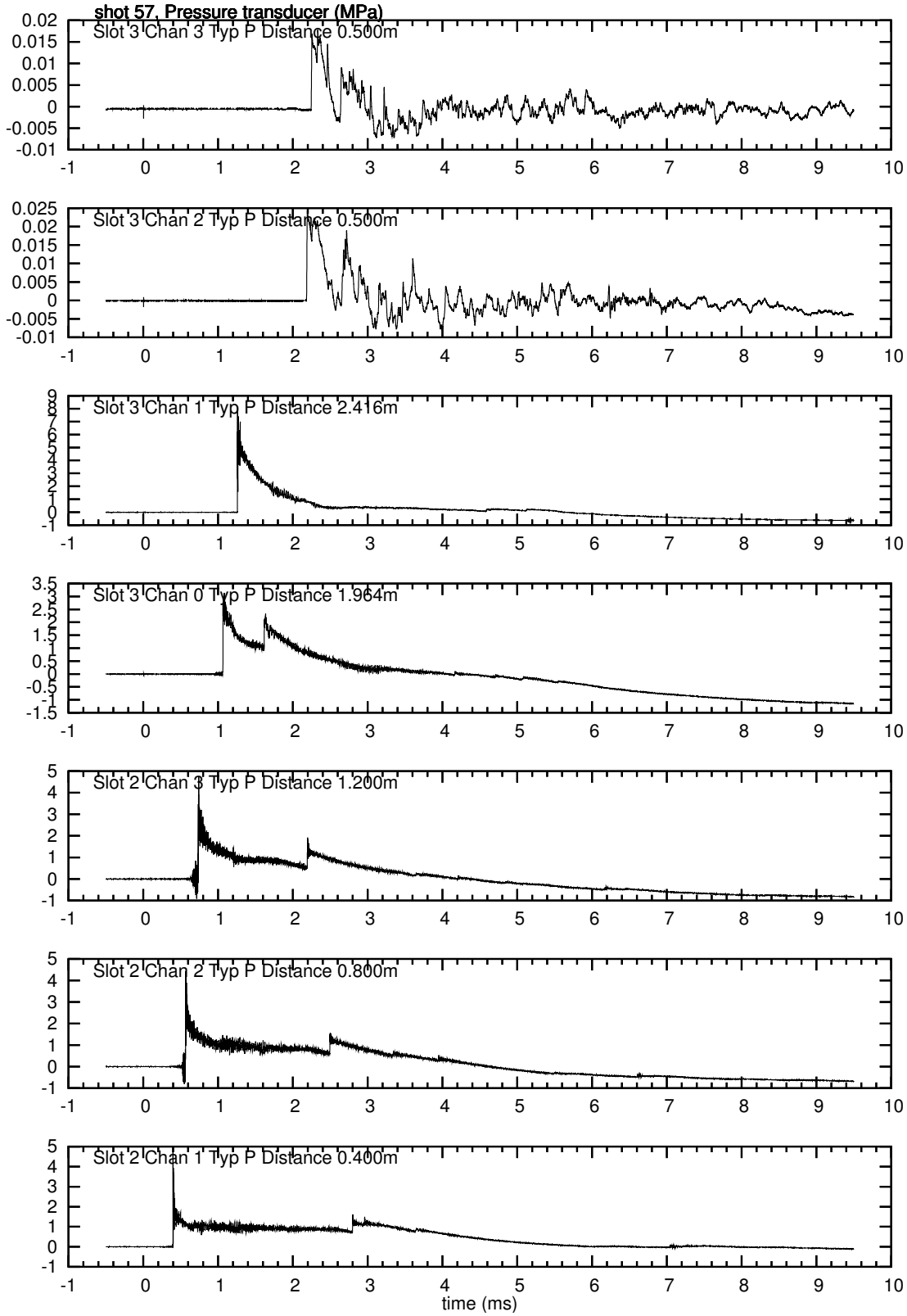

Figure 129: Pressure traces for shot 57

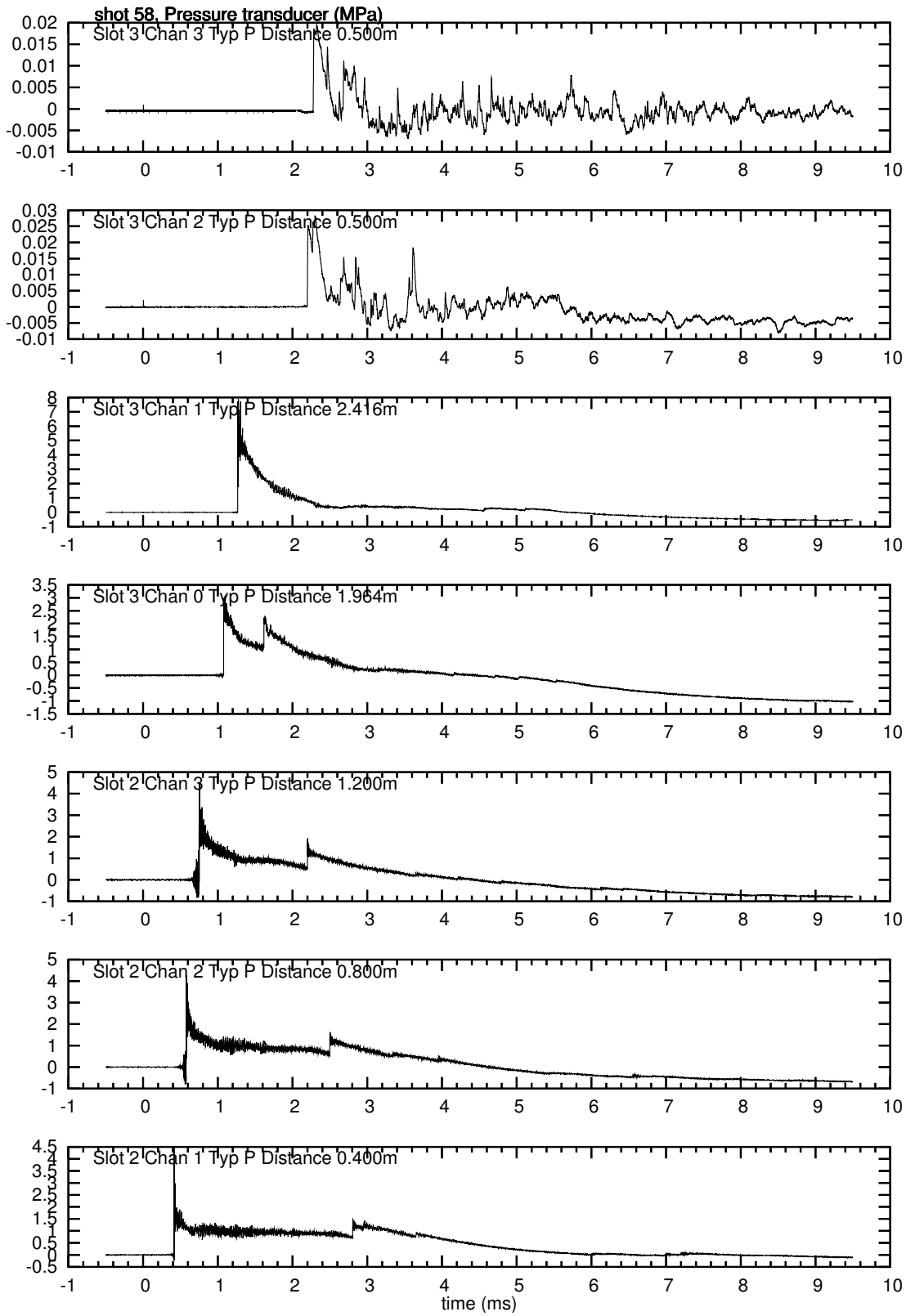

Figure 130: Pressure traces for shot 58

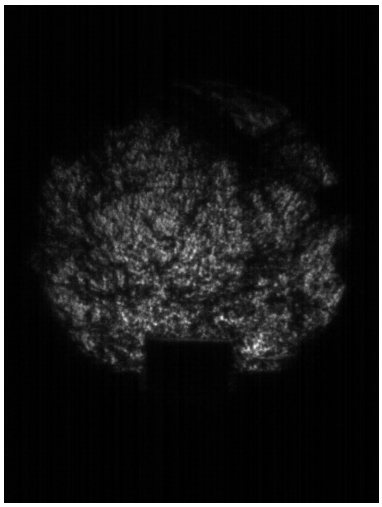

t=210μs

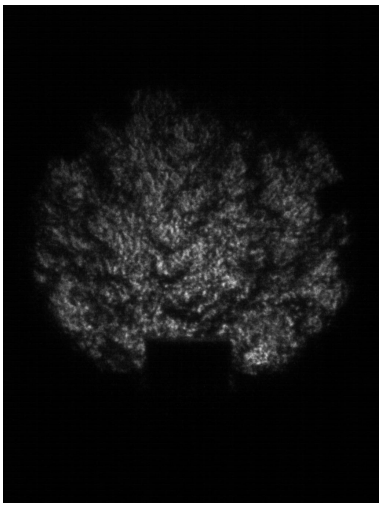

t=240μs

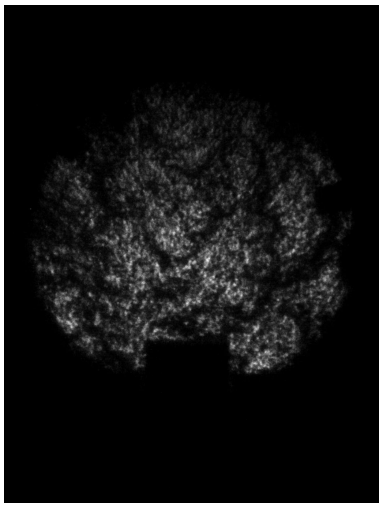

t=270μs

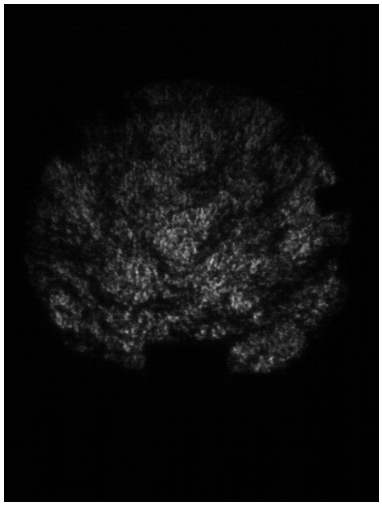

t=300μs

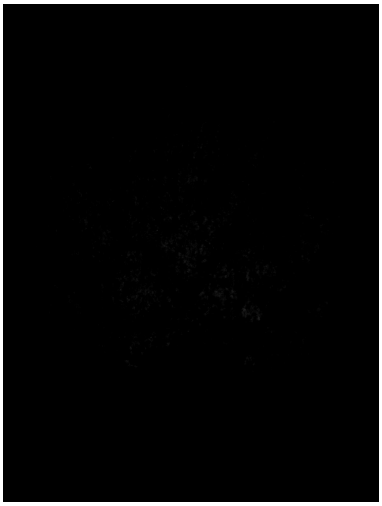

t=330μs

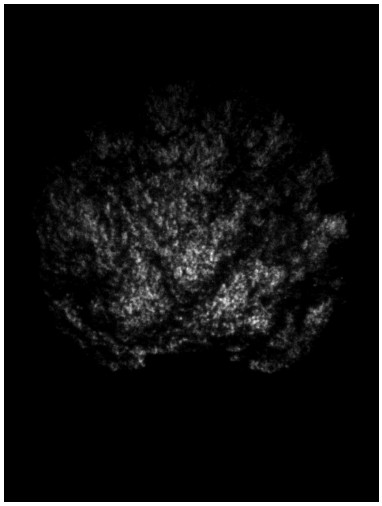

t=360μs

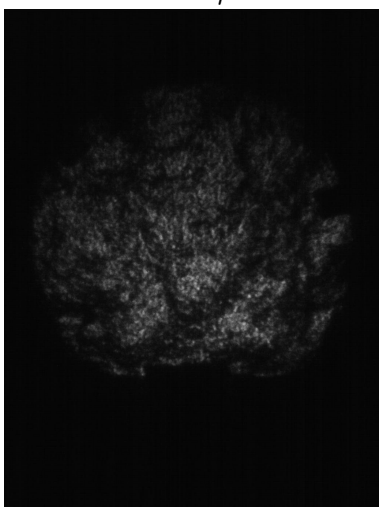

t=390μs

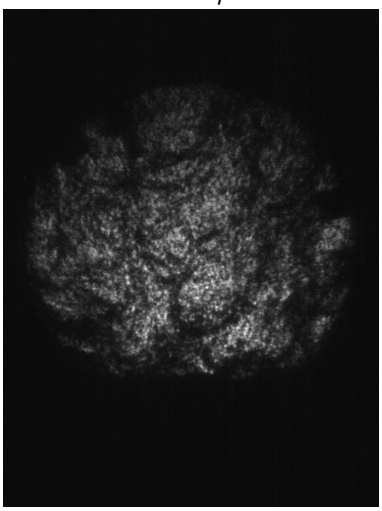

t=420μs

Figure 131: Blast wave images for shot 58.

D Thermal Stress

It is well known that temperature gradients can induce significant stresses in metals. This was observed for explosions inside a thick-wall tube in previous tests in the Explosion Dynamics Laboratories. Since that work was proprietary in nature and the distribution of the report restricted, a short discussion of the work and an excerpt of the text is given in this Appendix.

All experiments were carried out at initial pressure of $P_0 = 1$ bar and initial temperature of $T_0 = 300$ K. The CH_4-O_2 mixture composition was varied from $0.6 \leq O_2/C \leq 1.2$. A stainless steel (type 316) tube with a length of 1.25 m, inner diameter 127 mm, and a wall thickness of 12 mm was used for the experiments. The mixture was initiated by a glow plug at one end. Eight pressure transducer ports (P_0-P_7) were welded onto the tube sidewall and spaced at a distance of 127 mm. The pressure transducers were mounted in plugs that fit snugly within the ports, and the sensitive surface of the transducers was flush with the interior surface of the tube. A set of five strain gauges (S_0-S_4) was mounted on the outer tube surface, opposite to the pressure transducer ports P_2-P_6. The strain gauges of type CEA-06-032UW-120 (Vishay Measurements Group, Micro-Measurements Division) have a uni-axial strain gauge pattern and are oriented to measure the hoop strain of the tube. The gauges are operated with an excitation voltage of 10 V in the quarter bridge mode using the built-in 120 Ω dummy gauges of the signal conditioning amplifiers (Type 2310A, Vishay Measurements Group, Micro-Measurements Division). Depending on the peak strain in the experiment, the amplification factors for the strain gauge signals were varied from 500 to 10000 in order to employ the full range of the data acquisition system (±10V). The bridge circuits are balanced prior to the ignition event. The pressure and strain histories were recorded with a 12-bit data acquisition system sampling all channels with a maximum frequency of 2.5 MHz. The data acquisition system was triggered by the rising edge of the pressure transducer signal closest to the ignition flange. Tests were carried out with a portion of the interior of the tube insulated by a thick rubber sheet to demonstrate the thermal stress effect. The following excerpt from Pintgen and Shepherd (2005) describes the results of those tests and the analysis of the thermal stress effect.

"Representative pressure traces for the slow (sub-sonic) combustion regime are shown in Fig. 132. The pressure rises are nearly simultaneous throughout the tube. The peak pressure (0.5 MPa) is observed to be less than the calculated constant volume explosion pressure (P_{CV}=1.3 MPa), a consequence of the very slow flame propagation and the simultaneous cooling of the hot products inside the tube. In the slow combustion regime, the peak strain was measured to be on the order of 20–30 μ (Fig. 132b). As for the pressure transducers, a simultaneous rise is observed for the strain gauge signals throughout the tube. The highest

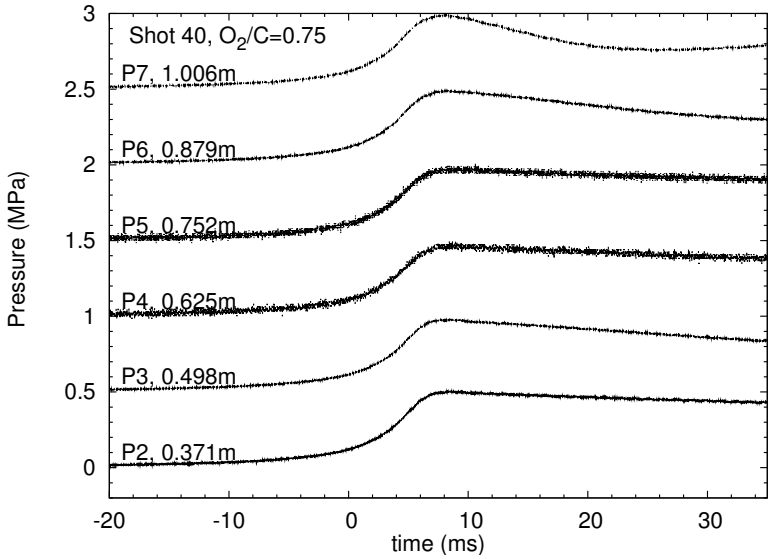

a)

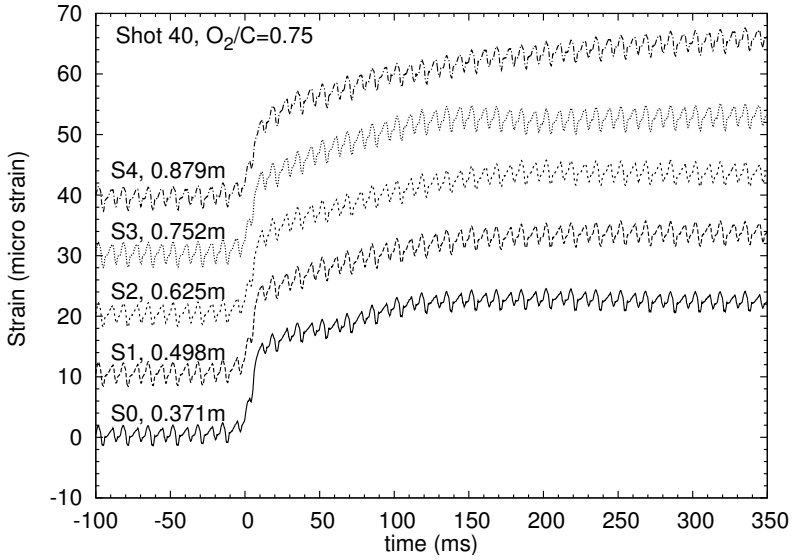

b)

Figure 132: Pressure (a) and strain histories (b) of shot 40, O_2/C=0.75, BR=0.37. Slow combustion regime.

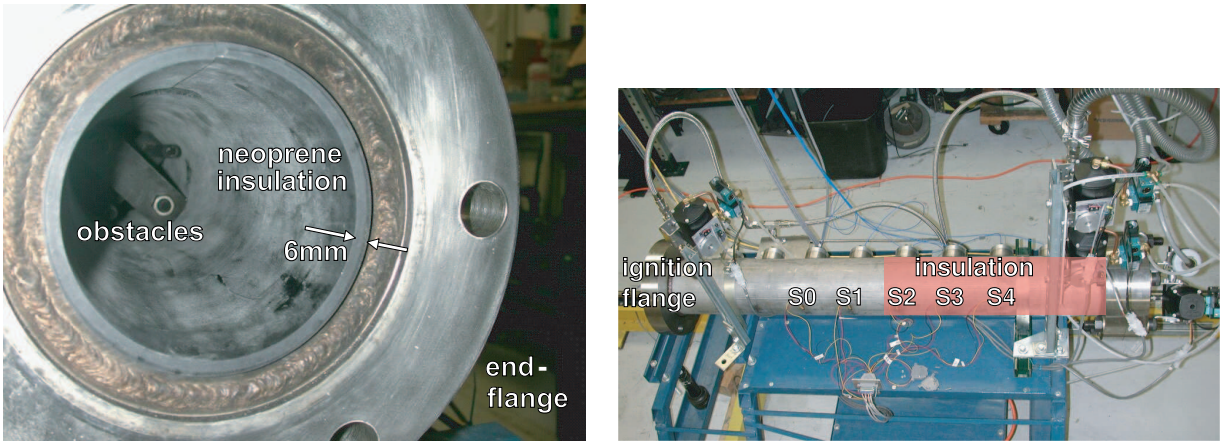

a) b)

Figure 133: a) Thermal insulation layer of 0.6 mm neoprene sheet on the inside of the tube. View into tube in the direction of the ignition-flange with end-flange removed. b) A 0.6 m long tube section was equipped with insulation. Strain gauges $S2$, $S3$, and $S4$ are not affected by thermal stresses.

amplification factor of 10000 had to be used to allow for the acquisition of the 100 μV peak signal resulting from the small peak strain. Despite careful shielding of the cable, a small amount of noise is visible for these very low signal experiments. The amplitude of the present noise in terms of the strain is approximately 3 μ. As the noise signal is observed prior to the ignition event, the signal is clearly not an effect of the tube oscillation but is electrical signal contamination with a frequency of approximately 120 Hz. For these very low signal experiments the presence of the noise required signal filtering for the precise determination of the peak strain.

Note that the strain measured on the tube outer surface in the slow combustion regime is not only originating from the high pressure inside the tube but also from thermal stresses. Heat transfer is taking place from the hot combustion products to the inner tube wall. This creates thin layer of heated metal on the inside of the tube. The thermal expansion of this layer creates a strain, which can be measured on the outer surface. The colder outer layer does not expand thermally but experiences strain from the expanding hot inner layer. This effect, known as thermal stress, contributes additionally to the hoop strain on the outer surface. To differentiate between the stresses originating from the internal pressure loading and the ones arising from the thermal loading, part of the tube was thermally insulated. A 6 mm thick neoprene layer was placed on the inside of the tube covering a 0.6 m long section of the tube over the entire circumference, (Fig.133). The tube section of strain gauges $S2$, $S3$, and $S4$ is, therefore, not affected by thermal stresses for this particular experiment. Shots 45 to 49 are equipped with the thermal insulation layer. All other experiments have

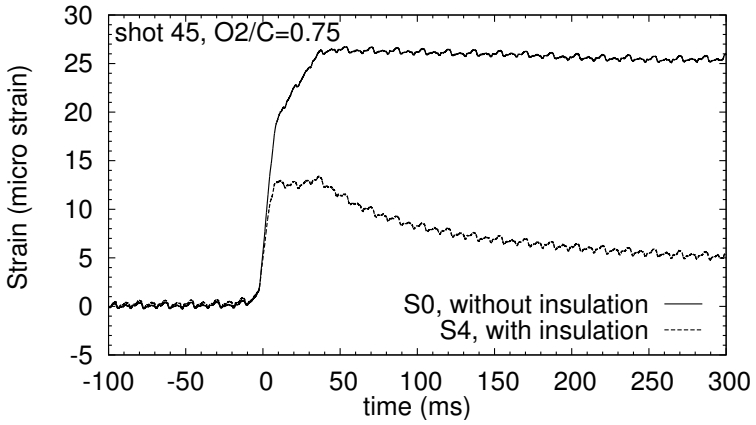

a)

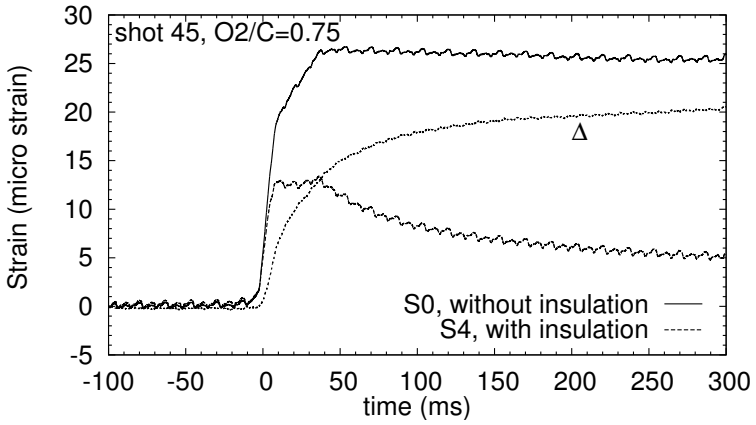

b)

Figure 134: a) Strain measurements in section without ($S0$) and with ($S4$) thermal insulation. b) The difference is the thermally induced strain Δ on outer tube surface.

been carried out without any insulation.

The insulation dramatically influences the strain measurements in the slow combustion regime (Fig. 134a). The peak strain measurements including thermal stresses are, for an O_2/C-ratio of 0.75 up to a factor of 2.3 higher. The thermal loading signal can be isolated by taking the difference Δ (Fig. 134b) between the strain gauge signal $S0$ which includes internal pressure and thermal loading and the signal of strain gauge $S4$ which includes only the pressure loading. The characteristic rise time of the thermal loading signal is approximately 50 ms and dominates the long time observation. An analytical estimation of the thermal stresses can be made with a simplified model. To do this, the characteristic penetration depth h of the heat into the inner tube layer and a characteristic temperature increase ΔT of that layer must be known (Fig. 135a). From the experimental observations, the characteristic time scale t_c of the heat transfer was determined to be approximately 50 ms.

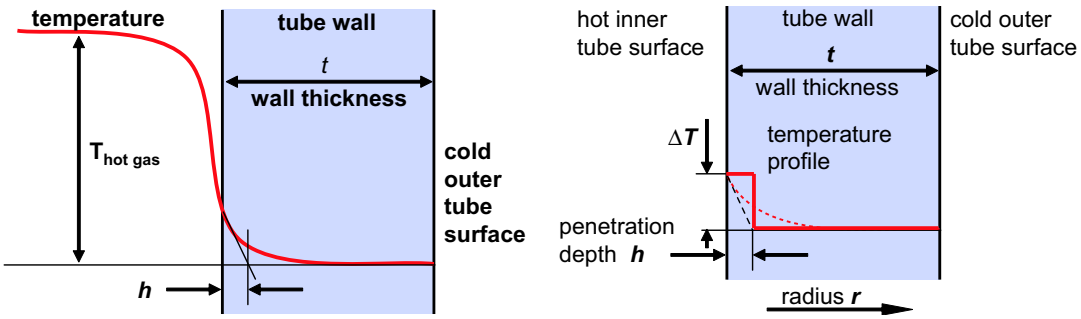

Figure 135: a) Thermal penetration depth into inner tube surface. b) Square wave approximation of temperature profile on the inner tube surface.

From the one-dimensional heat equation, the penetration depth is given as $h = \sqrt{\kappa t_c}$, where κ is the thermal diffusivity of steel. Given $\kappa_{steel} = 3.5 \cdot 10^{-6}$ m^2/s, the penetration depth h can be determined to be $h = 0.4$ mm. The temperature profile ideally has the form of the error function but is approximated here by a square-wave (Fig. 135b). This simplified situation corresponds to an inner tube layer of thickness h which is in temperature ΔT above the outer shell of the tube.

A model to derive the thermal stresses for a square temperature profile is to assume the tube to be separated into a warm, thin inner and a cold, thick outer shell; both are initially at the same tube temperature T_{out}. The outer radius of the inner shell and the inner radius of the outer shell are both r_c, the center radius. The inner shell is then heated up to $T_{out} + \Delta T$ and its outer radius r_{oI} expands to $r_{oI} = r_c + (\alpha r_c \Delta T)$. The shells are assumed to remain in contact at their interface, and the outer radius of the inner shell r_{oI} will decrease by Δr_{oI}. Correspondingly, the inner radius of the outer shell r_{iO} will expand by Δr_{iO}. The boundary conditions of displacement and normal stress (pressure) have to be matched at the interface. The displacement of the outer radius of the inner tube Δr_{oI} and inner radius of the outer tube Δr_{iO} are given from thick cylindrical shell theory by:

$$\Delta r_{oI} = \frac{P_{if}\, r_c\, (r_c{}^2 + r_i{}^2)}{E\, (r_c^2 - r_i^2)} \tag{16}$$

$$\Delta r_{iO} = \frac{P_{if}\, r_c\, (r_c^2 + r_o^2)}{E\, (-r_c{}^2 + r_o{}^2)}, \tag{17}$$

where P_{if} is the pressure at the interface. Note that a positive displacement is defined in the outside direction and P_{if} acts as internal pressure on the outer shell and as external load on the inner shell. The displacement condition to be matched is then given by $\Delta r_{iO} - \Delta r_{oI} =$

Δr_c, which enables, together with Eqs. 16 and 17, the determination of the interface pressure

$$P_{if} = \frac{\Delta r_c \, E \, ({r_c}^2 - {r_i}^2) \, ({r_c}^2 - {r_o}^2)}{2 \, {r_c}^3 \, ({r_i}^2 - {r_o}^2)}. \tag{18}$$

The stress $\sigma_{\theta\theta}$ and strain ϵ_θ on the tube's outer surface are then given by

$$\begin{aligned} \sigma_{\theta\theta} &= \frac{2 P_{if} r_c^2}{r_o^2 - r_c^2} \\ &= \frac{\alpha \, \Delta T \, E \, ({r_c}^2 - {r_i}^2)}{{r_o}^2 - {r_i}^2} \end{aligned} \tag{19}$$

$$\begin{aligned} \epsilon_\theta &= \sigma_{\theta\theta}/E \\ &= \frac{\alpha \, \Delta T \, ({r_c}^2 - {r_i}^2)}{{r_o}^2 - {r_i}^2}. \end{aligned} \tag{20}$$

As $h \ll r_i$, this can be further simplified using $r_c^2 - r_i^2 = (r_i + d)^2 - r_i^2 \approx 2 r_i h$, which leads to

$$\sigma_{\theta\theta} = \frac{\alpha \, \Delta T \, E \, 2 r_i h}{{r_o}^2 - {r_i}^2}. \tag{21}$$

A more sophisticated model can be used to check this result and extend it to the calculation of the thermally induced stress for arbitrary temperature profiles. The thermally induced hoop stress $\sigma_{\theta\theta}$ at a radial position r for an arbitrary temperature profile $\tau(r)$ is given (Noda et al., 2002) by

$$\sigma_{\theta\theta}(r) = \alpha E \left(\frac{1}{r^2} \int_{r_i}^{r_o} \tau(r) r \, dr + \frac{r^2 + r_i^2}{r^2 (r_o^2 - r_i^2)} \int_{r_i}^{r_o} \tau(r) r \, dr - \tau(r) \right), \tag{22}$$

where α is the coefficient of thermal expansion ($9.6 \cdot 10^{-6}$ K^{-1}), E is the Young's modulus (190 GPa), $\tau(r)$ is the temperature profile as a function of radius, and r_i and r_o are the inner and outer tube radius respectively. Setting $r = r_o$, the thermally induced stress on the outer surface simplifies Eq.22 to

$$\sigma_{\theta\theta}(r = r_o) = \alpha E \left(\frac{2}{r_o^2 - r_i^2} \int_{r_i}^{r_o} \tau(r) r \, dr - \tau(r_o) \right). \tag{23}$$

Using the temperature at the outer radius as a reference temperature for $\tau(r)$ and defining $\tau(r)$ as the temperature difference with respect to the temperature of the outer tube surface, the last term can be neglected since $\tau(r_o) = 0$. The thermal stresses are governed by the integral term of Eq. 23. The thermal stress on the outer surface is directly proportional to $\int_{r_i}^{r_o} \tau(r) \, r \, dr$. This integral, in turn, is directly proportional to the thermal energy content Q

	steel	hot gas
ρ[kg/m^3]	8238	0.917
k[W/(m K)]	13.4	0.5
c_p[J/(kg K)]	468	2934

Table 6: Thermal properties of steel and hot combustion products assuming constant volume combustion.

T[K]	P[bar]	u_g[MJ/kg]	$\epsilon_{\theta\ \text{thermal}}$ [μ strain]
2327	13.4	-1.97	0
1500	8.6	-3.85	10
1000	4.9	-6.16	22
500	1.7	-9.21	38
300	1.0	-9.49	39

Table 7: Gas pressure P, specific internal energy u_g, and calculated (Eq. 27) thermally induced strain during the cool down process from the constant volume combustion state (T_{CV}=2327 K).

per unit tube length

$$2\pi c\rho \int_{r_a}^{r_b} \tau(r)\, r\, dr = Q, \tag{24}$$

where c is the specific heat capacity of the tube and ρ is the density of the tube. Therefore, regardless of the specific temperature profile, the thermal stress on the outer tube surface is governed by only the total thermal energy content of the tube

$$\sigma_{\theta\theta}(r = r_o) = \frac{\alpha E}{2\pi c\rho}\frac{2}{r_o^2 - r_i^2} Q, \tag{25}$$

For the square-wave temperature profile $Q = 2\pi c\rho r_i h \Delta T$, the simplified model, Eq. 21, agrees with the results derived above

$$\sigma_{\theta\theta}(r = r_o) = \alpha E \frac{2 r_i h \Delta T}{r_o^2 - r_i^2}. \tag{26}$$

The fact that the thermal stress does not depend on the specific temperature profile within the tube simplifies the problem, as the thermal stress at a given time depends only on the total energy transferred from the hot gas to the tube wall up to that time. In order to estimate the thermally induced stress, an energy balance between the hot gas and the inner shell has to be considered. The constant volume combustion temperature for a O_2/C=0.75 mixture at $P_0 = 1$ bar was calculated to be T_{CV}=2327 K and the constant volume combustion pressure P_{CV}=13.3 bar using `stanjan` Reynolds (1986b). The specific heat capacity depends on the gas temperature. The specific internal energy u was calculated for several temperatures

during the cool-down process (Table. 7). The energy balance between the heat-affected inner tube shell and the hot gas initially at temperature T_{CV} cooling to T_{cool} is

$$\begin{aligned} \Delta E_{gas} &= \Delta E_{tube}, \\ \rho_g V g \ (u_g(T_{CV}) - u_g(T_{cool})) &= Ql, \end{aligned} \tag{27}$$

where $l = 1.25$ m is the tube length, u_g and ρ_g are the specific energy and density of the gas, respectively, and V is the volume of the tube. Assuming a square-wave temperature profile leads to

$$\rho_g V g \ (u_g(T_{CV}) - u_g(T_{cool})) \ = \ \rho_s \, 2\pi r_i h l \Delta T. \tag{28}$$

The heat transfer to the end flanges and obstacles are neglected in this simplified analysis. Assuming cooling to $T_{cool} = 1000\ K$ ($\Delta U = 4.2$ MJ/kg) results in a thermally induced stress and strain of $\sigma_{\theta\theta}$=4.6 MPa and ϵ_θ=22 μ. For a square-wave temperature assumption with $h = 0.4$ mm, this leads to ΔT=79 K. This is in good agreement with the thermal stresses of 20μ measured experimentally (Fig. 134b). Note that for long times, all excess energy in the gas will be transferred to the tube walls. The expected strain for $T_{cool} = 300$ K and long times based on this model is 39 μ. The discrepancies between the results and the model can be explained by the limited data recording time and the simplifications of the analysis. The thermal stresses influence the determination of the peak strain only in the slow combustion regime for two reasons. In the fast combustion regime, the time scale of the peak pressure loading is much shorter ($\approx 100\ \mu s$) than the characteristic time scale of the thermal loading (≈ 100 ms). Only in the slow combustion regime are the time scale of the pressure rise and the thermal loading comparable. Furthermore, the thermal loading is negligible in the fast combustion regime because the peak strain caused by the pressure loading is up to 40 times higher than that caused by thermal stresses. The strain caused by the thermal loading is too small and occurs too late to influence the peak strain measurements in the fast combustion regime.

In general, the strain measured on the outer surface is also a function of the overall tube temperature. When the tube temperature is increased uniformly over the throughout the wall thickness, the entire tube expands uniformly and no thermal stresses are induced. Nevertheless, the strain resulting from the thermal expansion is detected by the strain gauges. In this case, there is thermally induced strain without thermally induced stress. For the analysis shown above, the outer surface temperature was taken as the reference temperature for the assumed temperature profile within the tube ($\tau(r = r_o) = 0$). The temperature on the outer surface of the tube increases in the experimental setup during a series of ten shots

approximately up to 32° C, 10° above room temperature. This effect does not influence the strain gauge measurements over a series of experiments for two reasons. The strain gauge circuits are balanced prior to each experiment and the gas temperature of the hot combustion products is large compared to the slight increase of the tube temperature, causing a negligible effect on the heat transfer rate from the gas to the tube."[2]

[2]Quoted from pp. 5-13 of Pintgen and Shepherd (2005) with typographical errors corrected.